A geophysical study of propagating rifts at the Bight-Transform Fault on the southern part of the Reykjanes Ridge and in the Eastern Volcanic Zone of Iceland

Ásdís Benediktsdóttir

Faculty of Earth Sciences
University of Iceland
2019

A geophysical study of propagating rifts at the Bight-Transform Fault on the southern part of the Reykjanes Ridge and in the Eastern Volcanic Zone of Iceland

Ásdís Benediktsdóttir

Dissertation submitted in partial fulfillment of a
Philosophiae Doctor degree in Geophysics

Coordinator
Freysteinn Sigmundsson

PhD Committee
Dr. Freysteinn Sigmundsson, University of Iceland
Dr. Ólafur Guðmundsson, Uppsala University
Bryndís Brandsdóttir, University of Iceland

Opponents
Dr. Jason Phipps Morgan, Royal Holloway, University of London
Dr. Nicholas Rawlinson, University of Cambridge

Faculty of Earth Sciences
School of Engineering and Natural Sciences
University of Iceland
Reykjavik, June 2019

A geophysical study of propagating rifts at the Bight-Transform Fault on the southern part of the Reykjanes Ridge and in the Eastern Volcanic Zone of Iceland
Geophysical study at propagating rifts
Dissertation submitted in partial fulfillment of a *Philosophiae Doctor* degree in Geophysics

Faculty of Earth Sciences
School of Engineering and Natural Sciences
University of Iceland
Sturlugata 7
101, Reykjavik
Iceland

Telephone: 525-4000

Bibliographic information:
Ásdís Benediktsdóttir, 2019, *A geophysical study of propagating rifts at the Bight-Transform Fault on the southern part of the Reykjanes Ridge and in the Eastern Volcanic Zone of Iceland*, PhD dissertation, Faculty of Earth Sciences, University of Iceland, 61 pp.

ISBN 978-9935-9412-5-1

Printing: Háskólaprent
Reykjavik, Iceland, June 2019

Abstract

Iceland is located on the Mid-Atlantic Ridge and is the surface exposure of the ridge system on land. The influence of the plume has been shown to reach towards the south at least as far as the Bight Transform Fault. The ridge system in Iceland has also been evolving spatially and temporally during the life time of Iceland. One of the best documented and understood mechanisms, where by plate boundaries evolve, is the propagating rift mechanism. Two such areas are studied in the dissertation; Eyjafjallajökull volcano in South Iceland and the area between the Bight-Transform Fault and 80 km south of it. These two areas are both located in front of the advancing limb of a propagating rift.

Two papers focus on the Eyjafjallajökull volcano area. In the first paper the velocity structure of the volcano is presented. A fairly new method is used where long-time series of small surface waves are used as a source for tomography. The signal source of the method is the ambient noise, originating in the oceans. If such persistent signal is observed over long enough time and then cross-correlated between two seismic stations, a signal emerges that contains information on the path between the two receivers. Using data from a 7 month long period from stations located around the volcano, ambient seismic tomography was possible around Eyjafjallajökull. Reliable phase dispersion curves were obtained between 1-7 s and sensistivity kernels showed resolution down to 10 kilometers depth. The results show two high-velocity zones elongated E-W on either side of caldera. In between a zone of relatively lower-velocity is observed. The lower-velocity zone coincides with an inferred magma pathway under the volcano as observed from earthquakes in the 2010 Eyjafjallajökull volcano eruption. The higher-velocity zones are interpreted as zones of intrusive rocks.

The second paper on Eyjafjallajökull focuses on the tremor observed during the 2010 eruption. Tremor can be located in several different ways, e.g. if the source is isotropic a simple amplitude decay with distance can be used. This was not the case with the 2010 Eyjafjallajökull eruption. Tremor levels increased during the eruption and the tremor evolution during the eruption can be linked with other parameters, such as the eruption mechanism (i.e. effusive vs. explosive phase of the eruption). The paper addresses two main issues; location of the tremor source and analyses of the power ratios of different time series from different seismic stations. The location of the tremor was very stable in the 0.5-2 Hz frequency range during the entire span of the eruption. The location agrees well with the cauldrons formed in the eruption. Because the location was stable, many parameters in the amplitude decay equation stayed the same during the course of the eruption giving rise to a simple parameter-estimation problem with ample redundancy. Results suggests that the tremor was mostly composed of surface waves and that the Q values within the volcano are in the range of about 10-20. For

paths outside the volcano Q is between 20 and 50.

The second study area, the first 80 km south of the Bight Transform Fault (BTF), marks the location where the spreading on the Mid-Atlantic Ridge changes from 30° oblique to the trend of the ridge to the north of the transform, to the expected, orthogonal spreading relative to the trend of the ridge. By analysing magnetic anomalies <6 Ma in the region, the kinematic evolution of the area was revealed. A series of small-scale propagators transfer lithosphere from the Eurasian Plate to the North-American Plate. This observed asymmetric accretion of lithosphere fits well with the asymmetric crustal accretion that is found to the north, on the Reykjanes Ridge and on Iceland. The asymmetry to the north of the BTF can be attributed to the movement of the ridge system relative to the Iceland hotspot. It can therefore, be concluded that the influence of the Iceland hotspot reaches farther south than the BTF, 1000 km south of the Iceland hotspot.

Útdráttur

Á Íslandi rís Atlantshafshryggurinn yfir sjávarmál vegna samspils hans við heitan reit þar sem eldvirkni er mikil. Ásýnd hryggjarins er nokkuð flókin þar sem hann skiptist upp í nokkur misgömul rekbelti. Hryggurinn leitast við að liggja yfir miðju heita reitsins, sem í dag er undir vestanverðum Vatnajökli. Afstæð hreyfing heita reitsins og hryggjarins veldur því að eldri rekbelti, sem eru óvirk í dag, er að finna vestan núverandi rekása. Utan Íslands er ásýnd Atlantshafshryggjarins einfaldari, þar sem eitt rekbelti er virkt á hverjum tíma, en hryggurinn þróast samt sem áður í tíma og rúmi. Við hliðrun rekbelta myndast framsækin rekbelti, þ.e. kerfi þar sem einn armur rekbeltis vex á kostnað annars. Tveimur svæðum á framsæknum rekbeltum er lýst í doktorsritgerðinni; Eyjafjallajökli sem liggur í hinum framsækna hluta Eystra gosbeltisins og svæðinu suður af Bight-þverbrotabeltinu, við framsækna enda Reykjaneshryggjarins.

Tvær greinar fjalla um Eyjafjallajökul og nálæg svæði. Fyrri greinin lýsir nýju hraðalíkani yfirborðsbylgna innan eldfjallsins. Nýlegri aðferð er beitt, þar sem langar tímaraðir lítilla yfirborðsbylgna með upptök í úthöfunum eru mældar. Ef veikt merki sem þetta er endurtekið oft, má með víxlreikningum milli tveggja jarðskjálftamælistöðva, draga fram merki sem inniheldur upplýsingar um hraðaskipan jarðarinnar á milli stöðvanna. Þessi aðferð er kölluð suðtómografía. Suðtómografía var framkvæmd með gögnum frá sextán skjálftamælistöðvum umhverfis Eyjafjallajökul yfir 7 mánaða tímabil. Áreiðanlegir fasahraðaferlar voru mældir á lotubilinu 1 - 7 sekúndur. Næmnireikningar leiddu í ljós að líkanið hafði góða upplausn niður á 10 kílómetra dýpi. Niðurstöðurnar benda til þess að tvö háhraðasvæði, með austur-vestur stefnu, liggi beggja vegna gígsins í toppi eldfjallsins. Á milli þeirra er tiltölulega lágur hraði. Á því svæði urðu smáskjálftar í Eyjafjallajökulsgosinu árið 2010, sem benda til þess að þarna hafi verið kvikuuppstreymi. Háhraðasvæðin eru túlkuð sem eldri, kólnuð innskot. Önnur greinin um Eyjafjallajökul fjallar um óróann í eldgosinu árið 2010. Hægt er að staðsetja óróa á mismunandi hátt. Ef uppsprettan geislar bylgjum jafnt í allar áttir má skoða hvernig útslag minnkar með fjarlægð frá henni. Í ljós kom að þessa einföldun var ekki hægt að gera við úrvinnslu gagna frá 2010 gosinu. Greinilegur órói mældist á meðan á gosinu stóð og breytileika hans var hægt að tengja við gang gossins, t.d. hvort sprengivirkni hafi verið mikil eða lítil. Greinin tekur á tveimur vandamálum; staðsetningu uppsprettu óróans og greiningu aflhlutfalla milli ólíkra mælistöðva, sem breyttust með tíma á meðan gosið stóð yfir. Staðsetning uppsprettunnar var mjög stöðug allt gosið á tíðnibilinu 0.5-2 Hz og í góðu samræmi við sigkatla, sem mynduðust í jöklinum í byrjun gossins og gígana, sem mynduðust vegna ísbráðnunar. Stöðugleiki uppsprettunnar gerði það að verkum að hægt var að meta ýmsa eiginleika óróans með einfaldri aðfallsgreiningu. Niðurstöður þeirrar greiningar benda til þess að óróinn hafi aðallega verið samsettur af yfirborðsbylgjum og að Q-stuðull fyrir bylgjudeifingu

innan eldfjallsins sé um Q=10-20 en utan þess á milli 20 og 50. Mestur breytileiki í útslagsmynstri óróans mældist þegar sprengivirkni var við lágmark en uppsprettan var nær því að geisla jafnt í allar áttir á meðan sprengivirkni var mikil.

Hitt rannsóknarsvæðið nær frá Bight-þverbrotabeltinu og 80 km þar til suðurs, þar sem rekstefna Atlantshafshryggjarins breytist frá því að liggja 30° skáhallt á hrygginn í stefnu hornrétt á hrygginn. Reksaga svæðisins var rakin með því að greina segulmælingargögn síðustu 6 milljóna ára. Röð lítilla framsækinna hryggja færa stinnhvolf frá Evrasíuflekanum yfir á Norður-Ameríkuflekann. Þessi ósamhverfa í færslu stinnhvolfs frá einum fleka yfir á annan, kemur heim og saman við svipaða ósamhverfu norðan rannsóknarsvæðisins á Reykjaneshryggnum og á Íslandi. Ósamhverfuna á hryggnum norðan Bight-þverbrotabeltisins er hægt að skýra með afstæðum færslum heita reitsins og hryggjakerfisins. Það má því álykta að áhrifa frá heita reitnum á Íslandi gæti suður fyrir Bight-þverbrotabeltið, allt að 1000 kílómetrum suður af miðju heita reitsins á Íslandi.

Fyrir Anítu og Tönju, sem fæddust á meðan á doktorsnáminu stóð og gáfu lífi mínu magnaðan tilgang.

For Tanja and Aníta who came into the world during this work and gave me a sense of purpose.

Átta ára vegferð lýkur nú.
"Afhverju svona lengi?" hugsar þú.
Ég ól tvö börn á leiðinni
og það seinkaði förinni.

Eftir fimm ár
hóf ég störf hjá ÍSOR.
Það var mikið gæfuspor.
En ritgerðin varð
aukavinna -
um kvöld
og helgar
og á hátíðardögum.

Sautjándi júní,
þau fara í göngu.
Ég skrifa.

Páskarnir koma.
Ég vinn, þau fara í sumó.

Litlar stelpur og góður maður
sem var (og er) ALLTAf glaður!
"Ekkert þvaður
þú heldur áfram!"
sagði hann.
(takk Tryggvi!)

Þolinmóðir leiðbeinendur,
sem útskýra forsendur
aftur og aftur og aftur.

Pepp hér og þar

frá mömmu í gær
og pabba í dag.
"Hvernig gengur"
spyrja systur, vinkonur
og dætur.

Langir dagar, þreyttur hugur.
"Mamma ertu að vinna í viðgerðinni?"
spyr lítil stelpa.
Já, bara pínulítið eftir.

Þrautseigjan kom sér vel,
en ég samt tel
að án sterks stuðningsnets,
sé þetta ekki hægt!
Takk elsku fjölskylda!
Takk elsku vinir!

Sautjándi júní,
við *förum í göngu.*

Þegar öllu er á botninn hvolft
hvernig sem á það er horft
Þá er það fólkið þitt
sem mestu máli skiptir!

Preface

The thesis work started in 2011 within the Volcano Anatomay Project, which was a three-year project funded by the Icelandic Research Fund. A collaboration between the University of Iceland, Uppsala University in Sweden and the Icelandic Meteorological Office was important in the project. Freysteinn Sigmundsson, University of Iceland, was the coordinator for the project and my thesis work, but the supervision was in the hands of Ólafur Guðmundsson at Uppsala University with input from Bryndís Brandsdóttir at the University of Iceland.

The analysis of the magnetic data from the Reykjanes Ridge was supervised and worked in a close collaboration with Richard Hey and Fernando Martinez, at the Hawaiian Institute of Geophysics and Planetology, University of Hawaii, USA. That part of the thesis was partly funded by the National Energy Authority of Iceland and the National Science Foundation in the USA.

During the time span of the thesis work I gave birth to two daughters, first Aníta in August 2012 and then Tanja in June 2014.

Table of Contents

List of Figures

List of Original Papers

Paper I: Benediktsdóttir, Á., Hey, R., Martinez, F., Höskuldsson, Á. (2016). A new kinematic model of the Mid-Atlantic Ridge between $55°55'N$ and the Bight Transform Fault for the past 6 Ma. *Journal of Geophysical Research: Solid Earth*, 121, 455-468. doi:10.1002/2015JB012504

Paper II: Benediktsdóttir, Á., Gudmundsson, Ó., Brandsdóttir, B., Tryggvason, A. (2017). Ambient noise tomography of Eyjafjallajökull volcano, Iceland. *Journal of Volcanology and Geothermal Research*, 347, 250-263. doi:10.1016/j.jvolgeores.2017.09.017

Paper III: Benediktsdóttir, Á., Gudmundsson, Ó., Li, K.L., Brandsdóttir, B. (2019). Volcanic tremor of the 2010 Eyjafjallajökull eruption. In preparation for *Geophysical Journal International.*

Abbreviations

ANT	Ambient Noise Tomography
BFZ	Bight Fracture Zone
BTF	Bight Transform Fault
DR	Dying Rift
EVRZ	Eastern Volcanic Rift Zone
EVZ	Eastern Volcanic Zone
FR	Failed Rift
KR	Kolbeinsey Ridge
MAR	Mid-Atlantic Ridge
PF	Pseudofault
RP	Reykjanes Reninsula
RR	Reykjanes Ridge
SISZ	South Iceland Seismic Zone
SIVFZ	South Iceland Volcanic Flank Zone
TFZ	Tjörnes Fracture Zone
WVZ	Western Volcanic Zone
ZTL	Zone of Transferred Lithosphere

Acknowledgments

The journey of this thesis has been long, winding and full of obstacles, hindrances, and challenging tasks. First I would like to thank the people who accepted me as a Ph.D. student in the Volcano Anatomy Project without whom I would never have started the studies. I would like to thank the coordinator of the study, Freysteinn Sigmundsson, for being flexible and encouraging me to pursue what I am passionate about. Thanks for the never-ending positive attitute, solution based thinking, and for being an extremely good role-model.

I would like to thank Richard Hey for the weekly Skype conversations to Hawaii and for teaching me everything about propagating rifts and plate tectonics. Mostly, I thank him for teaching me great work ethics and for accepting me as a student in Hawaii prior to this work. Fernando Martinez I would like to thank for excellent and enlightening conversations and for easing me into the world of GMT and awk. I use many of his original scripts in my current work.

Ólafur Guðmundsson taught me everything I know about seismology and tomography. I would like to thank him for teaching me the importance of knowing your assumptions and limitations, which have proven to be some of the most important concepts in the world of underdetermined and non-linear problems. Thanks for being extremely thorough and patient when it comes to explaining concepts, arguing about something in the data or simply when it comes to writing text. Also, thanks for easing me into the C programming language and pointers.

I would like to thank Bryndís Brandsdóttir for great conversations about the geology and geophysics of volcanoes and for giving me valuable input into the thesis. Thanks for your passion and enthusiasm about geoscience, it is contagious and has effected me greatly. I always felt full of energy and driven to continue work after our conversations.

The thesis was supported by the Icelandic Research Fund (the Volcano Anatomy Project) and partially by the National Energy Authority of Iceland (Orkustofnun). I received a student stipend from the Nordic Earthquake Researcher Network (Nordquake) to attend a course on Seismology in Uppsala and a course on Seisan in Copenhagen. The Faculty of Earth Sciences gave me a travel grant to attend the AGU Fall meeting in 2014. I was alwo awarded a grant from the Science-and research fund of South Iceland (Vísinda- og rannsóknasjóður Suðurlands).

Sigurlaug, thanks for being the perfect office mate and for all the long conversations about something else than work. Thanks to Gro, Ásta, Stephanie, Vincent, Ríkey, Sófus, Olga, Ágúst, Sigrún and other fellow students and co-workers for making the years in Askja awesome.

Special thanks go to Tryggvi, the pep-master, who supported me through the entire journey, either by helping me with pointers, Python or some other computer problems,

or by taking care of Aníta and Tanja for long periods of time so I could work. Thanks for all the cheering and pep-talk. Also, thanks to Aníta and Tanja for being patient and allowing me to spend hours away working on the thesis.

Thanks to my parents, who always encouraged me to go for higher education, for the support and for 'knowing' all-along that I could do this. Thanks to Auður and Berglind for being a great moral support through the entire process.

Thanks to my fellow singers at Vocal Project, for giving my something to look forward to every Tuesday night.

Thanks to all the awesome, lovely and supporting people around me! Hanna, Stína, Björk, Björgvin, Lóló, Sissa, Tobba, Dísa, Arnar, Egill, Hansi, Gylfi, Knútur and other co-workers at ÍSOR.

Thanks to ÍSOR for giving me flexible hours to work on dissertation.

1 Introduction

The movement of tectonic plates shapes the world more than most can imagine. Complications within three main types of plate boundaries, divergent, convergent and transform, give rise to propagating rifts, island arc, back-arc basins, collision belts and various shear-zone complexities.The re-arrangement and evolution of the tectonic plates alters ocean circulation which in return changes the climate. For instance the uplift of the Tibetan plateau caused increased chemical weathering, which decreased the atmospheric CO_2, which led to cooling in the Cenozoic Era (Raymo and Ruddiman, 1992). Also, the closure of the central American seaway and the creation of the Panama Isthmus led to an intensified Gulf Stream, heating up the northern hemisphere (Haug and Tiedemann, 1998). If it weren't for the Panama Isthmus, Iceland might not be habitable! The relative movement of plates also plays an important role in modern day society as many places that are most prone to natural hazards are located at plate boundaries.

The study of plate tectonics includes the documentation of the temporal and spatial development of the plates. One of the best documented and understood plate boundary re-organization mechanism is the propagating rift. A ridge segment grows at the expense of an adjacent ridge segments in which spreading slowly ceases (e.g. Hey et al., 1980). This dissertation is based on geophysical research in two such regions, where major tectonic reorganizations are underway because of ridge segment propagation.

1.1 Research objectives

In order to improve our understanding of propagating rifts, two regions located in the non-spreading area in front of the advancing limb of the propagating rift system, were selected. The subaerial Eyjafjallajökull volcano and a section of the Mid-Atlantic Ridge. In the land-based setting the focus is on the velocity structure of Eyjafjallajökull and the volcanic tremor associated with its 2010 eruption. In the ocean-based settings the focus is on a fine-scaled tectonic model based on magnetic data spanning the last 6 Ma. The area is located between 55°55′N and the Bight Transform Fault (BTF) on the Mid Atlantic Ridge, i.e. in front of the southward propagating Reykjanes Ridge (RR) (Figure 1.1). In the work presented here the definition of the southern end of the RR is where it meets the Bight-Transform Fault (BTF).

The Eyjafjallajökull volcano is located within the South Iceland Volcanic Flank Zone (SIVFZ) (Figure 1.1), just south of the Eastern Volcanic Rift Zone (EVRZ) in Iceland. The EVRZ is currently undergoing south-westward propagation, thereby taking over the spreading from the Western Volcanic Zone (WVZ) (e.g. LaFemina et al., 2005). Although presently non-spreading there is ample volcanic activity within the

three volcanic systems in the SIVFZ, Eyjafjallajökull, Katla and the Vestmann Islands. Eyjafjallajökull is the focus of two dissertation papers.

Through a series of small-scale southward propagating rifts originating off the coast of Iceland, lithosphere is consistently transferred from the Eurasian to the North American Plate (Hey et al., 2010; Benediktsdóttir et al., 2012), causing the RR to migrate eastward. The tip of the oldest propagator is located at the BTF (Figure 1.1). South of the BTF the oblique spreading of the RR stops and the spreading direction of the ridge becomes orthogonal to the trend of the ridge (Appelgate and Shor, 1994; Benediktsdóttir et al., 2016). The tectonic history for the past 6 Ma of the area immediately south of the BTF is the focus of one paper in the dissertation.

Research questions

Land-based study area

- What is the seismic velocity structure of Eyjafjallajökull?
- What can the crustal velocity structure tell us about the magmatic pathways within the volcano?
- What characterized the seismic tremor of the 2010 eruption at Eyjafjallajökull?

Ocean-based study area

- Is the area south of the BTF migrating east as the RR system? If so, could that be considered to be caused by the Iceland plume?
- What characterizes the tectonic kinematics of the area south of the BTF?

1.2 Outline of the dissertation

The dissertation is based on three papers;

1. Benediktsdóttir, Á., Hey, R., Martinez, F., Höskuldsson, Á. (2016). A new kinematic model of the Mid-Atlantic Ridge between 55°55′N and the Bight Transform Fault for the past 6 Ma. *Journal of Geophysical Research: Solid Earth*, **121**(2), 455-468.
2. Benediktsdóttir, Á., Gudmundsson, Ó., Brandsdóttir, B., and Tryggvason, A. (2017). Ambient noise tomography of Eyjafjallajökull volcano, Iceland. *Journal of Volcanology and Geothermal Research*, **347**, 250-263.
3. Benediktsdóttir, Á., Gudmundsson, Ó., Li, K. L., and Brandsdóttir, B.. Volcanic tremor of the 2010 Eyjafjallajökull eruption. *To be submitted to Geophyscial Journal International*.

In the following sections we review the background of the two study areas and the geophysical methods used for each of the three papers. An overview of each of the three papers is given and the papers are then presented.

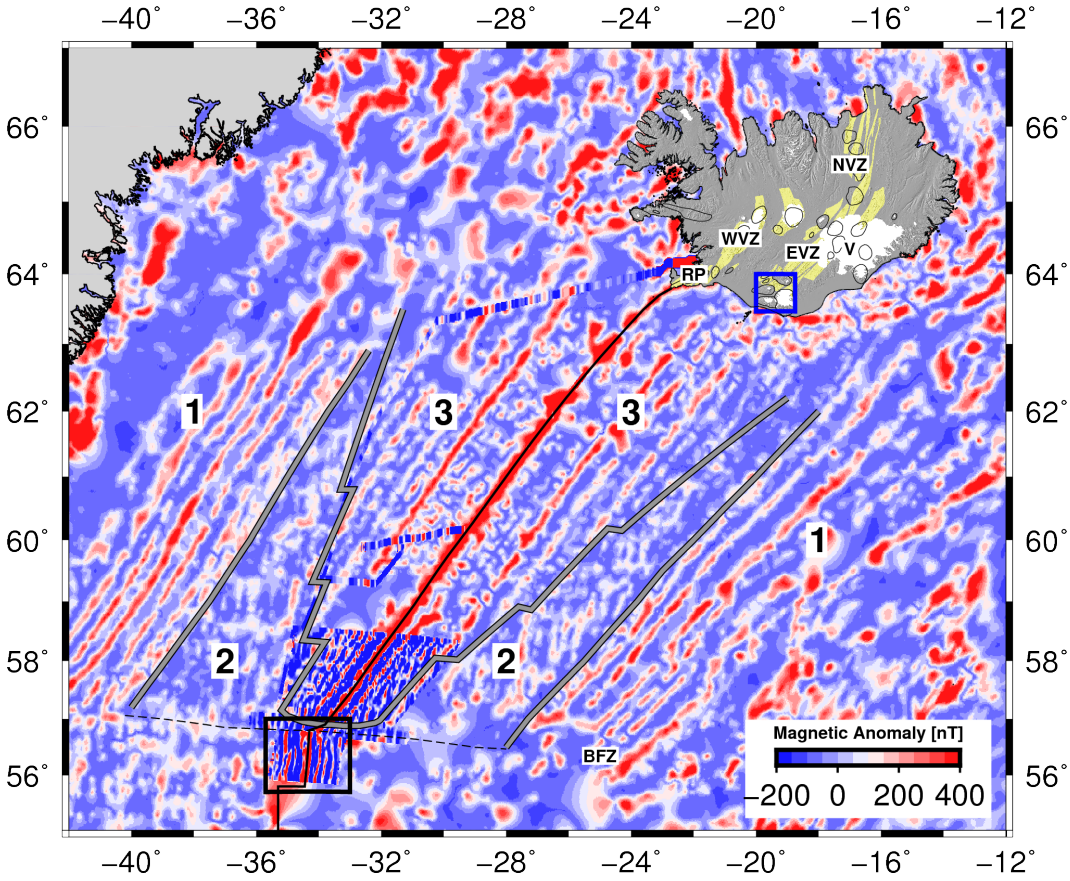

Figure 1.1. Overview of the two study areas of the dissertation. Location of the Eyjafjallajökull and Mid-Atlantic Ridge study areas shown in thick blue and black boxes, respectively. Marine magnetic anomalies (large scale data from Macnab et al. (1995) and detailed data by Hey et al. (2016)) reveal three distinct tectonic epochs in the NE Atlantic marked with numbers 1,2 and 3. Thick gray lines mark their boundaries. The boundary between 2 and 3 is referred to as the V-shaped boundary (from Hey et al. (2016)). Black solid line is the Reykjanes Ridge and dashed line is the BFZ. BFZ=Bight Fracture Zone; V=Vatnajökull; WVZ=Western Volcanic Zone; RP=Reykjanes Peninsula; EVZ=Eastern Volcanic Zone; NVZ=Northern Volcanic Zone.

2 Background for Paper I

2.1 The tectonic evoluction of the Mid-Atlantic Ridge in relation to the study area

Prior to plate spreading on the Reykjanes Ridge (RR), Greenland and Europe were separated from the North American Plate via plate spreading in the Labrador Sea on the Ran Ridge. At approximately magnetic anomaly 24 (60 Ma) (Vogt and Avery, 1974) plate spreading was initiated on the RR in the North-East Atlantic, creating a triple point south of Greenland between the Ran Ridge to the west, RR to the north and part of the Mid-Atlantic Ridge (MAR) lying further to the south. At that time, the spreading on the RR was orthogonal to the trend of the ridge (area number 1 in Figure 1.1) and the ridge started out as one long lineament, without any ridge offsets or transform faults. As spreading ceased on the Ran Ridge at 47 Ma (Le Pichon and Fox, 1971; Laughton, 1972) the spreading direction transitioned abruptly from 125° to 100° causing the ridge to break up into numerous segments oriented orthogonal to the new trend of the ridge (area number 2 in Figure 1.1). The triple junction ceased to exist and developed into a ridge offset, currently known as the Bight Transform Fault (BTF).

The most recent re-organization of the RR, changed the orientation of the ridge such that the spreading geometry changed from segmented orthogonal spreading to oblique spreading (area number 3 in Figure 1.1). This re-organization started between magnetic chrons 15 and 13 (35 and 33 Ma) (Hey et al., 2016), south of Iceland, and progressively made its way down the RR, eliminating all transform faults along the way. The tip of the re-organization is currently located at the Bight Transform Fault which is the first transform fault on the MAR south of Iceland and marks the end of the RR (in some cases the end of the RR is considered to be the Charlie-Gibbs Fracture Zone). The latest re-organization boundary is marked with a step-like V on the RR (Figure 1.1).

The 15 kilometer long right-stepping BTF (Figure 2.1) marks a change in the ridge azimuth and spreading geometry on the MAR. The area immediately to the south exhibits orthogonal plate-spreading geometry and the area to the north has an oblique spreading geometry, as discussed before. The evident changes in spreading geometry on the RR did not extend south of the BTF as the spreading azimuth there remained orthogonal to the trend of the ridge. The BTF, therefore, marks a long lived tectonic point on the MAR and the areas to the north and the south have very different characteristics.

Various ideas have been put forth on the cause of the latest reorganization event. In the generally accepted models, pulses from the Iceland plume propagate south, down the RR, eliminating the transform faults along the way (Vogt, 1971; White, 1997; Jones, 2003). The pulses can either be thermal (hotter than normal) or compositional (the melt contains more garnet pyroxine by volume). In the first proposed model (Vogt, 1971)

thermal pulses, in the form of hot astenosphere, rapidly rise beneath Iceland and spread laterally or are channeled down the ridge, creating the V-shaped ridges. Jones (2003) suggested that a thermal pulse of a few tens of degrees hotter material than normal weakens the lithosphere causing the ductile response of the lithosphere and sustaining an oblique spreading geometry with a ridge high instead of a ridge valley, such as found on slow spreading ridges. Parnell-Turner et al. (2014) proposed that after 35 Ma the temperature fluctuations in the mantle plume were $25 - 30^{\circ}C$ with a pulsing periodicity of 8 Ma. Similar temperatures have been suggested by others (White et al., 1995; Poore et al., 2011; Parnell-Turner et al., 2013). Geodynamic modelling by Ito (2001), favores radial flow from the Iceland mantle anomaly of solid state mantle material with thermal pulses embeded. Passive plate spreading draws the flowing material up, where the material is melted.

In an alternative model, where no thermal effect is needed, the current oblique RR is re-establishing the original linear geometry that it had before the change in opening direction (Martinez and Hey, 2017). Yet another study proposes that the V-shaped ridges are caused by the ridge-relocation on Iceland (Hardarson et al. (1997)). The ridge-relocations disrupt the flow down the ride creating a ridge-low instead of a ridge-high. In this scenario, the natural state of the RR is a ridge-high.

Recently, analysis of marine magnetic data, collected along the flow lines of the RR, showed that the crustal accretion of the RR has not been symmetric for the past 15 Ma (Hey et al., 2010; Benediktsdóttir et al., 2012). The asymmetric accretion can best be described as occurring discontinuously, and asynchronously along the ridge. Such an accretion pattern has most often been attributed to rift propagation (e.g. Hey and Vogt, 1977; Hey and Wilson, 1982), where lithosphere is transferred from one plate to another. The magnetic observations are consistent with rift propagation, but the propagation offset is so small that it most often falls within the wide neovolcanic zone of the RR.

What ever the cause of the recent reorganization episode, it started at Iceland and is now located at the BTF. It may or may not break through the BTF in the future. The first paper of the dissertation is focused on the area immediately to the south of the BTF, and one of the questions asked was if the influence of the plume reached farther south than the BTF.

2.2 Magnetic modeling

Forward modeling of marine magnetic anomalies was the basis for the work done in paper I (Section 4) and is reviewed below.

Magnetic Anomalies

At divergent plate boundaries two tectonic plates spread apart from one another, forming new lithosphere. Most of the spreading centers on Earth are in the oceans and the plate spreading concept is therefore often referred to as sea-floor spreading. As the new lithosphere cools below the Curie temperature, the remnant magnetization vector takes on the orientation of the current geomagnetic field. Also, the Earth's magnetic

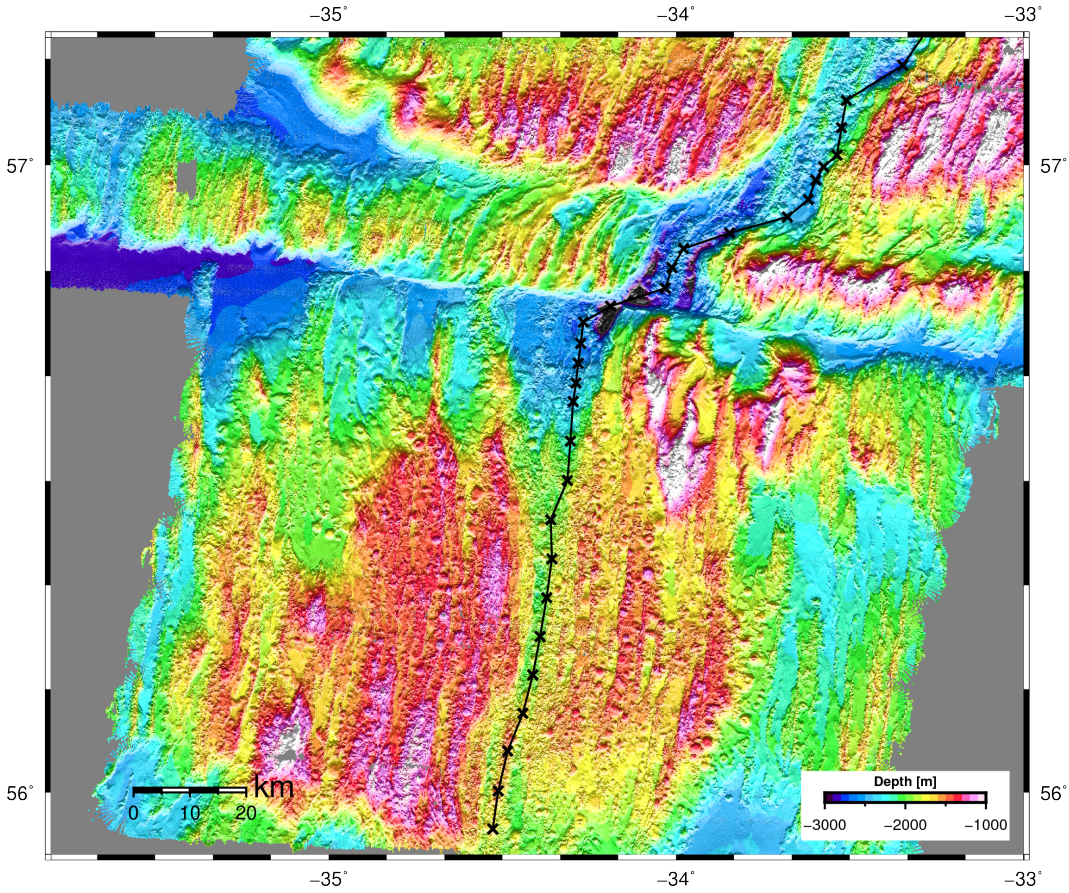

Figure 2.1. Bathymetry of the Mid-Atlantic Ridge study area shown in the black box in Figure 1.1. Black crosses mark the ridge center as identified by magnetic modeling. The Bight Transform Fault is a complicated 15 km long right-stepping transform fault. The area to the south is orthogonally spreading but the area to the north is obliquely spreading.

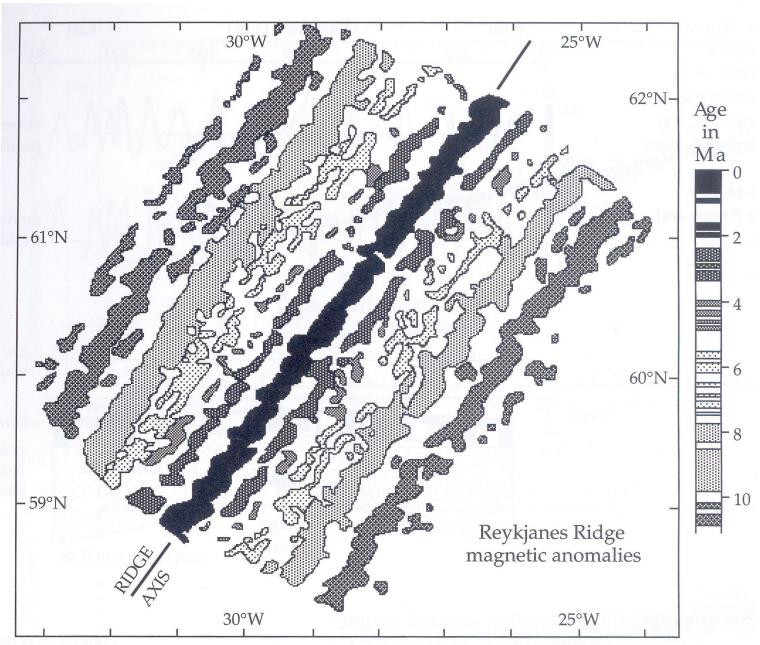

Figure 2.2. Magnetic anomalies symmetric about the Reykjanes Ridge (Heirtzler et al., 1968). The gray-scale to the right shows the polarity time-scale used.

field undergoes polarity reversals making the remanent magnetic field in the lithosphere either normally polarized or reversely polarized (in the same or opposite direction as the present geomagnetic field). These three factors; sea-floor spreading, remanent magnetization of rocks and polarity reversals of the Earth's magnetic field cause magnetic lineaments to form along the spreading centers of the Earth. The study of such magnetic lineaments makes is possible to determine the spreading history of a ridge, given a polarity time scale (e.g., Cande and Kent, 1995; Lourens et al., 2004). The textbook case for showing magnetic lineations is found in Heirtzler et al. (1968), where a map of the Reykjanes Ridge with symmetric magnetic lineations is shown (Figure 2.2).

The fundamental assumption in plate tectonics is that the plates are rigid and their relative motion can be described by a pole of rotation. The pole of rotation is described by its location (x,y,z) and an angular velocity between the two plates. The opening velocity at any given location of the ridge can be described by the following equation

$$v = \omega R sin(\theta) \tag{1}$$

where ω is the angular velocity of the two plates, R is the radius of the Earth and θ is the angular distance between the pole of rotation and the point on the ridge. The closer the point on the ridge is to the pole of rotation, the slower the spreading velocity.

Magnetic Modeling

The magnetic modeling described here is of the qualitative sort, as it is based on forward modeling only and the fit of the model to the data is judged by the eye of the modeler.

Figure 2.3 shows, schematically, the fundamental elements of magnetic modeling. Magnetic anomalies form on either side of the ridge, at the same rate, along the strike of the ridge, assuming 90° between spreading direction and azimuth of the ridge. Therefore, the strike of the magnetic structure is parallel to the trend of the ridge and all cross-sections parallel to the flow line across the ridge should reveal the same magnetic anomaly pattern (Figure 2.3A). The structure is, therefore, two-dimensional. The width of the different polarization, along with a magnetic polarity time scale allows the determination of the spreading rate of the ridge system (Figure 2.3B). The spreading rate history of the ridge system can then be constructed by investigating the magnetic lineaments as far back in time as they exist.

A flow line is a line which describes the movement of a lithosphere that was once at the ridge crest. If the spreading direction is orthogonal to the trend of the ridge, then the flow line is also orthogonal to the trend of the ridge. However, this is not the case where spreading direction is not orhogonal to the trend of the ridge. Then flowlines can be diagonal to the trend of the ridge. Also, a change in plate motion at some point in time may cause a change in azimuth of the flow line.

Talwani and Heirtzler (1964) described how to calculate magnetic anomalies caused by 2-D bodies of arbitrary shape. Figure 2.4 shows, schematically, how the forward model calculations are performed. The model is calculated on a flow line-parallel profile. At each point, where the model is obtained, the contribution from each magnetic body is calculated. The model value at that point is the sum of all the contributions. The profile runs along the flow line of the ridge; if the plate spreading is orthogonal the profile runs perpendicular to the strike of the ridge. A magnetic polarity time scale provides the timing of polarity boundaries. Therefore, in magnetic modeling it is possible to change the width of the magnetic block by changing the spreading rate. This is done iteratively until a desired fit to the magnetic anomalies is reached.

Propagating Rifts in Magnetic Modeling

Through rift propagation, ridge systems evolve in time and space. Figure 2.5 shows the concept of a continuously propagating rift. At a ridge-transform-ridge junction, instability occurs which leads to the propagation of one ridge segment into older lithosphere (e.g. Hey, 1977; Hey et al., 1980). Lithosphere that used to belong to plate B is transferred over to plate A and is defined by the zone of transferred lithosphere (ZTL). The rift propagation causes an offset in the magnetic anomaly lineations that looks like a displacement along a fault. The offset is known as pseudofaults, as these are not actual faults, but they might be accompanied by height difference due to different lithospheric ages. Two pseudofaults and one failed rift, which is the trace of the old ridge, accompany each propagating rift. The magnetic lineations in the ZTL usually undergo rotation due to shearing of the lithosphere, and thus the magnetic signal is distorted. If the transform offset is small, this signature of a propagating rift system might be hard to detect.

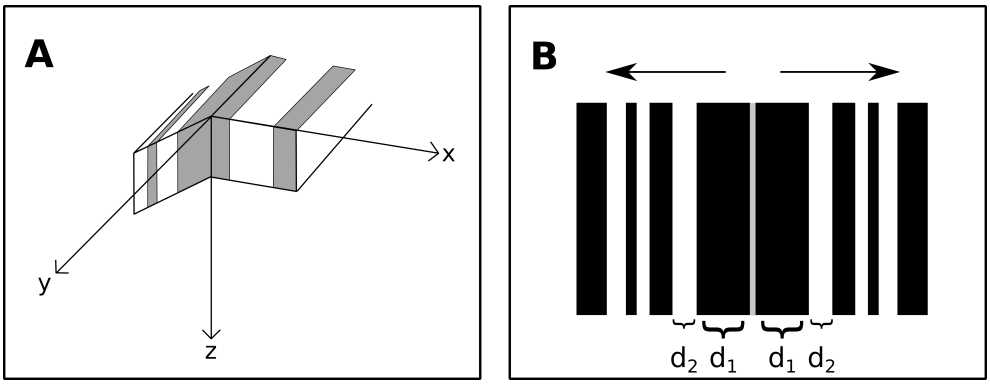

Figure 2.3. The basics of magnetic modeling. **A.** *The magnetic modeling problem is considered two-dimensional as the magnetic anomalies generated at the ridge axis are the same along the strike of the ridge (along y-axis), assuming a conventional ridge spreading. A cross-section anywhere along the flow line (x-axis if the spreading is orthogonal to the trend of the ridge) reveals the same magnetic anomaly pattern in the case of symmetric spreading.* **B.** *Map view of a ridge and its magnetic anomalies. Spreading at the ridge axis (grey) is symmetric, making the normally (black) and reversely (white) polarized lithosphere equally wide on either side of the ridge. The newest normally polarized lithosphere is closest to the ridge with a width of d_1 km and the newest reversely polarized lithosphere has a width of d_2. If the duration of the first normal and reversely polarizations were t_1 and t_2, respectively, then the spreading velocities at these times would be $v_1 = d_1/t_1$ and $v_2 = d_1/t_2$.*

A propagating rift changes the magnetic imprint of the tectonic evolution of a ridge. Instead of a simple symmetric spreading history where the width of the magnetic anomalies and a time scale can be used to uncover the history of the ridge, a part of the magnetic anomalies are cut from one plate and pasted to the other side of the ridge. The pattern created by PRs can be uncovered by forward calculating the magnetic data, given a certain transferal of lithosphere between plates. In a vertical cross-section, the signature of the PR looks as if an instantaneous jump of the locus of spreading has changed from the failed rift to the new spreading axis. If magnetic data are collected over several profiles that run parallel to the flow lines of the ridge, the different timings of such instantaneous ridge jumps can be compiled to derive the propagation history of the ridge.

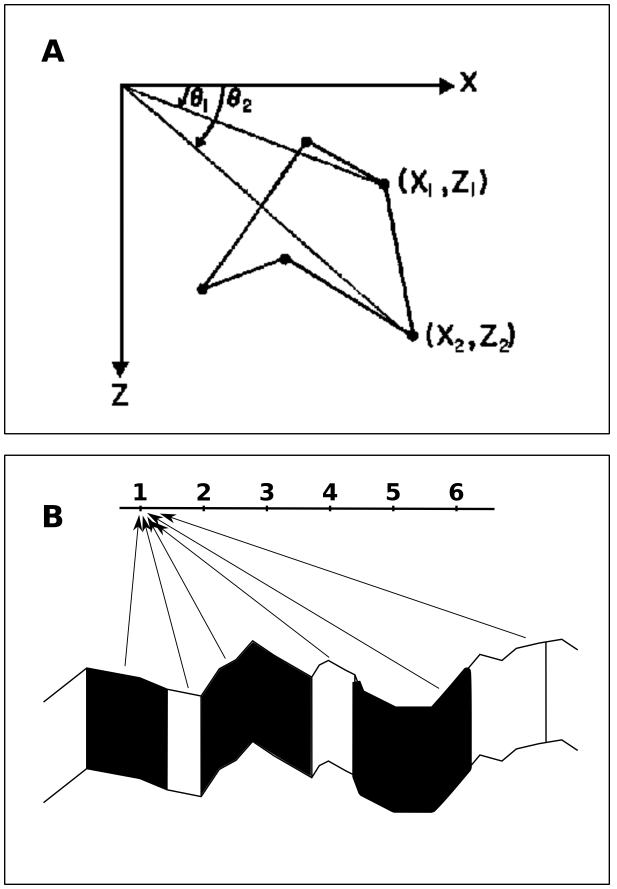

Figure 2.4. **A.** *Figure from Talwani and Heirtzler (1964) demonstrating how to compute the magnetic signal from a 2-D arbitrary shaped body at the center of the coordinate system. This particular arbitrary shape represents one black or white stripe in the magnetic pattern.* **B.** *Cross-section along the flow line of a ridge, revealing the magnetic pattern. The contribution of each normally (black) and reversely (white) polarized blocks is calculated to each of the measuring sites (1 through 6) along the profile by using the equations in Talwani and Heirtzler (1964) described in* **A.**. *The contributions are then summed up, at each of the numbered points, to form the model. The upper and lower bounds of the magnetized blocks are defined by the bathymetry of the ocean floor and the thickness of the magnetized blocks. The profile, along which the model is calculated, runs along the flow line of the ridge. If the plate spreading is orthogonal the profile is perpendicular to the strike of the ridge.*

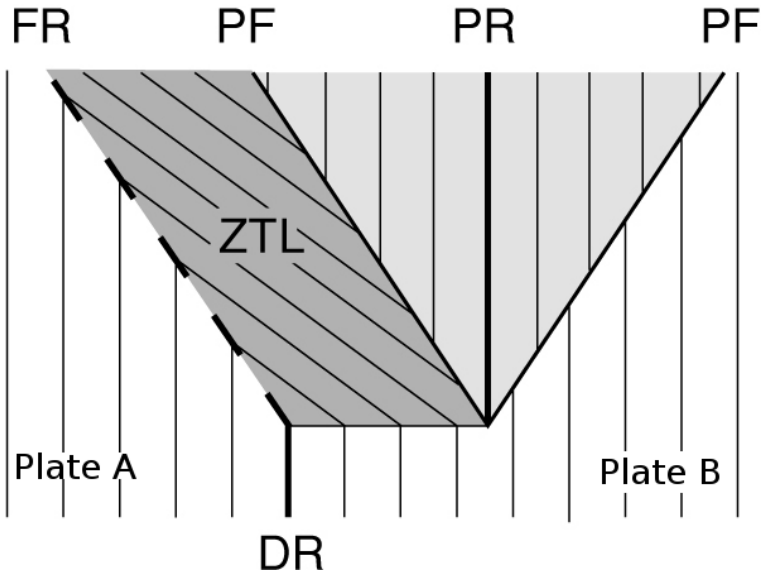

Figure 2.5. Map view of a propagating rift system (Hey, 1977). A ridge segment starts propagating (the propagating rift (PR)) into older lithosphere of plate B, taking over the other ridge segment (the dying rift (DR)). As the PR propagates, lithosphere that used to be on plate B is transferred to plate A. A wake of transferred lithosphere is created (zone of transferred lithosphere (ZTL)) behind the tip of the PR. Two pseaudofaults (PF) cause a discontinuity in the magnetic lineations (vertical lines). The failed rift (FR) is the trace of the old active spreading center.

3 Background for papers II and III

3.1 Tectonic evolution of Iceland in relation to the Iceland plume and the MAR

Iceland lies in the middle of the North-Atlantic ocean, and it is the surface exposure of the Mid-Atlantic ridge (MAR), linking the Reykjanes Ridge in the south to the Kolbeinsey Ridge in the north (Figure 1.1). The MAR separates the Eurasian Plate from the North-American Plate which are currently spreading apart with a rate of ≈ 2 cm/yr at the latitude of Iceland (DeMets et al., 1994; Merkouriev and DeMets, 2008; DeMets et al., 2010; Sigmundsson et al., 2018). The Reykjanes Ridge becomes subareal in Iceland at the Reykjanes Peninsula, which is connected with the Western Volcanic Zone (WVZ) to the northeast and the South Iceland Seismic Zone (SISZ) to the east. The SISZ further connects with the NE-SW lying Eastern Volcanic Zone (EVZ) that is composed of two areas; the Eastern Volcanic Rift Zone (EVRZ) in the north eastern part where spreading is taking place, and the South Iceland Volcanic Flank Zone (SIVFZ), where spreading has not begun but volcanic activity is ample. The EVZ connects with the Northern Volcanic Zone (NVZ) to the north that further connects to the Kolbeinsey Ridge via the Tjörnes Fracture Zone (TFZ).

During the life span of Iceland, a few episodes of well documented rift-relocations, where locus of spreading moves laterally, have occurred. These events have been documented by identifying hiatuses in the lava succession (Hardarson et al., 1997), the tilt of the lava pile (Hardarson et al., 1997), age discontinuities (based on radiometric dating) (Hardarson et al., 1997), and the existence of anticlines (such as the Borgarnes anticline (Jóhannesson, 1980)). Loading of new material in the rift zones in combination with lateral spreading is the reason why the lava pile outside the volcanic zone tilts toward the center of spreading (e.g., Pálmason, 1980). When a rift-relocation occurs, the locus of spreading and loading changes. Some lavas from the new spreading center are erupted over the material of the older spreading center after some time causing a hiatus in between those successions. They have a different tilt because they originate from different spreading centers.

From observations such as these the tectonic history of Iceland has emerged. Lavas on the western side of the Westfjords dip toward the ocean, indicating a paleo-spreading center offshore that was active until 15 Ma (Hardarson et al., 1997). At that time, the Snæfellsnes-Skagi (sometimes called Húnaflói rift) spreading center became active (Jóhannesson, 1980) and it changed to an off-rift volcanic zone between 7 and 5 Ma (Sæmundsson, 1979; Jóhannesson, 1980; Martin et al., 2011) with some renewed melting at 3 Ma (Walters et al., 2013). Spreading in the NVZ was initiated at about 8 Ma (Garcia et al., 2003), indicating an overlapping spreading segment configuration between

the Snæfellsnes-Skagi and NVZ for a few million years. The currently spreading WVZ was initiated at about 7 Ma and has been the main spreading center in South Iceland for most of the time ever since (Kristjánsson and Jónsson, 1998; Einarsson, 2008). The southward propagating East Volcanic Zone has been taking over the receding WVZ for the past 2-3 Ma (Jónsson et al., 1997; LaFemina et al., 2005).

The total spreading across the WVZ and the EVRZ equals the full spreading rate across Iceland of about 20 km/Ma (DeMets et al., 1994; Merkouriev and DeMets, 2008; DeMets et al., 2010). LaFemina et al. (2005) showed that spreading rates across the WVZ increases from 2.6 mm/yr to 7.0 mm/yr from north to south, but decreases from 19.8 mm/yr to 8.0 mm/yr from north to south in the EVRZ. These observations have been confirmed by other authors (Geirsson et al., 2006, 2010). Therefore, it has been concluded that spreading is diminishing in the WVZ and the southward propagating EVRZ is slowly taking over, similar to overlapping spreading systems (e.g. Sempere and Macdonald, 1986) and propagating rift systems on mid-ocean ridges (e.g. Hey, 1977; Hey et al., 1980). Similarly, in the north of Iceland a synchronous spreading was ongoing between 3 and 8 Ma in the NVZ and in a spreading system to the west, with the NVZ taking over (Hardarson et al., 1997; Garcia et al., 2002; Karson, 2017). In the two examples propagation occurs *away* from the center of Iceland.

Recently, Karson (2017) summarized the indicators of a propagating plate boundary system in Iceland, including the evidence for pseudofault existence. The observed age unconformity, where young lavas overly much older and deformed lavas are also one of the indicators of a propagating rift (e.g. in Skjálfandi bay, see Jancin et al., 1985). The geometry of the transform faults of the TFZ has changed with northward propagation of the NVZ. Figure 3.1 shows how Karson (2017) drew up the propagating system on Iceland with a series of abandoned ridges to the west of the NVZ, similar to what can be seen in propagating rift systems (Figure 2.5). The northward propagation of the NVZ is located within the TFZ and the southward propagating tip of the EVRZ is located south of the Vestmann Islands.

The focus of the study in papers II and III is the Eyjafjallajökull volcano, located in the SIVFZ.

3.2 Eyjafjallajökull

Eyjafjallajökull is located at the southern end of the southward propagating EVRZ (Figure 3.1). No plate spreading has been measured in the vicinity of Eyjafjallajökull, but recent volcanic activity farther south, in the Vestmann Islands, show that the propagating realm reaches farther south than where the acutal spreading takes place. Eyjafjallajökull is a 1651 meter high east-west oriented stratovolcano (Figure 3.1). It extends 25 km east-west, 15 km north-south, and its southern cliffs are located only a few kilometers from the coastline. It has a 2.5 km wide ice-filled caldera.

In the past 30 years four periods of unrest in the volcano have been recorded. In 1994 and 1999-2000 earthquakes and uplift were recorded and modeled as two horizontal sill intrusions (Dahm and Brandsdóttir, 1997; Sturkell et al., 2003; Pedersen and Sigmundsson, 2004, 2006; Hooper et al., 2009) and in 1996 a deep earthquake

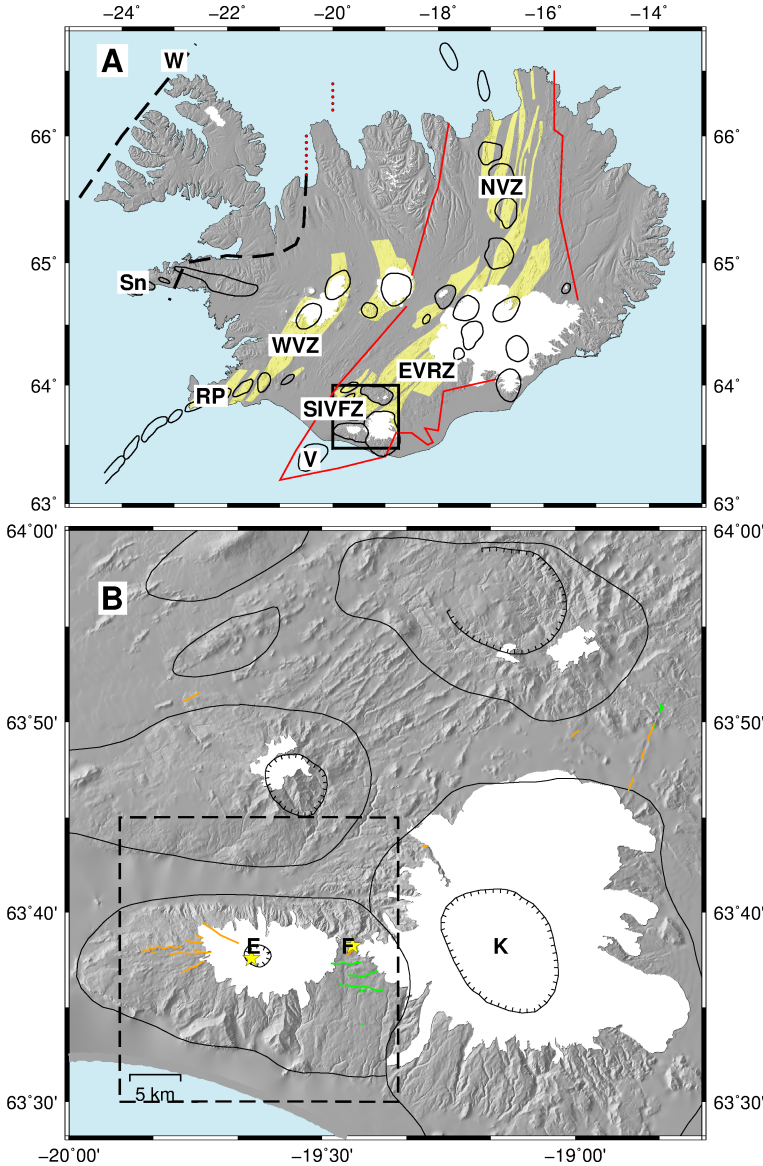

Figure 3.1. Tectonic setting of Eyjafjallajökull in the context of Iceland. **A.** *Fissure swarms are in yellow, black dashed lines are paleo-spreading centers in Iceland (after Sæmundsson (1979)) and solid lines are outlines of central volcanic systems. The box shows the area of* **B** *and is the same as the blue box in Figure 1.1. Red solid and dashed lines are pseaudofaults and failed rifts, respectively, as interpreted by Karson (2017). WVZ=Western Volcanic Zone, EVRZ=Eastern Volcanic Rift Zone, SIVFZ=South Iceland Volcanic Flank Zone, NVZ=Northern Volcanic Zone, RP=Reykjanes Peninsula, V=Vestmann Islands, Sn=Snæfellsnes-Skagi paleo spreading center, W=Westfjords paleo spreading center.* **B.** *Solid and hatched lines are outlines of central volcanic systems and calderas, respectively. E=Eyjafjallajökull, F=Fimmvörduháls, K=Katla. Orange lines are eruptive fissures and green lines are faults (data compiled by Einarsson & Hjartardóttir 2015, see references therein). The dashed rectangular box shows the area of the ambient tomography study presented in the dissertation.*

swarm at 20-25 km depth was detected (Hjaltadóttir et al., 2015). In 2010 there were two eruptions, a flank eruption at Fimmvörðuháls (F in Figure 3.1) and the other in the caldera of Eyjafjallajökull (E in Figure 3.1). Prior to and during the two eruptions uplift and earthquakes were recorded (Sigmundsson et al., 2010; Tarasewicz et al., 2011, 2012, 2014).

Including the latest eruption, there have been four known eruptions in Eyjafjallajökull during the past 1200 years. In the 10^{th} century a trachytic lava eruption, 2 km WNW from the caldera, with mafic and silicic tephra components, formed the NW trending Skerin ridge (Óskarsson, 2009). A poorly described eruption in 1612 or 1613 (Jónsson, 1774; Larsen et al., 1999) and a summit eruption in December 1821-January 1823, producing highly silicic magma (Larsen et al., 1999; Gudmundsson et al., 2010).

Until present, the internal material properties of Eyjafjallajökull have been approximated as a homogeneous and isotropic half-space in numerical deformation models (Sigmundsson et al., 2010; Albino and Sigmundsson, 2014; Hjaltadóttir et al., 2015). However, there are a number of studies suggesting spatial variations in material properties, such as seismic studies of Eyjafjallajökull (Dahm and Brandsdóttir, 1997; Jónsdóttir et al., 2007; Tarasewicz et al., 2011, 2012, 2014; Hjaltadóttir et al., 2015) and a resistivity study (Miensopust et al., 2014). Several conceptual models have been proposed for the volcano (Sigmundsson et al., 2010; Tarasewicz et al., 2014; Einarsson and Hjartardóttir, 2015).

3.3 Seismic Tomography

Seismic tomography is a method to image the sub-surface of the Earth with seismic waves. The waves include body waves (P-and S-waves), that travel through the interior of the Earth, and surface waves (Rayleigh-and Love waves), that propagate at the interfaces between two media (the surface of the Earth and the atmosphere in this case).

Conventional seismic methods involve earthquakes (passive) or man-made seismic waves (i.e. explosions) (active) that generate seismic signal. Through inversion of these data, the tomographic model parameters can be evaluated (e.g. the inverse of velocity, slowness, of the Earth).

The scale of seismic tomography studies range from local models (e.g. Toomey and Foulger, 1989; Jeddi et al., 2016), to regional (e.g Jonge et al., 1994; Rickers et al., 2013) and global models (e.g. Montagner and Tanimoto, 1991; Li et al., 2008). The part of the seismic signal used in tomographic inversion include the primary (P) and secondary (S) waves (e.g. Inoue et al., 1990; Berk Biryol et al., 2011), the surface waves (e.g. Snieder, 1988; Fang et al., 2015) or coda waves (e.g. Grêt et al., 2005; Sens-Schönfelder and Wegler, 2006).

Ambient noise has, until recently, been considered useless, and was usually filtered out. Data were only stored if the time-series included earthquakes. With increased computer power and data storage, seismic data are now continuously recorded and stored, earthquakes or not, resulting in huge databases of seismic data. Correlating long time-series of similar wave forms, where the signal is small but repeated over a long time, has resulted in a new type of tomography, ambient noise tomography (ANT).

In Section 3.4 the ANT method is discussed which was used to infer the internal velocity structure of Eyjafjallajökull, which is the topic of paper II.

3.4 Ambient Noise Tomography

Ambient Noise Tomography has become a widely used method to image the subsurface of the Earth both globally (Nishida et al., 2009), regionally (Shapiro et al., 2005; Gudmundsson et al., 2007; Moschetti et al., 2007; Gao and Shen, 2015; Korostelev et al., 2015) and on a smaller-scale where magma bodies and chambers have been imaged (Brenguier et al., 2007; Stankiewicz et al., 2010; Jay et al., 2012; Matos et al., 2015; Tamura and Okada, 2016; Obermann et al., 2016). The method is used to infer the S-wave velocity structure in the subsurface by traditional surface-wave inversion. The data, however, are not direct measurements of surface wave arrivals from earthquake occurrence, rather they are obtained from many months of continuously recorded ambient noise on seismometers.

The procedure for the ANT done in Eyjafjallajökll is as follows:

1. Time-series between all combinations of seismographs are cross-correlated; resulting in a correlogram for each pair. The correlogram is used as a deterministic seismogram between the two seismic stations, where one station is considered to be the earthquake location and the other the recording of the signal

2. Phase-velocity dispersion curves are obtained from each correlogram. Thus frequency dependent phase-velocity for the path between the two seismographs is available.

3. The inversion itself is divided into two parts:

   (a) The phase-velocity dispersion curves are inverted for phase-velocity maps.

   (b) The phase-velocity maps are sampled at different locations, to produce local dispersion curves. Each local dispersion curve is inverted in one dimension to obtain a velocity-depth relation for that location. These one-dimensional models are combined into a 3D shear-wave velocity model.

Below these steps will be described in more detail.

Source of the ANT signal

Microseisms are a widespread signal recorded at most (if not all) seismometers. They are a noise signal as they are continuously present and recorded as short-period surface waves. Their frequency spectrum is characterized by two peaks, primary and secondary microseisms. The secondary microseisms are more pronounced and are found at higher frequencies (3-10 s), compared to the primary microseisms (15-20 s). The interaction of oceanic gravity waves with the ocean bottom, creates short-period surface waves, mostly Rayleigh waves, but they have also been found to contain horizontally polarized Love-waves (Juretzek and Hadziioannou, 2016).

The primary microseisms are associated with direct interaction of ocean-waves with the sea floor. The pressure disturbance associated with the ocean wave decays exponentially with depth, and the primary micorseisms are therefore generated in shallow waters (Hasselmann, 1963; Haubrich et al., 1963).

Although still under investigation, it is thought that the secondary microseisms are generated by a non-linear interaction of two wave trains, of the same frequency content as the primary microseisms, that propagate in opposite directions, producing a standing-wave on the ocean (Longuet-Higgins, 1950). The frequencies of the secondary microseisms are therefore double those of the primary microseisms (Kedar et al., 2008; Stutzmann et al., 2012). The standing wave does not decay with depth and the secondary microseisms can therefore be generated in the deep ocean. The secondary microseisms have also been found to originate from coastal reflections. Stutzmann et al. (2012) successfully modeled the microseisms using a deep-water source and coastal reflections. They found that the strongest sources are located at $30^\circ - 50^\circ$ latitudes (both north and south) during local winters. Ardhuin et al. (2011) classified the generation of microseisms into three categories (i) by broad storms radiating ocean waves over a wide range of direction so that seismographs sense microseism coming from many directions, (ii) contribution from coastal reflections and (iii) interaction of two independent wave systems originating from separate storms.

Signal Emergence: Correlograms and Green's Function

The Correlogram

Consider two time series recorded at different seismic stations $u_1(t)$ and $u_2(t)$. Their covariance is

$$C_{12}(\tau) = \frac{1}{T}\int_0^T u_1(t)u_2(t+\tau)dt \tag{2}$$

and the correlation is

$$R_{12}(\tau) = \frac{C_{12}(\tau)}{\sqrt{C_{11}(0)C_{22}(0)}} \tag{3}$$

In the sections to come, we will refer to the cross-correlated signal as the correlogram, which strictly speaking is the covariogram.

Several authors (Wapenaar et al., 2005; Sánchez-Sesma and Campillo, 2006; Snieder and Larose, 2013) have derived how the correlogram between two seismic stations relates to the Green's function for the path between them

$$\langle C(\omega)\rangle \propto i\omega^n P(\omega)[G(\omega) - G^{\#}(\omega)] \tag{4}$$

where C is the correlation, $\langle\rangle$ stands for statistical expectation, ω, P and G are the frequency, the power spectrum, and the appropriate Green's function, respectively. Here # stands for the complex conjugate. The exponent, n, depends on the number of dimensions.

Equation 4 is derived under the assumption that the noise field is temporally and spatially incoherent and the power of the noise is isotropic. Two scenarios fulfill these

assumptions; 1) a uniform distribution of isotropic scatterers around the seismographs, and 2) plane waves arriving at different times from all angles with equal energy density.

When describing microseisms generated at distance scenario 2 is applicable. Consider a single plane wave passing two seismographs as in Figure 1. The time delay between the arrivals of the wave at the two seismographs, τ, has a simple relation with its direction of propagation, θ, relative to the axis connecting the two seismographs:

$$\tau = \frac{r}{c} cos\theta = \tau_0 cos\theta \tag{5}$$

where r is the distance between the two seismographs and c is the velocity of the medium, i.e. of the direct plane wave along the path between the two seismographs.

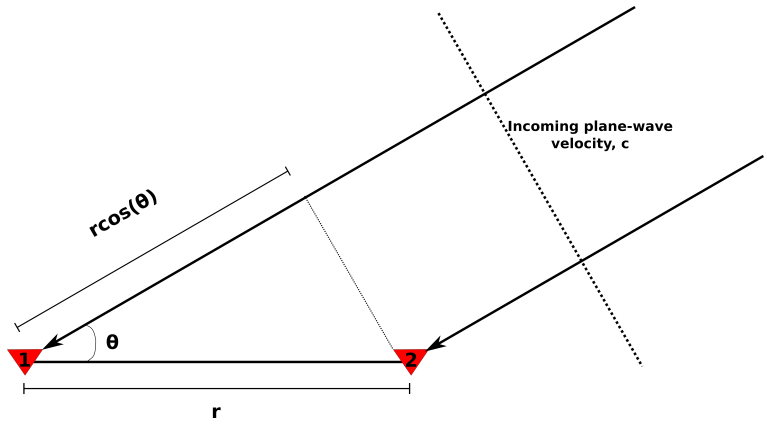

Figure 3.2. Two seismometers, 1 and 2, record an incoming plane wave with a velocity c. The wave is recorded at both stations with a time-lag of $rcos(\theta)/c$. A cross-correlation of the time-series recorded at the two stations would reveal a peak at $t = rcos(\theta)/c$.

Equation 5 defines a limited range of time lags; it is at maximum ($\tau = \pm r/c$) when the direction of the plane wave is in line with the axis connecting the two seismographs and at a minimum ($\tau = 0$) when the angle is perpendicular to that axis. If multiple such waves arrive from different directions, with random timing, the assumptions of Equation 4 are met.

The cross-correlation of time-series from the two seismographs will isolate each contributing wave at a time lag that is controlled by θ. If waves arrive from all different directions at different times, then energy will exist in the correlogram at all possible time lags. Also, if waves arrive, at different times, from the same direction during the time of integration (T) the correlation will have an increased amplitude at the time delay corresponding to the angle of incidence (θ). Therefore, the expectation of the correlation will be proportional to an integral over all angles of the cumulative energy density from each direction (e.g. Sadeghisorkhani et al., 2016):

$$\langle C(\tau) \rangle \propto \int_0^{2\pi} \varepsilon(\theta) \delta(\tau - \tau_0 cos\theta) d\theta \tag{6}$$

where $\varepsilon(\theta)$ is the cumulative energy density. If we assume a uniform energy density, ε_0, then:

$$\langle C(\tau)\rangle \propto \frac{\varepsilon_0}{\sqrt{\tau_0^2-\tau^2}} \tag{7}$$

The function in Equation 7 is shown in Figure 3.3 and demonstrates the relation between the correlogram and the time lag (θ). It is limited to time lags in the range $-\tau_0 \leq \tau \leq \tau_0$ and is singular at the end points. It shows how the correlation works as a geometrical filter that emphasizes time lags close to the endpoints of the possible range. The endpoints relate to plane waves that travel along the axis connecting the two seismographs. If the energy density is not uniform, those waves that arrive from directions near this axis will still be amplified in the same manner.

The properties of the geometrical filter, described in equation 4, change with the wavelength of the incoming plane waves. Two plane waves, one propagating parallel to the axis ($\theta = 0$) and the other at an angle, θ, interfere constructively if

$$\tau_0 - \tau = \tau_0(1-cos\theta) \leq T/4 \Rightarrow \theta \leq \sqrt{T/2\tau_0} = sqrt\lambda/2r = \theta_F \tag{8}$$

where T and λ are the period and wavelength of the incoming waves. That is, the higher the frequency, the smaller the angle (Fresnel angle). Therefore high-frequency waves are better focused than long-period waves along the axis by the correlation. We refer the reader to Sadeghisorkhani et al. (2017) for a more detailed discussion.

To sum up:

- The source of the ANT signal is composed of short-period surface waves originating from ocean gravity waves
- By cross-correlating temporally and spatially incoherent noise propagating in two dimensions between two seismographs, the signal of waves propagating in the direction of the axis connecting the two seismographs is isolated from the noise.
- The higher the frequency, the better the geometrical isolation

The Green's Function

Let's now consider the Green's function that we presented in Equation 4.

The appropriate Green's function in this case, which is applicable to correlation of vertical components of noise, is the cylindrical Green's function (Sánchez-Sesma and Campillo, 2006):

$$G(\tau) \propto \frac{1}{\sqrt{t^2-\tau_0^2}}, t \geq \tau_0 \tag{9}$$

and in terms of contributions from impulsive sources at either seismographs recorded at the other and in terms of time lag, τ:

$$G(\tau) \propto \frac{1}{\sqrt{\tau^2-\tau_0^2}}, |\tau| \geq \tau_0 \tag{10}$$

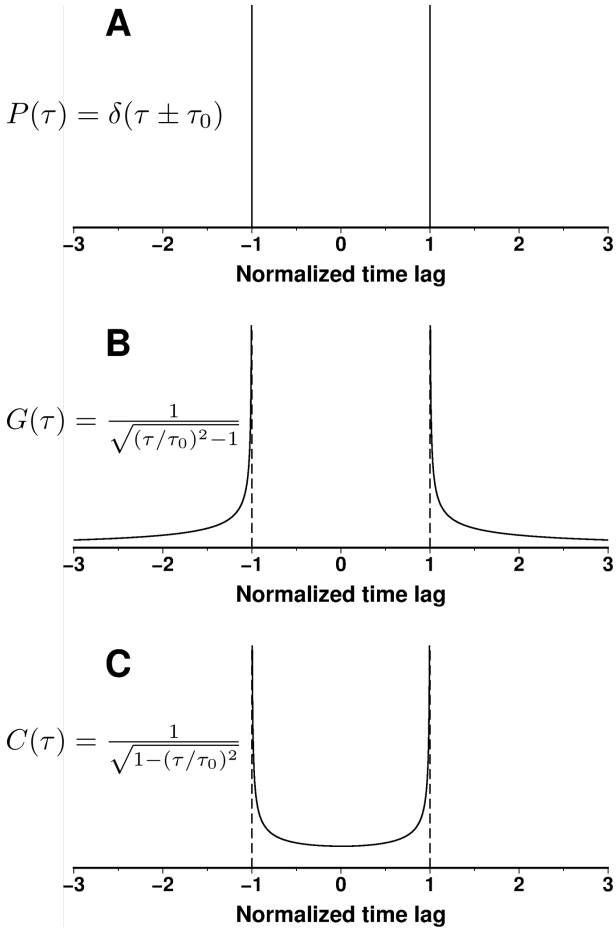

*Figure 3.3. The relation of the impulsive signal of two plane waves (***A***), the Green's function (***B***) and the correlogram (***C***)*

The expected correlogram (Equation 7), the two-sided cylindrical Green's function (Equation 10), and the two-sided response due to impulsive plane waves arriving at the two seismographs along the axis from opposite directions ($\theta = 0$) are shown in Figure 3.3. This demonstrates the relationship between the energy distribution of the theoretical correlogram and the corresponding Green's function in relation to the transit time between the two seismographs. With respect to the plane-wave transit time the theoretical correlogram is entirely acausal, while the Green's function is of course entirely causal. The two are not the same. However, the Green's function can be recovered from the correlogram because it has common features with it, in particular a singularity at the transit time. In fact, the two are related by a simple asymptotic phase shift of $\pi/2$ at high frequencies.

The Green's function and the correlogram are singular at the same time lags as the impulsive plane wave is a constant. When measuring the phase of the signal there is a slight difference between the singular functions and the impulsive plane wave. The correlogram is early compared to the impulsive plane waves by $\pi/4$, because of the constructive interference pattern described in Equation 8. The Green's function is late compared to the impulsive plane waves by $\pi/4$ because of the cylindrical geometry.

The relationship between the correlogram and Green's fucntion involves no derivative, therefore the exponent n in Equation 4 is $n = 1$, in this case. However, the phase shift of $\pi/2$ between them is represented by the imaginary i in Equation 4.

These phase differences correspond to corrections applied to measurements (discussed in the "Phase-Velocity Measurements" section) of the average phase velocity between two seismographs based on correlograms of ambient noise between them.

Having isolated wave components with known geometry from the mixture of the ambient noise by cross correlation, we can treat the correlogram as a deterministic seismogram and measure the average phase or group velocity between the two correlated seismographs.

Signal Emergence: Calculating Correlograms

The time-shift extracted from the correlogram, (τ), is based on the phase difference of the data from the two seismographs. Therefore, the amplitude does not play an important role in ANT. Each seismograph affects the measured signal with its response, which can be thought of as a filter. Thus, if the phase difference between two seismographs is measured, they need to be of the same kind. If that is not the case, the two responses need to be equalized such that the effect on the measurement on the phase from the two seismometers is the same. In our ANT study, all the instruments are the same (Lennartz 5s) with one exception (Guralp broadband instrument at station god). We, therefore, filtered the broadband recording by deconvolving its instrument's response and convolving the response of the Lennartz instrument. Thus, all recordings are equalized in their phase response.

The recorded time series at two seismographs contain continuous ambient noise, but also occasional earthquakes and other short-term transient disturbances. These transients can exceed the amplitude of the noise by orders of magnitude, but occupy in general a small proportion of time. Several methods are applied in the literature to suppress the effect of these transients on the correlogram (see summary by Bensen

et al. (2007)). We have applied the one bit time-domain normalization for this purpose. This removes all direct amplitude information from the time series. However, phase information is preserved in the zero crossings of the one-bit time series.

The time-series are also filtered between 0.05 and 4 Hz and decimated from 100 Hz to 10 Hz, prior to the cross-correlation calculations. This reduces the time it takes to calculate the cross-correlations.

Daily correlograms are computed, for any pair of seismographs, and then stacked over their common recording time, which varies from tens of days to seven months in length. In the stacking we apply weights that are proportional to an estimate of the signal-to-noise ratio for each daily correlogram. This ratio is computed from the amplitude within the expected arrival of inter-station surface waves and within its distant coda.

Phase-Velocity Measurements

With the correlograms in hand, they are treated as deterministic seismograms. The best way to visualize this is to imagine that one seismograph is the earthquake location and the other is the seismograph recording its signal. The following steps describe conventional surface-wave tomography.

A phase-velocity dispersion curve is obtained from each correlogram by frequency-time analysis using the multiple-filter method in Computer Programs in Seismology (Herrmann, 1973, 2013). A phase-velocity dispersion curve estimates the velocity of the surface-wave at each frequency, along the path between the two stations. In this part of the analysis the $\pi/2$ phase shift correction, described in the "Correlogram" section, is applied. Because of the application of narrow-band filters in the measurements a cycle-skipping ambiguity exist and a multitude of phase-velocity dispersion curves is possible. The dispersion curve is chosen based on the apparent velocity at the longest periods and apriori knowledge for example about the group velocity (see Figure 3.4).

Phase-Velocity Maps

From the phase-velocity dispersion curves, phase-velocity maps are obtained through inversion.

We used the Fast Marching Surface Tomography (FMST) inversion code of Rawlinson and Sambridge (2005). The average phase-velocities are transformed into travel-times (or the inverse of that, travel-slowness). The relationship between the velocity and travel-time is non-linear. The Fast Marching Method is used to calculate the forward problem. It is a numerical grid-based method that computes the travel-time field by solving the Eikonal equation with finite difference approximations. By combining an iterative call to the FMM and a linearized inversion, the non-linear relationship between the velocity and travel-time is approximated.

The objective function that is minimized involves the difference between observed travel-times and predicted travel-times, and the difference between the model and a reference model (model size). A damping parameter was chosen by exploration of the trade-off between datafit and model size.

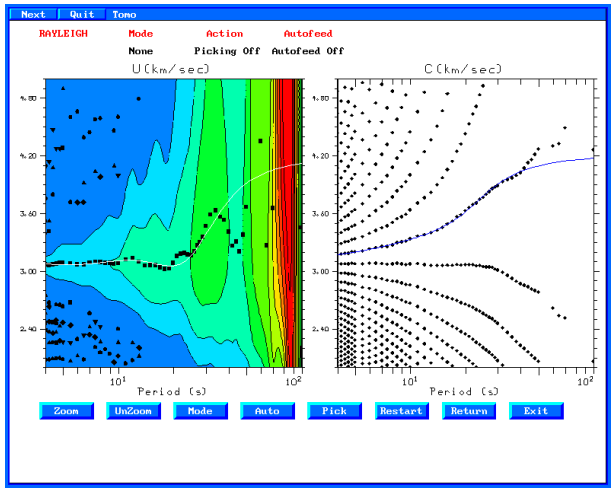

Figure 3.4. Phase-velocity and group-velocity measurements in the program "Computer Programs in Seismology" (Herrmann, 1973, 2013) showing arbitrary data. **Left panel** *shows the group-velocity curve for a correlogram. The black points are the peak of the envelope of a narrow-band filtered correlogram at the central frequency. Colors denote the energy in the correlogram at each frequency.* **Right panel** *shows the corresponding phase-velocity curves (black points) and the blue line shows the curve chosen. Many curves are possible because of the cycle-skipping ambiguity.*

Depth Inversion

The resulting phase-velocity maps are used to invert for the change in velocity with depth. Local dispersion curves are constructed at each node on the grid of the phase velocity maps, where the resolution is satisfactory. Each dispersion curve is inverted in one-dimension, resulting in a shear-wave-velocity model where the velocity changes with depth. We used the program SURF96 in Computer Programs in Seismology (Herrmann and Ammon, 2002) for the non-linear inversion to obtain the local, one-dimensional shear-velocity structure.

3D Shear-Wave Velocity Model and its Uncertainties

The three-dimensional shear-velocity model is constructed through an interpolation of the one-dimensional models.

To estimate the uncertainty of the phase-velocity measurements, they were evaluated from different monthly stacks of data. The variation of those repeated measurements was used to estimate their uncertainty. Those uncertainty estimates were then propagated through the 3D shear-velocity inversion.

The propagation of the variability of the dispersion curves into the final 3D shear-wave velocity model was such:

1. For each path a set of dispersion curves, obtained from montly stacked correlo-

grams, were gathered. The standard deviation of these gave the period-dependent error for that path in the phase-velocity map inversion.

2. After the phase-velocity map inversion was finished, we obtained an estimate of their error. The best-fitting phase-velocity maps were used to calculate path-averaged velocities at each period. These data were inverted 80 times with random noise added. The variance of the random noise was equal to the residual-data variance of the phase-velocity map inversion. By doing this, the model space was explored to see the variability in models that could fit the data, given the residual-data variance. The resulting 80 models gave 80 different estimates of velocity at a given location and period and the standard deviation of these measurements feed into point number 3.

3. From the results in 2 we can construct 80 different local phase-velocity dispersion curves at the nodes where the depth-inversion was performed. The variance of the 80 measurements are the error for the dispercion curves used in the depth-inversion.

4. The same scheme was used to propagate the error through the depth-inversion.

3.5 Volcanic Tremor

It is important to understand the mechanics and behavior of a volcano for better risk management. Monitoring the seismic signals originating at the volcano can give insights into injection and movement of magma within the volcano.

Volcanic tremor is a signal recorded at seismic stations in the proximity of volcanoes and hydrothermal vents. Konstantinou and Schlindwein (2003) defined volcanic tremor as "a persistent seismic signal that is observed only near active volcanoes, lasting from several minutes to several days, preceding and/or accompanying most volcanic eruptions" (Fehler, 1983; Julian, 1994; Ripepe, 1996; Métaxian et al., 1997). The cause of volcanic tremor is usually attributed to fluid movement within the volcano. It has been modeled as a fluid-filled tensile crack (Aki et al., 1977) where tremor is produced by an excess pressure in the magma resulting in a jerky opening of the crack; as a nonlinear excitation by fluid flow (Julian, 1994), as an acoustic resonance of a fluid-filled volcanic pipe triggered by excess gas pressure (Chouet, 1985), and as continuous bursts of small gas bubbles in the upper part of the magmatic column (Ripepe, 1996).

Hydrothermal vents are usually found in volcanic areas and therefore tremor from hydrothermal areas is considered a volcanic tremor. Such tremor is defined as "non-eruptive tremor" by Leet (1988). An example of such a tremor is found at the Old Faithful Geysir, USA (Vandemeulebrouck et al., 2013) and at Ölkelduháls, Iceland (Gudmundsson and Brandsdóttir, 2010).

The character of the tremor signal varies; it can be characterized by a fundamental frequency and its harmonics (e.g. Mt. Semeru- Schlindwein et al., 1995), by a monochromatic peak (e.g. Mt. Ruapehu- Hurst, 1992), tremor bursts with quiescence in between (e.g. Mt. Miyakejima- Fujita, 2008) or by a continuous tremor with varying amplitude (e.g. Mt. Krafla- Brandsdóttir and Einarsson, 1992). These are only a

few examples of how a volcanic tremor can be classified but the list is far from being exhaustive.

Understanding volcanic tremor has become an important task as it is often associated with the beginning of an eruption. The tremor may start after earthquake activity has stopped and a magma pathway has been established for the magma to the surface Einarsson and Brandsdóttir (1984); Vogfjörd et al. (2005). The characteristics of volcanic tremor vary, not only from one volcano to another, but also between eruptions of the same volcano (Hofstetter and Malone, 1986). For a very comprehensive overview on volcanic tremor, see Konstantinou and Schlindwein (2003).

Although the cause of volcanic tremor varies, it is usually attributed to magma movement and it, therefore, depends on processes ongoing at a given time within a volcano. Therefore, the analysis of tremor can give valuable insight into magma dynamics within a volcano.

A Simple Description of Volcanic Tremor

The decay of amplitude away from the source can be described by

$$A = A_0 g(r) s(r) \tag{11}$$

where A_0 represents the source strength, $g(r)$ is a geometrical spreading function of distance, r, and $s(r)$ describes attenuation (e.g. Battaglia and Aki, 2003; Battaglia et al., 2005; Di Grazia et al., 2006).

For a homogeneous medium (velocity) the geometrical spreading is $g(r) = r^{-a}$, where the exponent parameter is a=1 for body waves and a=0.5 for surface waves. The attenuation factor is,

$$s(r) = exp(\frac{-\pi f r}{Qv}) \tag{12}$$

when attenuation is also uniform. Here Q is an attenuation quality factor, v is the velocity of the wave, r is distance from the source, and f is frequency. When velocity and attenuation are not uniform the factors $g(r)$ and $s(r)$ become path or station dependent. For the i-th station we write

$$g_i = \gamma_i {r_i}^{-a} \tag{13}$$

introducing a station amplitude correction γ_i. The attenuation term becomes

$$s_i = exp(-\pi f \int_{path_i} \frac{dr}{Qv}) = exp(-\pi f q_i) \tag{14}$$

where

$$q_i = \int_{path_i} \frac{dr}{Qv} \tag{15}$$

This simple formulation has been commonly used in analyses of tremor amplitude (e.g Battaglia and Aki, 2003; Battaglia et al., 2005).

The parameters γ and q are path dependent. If the source location changes during an eruption, these parameters will also change. However, if the location of the source is stationary during the course of an eruption, these parameters remain constants if the propagating medium does not change. Therefore, this method can only be used in periods while the source remains stationary. This formulation is admittedly simplistic. Elements of an inevitable scattering process at a volcano that are not random cannot simply be absorbed in a scattering contribution to effective attenuation and may render path-dependent geometrical-spreading effects frequency dependent.

Locating Tremor

Volcanic tremor does usually not have a clear onset so standard arrival time methods can not be used to locate the volcanic tremor (there are a few exceptions (Aki et al., 1977; Fehler, 1983)). Also, the heterogeneity of volcanoes and strong site effects (e.g. topography) add to the complexity of the location problem.

Other non-traditional techniques have, therefore, been developed to locate the tremor origins. These including analyses of amplitude decay of the signal with distance from the source (e.g. Gottschämmer and Surono, 2000; Battaglia and Aki, 2003; Di Grazia et al., 2006) where the source is assumed to radiate isotropically. If the source behaves as such, the method works well. However, this is not always the case, as in the case of the 2010 Eyjafjallajökull eruption, which is the topic of paper III (Section 6). Furumoto et al. (1990, 1992) used the semblance technique of Neidell and Taner (1971) to locate tremor at Mt. Izu-Oshima, Japan. It is a seismic-array method based on phase coherency of signals between stations, yielding information about the local slowness vector. Others have developed a similar approach for long period tremor (e.g. Dawson et al., 2004).

Correlograms of tremor recordings can tell us something about the location of its source. If the tremor were caused by one impulsive point source, then auto-correlations would have one spike at a zero time-lag and cross-correlations would have a single spike at the time lag corresponding to the differential distance to the source and the velocity of the wave generated by the source. Using cross-correlations of tremor recordings within a broader network of seismographs to locate the tremor source has proven to work well in several areas (Gudmundsson and Brandsdóttir, 2010; Ballmer et al., 2013; Droznin et al., 2015; Sgattoni et al., 2017). The cross-correlation-location method is like the semblance method, based on phase information in the tremor. The time-series from two seismic stations are cross-correlated to reveal a signal at some time delay that depends on the differential distance from the source to the two receivers and the velocity of the medium. Using a two-dimensional grid search, where every node in the grid is treated as a hypothetical source location, attributes of the correlograms at the corresponding time-delays are added up. The correlograms are back projected to each hypothetical source and stacked. The result is an image of possible source locations. This back-projected image does, however, not provide information about uncertainty of the location. If the source has a finite spatial distribution this will be convolved into the resulting image as will temporal correlation in the source. Secondary sources (scattered phases) will also be present, albeit with reduced amplitude as they will not stack universally unless the scattering process is isotropic. Secondary sources are somewhat reduced in amplitude by application of higher-order correlations (Li et al.,

2017a,b).

Li and Gudmundsson (2019) have modified the cross-correlation location strategy by introducing probability calculations. The correlogram envelope, that is assumed to be the sum of a signal and noise, is transformed into a probability density at any given point in time. After applying Bayes rule and assuming a low probability of the presence of signal, the probability function is found to depend on the convolution of the noise probability density (p(n)) convolved with the Heavyside function. p(n) is found for each correlogram and the probability is then back-projected from the time domain into two-dimensional space to construct a spatial probability density. There is always uncertainty in the velocity, which affects the back projection of the correlogram. To address this issue, Li and Gudmundsson (2019) define a variation in the velocity, compute the corresponding variation in the time measurement which results in a filter that is convolved with the back-projected probability density. From these steps a likelihood for each correlogram is obtained. The likelihood functions are independent and by multiplying them the final joint likelihood function is obtained. The peak of that function defines the location of the source and the width of the likelihood distribution defines the uncertainty of the location. Li and Gudmundsson (2019) studied the calibration of their method through synthetic examples and find that it gives a realistic estimate of uncertainty, although a slight underestimation (by a factor of 2 given a frequency range and observational geometry similar to that of the Eyjafjallajökull tremor). We apply this method of Li and Gudmundsson (2019) to infer the location of the primary source of tremor during the Eyjafjallajökull eruption in 2010 in paper III.

4 Paper I: Tectonic evolution immediately south of the Bight Transform Fault during the past 6 Ma

Reference: Benediktsdóttir, Á., Hey, R., Martinez, F., Höskuldsson, Á. (2016). A new kinematic model of the Mid-Atlantic Ridge between 55°55′N and the Bight Transform Fault for the past 6 Ma. Journal of Geophysical Research: Solid Earth, 121(2), 455-468.

4.1 Summary

Marine magnetic anomalies, collected along the flowlines of the MAR, were used to infer the kinematics of the area just south of the Bight Transform Fault during the past 6 Ma (Figure 4.1). In this area the oblique and anomalous Reykjanes Ridge ends and conventional orthogonal spreading takes place. Analysis of marine magnetic anomalies on the Reykjanes Ridge have revealed subtle asymmetric spreading on the Reykjanes Ridge (Hey et al., 2010; Benediktsdóttir et al., 2012). Lithosphere is consistently transferred from the Eurasia Plate to the North American Plate, caused by a series of southbound propagating rifts originating close to Iceland. The sense of asymmetry is consistent with the ridge-relocation observed on Iceland, where the ridge system has repeatedly been shifted eastward toward the Iceland plume, causing an asymmetry in the layout of Iceland, with a majority of Iceland on the North-American side. Questions arise whether similar asymmetry is observed farther down the ridge, beyond the Bight Transform Fault.

Magellan, a forward modeling program for magnetic anomalies, was used to model the accretion process on the ridge. The modeling was two dimensional and assumed a change in magnetic structure along the flow lines and with depth. Spreading rates from Lourens et al. (2004) were fixed to the nearest decimal to fit the major magnetic anomalies, prior to modeling, to reduce the number of unknowns in the modeling. After fixing the spreading rates, the model was compared with the dataset. If asymmetry was detected, the preferred modeling mechanism was ridge propagation, as it is the best documented mechanism for temporal and spatial ridge evolution. A model for each of the profiles was chosen, that best fit the data and that provided a consistency between adjacentprofiles, such that a tectonic evolution could be inferred.

Figure 4.2 shows a compilation of the timing of the inferred propagators as a function of distance away from Iceland, revealing the temporal and spatial evolution of the propagation history past 6 Ma. The location of the propagating rifts overlaid on

bathymetry are shown in Figure 4.3

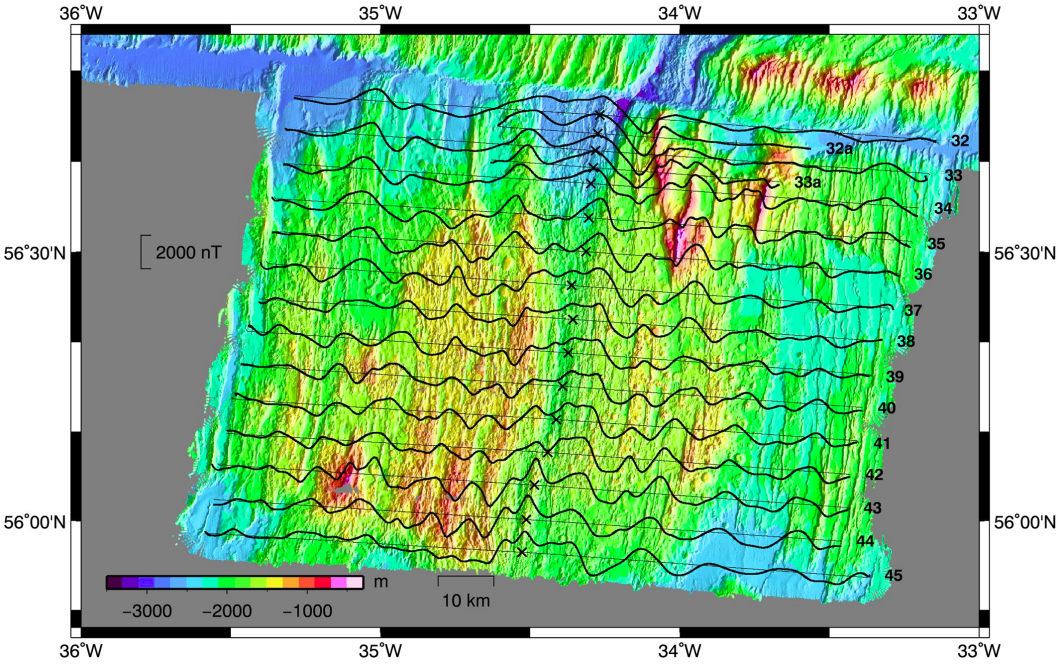

Figure 4.1. The magnetic data (black wiggles) from the Mid-Atlantic Ridge study area superimposed on the bathymetry data. The numbering convention for our profiles are as indicated here. Thin lines are ship tracks, and crosses are the ridge axes picks.

4.2 Main findings

1. Very good data fit between the magnetidc data and models for profiles in 30-60 km south of the BTF. The models provide a consistent kinematic story of the tectonic history of the area during the past 6 Ma. The first 30 km south of the BTF is more complicated.

2. Propagating rifts (propagators) are observed in the area, mainly transferring lithosphere from the Eurasia Plate to the North American Plate. Propagation rates are 10-130 km/Myr, similar to the slower of the Reykjanes Ridge propagators. The amount of lithosphere, that is transferred between the two plates, is generally small (2-5 km) for each propagator and the propagating events are short lived, extending <100 km. Unlike propagators on the Reykjanes Ridge that propagate south, away from Iceland, the ones modeled here propagate both north and south.

3. Two propagators closest to the BTF are different from those described in point 2. The central Brunhes anomaly just south of the BTF exhibits an anomalous shape;

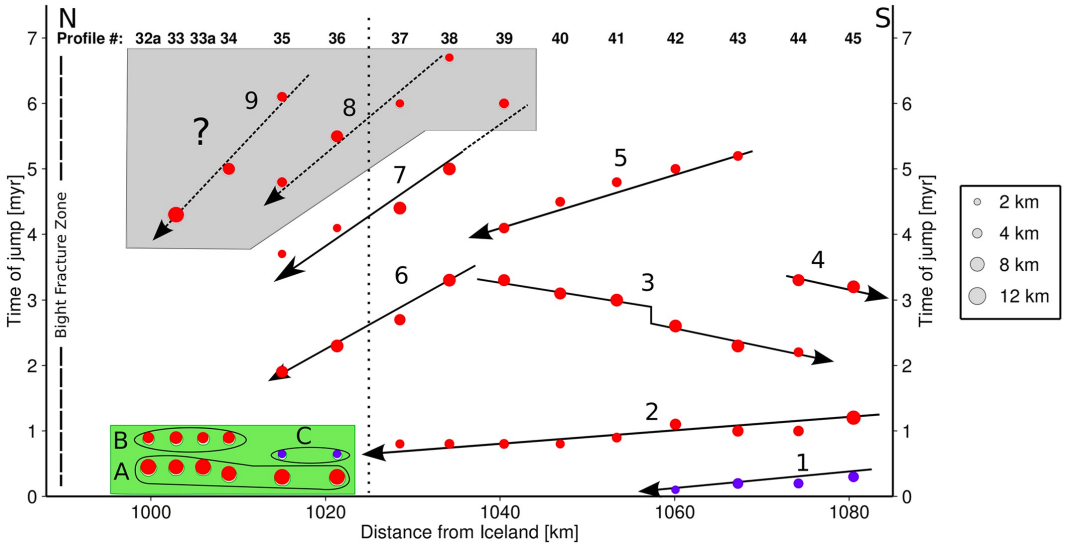

Figure 4.2. Time of jump (that is, the time when the propagator reached the profile) from the magnetic models versus distance from the Reykjanes Peninsula (at 63.7°N, 22.75°W) on Iceland. The distance from the Reykjanes Peninsula is calculated from the intersection of the individual profile with the ridge. The profile number is indicated at the top of the figure. Red and blue circles correspond to jumps transferring lithosphere to North America and Eurasia, respectively, and the circle size indicates how much lithosphere was transferred. Arrows show direction of propagation. The shaded box shows the jumps identified in the magnetic modeling where only one side was available to constrain the age of a jump; these results are therefore speculative predictions. The vertical dotted line divides the study area into the northern, where the tecotonic evolution is more complex, and southern part, where the evolution is more readily modeled by magnetic anomalies. The largest spreading center jumps in the green box are necessary to produce two areas of Brunhes separated by reversely magnetized crust. The A–C propagators suggest extremely rapid propagation (since their slope on the graph is zero, the speed approaches infinity, and we can therefore not determine the direction of propagation), which is indistinguishable but more physically plausible than an instantaneous relocation of the entire ridge segment.

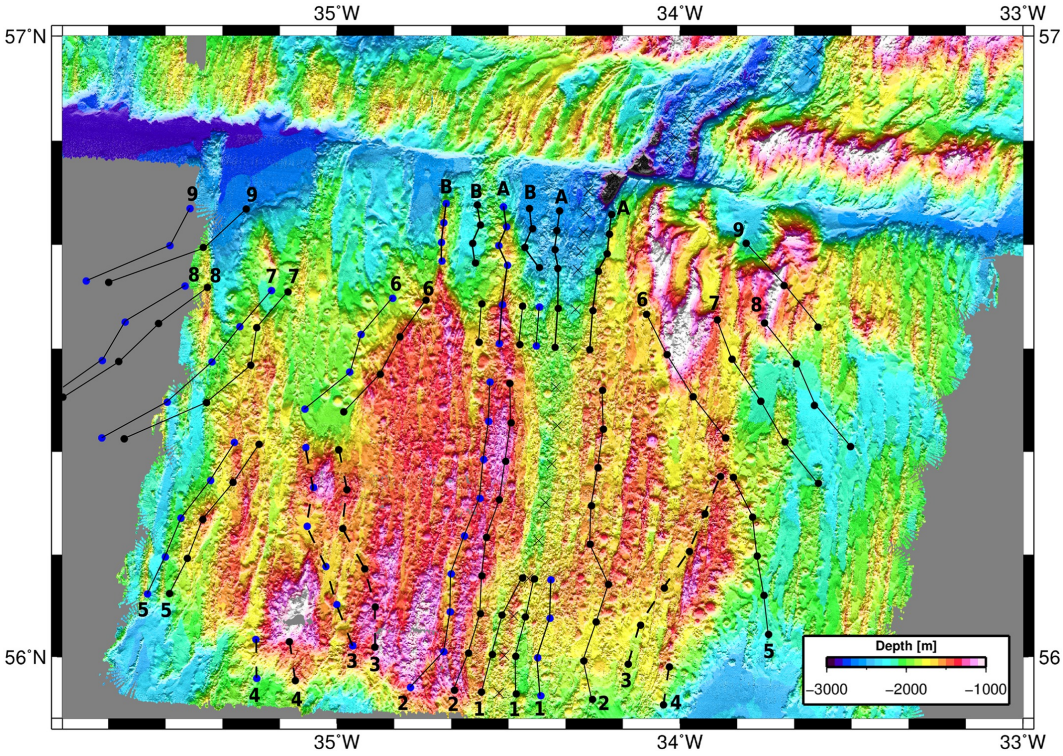

Figure 4.3. The location of propagators with the naming convention as in Figure 4.2, overlain on bathymetry data from the 2013 research cruise. Blue and black circles are failed rifts and pseudofaults, respectively. Pseudofaults and failed rifts are connected with dashed and solid lines for southward and northward propagators, respectively.

it is divided into two peaks. This is explained by two lateral relatively large (6 km and 9 km) ridge relocations in the area that seemed to have propagated very fast. The sense of asymmetry caused by these events is the same as on the Reykjanes Ridge.

4. Eastward shift of the rift in Iceland is caused by the presence of the Iceland plume and that behavior of the ridge is most likely the cause of the sense of asymmetry south of the BTF. We suggest that this reflects influence of the Iceland plume extending south of the BTF.

5 Paper II: Ambient Noise Tomography of Eyjafjallajökull

Reference: Benediktsdóttir, Á., Gudmundsson, Ó., Brandsdóttir, B., and Tryggvason, A. (2017). Ambient noise tomography of Eyjafjallajökull volcano, Iceland. Journal of Volcanology and Geothermal Research, 347, 250-263.

5.1 Summary

Seven months of data from six permanent stations and ten temporary seismic stations were used to infer the shear-velocity structure of Eyjafjallajökull volcano, south Iceland by ambient noise tomography. The tectonic settings of Eyjafjallajökull and the seismic stations used in this study are shown in Figure 5.1. The inter-station distance ranged from a few hundred meters to more than 50 kilometers and the number of station pairs was 74. The shortest inter-station distance was limited to the longest wavelength of a surface-wave used in this study, which was roughly 15 kilometers. Vertical components of the time series were cross-correlated resulting in 30 robust phase-velocity dispersion curves for periods between 1.6 s and 6.5 s. The error-based-weighted average velocity ranged from 2.1 km/s to 2.7 km/s for periods between 2 s and 6 s. The variation in the dispersion curves was $\pm 20\%$, which demonstrates a high-degree of velocity heterogeneity in the volcano. The uneven distribution of noise sources was estimated to cause less than 2% uncertainty in the dispersion velocity measurements. Sensitivity kernels displayed resolution down to 10 km, and a checker-board test demonstrated a 5 km lateral resolution in the phase-velocity maps.

5.2 Main findings

1. A $\pm 20\%$ variation in dispersion-curve measurements was found, demonstrating the high-degree of velocity-heterogeneity in Eyjafjallajökull.

2. The shear-wave velocity model had resolution down to a depth of 10 km and lateral anomalies 5 km across could be resolved.

3. Several prominent velocity anomalies emerged in the shear-wave velocity model within the uppermost 10 km, seen in vertical (Figure 5.2) and horizontal (Figure 5.3) slices through the S-wave velocity model.

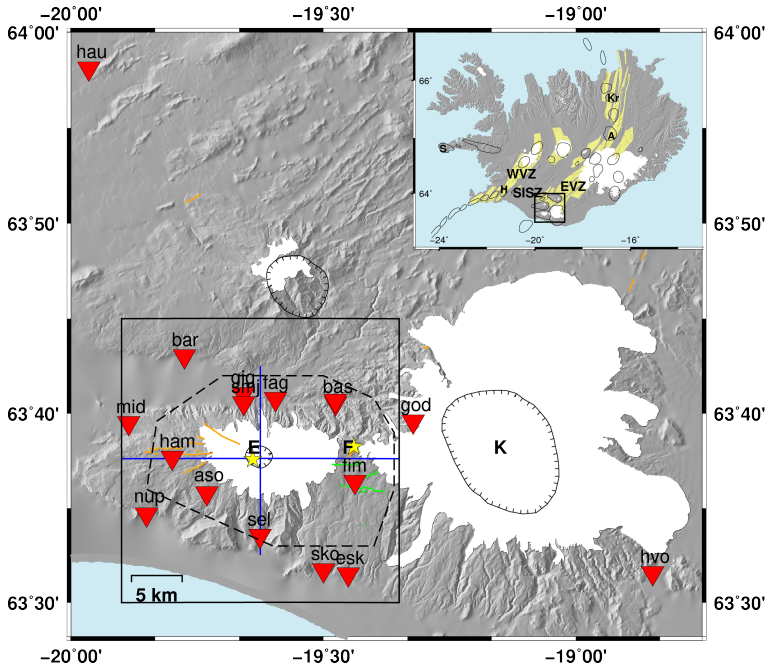

Figure 5.1. Tectonic setting of Eyjafjallajökull. Seismic stations are inverted triangles, and solid and hatched lines are outlines of central volcanic systems and calderas, respectively. E=Eyjafjallajökull, F=Fimmvörduháls, K=Katla. Orange lines are eruptive fissures and green lines are faults (data compiled by Einarsson & Hjartardóttir 2015, see references therein). The rectangular box shows the area of Figure 5.2 and the blue lines show the location of the cross sections in Figure 5.3. In the small inlet; WVZ=Western Volcanic Zone, EVZ=Eastern Volcanic Zone, SISZ=South Iceland Seismic Zone.

(a) A low-velocity zone stretching southwest from underneath the caldera

(b) Two east-west trending high-velocity zones (Figure 5.3), interpreted as large intrusive bodies or magma cumulates. The east-west orientation agree with other geological features in Eyjafjallajökull and are interpreted as further evidence for the N-S orientation of the local maximum tensile forces in the area.

(c) A narrow zone, of relatively low velocity, in between the high-velocity zones, which coincides with the locations of earthquakes during the summit eruption in Eyjafjallajökull, possibly indicating the magma pathway from a deeper source.

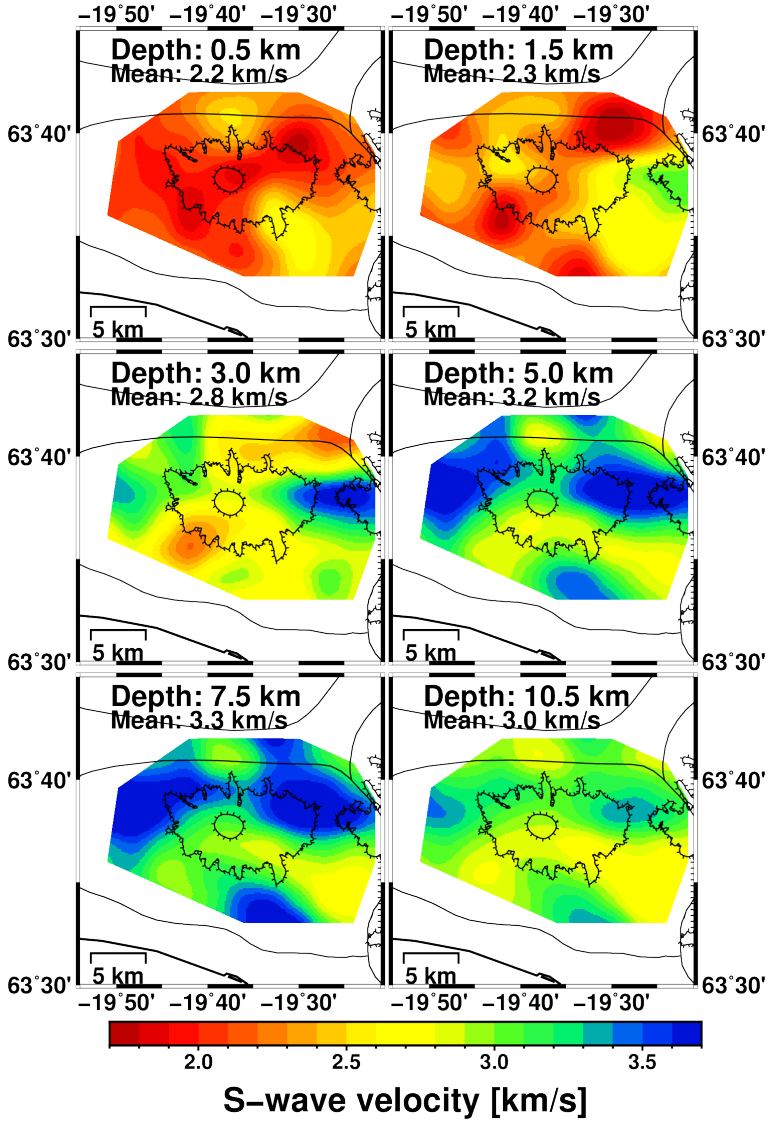

Figure 5.2. Depth slices with a first order correction for topography. Mean velocities for each layer are indicated.

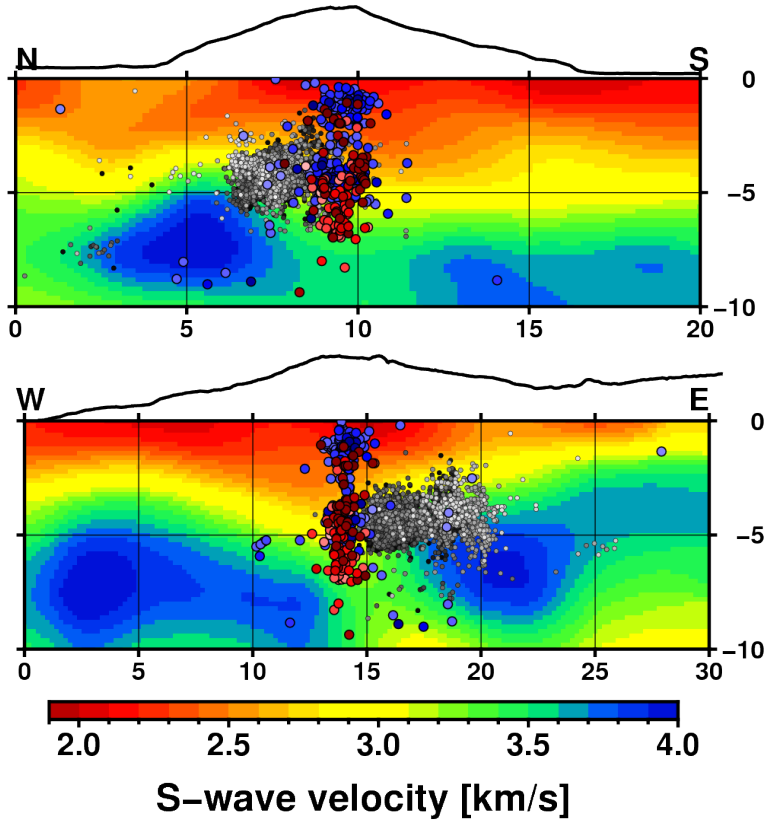

Figure 5.3. Vertical S-wave velocity profiles for the first order corrected model. The location of the cross sections are shown as blue lines in Figure 5.1. Upper and lower panels are North-South and East-West cross sections, respectively. Black lines show the topography of Eyjafjallajökull, with a vertical exaggaeration of 2.5. Black, blue and magenta circles are earthquakes from March $5^{th} - 20^{th}$, April $13^{th} - 14^{th}$, and May 2010 respectively (earthquakes from Tarasewicz et al. (2012)). All color codes progress from early (light) to late (dark), during the indicated time span of each dataset.

6 Paper III: Volcanic tremor of the 2010 Eyjafjallajökull eruption

Reference: Benediktsdóttir, Á., Gudmundsson, Ó., Li, K. L., and Brandsdóttir, B.. Volcanic tremor of the 2010 Eyjafjallajökull eruption. In preparation for Geophysical Journal International, 2019.

6.1 Summary

The summit eruption at Eyjafjallajökull volcano lasted from April 14^{th} to May 22^{nd} 2010. Data from 12 seismic stations, six permanent stations operated by the Iceland Meterological Office, and six temporary stations deployed by the Institute of Earth Sciences, University of Iceland were used in this study. The tremor was detected at stations 40 kilometers away from the eruption site with most of the tremor power recorded in the 0.5-4 Hz range and at frequencies up to 10 Hz nearest to the eruption side. The temporal characteristics of the tremor source was well correlated with the four phases that were defined by Gudmundsson et al. (2012) based on a combination of different datasets, including tephra fallout data, tephra dispersal outside Iceland and plume height (Figure 6.1).

The temporal evolution of the tremor during the first 3 days of the eruption is shown in Figure 6.2. The first signs of an imminent eruption was an intense microearthquake swarm at 22:30 on April 13^{th} (Tarasewicz et al., 2012; Karlsdóttir et al., 2012) (1 in Figure 3), with earthquake locations clustered at 4-5 km depth within the caldera. Shortly after that, at 23:00, another microearthquake swarm started at about 1 km depth followed by elevated tremor levels (1a in Figure 6.2). As microearthquake activity ceased tremor levels became steady at approximately 1:10 on April 14^{th} (2 in Figure 6.2) and the eruption had started.

The likelihood of daily tremor locations was estimated using a probabilistic inference method (Li and Gudmundsson, 2019) which is based on the envelope of inter-station correlograms. The method was applied on surface waves in two dimensions assuming a homogeneous velocity medium. The measured group velocities by Benediktsdóttir et al. (2017) (paper II) and Jeddi et al. (2017) were extrapolated to find a rough estimate of the group velocity of the tremor. These were then narrowed down to the velocities that best focused the likelihood, judged by visual inspection, resulting in 1.4 km/s, 1.3 km/s and 1.2 km/s for the 0.5-1 Hz, 1-2 Hz and 2-4 Hz frequency intervals, respectively. The location was very stable during the course of the eruption and by stacking daily cross-correlations one location could be inferred. Figure 6.3 shows the location likelihood of

the tremor for eruption-long correlograms for three different frequency intervals along with the temporal stability of the location.

Because the location of the tremor was stable during the eruption, for two frequency intervals, many parameters in the tremor-amplitude decay equation were also constants during the time-span of the eruption. By analyzing the power-ratios between a reference station, *fag*, and other stations, it became clear that there was a time-dependent behavior in the data. We divided the eruption into 10 time epochs, based on the time-variation in the power-ratios between stations. This was done independent of other data.

Following the power-ratio analyses, parameters were estimated, by simple least-squares optimization. The parameters include the quality factor (Q), geometrical spreading factor and relative station correction. The geometrical spreading factor was indicative that the main wave content were surface waves. The parametrization of the inverse problem was not sufficient to explain the variation in the data and because of the stability of the source it was inferred that the time-behavior could be attributed to a variable non-isotropic power-radiation pattern of the source.

At 1 Hz and with a phase velocity of approximately 1.5 km/s (somewhat higher than the group velocity) the wavelength of a surface wave is 1.5 km. The eigenfunctions of fundamental-mode surface waves with that wavelength peak at about 0.5-1 km depth. Thus, if the surface waves are fundamental mode, they are most effectively excited quite near the surface, i.e. approximately in the top kilometer or less. Note that if the source is at depth, then that would cause a common phase shift to the surface waves at two stations, which cancels in the correlation.

6.2 Main findings

1. Most of the power of the tremor was in the frequency range between 0.5-4 Hz and up to 10 Hz for stations closest to the eruption source.

2. The location of the tremor source of the Eyjafjallajökull eruption was very stable during the span of the eruption in the frequency band 0.5-2 Hz.

3. The tremor source was located 400 m and 700 m SW of one of the most active craters in the eruption in the 0.5-1 Hz and 1-2 Hz frequency bands, respectively. This is indistinguishable from the crater location within error.

4. The tremor was mostly composed of surface waves.

5. The power-radiation pattern of the source was not isotropic, particularly during the effusive part of the eruption.

6. The estimate of the quality factor (Q) was about 15 for paths inside the volcano and between 40 and 50 for paths outside the volcano.

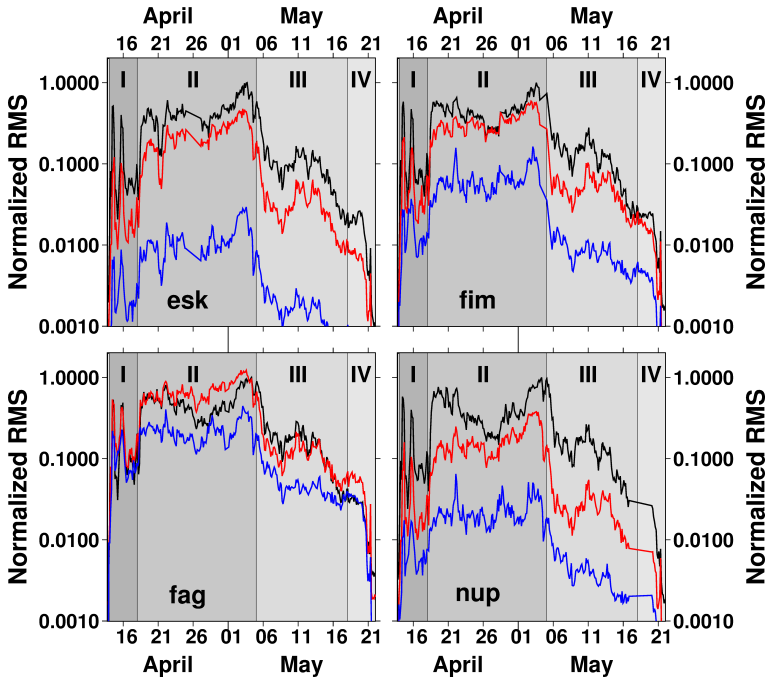

Figure 6.1. Semi-log plots of normalized one-hour-RMS amplitudes during the 2010 Eyjafjallajökull summit eruption for stations fag, nup, fim and esk for three different frequency ranges (0.5-1 Hz (black), 1-2 Hz (red) and 2-4 Hz (blue)), normalized by the maximumm amplitude of the 0.5-1 Hz frequency range. Four different time intervals, as defined by Gudmundsson et al. (2012), are indicated by gray shading (I - IV).

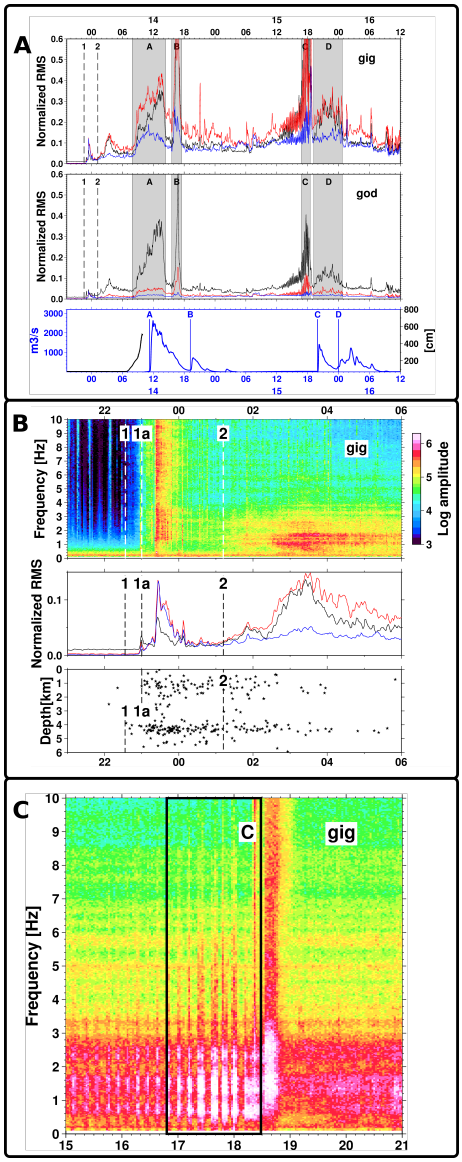

Figure 6.2. **A** *Root mean square amplitude over 2 minutes for stations gig (top) and god (middle) during the first 2.5 days of the eruption. Black, red and blue are the 0.5-1 Hz, 1-2 Hz and 2-4 Hz frequency bands, respectively, normalized by the maximum amplitude of the 0.5-1 Hz at station gig. Shaded areas indicate four tremor pulses observed, A-D. 1 and 2 refer to the onset of an microearthquake swarm and the onset of the eruption (Karlsdóttir et al. (2012)) when tremor levels increased considerably, respectively. The bottom panel shows flow data from a gauge in Markarfljót (Vedurstofa Íslands, 2019a) (blue) and water level at a gauge just north of Gígjökull (black) (Vedurstofa Íslands, 2019b), see gauge locations in Figure 1.1. Flow peaks A-D correlate with the corresponding tremor peaks. See text for detail.* **B** *Amplitude spectra on April* 14^{th} *for the first few hours of the eruption at station gig (top), normalized rms for station gig (colors and normalization as in* **A***) (middle) and earthquakes in the caldera (from (Tarasewicz et al., 2012). 1 and 2 are as in* **A** *and 1a is when the earthquakes get shallower.* **C** *Spectrogram of station gig during tremor pulse C on April* 15^{th} *(black box).*

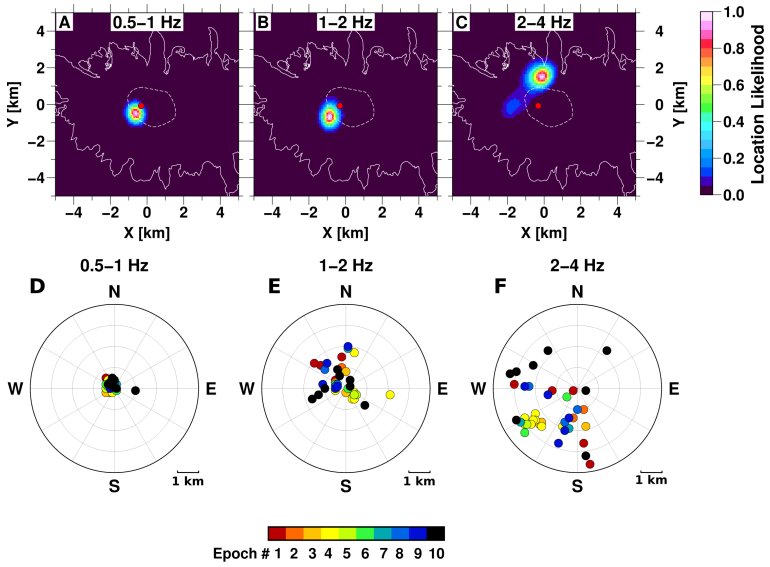

Figure 6.3. Results of the backprojection of the tremor signal. **A**, **B**, **C** *are the location of the tremor source locations for eruption-long-correlograms filtered between 0.5-1 Hz, 1-2 Hz and 2-4 Hz, respectively. White and dashed lines are the outline and caldera of Eyjafjallajökull, respectively. The color palette denotes the location likelihood and the red circle is the location of the eruption (Gudmundsson et al., 2012).* **D-F** *show the location of daily backprojections for the three different frequency intervals, relative to the location shown in* **A-C**. *The color palette refers to the 10 epochs defined from the power-ratio analyses. The radial gridlines are every 1 kilometer.*

References

Aki, K., Fehler, M., and Das, S. (1977). Source mechanism of volcanic tremor: fluid-driven crack models and their application to the 1963 Kilauea eruption. *J. Volcanol. Geotherm. Res.*, 2(3):259–287.

Albino, F. and Sigmundsson, F. (2014). Stress transfer between magma bodies: Influence of intrusions prior to 2010 eruptions at Eyjafjallajökull volcano, Iceland. *J.Geophys. Res.*, 119(4):2964–2975.

Appelgate, B. and Shor, A. N. (1994). The northern Mid-Atlantic and Reykjanes Ridges: Spreading center morphology between 55°50′N and 63°00′N. *J. Geophys. Res.*, 99(B9):17935–17956.

Ardhuin, F., Stutzmann, E., Schimmel, M., and Mangeney, A. (2011). Ocean wave sources of seismic noise. *J. Geophys. Res.*, 116. C09004.

Ballmer, S., Wolfe, C., Okubo, P., Haney, M., and Thurber, C. (2013). Ambient seismic noise interferometry in Hawai'i reveals long-range observability of volcanic tremor. *Geophys. J. Int.*, page ggt112.

Battaglia, J. and Aki, K. (2003). Location of seismic events and eruptive fissures on the Piton de la Fournaise volcano using seismic amplitudes. *J. Geophys. Res.*, 108(B8).

Battaglia, J., Aki, K., and Ferrazzini, V. (2005). Location of tremor sources and estimation of lava output using tremor source amplitude on the Piton de la Fournaise volcano: 1. Location of tremor sources. *J. Volcanol. Geotherm. Res.*, 147(3-4):268–290.

Benediktsdóttir, Á., Gudmundsson, Ó., Brandsdóttir, B., and Tryggvason, A. (2017). Ambient noise tomography of Eyjafjallajökull volcano, Iceland. *J. Volc. Geotherm. Res.*, 347:250–263.

Benediktsdóttir, Á., Hey, R., Martinez, F., and Höskuldsson, Á. (2012). Detailed tectonic evolution of the Reykjanes Ridge during the past 15 Ma. *Geochem. Geophys. Geosys.*, 13(2). Q02008.

Benediktsdóttir, Á., Hey, R., Martinez, F., and Höskuldsson, Á. (2016). A new kinematic model of the Mid-Atlantic Ridge between 55°55′N and the Bight Transform Fault for the past 6 Ma. *J. Geophys. Res.*, 121(2):455–468.

Bensen, G., Ritzwoller, M., Barmin, M., Levshin, A., Lin, F., Moschetti, M., Shapiro, N., and Yang, Y. (2007). Processing seismic ambient noise data to obtain reliable broad-band surface wave dispersion measurements. *Geophys. J. Int.*, 169(3):1239–1260.

Berk Biryol, C., Beck, S., Zandt, G., and Özacar, A. (2011). Segmented African lithosphere beneath the Anatolian region inferred from teleseismic P-wave tomography. *Geophys. J. Int.*, 184(3):1037–1057.

Brandsdóttir, B. and Einarsson, P. (1992). Volcanic tremor and low-frequency earth-

quakes in Iceland. In *Volcanic seismology*, pages 212–222. Springer.
Brenguier, F., Shapiro, N., Campillo, M., Nercessian, A., and Ferrazzini, V. (2007). 3-D surface wave tomography of the Piton de la Fournaise volcano using seismic noise correlations. *Geophys. Res. Lett.*, 34(2). L02305.
Cande, S. and Kent, D. (1995). Revised calibration of the geomagnetic polarity timescale for the Late Cretaceous and Cenozoic. *J. Geophys. Res.*, 100(B4):6093–6095.
Dahm, T. and Brandsdóttir, B. (1997). Moment tensors of microearthquakes from the Eyjafjallajökull volcano in South Iceland. *Geophys. J. Int.*, 130(1):183–192.
Dawson, P., Whilldin, D., and Chouet, B. (2004). Application of near real-time radial semblance to locate the shallow magmatic conduit at Kilauea Volcano, Hawaii. *Geophys. Res. Lett.*, 31(21). L21606.
DeMets, C., Gordon, R.G. Argus, D., and Stein, S. (1994). Effect of recent revisions to the geomagnetic reversal time scale on estimate of current plate motions. *Geophys. Res. Lett.*, 21(20):2192–2194.
DeMets, C., Gordon, R., and Argus, D. (2010). Geologically current plate motions. *Geophys. J. Int.*, 181(1):1–80.
Di Grazia, G., Falsaperla, S., and Langer, H. (2006). Volcanic tremor location during the 2004 Mount Etna lava effusion. *Geophys. Res. Lett.*, 33(4). L04304.
Droznin, D., Shapiro, N., Droznina, S. Y., Senyukov, S., Chebrov, V., and Gordeev, E. (2015). Detecting and locating volcanic tremors on the Klyuchevskoy group of volcanoes (Kamchatka) based on correlations of continuous seismic records. *Geophys. J. Int.*, 203(2):1001–1010.
Einarsson, P. (2008). Plate boundaries, rifts and transforms in Iceland. *Jökull*, 58:35–58.
Einarsson, P. and Brandsdóttir, B. (1984). Seismic activity preceding and during the 1983 volcanic eruption in Grímsvötn, Iceland. *Jökull*, 34:13–23.
Einarsson, P. and Hjartardóttir, Á. (2015). Structure and tectonic position of the Eyjafjallajökull volcano, S. Iceland. *Jökull*, 65.
Fang, H., Yao, H., Zhang, H., Huang, Y., and van der Hilst, R. (2015). Direct inversion of surface wave dispersion for three-dimensional shallow crustal structure based on ray tracing: Methodology and application. *Geophys. J. Int.*, 201(3):1251–1263.
Fehler, M. (1983). Observations of volcanic tremor at Mount St. Helens volcano. *J. Geophys. Res.*, 88(B4):3476–3484.
Fujita, E. (2008). Banded tremor at Miyakejima volcano, Japan: Implication for two-phase flow instability. *J. Geophys. Res.*, 113. B04207.
Furumoto, M., Kunitomo, T., Inoue, H., Yamada, I., Yamaoka, K., Ikami, A., and Fukao, Y. (1990). Twin sources of high-frequency volcanic tremor of Izu-Oshima Volcano, Japan. *Geophys. Res. Lett.*, 17(1):25–27.
Furumoto, M., Kunitomo, T., Inoue, H., and Yamaoka, K. (1992). Seismic image of the volcanic tremor source at Izu-Oshima volcano, Japan. In *Volcanic Seismology*, pages 201–211. Springer.
Gao, H. and Shen, Y. (2015). A Preliminary Full-Wave Ambient-Noise Tomography Model Spanning from the Juan de Fuca and Gorda Spreading Centers to the Cascadia Volcanic Arc. *Seis. Res. Lett.*, 86(5):1253–1260.
Garcia, S., Angelier, J., Bergerat, F., and Homberg, C. (2002). Tectonic analysis of an oceanic transform fault zone based on fault-slip data and earthquake focal mechanisms: the Húsavík–Flatey Fault zone, Iceland. *Tectonophysics*, 344(3-4):157–

174.

Garcia, S., Arnaud, N., Angelier, J., Bergerat, F., and Homberg, C. (2003). Rift jump process in Northern Iceland since 10 Ma from 40Ar/39Ar geochronology. *Earth and Planetary Science Letters*, 214(3-4):529–544.

Geirsson, H., Árnadóttir, T., Hreinsdóttir, S., Decriem, J., LaFemina, P., Jónsson, S., Bennett, R., Metzger, S., Holland, A., Sturkell, E., et al. (2010). Overview of results from continuous GPS observations in Iceland from 1995 to 2010. *Jökull*, 60:3–22.

Geirsson, H., Árnadóttir, T., Völksen, C., Jiang, W., Sturkell, E., Villemin, T., Einarsson, P., Sigmundsson, F., and Stefánsson, R. (2006). Current plate movements across the Mid-Atlantic Ridge determined from 5 years of continuous GPS measurements in Iceland. *J. Geophys. Res.*, 111(B09407).

Gottschämmer, E. and Surono, I. (2000). Locating tremor and shock sources recorded at Bromo Volcano. *J. Volcanol. Geotherm. Res.*, 101(1):199–209.

Grêt, A., Snieder, R., Aster, R., and Kyle, P. (2005). Monitoring rapid temporal change in a volcano with coda wave interferometry. *Geophys. Res. Lett.*, 32(6). L06304.

Gudmundsson, M., Pedersen, R., Vogfjörd, K., Thorbjarnardóttir, B., Jakobsdóttir, S., and Roberts, M. (2010). Eruptions of Eyjafjallajökull Volcano, Iceland. *Eos, Transactions American Geophysical Union*, 91(21):190–191.

Gudmundsson, M., Thordarson, T., Höskuldsson, Á., Larsen, G., Björnsson, H., Prata, F., Oddsson, B., Magnússon, E., Högnadóttir, T., Petersen, G., et al. (2012). Ash generation and distribution from the april-may 2010 eruption of eyjafjallajökull, iceland. *Scientific reports*, 2:572.

Gudmundsson, Ó. and Brandsdóttir, B. (2010). Geothermal noise at Ölkelduháls, SW Iceland. *Jökull*, 60:89–102.

Gudmundsson, Ó., Khan, A., and Voss, P. (2007). Rayleigh-wave group-velocity of the Icelandic crust from correlation of ambient seismic noise. *Geophys. Res. Lett.*, 34(14). L14314.

Hardarson, B., Fitton, J., Ellam, R., and Pringle, M. (1997). Rift relocation–a geochemical and geochronological investigation of a palaeo-rift in northwest Iceland. *Earth Planet. Sci. Lett.*, 153(3-4):181–196.

Hasselmann, K. (1963). A statistical analysis of the generation of microseisms. *Rev. Geophys.*, 1(2):177–210.

Haubrich, R., Munk, W., and Snodgrass, F. (1963). Comparative spectra of microseisms and swell. *Bull. Seism. Soc. Am.*, 53(1):27–37.

Haug, G. H. and Tiedemann, R. (1998). Effect of the formation of the Isthmus of Panama on Atlantic Ocean thermohaline circulation. *Nature*, 393(6686):673.

Heirtzler, J., Dickson, G., Herron, E., Pitman, W., and Le Pichon, X. (1968). Marine magnetic anomalies, geomagnetic field reversals, and motions of the ocean floor and continents. *J. Geophys. Res.*, 73(6):2119–2136.

Herrmann, R. (1973). Some aspects of band-pass filtering of surface waves. *Bull. Seis. Soc. Am.*, 63(2):663–671.

Herrmann, R. (2013). Computer programs in seismology: an evolving tool for instruction and research. *Seis. Res. Lett.*, 84(6):1081–1088.

Herrmann, R. and Ammon, C. (2002). Computer programs in seismology: Surface waves, receiver functions and crustal structure. *St. Louis University, St. Louis, MO*.

Hey, R. (1977). A new class of pseudofaults and their bearing on plate tectonics: a

propagating rift model. *Earth Planet. Sci. Lett.*, 37:321–325.

Hey, R., Duennebier, F., and Morgan, W. (1980). Propagating rifts on mid-ocean ridges. *J. Geophys. Res.*, 85(B7):3647–3658.

Hey, R., Martinez, F., Höskuldsson, A., and Benediktsdóttir, A. (2010). Propagating rift model for the V-shaped ridges south of Iceland. *Geochem. Geophys. Geosyst*, 11(3). Q03011.

Hey, R., Martinez, F., Höskuldsson, Á., Eason, D., Sleeper, J., Thordarson, S., Benediktsdóttir, Á., and Merkuryev, S. (2016). Multibeam investigation of the active north atlantic plate boundary reorganization tip. *Earth Planet. Sci. Lett.*, 435:115–123.

Hey, R. and Vogt, P. (1977). Spreading center jumps and sub-axial asthenosphere flow near the Galapagos hotspot. *Tectonophysics*, 37(1-3):41–52.

Hey, R. and Wilson, D. (1982). Propagating rift explanation for the tectonic evolution of the northeast pacific–the pseudomovie. *Earth Planet. Sci. Lett.*, 58(2):167–188.

Hjaltadóttir, S., Vogfjörd, K. S., Hreinsdóttir, S., and Slunga, R. (2015). Reawakening of a volcano: Activity beneath Eyjafjallajökull volcano from 1991 to 2009. *J. Vol. Geoth. Res.*, 304:194–205.

Hofstetter, A. and Malone, S. (1986). Observations of volcanic tremor at Mount St. Helens in April and May 1980. *Bull. Seismol. Soc. Am.*, 76(4):923–938.

Hooper, A., Pedersen, R., and Sigmundsson, F. (2009). Constraints on magma intrusion at Eyjafjallajökull and Katla volcanoes in Iceland, from time series SAR interferometry. In Bean, C., Braiden, A., Lokmer, I., Martini, F., and O'Brien, G., editors, *The VOLUME Project–Volcanoes: Understanding Subsurface Mass Movement.*, pages 13–24.

Hurst, A. (1992). Stochastic simulation of volcanic tremor from Ruapehu. *J. Volcanol. Geotherm. Res.*, 51(3):185–198.

Inoue, H., Fukao, Y., Tanabe, K., and Ogata, Y. (1990). Whole mantle P-wave travel time tomography. *Physics of the Earth and Planetary Interiors*, 59(4):294–328.

Ito, G. (2001). Origin of V-shaped Reykjanes ridges from a pulsing and dehydrating mantle plume. *Nature*, 411:681–684.

Jancin, M., Young, K., Voight, B., Aronson, J. L., and Sæmundsson, K. (1985). Stratigraphy and K/Ar ages across the west flank of the northeast Iceland axial rift zone, in relation to the 7 Ma volcano-tectonic reorganization of Iceland. *J. Geophys. Res.*, 90(B12):9961–9985.

Jay, J. A., Pritchard, M., West, M., Christensen, D., Haney, M., Minaya, E., Sunagua, M., McNutt, S., and Zabala, M. (2012). Shallow seismicity, triggered seismicity, and ambient noise tomography at the long-dormant Uturuncu Volcano, Bolivia. *Bull. Vol.*, 74(4):817–837.

Jeddi, Z., Gudmundsson, O., and Tryggvason, A. (2017). Ambient-noise tomography of Katla volcano, south Iceland. *J. Volc. Geotherm. Res.*, 347:264–277.

Jeddi, Z., Tryggvason, A., and Gudmundsson, O. (2016). The Katla Volcanic system imaged using local earthquakes recorded with a temporary seismic network. *J. Geophys. Res.*, 121(10):7230–7251.

Jóhannesson, H. (1980). Evolution of rift zones in west Iceland. *Náttúrufrædhingurinn*, 50:13–31.

Jones, S. (2003). Test of a ridge-plume interaction model using oceanic crustal structure around Iceland. *Earth Planet. Sci. Lett.*, 208(3-4):205–218.

Jonge, M., Wortel, M., and Spakman, W. (1994). Regional scale tectonic evolution and the seismic velocity structure of the lithosphere and upper mantle: the Mediterranean region. *J. Geophys. Res.*, 99(B6):12091–12108.

Jónsdóttir, K., Tryggvason, A., Roberts, R., Lund, B., Soosalu, H., and Bödvarsson, R. (2007). Habits of a glacier-covered volcano: seismicity patterns and velocity structure of Katla volcano, Iceland. *Annals of Glaciology*, 45(1):169–177.

Jónsson, B. (1774). *Annalar Thess Froma og velvitra Sauluga Biørns Jonssonar a Skardsau Fordum Løgrettumanns i Hegranes-sýslu*. Skardsárannáll. Available at: http://baekur.is/bok/000043701/Annalar_THess_froma_og.

Jónsson, S., Einarsson, P., and Sigmundsson, F. (1997). Extension across a divergent plate boundary, the Eastern Volcanic Rift Zone, south Iceland, 1967–1994, observed with GPS and electronic distance measurements. *J. Geophys. Res.*, 102(B6):11913–11929.

Julian, B. R. (1994). Volcanic tremor: nonlinear excitation by fluid flow. *J. Geophys. Res.*, 99(B6):11859–11877.

Juretzek, C. and Hadziioannou, C. (2016). Where do ocean microseisms come from? A study of Love-to-Rayleigh wave ratios. *J. Geophys. Res.*, 121(9):6741–6756.

Karlsdóttir, S., Gylfason, Á., Höskuldsson, Á., Brandsdóttir, B., Ilyinskaya, E., Gudmundsson, M., and Högnadóttir, T. (2012). In Thorkelsson, B., editor, *The 2010 Eyjafjallajökull eruption, Iceland, IMO, IES and NCIP-DCPEM Rport to ICAO 2012*, page 209.

Karson, J. (2017). The Iceland Plate Boundary Zone: Propagating Rifts, Migrating Transforms, and Rift-Parallel Strike-Slip Faults. *Geochem. Geophys. Geosys.*, 18(11):4043–4054.

Kedar, S., Longuet-Higgins, M., Webb, F., Graham, N., Clayton, R., and Jones, C. (2008). The origin of deep ocean microseisms in the North Atlantic Ocean. *Proc. R. Soc. London Ser. A.*, 464(2091):777–793.

Konstantinou, K. I. and Schlindwein, V. (2003). Nature, wavefield properties and source mechanism of volcanic tremor: a review. *J. Volcanol. Geotherm. Res.*, 119(1):161–187.

Korostelev, F., Weemstra, C., Leroy, S., Boschi, L., Keir, D., Ren, Y., Molinari, I., Ahmed, A., Stuart, G., Rolandone, F., et al. (2015). Magmatism on rift flanks: Insights from ambient noise phase velocity in Afar region. *Geophys. Res. Lett.*, 42(7):2179–2188.

Kristjánsson, L. and Jónsson, G. (1998). Aeromagnetic results and the presence of an extinct rift zone in western Iceland. *J. Geodyn.*, 25(1-2):99–108.

LaFemina, P., Dixon, T. H., Malservisi, R., Árnadóttir, T., Sturkell, E., Sigmundsson, F., and Einarsson, P. (2005). Geodetic GPS measurements in south Iceland: Strain accumulation and partitioning in a propagating ridge system. *J. Geophys. Res.*, 110. B11405.

Larsen, G., Dugmore, A., and Newton, A. (1999). Geochemistry of historical-age silicic tephras in Iceland. *The Holocene*, 9(4):463–471.

Laughton, A. (1972). The southern Labrador Sea - A Key to the Mesozoic and early Tertiary evolution of the North Atlantic. In Laughton, A. e. a., editor, *Initial Reports of the Deep Sea Drilling Project , Vol. XII*, pages 1155–1179. US Govt. Printing Office, Washington.

Le Pichon, X. and Fox, P. (1971). Marginal offsets, fracture zones, and the early opening of the North Atlantic. *J. Geophys. Res.*, 76(26):6294–6308.

Leet, R. C. (1988). Saturated and subcooled hydrothermal boiling in groundwater flow channels as a source of harmonic tremor. *J. Geophys. Res.*, 93(B5):4835–4849.

Li, C., Van Der Hilst, R., Engdahl, E., and Burdick, S. (2008). A new global model for P wave speed variations in Earth's mantle. *Geochem., Geophys., Geosys.*, 9(5).

Li, K. and Gudmundsson, O. (2019). A probabilistic tremor location method. *In preparation*.

Li, K., Sgattoni, G., Sadeghisorkhani, H., Roberts, R., and Gudmundsson, O. (2017a). A double-correlation tremor-location method. *Geophys. J. Int.*, 208(2):1231–1236.

Li, K. L., Sadeghisorkhani, H., Sgattoni, G., Gudmundsson, O., and Roberts, R. (2017b). Locating tremor using stacked products of correlations. *Geophys. Res. Lett.*, 44(7):3156–3164.

Longuet-Higgins, M. (1950). A theory of the origin of microseisms. *Phil. Trans. R. Soc. Lond. A*, 243(857):1–35.

Lourens, L., Hilgen, F., Laskar, J., Shackleton, N., and Wilson, D. (2004). The Neogene Period. In Gradstein, F., Ogg, J., and Smith, A., editors, *A Geologic Time Scale 2004*, pages 409–440. Cambridge University Press Cambridge, UK.

Macnab, R., Verhoef, J., Roest, W., and Arkani-Hamed, J. (1995). New database documents the magnetic character of the Arctic and North Atlantic. *Eos, Transactions American Geophysical Union*, 76(45):449–458.

Martin, E., Paquette, J.-L., Bosse, V., Ruffet, G., Tiepolo, M., and Sigmarsson, O. (2011). Geodynamics of rift–plume interaction in Iceland as constrained by new 40 Ar/39 Ar and in situ U–Pb zircon ages. *Earth Planet. Sci. Lett.*, 311(1):28–38.

Martinez, F. and Hey, R. (2017). Propagating buoyant mantle upwelling on the Reykjanes Ridge. *Earth Planet Sci. Lett.*, 457:10–22.

Matos, C., Silveira, G., Matias, L., Caldeira, R., Ribeiro, M., Dias, N., Krüger, F., and dos Santos, T. (2015). Upper crustal structure of Madeira Island revealed from ambient noise tomography. *J. Vol. Geoth. Res.*, 298:136–145.

Merkouriev, S. and DeMets, C. (2008). A high-resolution model for Eurasia–North America plate kinematics since 20 Ma. *Geophys, J. Int.*, 173(3):1064–1083.

Métaxian, J., Lesage, P., and Dorel, J. (1997). Permanent tremor of Masaya Volcano, Nicaragua: Wave field analysis and source location. *J. Geophys. Res.*, 102(B10):22529–22545.

Miensopust, M., Jones, A., Hersir, G., and Vilhjálmsson, A. (2014). The Eyjafjallajökull volcanic system, Iceland: insights from electromagnetic measurements. *Geophys. J. Int.*, 199(2):1187–1204.

Montagner, J. and Tanimoto, T. (1991). Global upper mantle tomography of seismic velocities and anisotropies. *J. Geophys. Res.*, 96(B12):20337–20351.

Moschetti, M., Ritzwoller, M., and Shapiro, N. (2007). Surface wave tomography of the western United States from ambient seismic noise: Rayleigh wave group velocity maps. *Geochem. Geophys. Geosys.*, 8(8). Q08010.

Neidell, N. and Taner, M. (1971). Semblance and other coherency measures for multichannel data. *Geophysics*, 36(3):482–497.

Nishida, K., Montagner, J. P., and Kawakatsu, H. (2009). Global surface wave tomography using seismic hum. *Science*, 326(5949):112–112.

Obermann, A., Lupi, M., Mordret, A., Jakobsdóttir, S., and Miller, S. (2016). 3D-ambient noise Rayleigh wave tomography of Snæfellsjökull volcano, Iceland. *J. Vol. Geoth. Res.*, 317:42–52.

Óskarsson, B. V. (2009). *The Skerin ridge on Eyjafjallajökull, south Iceland: Morphology and magma-ice interaction in an ice-confined silicic fissure eruption. Master's thesis.* Faculty of Earth Sciences, University of Iceland. Available at: http://hdl.handle.net/1946/4375.

Pálmason, G. (1980). Continuum model of crustal generation in Iceland-kinematic aspects. *J. of Geophys.*, 47(1-3):7–18.

Parnell-Turner, R., White, N., Henstock, T., Murton, B., Maclennan, J., and Jones, S. (2014). A continuous 55-million-year record of transient mantle plume activity beneath Iceland. *Nature Geoscience*, 7(12):914.

Parnell-Turner, R., White, N., Maclennan, J., Henstock, T., Murton, B., and Jones, S. (2013). Crustal manifestations of a hot transient pulse at 60°N beneath the Mid-Atlantic Ridge. *Earth and Planetary Science Letters*, 363:109–120.

Pedersen, R. and Sigmundsson, F. (2004). InSAR based sill model links spatially offset areas of deformation and seismicity for the 1994 unrest episode at Eyjafjallajökull volcano, Iceland. *Geophys. Res. Lett.*, 31(14). L14610.

Pedersen, R. and Sigmundsson, F. (2006). Temporal development of the 1999 intrusive episode in the Eyjafjallajökull volcano, Iceland, derived from InSAR images. *Bull. Volcanol.*, 68(4):377–393.

Poore, H., White, N., and Maclennan, J. (2011). Ocean circulation and mantle melting controlled by radial flow of hot pulses in the Iceland plume. *Nature Geoscience*, 4(8):558.

Rawlinson, N. and Sambridge, M. (2005). The fast marching method: an effective tool for tomographic imaging and tracking multiple phases in complex layered media. *Explor. Geophys.*, 36(4):341–350.

Raymo, M. E. and Ruddiman, W. F. (1992). Tectonic forcing of late Cenozoic climate. *Nature*, 359(6391):117.

Rickers, F., Fichtner, A., and Trampert, J. (2013). The Iceland–Jan Mayen plume system and its impact on mantle dynamics in the North Atlantic region: evidence from full-waveform inversion. *Earth Planet. Sci. Lett.*, 367:39–51.

Ripepe, M. (1996). Evidence for gas influence on volcanic seismic signals recorded at Stromboli. *J. Volcanol. Geotherm. Res.*, 70(3):221–233.

Sadeghisorkhani, H., Gudmundsson, O., Roberts, R., and Tryggvason, A. (2016). Mapping the source distribution of microseisms using noise covariogram envelopes. *Geophys. J. Int.*, 205(3):1473–1491.

Sadeghisorkhani, H., Gudmundsson, Ó., Roberts, R., and Tryggvason, A. (2017). Velocity-measurement bias of the ambient noise method due to source directivity: a case study for the Swedish National Seismic Network. *Geophys. J. Int.*, 209(3):1648–1659.

Sæmundsson, K. (1979). Outline of the geology of Iceland. *Jökull*, 29:7–28.

Sánchez-Sesma, F. and Campillo, M. (2006). Retrieval of the Green's function from cross correlation: the canonical elastic problem. *Bull. Seism. Soc. Am.*, 96(3):1182–1191.

Schlindwein, V., Wassermann, J., and Scherbaum, F. (1995). Spectral analysis of

harmonic tremor signals at Mt. Semeru volcano, Indonesia. *Geophys. Res. Lett.*, 22(13):1685–1688.

Sempere, J. and Macdonald, K. (1986). Overlapping spreading centers: Implications from crack growth simulation by the displacement discontinuity method. *Tectonics*, 5(1):151–163.

Sens-Schönfelder, C. and Wegler, U. (2006). Passive image interferometry and seasonal variations of seismic velocities at Merapi Volcano, Indonesia. *Geophys. Res. Lett.*, 33(21). L21302.

Sgattoni, G., Gudmundsson, Ó., Einarsson, P., Lucchi, F., Li, K. L., Sadeghisorkhani, H., Roberts, R., and Tryggvason, A. (2017). The 2011 unrest at Katla volcano: Characterization and interpretation of the tremor sources. *J. Volcanol. Geotherm. Res.*, 338:63–78.

Shapiro, N., Campillo, M., Stehly, L., and Ritzwoller, M. (2005). High-resolution surface-wave tomography from ambient seismic noise. *Science*, 307(5715):1615–1618.

Sigmundsson, F., Einarsson, P., Hjartardóttir, Á., Drouin, V., Jónsdóttir, K., Árnadóttir, T., Geirsson, H., Hreinsdóttir, S., Li, S., and Ófeigsson, B. (2018). Geodynamics of Iceland and the signatures of plate spreading. *J. Vol. Geotherm. Res.*

Sigmundsson, F., Hreinsdóttir, S., Hooper, A., Árnadóttir, T., Pedersen, R., Roberts, M., Óskarsson, N., Auriac, A., Decriem, J., Einarsson, P., et al. (2010). Intrusion triggering of the 2010 Eyjafjallajokull explosive eruption. *Nature*, 468(7322):426–430.

Snieder, R. (1988). Large-Scale waveform inversions of surface waves for lateral heterogeneity: 2. Application to surface waves in Europe and the Mediterranean. *J. Geophys. Res.*, 93(B10):12067–12080.

Snieder, R. and Larose, E. (2013). Extracting Earth's elastic wave response from noise measurements. *Annu. Rev. Earth and Planet. Sci.*, 41:183–206.

Stankiewicz, J., Ryberg, T., Haberland, C., Natawidjaja, D., et al. (2010). Lake Toba volcano magma chamber imaged by ambient seismic noise tomography. *Geophys. Res. Lett.*, 37(17). L17306.

Sturkell, E., Sigmundsson, F., and Einarsson, P. (2003). Recent unrest and magma movements at Eyjafjallajökull and Katla volcanoes, Iceland. *J. Geophys. Res.*, 108(B8).

Stutzmann, E., Ardhuin, F., Schimmel, M., Mangeney, A., and Patau, G. (2012). Modelling long-term seismic noise in various environments. *Geophys. J. Int.*, 191(2):707–722.

Talwani, M. and Heirtzler, J. (1964). Computation of magnetic anomalies caused by 2-D structures of arbitrary shapes. *Computers in the Mineral Industry, Part I: Standford Univ. Publ. Geol. Sci.*, 9:464–480.

Tamura, J. and Okada, T. (2016). Ambient noise tomography in the Naruko/Onikobe volcanic area, NE Japan: implications for geofluids and seismic activity. *Earth, Planets and Space*, 68(1):1–11.

Tarasewicz, J., Brandsdóttir, B., White, R., Hensch, M., and Thorbjarnardóttir, B. (2012). Using microearthquakes to track repeated magma intrusions beneath the Eyjafjallajökull stratovolcano, Iceland. *J. Geophys. Res.*, 117. B00C06.

Tarasewicz, J., White, R., Brandsdóttir, B., and Schoonman, C. (2014). Seismogenic

magma intrusion before the 2010 eruption of Eyjafjallajökull volcano, Iceland. *Geophys. J. Int.*, 198(2):906–921.

Tarasewicz, J., White, R., Brandsdóttir, B., and Thorbjarnardóttir, B. (2011). Location accuracy of earthquake hypocentres beneath Eyjafjallajökull, Iceland, prior to the 2010 eruptions. *Jökull*, 61:33–50.

Toomey, D. and Foulger, G. (1989). Tomographic inversion of local earthquake data from the Hengill-Grensdalur central volcano complex, Iceland. *J. Geophys. Res.*, 94(B12):17497–17510.

Vandemeulebrouck, J., Roux, P., and Cros, E. (2013). The plumbing of Old Faithful Geyser revealed by hydrothermal tremor. *Geophys. Res. Lett.*, 40(10):1989–1993.

Vedurstofa Íslands (2019a). Gagnabanki Vedurstofu Íslands. afgreidsla nr. 2019-02-11/01.

Vedurstofa Íslands (2019b). Gagnabanki Vedurstofu Íslands. afgreidsla nr. 2019-03-01/01.

Vogfjörd, K., Jakobsdóttir, S., Gudmundsson, G., Roberts, M., Ágústsson, K., Arason, T., Geirsson, H., Karlsdóttir, S., Hjaltadóttir, S., Ólafsdóttir, U., et al. (2005). Forecasting and monitoring a subglacial eruption in Iceland. *Eos, Transactions American Geophysical Union*, 86(26):245–248.

Vogt, P. (1971). Asthenosphere motion recorded by the ocean floor south of Iceland. *Planet. Sci. Lett.*, 13(1):153–160.

Vogt, P. and Avery, O. (1974). Detailed magnetic surveys in the northeast Atlantic and Labrador Sea. *J. Geophys. Res.*, 79(2):363–389.

Walters, R., Jones, S., and Maclennan, J. (2013). Renewed melting at the abandoned Húnafloí Rift, northern Iceland, caused by plume pulsing. *Earth and Planetary Science Letters*, 377:227–238.

Wapenaar, K., Fokkema, J., and Snieder, R. (2005). Retrieving the Green's function in an open system by cross correlation: A comparison of approaches. *J. Acoust. Soc. Am,*, 118(5):2783–2786.

White, R. (1997). Rift–plume interaction in the North Atlantic. *Philos. Trans. R. Soc. London, Ser. A*, 355(1723):319–339.

White, R., Bown, J., and Smallwood, J. (1995). The temperature of the Iceland plume and origin of outward-propagating V-shaped ridges. *J. Geol. Soc.*, 152(6):1039–1045.

Paper I

A new kinematic model of the Mid-Atlantic Ridge between $55°55'$ and the Bight Transform Fault for the past 6 Ma

Ásdís Benediktsdóttir, Richard Hey, Fernando Martinez, Ármann Höskuldsson, 2016. Journal of Geophysical Research: Solid Earth, 121, p.455-468. doi:10.1002/2015JB012504

AGU PUBLICATIONS

JGR

Journal of Geophysical Research: Solid Earth

RESEARCH ARTICLE
10.1002/2015JB012504

A new kinematic model of the Mid-Atlantic Ridge between 55°55′N and the Bight Transform Fault for the past 6 Ma

Á. Benediktsdóttir[1], R. Hey[2], F. Martinez[2], and Á. Höskuldsson[1]

[1]Nordic Volcanological Center, Institute of Earth Sciences, University of Iceland, Reykjavík, Iceland, [2]Hawai'i Institute of Geophysics and Planetology, University of Hawai'i at Mānoa, Honolulu, Hawai'i, USA

Key Points:
- There is asymmetry in the lithospheric accretion immediately south of the Bight Transform Fault
- The observed asymmetry can be explained by short-lived propagating rifts
- Lithosphere is transferred to the NA plate as on the Reykjanes Ridge and in Iceland

Supporting Information:
- Tables S1–S4 and Table S5 Caption
- Table S5

Correspondence to:
Á. Benediktsdóttir,
asb1@hi.is

Citation:
Benediktsdóttir, Á., R. Hey, F. Martinez, and Á. Höskuldsson (2016), A new kinematic model of the Mid-Atlantic Ridge between 55°55′N and the Bight Transform Fault for the past 6 Ma, *J. Geophys. Res. Solid Earth*, *121*, 455–468, doi:10.1002/2015JB012504.

Received 6 SEP 2015
Accepted 13 JAN 2016
Accepted article online 25 JAN 2016
Published online 6 FEB 2016

Abstract We present a new fine-scaled tectonic model of the Mid-Atlantic Ridge between 55°55′N and the Bight Transform Fault for the past 6 Ma. We model our new marine magnetic data, providing a robust kinematic model for the area. The new model uses propagating rifts to explain observed asymmetry in high-resolution marine magnetic data. The area closest to the Bight Transform Fault has undergone two relatively large (9 km and 6 km) relocations of the spreading center within the past 1 Ma, which explains the divided central anomaly; we attribute this relocation to two very fast propagations. The amount of lithosphere transferred between the plates during each propagation event is 2–10 km, and the propagators identified are short-lived (0.5–4.0 Ma). Most of the propagation in the area is to the north, and all but two propagators transfer lithosphere from the Eurasian plate to the North American plate, which is consistent with the overall eastward relocation of the Reykjanes Ridge.

1. Introduction

The slow- and oblique-spreading Reykjanes Ridge is one of the most extensively studied "hot spot" influenced mid-oceanic ridges [*Heirtzler et al.*, 1966; *Vogt*, 1971; *Talwani et al.*, 1971; *Schilling*, 1973; *Sun et al.*, 1975; *Schilling et al.*, 1982; *Parson et al.*, 1993; *White et al.*, 1995; *Searle et al.*, 1998; *Smallwood and White*, 2002; *Hey et al.*, 2010]. The axial high morphology on the Reykjanes Ridge [*Talwani et al.*, 1971] has been explained by the presence of a hot spot underneath Iceland (hereafter referred to as the Iceland melting anomaly) [*Wilson*, 1963; *Morgan*, 1971]. The Reykjanes Ridge extends from Iceland down to the 15–17 km right-stepping Bight Transform Fault (BTF), located at 56°47′N [*Appelgate and Shor*, 1994]. The BTF is the first transform fault on the Mid-Atlantic Ridge (MAR) south of Iceland.

The BTF is the location of the tip of the reorganization that started on the Reykjanes Ridge at ~40 Ma [*Vogt*, 1971; *Vogt and Avery*, 1974; *White*, 1997; *Jones et al.*, 2002; *Hey et al.*, 2016], and whether it has stopped or is ongoing is still not known (for a more detailed discussion see *Hey et al.* [2016]). The Bight Fracture Zone extends into at least 36 Ma old crust and even 49 Ma old crust [*Müller and Roest*, 1992], indicating that the BTF has been long-lived and is a robust offset on the MAR. The BTF seems to have evolved from an earlier triple junction between the now extinct Ran Ridge in the Labrador Sea, the Reykjanes Ridge, and the Mid-Atlantic Ridge [*Vogt and Avery*, 1974].

The spreading on the MAR changes from oblique (30° from perpendicular to the ridge) north of the BTF to a direction perpendicular to the trend of the ridge immediately south of the BTF. The area south of the BTF has not been studied as extensively as the Reykjanes Ridge, leaving questions unanswered about how this area responds to the tectonic changes north of the BTF. Until recently, there was a large data gap around the BTF. *Appelgate and Shor* [1994] collected one track of Sea MARC II sidescan sonar along the ridge crest of the MAR between 55°50′N and 63°N which is too limited to infer something about the tectonic history of the MAR. Here we present a detailed tectonic evolution of the MAR from 55°55′N to the BTF for the past 6 Ma.

2. Data

To examine the tectonic spreading history of the MAR between 55°55′N and the BTF, we forward model the marine magnetic data collected on R/V *Marcus G. Langseth* in August–September 2013. In this expedition data were also collected north of the BTF (Figure 1, survey box). The ridge to the north of the BTF is the

AGU Journal of Geophysical Research: Solid Earth 10.1002/2015JB012504

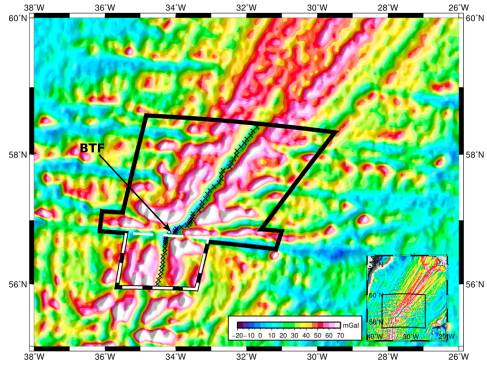

Figure 1. Satellite gravity [*Sandwell et al.*, 2013] with our entire survey outlined with heavy black lines. Dashed white lines show the part of the survey area we study in this paper. Crosses are the ridge axes picks. BTF = Bight Transform Fault.

southernmost part of the Reykjanes Ridge, which is obliquely spreading, and the morphology of the ridge and its flanks are characterized by complicated patterns of axial volcanic ridges that are oriented subparallel to the ridge orientation [*Appelgate and Shor*, 1994; *Searle et al.*, 1998; *Searle and Laughton*, 1981; *Parson et al.*, 1993; *Keeton et al.*, 1997; *Hey et al.*, 2016]. However, in the area just south of the BTF the spreading direction is perpendicular to the orientation of the ridge and the morphology is characterized by ridge segments that are parallel to the orientation of the ridge [*Appelgate and Shor*, 1994] and bathymetry in Figure 2. It is because of these large tectonic differences of the areas north and south of the BTF that we decided to focus explicitly on the southern part in this study (white dashed box, Figure 2).

The data were collected along spreading flow lines as predicted by the poles of rotation in *Smallwood and White* [2002]. Figure 2 shows the numbering convention for our ship tracks.

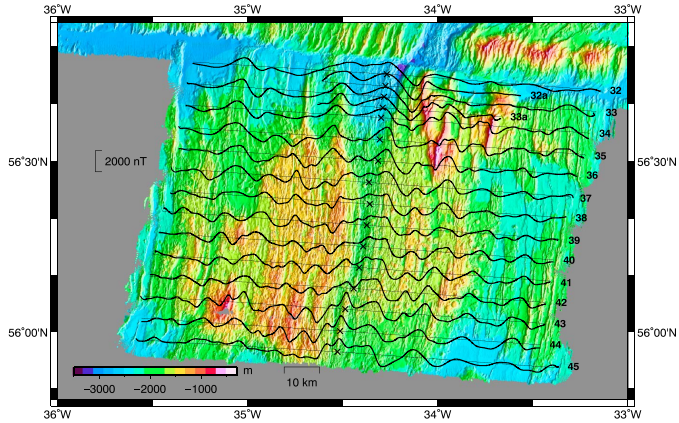

Figure 2. The magnetic data from the area outlined by the white dashed lines in Figure 1 superimposed on the bathymetry data. The numbering convention for our profiles are as indicated here. Thin lines are ship tracks, and crosses are the ridge axes picks.

AGU Journal of Geophysical Research: Solid Earth 10.1002/2015JB012504

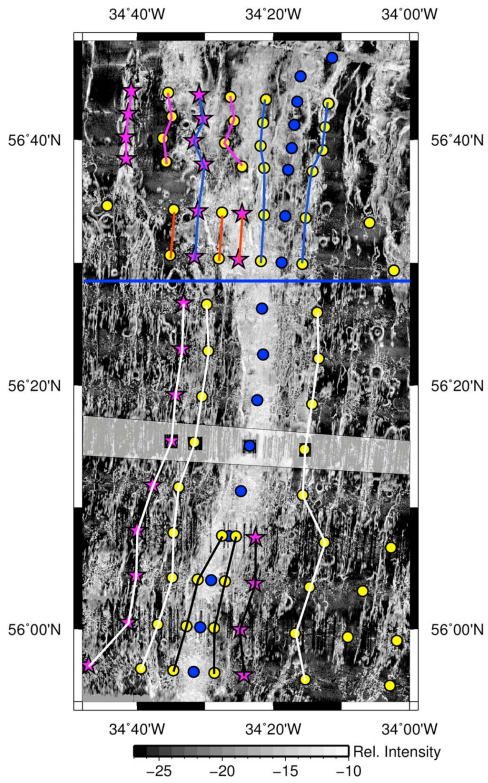

Figure 3. Ridge axis picks (blue circles), pseudofaults (yellow circles), and failed rift (purple stars) from the magnetic modeling superimposed on backscatter data. Brighter and darker tones indicate a strong intensity and weak intensity, respectively. North of the blue horizontal line shows the location on the ridge where we use the magnetic data and not the backscatter to identify the ridge axis. For reference, profiles 36 and 37 are north and south of the blue line, respectively. Pseudofaults and failed rifts are connected with a specific color for each propagator. Naming convention of propagators is given in Figure 7, and the colors are blue, purple, red, white, black, for propagators A, B, C, 2, and 1 respectively. The greyed out profile in the middle of the figure is due to bad weather during data collection.

3. Methods

We use a newly developed marine magnetic forward modeling program Magellan (Á. Benediktsdóttir et al., manuscript in preparation, 2016) to model our magnetic data. The program computes the magnetic field produced by magnetized blocks that are arranged according to spreading rates, a magnetic timescale of *Lourens et al.* [2004] and jump parameters (discussed later). For a more detailed discussion of the program, see *Benediktsdóttir et al.* [2012].

3.1. Picking the Axis Location

Unlike a similar study where the ridge axis was picked to be in the middle of the Brunhes [*Benediktsdóttir et al.*, 2012], we pick our ridge axis mainly from the sidescan sonar data. Figure 3 shows the backscatter and how the axis is interpreted to be in the middle of the highest backscatter. There are some profiles where we are unable to use the backscatter data, and in those cases, we use magnetic data to aid us (profiles north of the blue line in Figure 3). The reason for not using the middle of the Brunhes is that it either seems to be shifted east relative to the middle of the backscatter (profiles 43–45) or that it is completely divided into two peaks

AGU Journal of Geophysical Research: Solid Earth 10.1002/2015JB012504

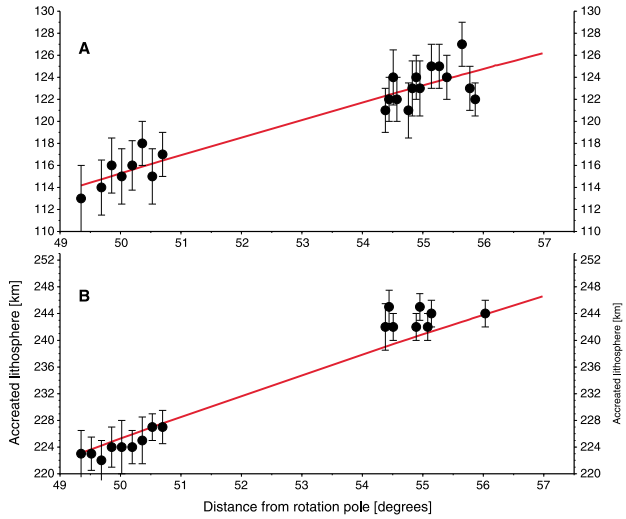

Figure 4. Total amount of accreted lithosphere (from supporting information Table S3) (black circles with error bars) and lithospheric accretion predicted by spreading rates from supporting information Table S4 (red line) versus distance from rotation pole (from supporting information Table S2) at (a) 6.033 Ma and (b) 11.04 Ma. Profiles 17–25 from *Benediktsdóttir et al.* [2012] are the group closest to the pole, and the data from this study are farther away from the pole. See Figure 2 for location of profiles within our survey area.

(profiles 32–35 and 46–47). These complexities suggest that the ridge has undergone a tectonic change within the Brunhes. The location of our ridge axis picks are given in supporting information Table S1.

3.2. Spreading Rates

The spreading rates of the ridge control the location of the magnetized blocks, and thus the location of the magnetic anomalies in the magnetic model, and they are therefore some of the most important input parameters in the forward modeling. These rates can be determined by trial and error for each profile or they can be calculated from best fitting model parameters such as the ones found in *Merkouriev and DeMets* [2008] and *DeMets et al.* [2010]. Spreading rates found from the latter method do not include ridge-specific processes (such as asymmetric spreading or rift propagation), and they are only sensitive to changes greater than 1 km/Myr (C. DeMets, personal communication, 2010).

When one does forward modeling of any kind, there is always a trade-off between the number of free parameters and the goodness of fit. We reduce the number of free parameters by determining the spreading rates for the entire survey area independently of the magnetic modeling.

Our ship tracks were designed using the pole of rotation given by the chron 5A closure pole in *Smallwood and White* [2002] (supporting information Table S2). Assuming that our ship tracks are a good estimate of the true flow lines of the ridge, we obtain new spreading rates using the location of this pole of rotation. We need to determine the angular rate of the pole of rotation, and for that we pick chrons on the Eurasian and North American plates to get the cumulative opening for all of our profiles.

Figure 4 shows the total amount of accreted crust for chrons 3ro (6.033 Ma) and 5n2no (11.04 Ma), gathered from our magnetic data (black circles with error bars, from supporting information Table S3) and from the magnetic data in *Benediktsdóttir et al.* [2012]. To get an estimate of the total amount of crust produced for these chrons without assuming the location of the axis, we simply measure the distance to the chrons on both sides and add the distances. Note that we only use the profiles north of the BTF to obtain the spreading rates, because the profiles in the south are too short for anomalies to be identified (or they can only be identified

AGU Journal of Geophysical Research: Solid Earth 10.1002/2015JB012504

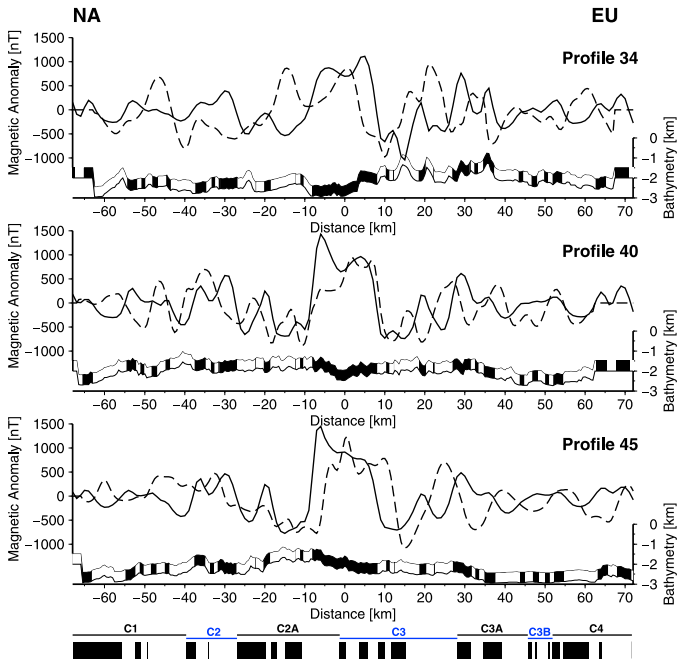

Figure 5. Magnetic modeling demonstrating how symmetric spreading does not explain the data well. The model was created assuming purely symmetric spreading. Black solid and dashed lines are model and data, respectively. The normal (black) and reversely (white) magnetized blocks are 0.5 km thick and follow the bathymetry. North American (NA) and Eurasian (EU) sides are labeled. Reference magnetic polarity timescale is shown at the bottom.

on the Eurasian plate) and they are not included in the table. In order to get a new set of spreading rates, we use the location of the pole which we used to lay out our ship tracks and the total amount of lithosphere accreted. We then minimize the sum of squares and obtain angular rates that best fit our data. Predicted crustal accretion is shown as red lines in Figure 4; new stage poles and spreading rates are given in supporting information Tables S2 and S4, respectively.

Since we are exploring the fine-scaled tectonic evolution, we want as detailed spreading rates as possible for the survey area. For rigid plate tectonic consistency between profiles, we want the spreading rates to increase with the sine of the angular distance away from the location of the rotation pole [*Morgan*, 1968]. Therefore, we combine the location of the anomalies in our data with the known rotation parameters and define a new set of rotation parameters, predicting new set of spreading rates.

4. Magnetic Modeling

Once we have determined the spreading rates for each profile, we investigate if the data are well fit. Figure 5 shows profiles from the northern, middle, and southern parts of the survey area (profiles 34, 40, and 45, respectively) modeled with only symmetric spreading, using the spreading rates obtained above. The models do not fit the data well, and we observe the following complications.

1. The Brunhes central anomaly is divided into two peaks in profile 34 with a shift westward relative to our model (and this is true for all profiles north of profile 37, see magnetic data in Figure 2).
2. We need more lithosphere on the North American plate and less on the Eurasian plate to fit data outside the Brunhes central anomaly in profiles 40 and 45.

AGU Journal of Geophysical Research: Solid Earth 10.1002/2015JB012504

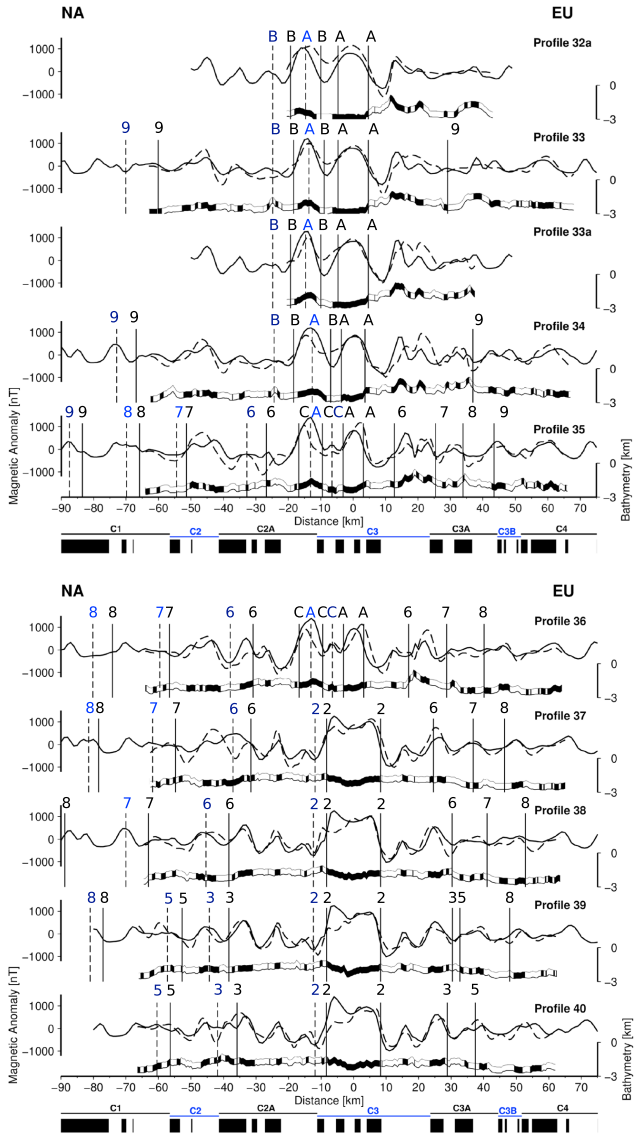

Figure 6. Magnetic models for profiles 33-47 (see Figure 2 for location of the profiles). Solid and dashed black wiggles are the model and data, respectively. Black and white boxes are normal and reversed magnetized blocks, respectively, following the bathymetry. Black solid and dashed vertical lines are pseudofaults and failed rifts, respectively. Pseudofaults and failed rifts (blue numbers and letters, respectively) follow the naming convention in Figure 7. Note that where there are no data the bathymetry is kept at a constant depth of 1.5 km. The predicted pseudofaults and failed rifts that are located where there is no data are shown in the shaded area in Figure 7. North American (NA) and Eurasian (EU) sides are labeled. Reference magnetic polarity timescale is shown at the bottom.

AGU Journal of Geophysical Research: Solid Earth 10.1002/2015JB012504

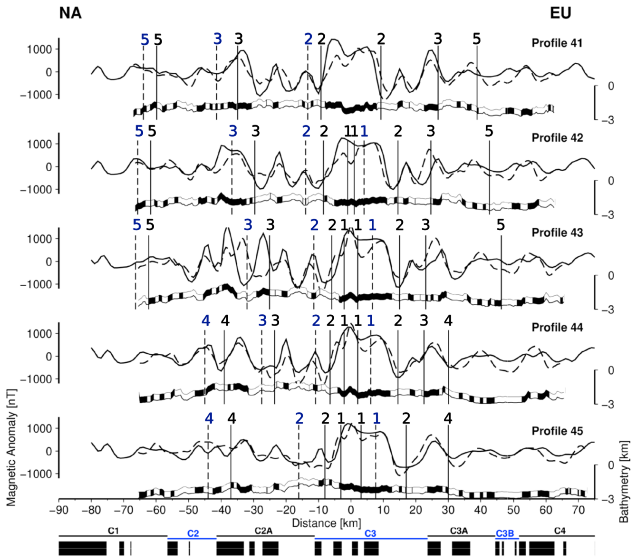

Figure 6. (continued)

3. The central anomaly is shifted eastward relative to our model in profile 45 (and this is true for profiles south of profile 41). Recall that we mainly used the backscatter data to determine the location of the axis.

We seek to explain the complexities in the magnetic data with rift propagation within the survey area. If the main cause for the complexities were asymmetric accretion, then we would expect the asymmetry to be systematic in the survey area, since its north-south length is ~100 km. In the case of our data, we have already observed that the Brunhes central anomaly is shifted both west (profiles 37 and north) and east (profiles 42 and south) relative to the symmetric model, within our survey area.

4.1. Propagating Rifts in Magnetic Modeling

Rift propagation is the primary mechanism for asymmetric accretion in various places around the globe [*Shih and Molnar*, 1975; *Hey and Vogt*, 1977; *Hey et al.*, 1980; *Vogt et al.*, 1983; *Wilson et al.*, 1984; *Hey et al.*, 1988; *Brozena and White*, 1990; *Naar and Hey*, 1991; *Caress et al.*, 1988; *Phipps Morgan and Sandwell*, 1994; *Wilson and Hey*, 1995; *Kleinrock et al.*, 1997; *Christie et al.*, 1998; *Mihut and Müller*, 1998; *Bruguier et al.*, 2003], and we therefore choose to use it to explain the observed asymmetry in the magnetic data. There are two pseudofaults and one failed rift associated with every propagating rift. The pseudofaults are not tectonic faults but rather an age discontinuity in the lithosphere (and therefore there might be some activity on the pseudofaults due to a difference in lithospheric thickness across them). They are the trace of the propagator, where it has broken up older crust to start new spreading. The failed rift is the old spreading center that was active before the propagator took over the spreading but is now inactive. Our profiles are oriented along the flow lines of the ridge. A ridge propagation event can be identified as an instantaneous ridge jump in each profile and a ridge jump record for a series of profiles can reveal the propagation history in a map view. *Benediktsdóttir et al.* [2012] describe the relationship between ridge propagation and ridge jumps in a more detailed fashion.

4.2. Marine Magnetic Models

All magnetic models for profiles south of the BTF are shown in Figure 6 with modeling parameters (e.g., spreading rates, magnetization, and ridge jumps) in supporting information Tables S4 and S5. The resolution of the

AGU Journal of Geophysical Research: Solid Earth 10.1002/2015JB012504

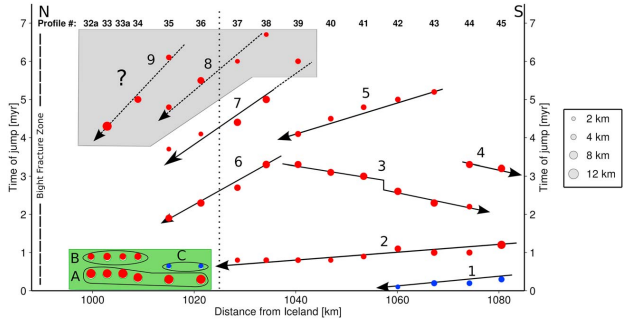

Figure 7. Time of jump (that is, the time when the propagator reached the profile) from the magnetic models versus distance from the Reykjanes Peninsula (at 63.7°N, 22.75°W) on Iceland. Red and blue circles correspond to jumps transferring lithosphere to North America and Eurasia, respectively. Arrows show direction of propagation. The shaded box shows the jumps identified in the magnetic modeling where only one side was available to constrain the age of a jump; these results are therefore speculative predictions. The largest spreading center jumps in the green box are necessary to produce two areas of Brunhes separated by reversely magnetized crust. The A–C propagators suggest extremely rapid propagation (since their slope on the graph is zero, the speed approaches infinity, and we can therefore not determine the direction of propagation), which is indistinguishable but more physically plausible than an instantaneous relocation of the entire ridge segment.

size and timing of each jump is ~0.5 km and ~0.5 Ma, respectively. We do not model profile 32 because it crosses the southern half of the BTF (see location of profile 32 in Figure 2), which violates the assumption of a 2-D magnetic model.

5. Results

Figure 7 shows time of jump, obtained from the magnetic models shown in Figure 6, versus distance from Iceland for profiles 33–47. Lithosphere has mostly been transferred to the North American plate as indicated by the red circles. The blue circles show where lithosphere has been added to the Eurasian plate. Figure 8 shows the location of the propagators overlain on bathymetry. Figure 9 shows the age of the lithosphere as predicted by our magnetic modeling with the location of the propagators superimposed.

Our data are generally well fit out to 5 Ma and 3 Ma south and north of profile 37, respectively. The large amount of lithosphere that is transferred from the Eurasian plate to the North American plate north of profile 37 causes a large asymmetry in the age of the anomalies as a function of distance from the ridge. Since we need to see data on both sides of the ridge to investigate the tectonic spreading history of the ridge, we mark the jumps we are not confident in with a star in supporting information Table S5. These jumps can be seen outside the data range in Figure 6 and are in the shaded region in Figure 7. Note that we assume a constant water depth of 1.5 km in the magnetic models where there is no data.

Most of the propagation is to the north, toward the BTF, and each propagator is not long-lived. *Benediktsdóttir et al.* [2012] found a series of similar northward propagators in a study on the Reykjanes Ridge (at ~63°N). These are unlike large propagators that propagate away from hot spots and can be traced for hundreds of kilometers [*Hey and Vogt*, 1977; *Searle et al.*, 1989; *Naar and Hey*, 1991; *Bruguier et al.*, 2003; *Benediktsdóttir et al.*, 2012].

The shaded region in Figure 7 shows where we are not confident in our modeling. These jumps are a result of magnetic modeling on only one flank. We choose not to discuss these further here and leave them as a prediction of what might be occurring farther out on the ridge flanks.

We divide our survey area into two subregions, north and south of profile 37. There is a transition zone between these two seen in the magnetic and backscatter data (see blue line in Figure 3). The region immediately south of the BTF is more complex than the one farther south with complexities such as a central anomaly with two peaks.

AGU Journal of Geophysical Research: Solid Earth 10.1002/2015JB012504

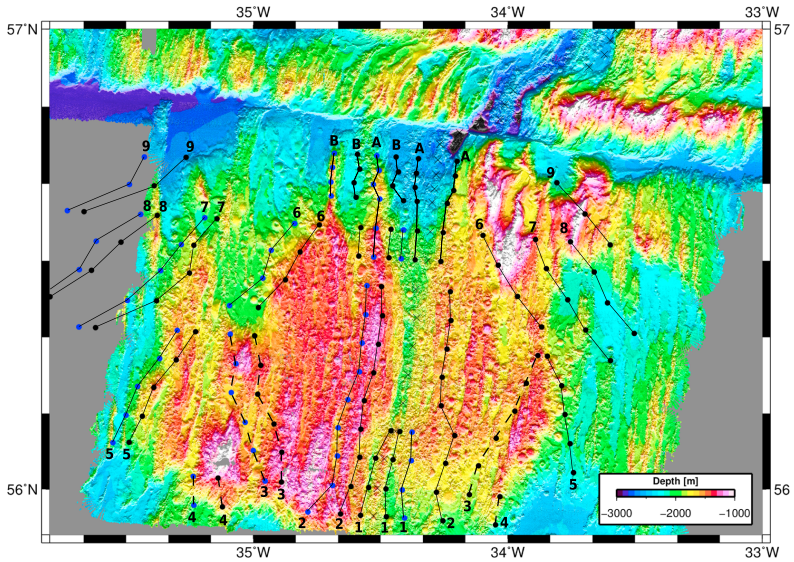

Figure 8. The location of propagators with the naming convention as in Figure 7, overlain on bathymetry data from the 2013 research cruise. Blue and black circles are failed rifts and pseudofaults, respectively. Pseudofaults and failed rifts are connected with dashed and solid lines for southward and northward propagators, respectively.

5.1. Profile 37 and South

The magnetic models for this part of the survey area fit well with the magnetic data, and a consistent propagation history has emerged. The propagators within this area are marked from 1 to 7 in Figure 7. They all, except for propagator 1, transfer lithosphere from the Eurasian plate to the North American plate, and they are all northward propagating, except for two (propagators 3 and 4). Below we discuss each of these propagators.

1. *Propagator 1* is the most recent propagator south of profile 36, and it is the only one that transfers lithosphere to the Eurasian plate. Propagator 1 can be found in profiles 42–45. It transfers 3–5 km of lithosphere to the Eurasian plate, and its propagation rate is ∼110±20 km/Myr. When picking the axis for profiles 42–45, we noticed that the Brunhes and the highest reflection in the backscatter did not line up. We decided to use the backscatter to pick the axis, which caused an asymmetry in the magnetic data. Propagator 1, which lies within the Brunhes, explains the observed asymmetry. Propagator 1 seems to be continuing its way north to profile 41, and its present tip is on profile 42.
2. *Propagator 2* is the longest in the survey area, extending over 50 km, and it might extend farther south. We cannot trace propagator 2 north of profile 36. A right-stepping offset in the ridge axis location between profiles 36 and 37 might be the cause or result of the termination of propagator 2 (see location of high backscatter in Figure 3). The propagation rate is ∼30 ± 40 km/Myr with a 3–5.5 km transfer of lithosphere from the Eurasian to the North American plate. Profile 45 is an outlier for this propagator because the amount of lithosphere transferred is 8 km to the North American plate, drastically more than in the other profiles. Another survey farther south might explain why there is more lithosphere transferred at profile 45.
3. *Propagator 3* is the only well-identified southward propagator within the survey area. The propagation rate is ∼40 ± 10 km/Myr with a 4–7 km transfer of lithosphere to the North American plate. Propagator 3 stalls for ∼0.3 Ma between profiles 41 and 42. The propagation rate before and after stalling is the same. This propagator is terminated at profile 45, suggesting the existence of some kind of transition area.
4. *Propagator 4*: We will not discuss this propagator here since it is barely noticeable. It is most likely propagating south, and we are not confident in determining the propagation rate with jumps on only two profiles.

AGU Journal of Geophysical Research: Solid Earth 10.1002/2015JB012504

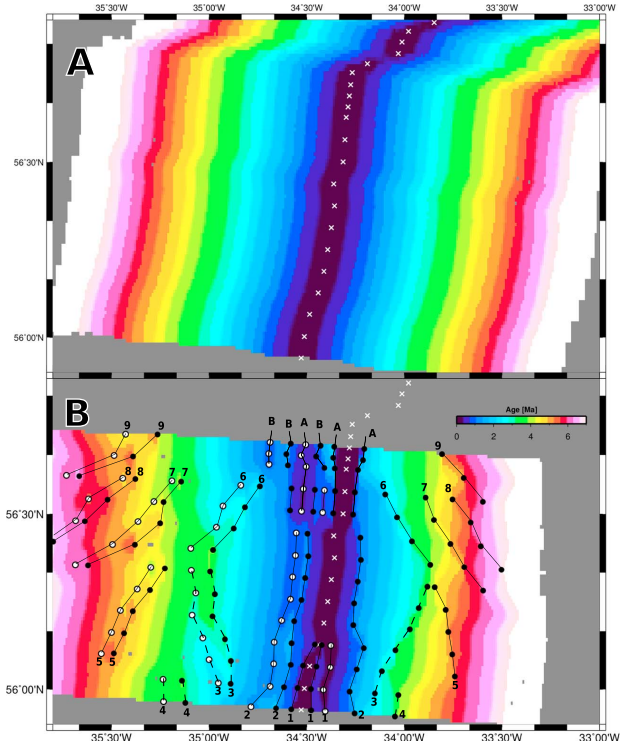

Figure 9. Maps showing ages in the survey area (a) as predicted by the poles of rotation (uncorrected for outward displacement) by *Merkouriev and DeMets* [2014] and (b) as predicted by the magnetic modeling in this paper. White crosses show our ridge axis picks. The location of propagators and naming convention as in Figure 7. White and black circles are failed rifts and pseudofaults, respectively. Pseudofaults and failed rifts are connected with dashed and solid lines for southward and northward propagators, respectively.

5. *Propagator 5* is located between profiles 39 and 43. It is propagating north with a propagation rate of ~25 ± 5 km/Myr, transferring 4–5 km of lithosphere to the North American plate.
6. *Propagator 6* is located between profiles 35 and 38 and therefore lies within the more complicated area north of profile 37. It is propagating north with a propagation rate of ~15 ± 5 km/Myr, transferring 5–7 km of lithosphere to the North American plate. It is initiated at the same point in space and time as propagator 3. The pseudofault on the North American plate roughly corresponds with a bathymetric scarp and the pseudofaults on profiles 35 and 36 on the Eurasian plate form the western scarp of the large mountainous area (see Figure 8).
7. *Propagator 7* is located between profiles 35 and 38 (and even farther south to profile 39) and like propagator 6 lies within the more complicated area north of profile 37. It is propagating north with a propagation rate of ~10 ± 5 km/Myr, transferring 3–7 km of lithosphere to the North American plate.
8. *Propagators 8 and 9* will not be discussed here since they are found by modeling only one side of the magnetic data and their existence is therefore not well established.

5.2. Profile 36 and North—Immediately South of the BTF

This area is more complicated than the area in the south in that the propagation history is not as well established. Figure 7 shows the propagation history for the entire survey area, and the region immediately south of the BTF we discuss here is to the left of the dashed line. We discussed propagators 6–9 earlier.

AGU Journal of Geophysical Research: Solid Earth 10.1002/2015JB012504

The lithosphere that is younger than 1.0 Ma (green area in Figure 7) has undergone rapid and large rift relocations. All the profiles in this area (profiles 32a, 33, 33a, 34, 35, and 36) have a two-peaked Brunhes (see Figure 6). We attribute this feature to a propagator transferring lithosphere to the North American plate, with a transfer of 9–10 km, by far the largest transfer of lithosphere in the survey area. We call this propagator A (see Figure 7 and supporting information Table S5). If the transfer of lithosphere were smaller, we could not fit the data as well as we have here. Also, we cannot think of any other mechanism that could produce this prominent feature in the magnetic data. Figure 9b shows an age map of the survey area as predicted by our magnetic modeling, and it shows how propagators A and B have transferred large amounts of lithosphere to the Eurasian plate, resulting in a large age discontinuity on the North American plate (jump from very dark blue to light blue). In comparison, Figure 9a shows an age map as predicted by the newest set of rotation poles for the North American-Eurasian plate pair [*Merkouriev and DeMets*, 2014].

The region north of the blue line in Figure 3 shows the axis picks for this region overlain on backscatter data. Both the backscatter and magnetic data in this area are very complex, and we use a combination of these two data sets to pick the ridge axis location. Below, we discuss the propagators we call A–C, with a different notation to underline that they are different in character than the others we have identified with numbers. We do not determine the propagation direction of these three since the timing of each jump within each profile is almost the same as for the other profiles.

1. *Propagator A* is the largest within the entire survey area, transferring 9–10 km of lithosphere to the North American plate. We attribute the two-peaked Brunhes to this propagator. The failed rift associated with this jump corresponds to a ridge in the bathymetry (see Figure 8) which also has a higher backscatter (see yellow stars connected with purple lines in Figure 3).
2. *Propagator B* is observed in tracks 32a, 33, 33a, and 34, and it transfers 5–7 km of lithosphere to the North American plate. Propagator B is not well constrained on profiles 32a and 33a since they are very short. The failed rift corresponds to a topographic high (see Figure 8 in the bathymetry) and an area of high backscatter (see yellow stars connected with blue lines in Figure 3). Both of the pseudofaults are on the North American plate as shown in Figures 3 and 8. The one on the Eurasian plate was transferred over to the North American plate via propagator A.
3. *Propagator C* is very short-lived and is only observed on profiles 35 and 36. Propagator C transfers 3 km of lithosphere to the Eurasian plate and is one of two propagators in the entire survey area that does so. Both of its associated pseudofaults are on the North American plate (see red lines in Figures 3 and 8). The one on the Eurasian plate was transferred over to the North American plate via propagator A.

5.3. Propagators and Bathymetry

We used the bathymetry to guide our magnetic modeling for propagators A and B. The magnetic data, backscatter, and bathymetric data are all very complex in this area. Two additional features guided our magnetic modeling in the complex area; two bathymetric ridges with high backscatter (Figures 3 and 8) and a divided Brunhes anomaly (Figures 2 and 6).

We did not use the bathymetry to guide our modeling for any other propagators, and the coincidence of features in the bathymetry and propagators therefore strongly supports their existence. Before propagator 2 plowed through almost the entire survey area, there was a location on the ridge where propagators 3 and 6 were initiated from at 3 Ma. Propagator 5 stopped there just before, at 3.5 Ma (Figure 7). Also, there is a large circular low in the bathymetry where propagators 3 and 6 started from on the North American plate (Figure 8). Furthermore, there is no sufficient data on the ridge flanks to determine whether propagators 7 and 8 were initiated from the same location on the ridge. We therefore speculate that at a location 1040 km from Iceland (Figure 7) there used to be a small discontinuity on the ridge where small tectonic events were initiated or terminated. The segmentation at this point on the ridge was concluded when propagator 2 came through the area.

Propagator 1 is the youngest one, and its tip is located at a minor discontinuity on the ridge. It is changing this minor discontinuity from a left-stepping segment to an almost right stepping one. Also, propagator 3 stalls for ~0.3 Ma at a location on the ridge where the tip of propagator 1 is located today.

AGU Journal of Geophysical Research: Solid Earth 10.1002/2015JB012504

6. Discussion

We explain the divided Brunhes central anomaly in profiles 32a, 33, 33a, 34, 35, and 36 with propagator A. The fit of the model to the magnetic data where the split Brunhes is observed is very good, and it is impossible to create such a feature when more lithosphere is constantly being added to one plate over the other, that is, with continuous asymmetric spreading. There has to be some reversely magnetized lithosphere within the Brunhes anomaly to divide it into two peaks. This can be done with a propagating rift.

It is noteworthy to mention that in our methodology we assume that there is one active spreading center at any given time on each profile. Therefore, it is assumed that the shift from a failed ridge to a new ridge is instantaneous on each profile. We are limited to the aforementioned assumption. It may be that some extension and volcanism is partitioned among the three high backscatter areas (see Figure 3) and in that case we have a distributed synchronous source of creating new lithosphere rather than a single active spreading center. Should that be the case then our forward magnetic modeling is not suitable for a kinematic study.

If the spreading in the area of the two-peaked Brunhes is focused on one spreading center at any given time, one might speculate that the change in axial morphology from a deep axial valley (below profiles 32a–36) to a narrower and shallower ridge axis (below profiles 37–45) could somehow cause the difference in the Brunhes anomaly across the ridge. However, no process other than a ridge jump (or dual active spreading centers) seems to be capable of explaining a divided Brunhes anomaly, no matter the axial morphology. For example, although axial valleys might accommodate the stress release by faulting (as for profiles 32a–36), even median valleys with more magmatic release still require a mechanism that shifts the locus of spreading laterally. We welcome any alternative explanation to rift propagation but can think of none ourselves.

We provide a very good fit to the magnetic data for profiles 37–45 with propagation mostly toward but also some away from the BTF, with all propagators, except for one, transferring lithosphere to the North American plate. Most of the propagators we identify in this study extend over areas <100 km, in contrast to the area on the Reykjanes Ridge where propagators extend over areas >200 km [*Benediktsdóttir et al.*, 2012; *Hey et al.*, 2010]. Propagation rates in the southern part of the survey area are similar and lower (10–130 km/Myr) compared to the propagation rates observed by *Benediktsdóttir et al.* [2012] on the Reykjanes Ridge (60–300 km/Myr) and comparable to the rate of the propagating TAMMAR segment at 21.5°N on the MAR [*Gente et al.*, 1995] and at 26°N on the MAR [*Kleinrock et al.*, 1997]. Also, *Kleinrock et al.* [1997] identified that the amount of transferred lithosphere at 26°N on the MAR was ~7 km, which is the same order of magnitude as we observed in our study area.

We also provide a good fit for profiles 32–36, but we had two problems in this area:

1. Large jumps are present in each of these profiles, but the direction of propagation is uncertain since they all seem to take place at the same time.
2. We were not able to confidently fit the flanks of these profiles beyond 4 Ma since there was so much lithosphere transferred to the North American plate via younger jumps.

Sempéré et al. [1995] observed asymmetric accretion on the MAR between 29°N and 31°30′N where the sense and amount of asymmetry was different for every ridge segment. They concluded that on timescales of 1–2 Myr the plates do not behave rigidly and are thus "independent" of each other, but on a larger timescale this behavior is canceled out and the segments behave as rigid plates and belong to the same plate.

Although *Sempéré et al.* [1995] did not attribute the observed asymmetry to ridge propagation, their observation is noteworthy. We suggest that ridge segments change in time and space via rift propagation, as we have shown in our survey area. Some ridge segments exist for longer times than others, and some boundaries are very stable (such as the BTF). *Benediktsdóttir et al.* [2012] found short-lived northward propagators on the Reykjanes Ridge, similar to the ones we have identified. The difference between the two studies is the distance from the Iceland melting anomaly and the orientation of the ridge with respect to the spreading flow lines. These factors will most likely affect the evolution and pattern of ridge segments and propagation events therein.

Figure 9 shows two different age maps, one as predicted by *Merkouriev and DeMets* [2014] and the other as predicted by our study. The one by *Merkouriev and DeMets* [2014] is a large regional study which is valuable

AGU Journal of Geophysical Research: Solid Earth 10.1002/2015JB012504

for understanding the large-scale tectonic history, but it does not detect small-scale changes such as those presented here. A study such as this is therefore important in order to understand the fine-scale tectonic history.

7. Speculations

The BTF is the first transform fault south of Iceland and is a tectonically important location. To the north the spreading is 30° oblique on the Reykjanes Ridge and it changes to orthogonal spreading south of the BTF. The conventional wisdom is that the Iceland melting anomaly sustains the oblique spreading on the Reykjanes Ridge, and therefore, its influence on the MAR terminates at the BTF.

Repeated eastward relocations of spreading centers in Iceland, relative to the Iceland melting anomaly, cause lithosphere to be consistently transferred from the Eurasian plate to the North American plate [*Sæmundsson*, 1979; *Schilling et al.*, 1982; *Hardarson et al.*, 1997; *Einarsson*, 2008]. Also, except for one, the long southward propagators identified by *Benediktsdóttir et al.* [2012] and *Hey et al.* [2010] all transferred lithosphere over to the North American plate. Our observation is the same, suggesting that the Iceland melting anomaly controls the overall sense of asymmetry on the MAR.

We show that the overall asymmetry in our survey area is the same as the sense of asymmetry north of the BTF. Nine out of 12 identified propagators transfer lithosphere to the North American plate. It can therefore be argued, based on these findings, that the influence of the Iceland melting anomaly is the cause of this asymmetry, and its influence therefore reaches south of the BTF.

The characteristics of our southernmost profile, profile 45, are a little different from the other ones. Propagator 2 transferred 8 km of lithosphere, 3–5 km more than for other profiles. Also, propagator 4 most likely extends farther south. This indicates that a geophysical survey farther south of our survey area will reveal if this is true or not.

We were not able to confidently model the area immediately south of the BTF out to crust older than 4 Ma, but we suggest that there are a number of northward propagators, namely, our propagators number 8 and 9 (see Figures 7 and 8).

8. Conclusions

We modeled magnetic anomalies out to 6 Ma, in a forward way, for the area on the Mid-Atlantic Ridge between 55°55′N and the BTF. Our new kinematic models produce outstanding fits to our new marine magnetic data. These models suggest that propagation is ongoing in the survey area with propagation mostly toward the BTF where propagators predominantly transfer lithosphere to the North American plate. The propagators are comparable to others found on the Reykjanes Ridge suggesting that they are the mechanism for ridge segments to evolve in space and time.

Acknowledgments
We thank the government of Iceland for permission to work in Iceland waters. We thank the captain and crew of the R/V *Marcus G. Langseth* for expedition help. All figures were made using Generic Mapping Tools of P. Wessel and W. Smith. We thank two reviewers for comments and suggestions, which greatly improved the paper. This work was supported by NSF grant OCE-1154071 and a grant from Orkustofnun, the National Energy Authority of Iceland. The magnetic modeling program Magellan and its input files are available from the authors upon request (asb1@hi.is), and the data will be archived by the National Geophysical Data Center. Shipboard data publicly available at www.rvdata.us/catalog/MGL1309.

References

Appelgate, B., and A. Shor (1994), The northern Mid-Atlantic and Reykjanes Ridges: Spreading center morphology between 55°50′N and 63°N, *J. Geophys. Res.*, *99*(B9), 17,935–17,956, doi:10.1029/93JB03459.
Benediktsdóttir, Á., R. Hey, F. Martinez, and Á. Höskuldsson (2012), Detailed tectonic evolution of the Reykjanes Ridge during the past 15 Ma, *Geochem. Geophys. Geosyst.*, *13*, Q02008, doi:10.1029/2011GC003948.
Brozena, J., and R. White (1990), Ridge jumps and propagations in the South Atlantic Ocean, *Nature*, *348*, 149–153, doi:10.1038/348149a0.
Bruguier, N., T. Minshull, and J. Brozena (2003), Morphology and tectonics of the Mid-Atlantic Ridge, 7°–12°S, *J. Geophys. Res.*, *108*(B2), 2093, doi:10.1029/2001JB001172.
Caress, D., H. Menard, and R. Hey (1988), Eocene reorganization of the Pacific-Farallon spreading center north of the Mendocino fracture zone, *J. Geophys. Res.*, *93*(B4), 2813–2838.
Christie, D., B. West, D. Pyle, and B. Hanan (1998), Chaotic topography, mantle flow and mantle migration in the Australian–Antarctic discordance, *Nature*, *394*(6694), 637–644, doi:10.1038/29226.
DeMets, C., R. Gordon, and D. Argus (2010), Geologically current plate motions, *Geophys. J. Int.*, *181*(1), 1–80, doi:10.1111/j.1365-246X.2009.04491.x.
Einarsson, P. (2008), Plate boundaries, rifts and transforms in Iceland, *Jokull*, *58*, 35–58.
Gente, P., R. Pockalny, C. Durand, C. Deplus, M. Maia, G. Ceuleneer, C. Mével, M. Cannat, and C. Laverne (1995), Characteristics and evolution of the segmentation of the Mid-Atlantic Ridge between 20°N and 24°N during the last 10 million years, *Earth Planet. Sci. Lett.*, *129*(1), 55–71, doi:10.1016/0012-821X(94)00233-O.
Hardarson, B., J. Fitton, R. Ellam, and M. Pringle (1997), Rift relocation—A geochemical and geochronological investigation of a palaeo-rift in northwest Iceland, *Earth Planet. Sci. Lett.*, *153*(3–4), 181–196, doi:10.1016/S0012-821X(97)00145-3.
Heirtzler, J., X. Pichon, and J. Baron (1966), Magnetic anomalies over the Reykjanes Ridge, *Deep Sea Res.*, *13*, 427–443.

AGU Journal of Geophysical Research: Solid Earth 10.1002/2015JB012504

Hey, R., and P. Vogt (1977), Spreading center jumps and sub-axial asthenosphere flow near the Galapagos hotspot, *Tectonophysics*, *37*(1–3), 41–52, doi:10.1016/0040-1951(77)90038-5.
Hey, R., F. Duennebier, and W. Morgan (1980), Propagating rifts on mid-ocean ridges, *J. Geophys. Res.*, *85*(137), 3647–3658.
Hey, R., H. Menard, T. Atwater, and D. Caress (1988), Changes in direction of seafloor spreading revisited, *J. Geophys. Res.*, *93*(B4), 2803–2811.
Hey, R., F. Martinez, Á. Höskuldsson, and Á. Benediktsdóttir (2010), Propagating rift model for the V-shaped ridges south of Iceland, *Geochem. Geophys. Geosyst.*, *11*, Q03011, doi:10.1029/2009GC002865.
Hey, R., F. Martinez, Á. Höskuldsson, D. Eason, J. Sleeper, S. Thordarson, Á. Benediktsdóttir, and S. Merkuryev (2016), Multibeam investigation of the Active North Atlantic plate boundary reorganization tip, *Earth Planet. Sci. Lett.*, *435*, 115–123, doi:10.1016/j.epsl.2015.12.019.
Jones, S., N. White, and J. Maclennan (2002), V-shaped ridges around Iceland: Implications for spatial and temporal patterns of mantle convection, *Geochem. Geophys. Geosyst.*, *3*(10), 1059, doi:10.1029/2002GC000361.
Keeton, J., R. Searle, C. Peirce, B. Parsons, R. White, M. Sinha, B. Murton, and L. Parson (1997), Bathymetry of the Reykjanes Ridge, *Mar. Geophys. Res.*, *19*(1), 55–64, doi:10.1023/A:1004266721393.
Kleinrock, M., B. Tucholke, J. Lin, and M. Tivey (1997), Fast rift propagation at a slow-spreading ridge, *Geology*, *25*(7), 639–642, doi:10.1130/0091-7613(1997).
Lourens, L., F. Hilgen, J. Laskar, N. Shackleton, and D. Wilson (2004), The neogene period, in *A Geologic Time Scale*, vol. 2004, edited by F. Gradstein, J. Ogg, and A. Smith, pp. 409–440, Cambridge Univ. Press, Cambridge, U. K.
Merkouriev, S., and C. DeMets (2008), A high-resolution model for Eurasia–North America plate kinematics since 20 Ma, *Geophys. J. Int.*, *173*(3), 1064–1083, doi:10.1111/j.1365-246X.2008.03761.x.
Merkouriev, S., and C. DeMets (2014), High-resolution Neogene reconstructions of Eurasia-North America Plate motion, *Geophys. J. Int.*, *198*, 366–384, doi:10.1093/gji/ggu142.
Mihut, D., and R. Müller (1998), Volcanic margin formation and Mesozoic rift propagators in the Cuvier Abyssal Plain off Western Australia, *J. Geophys. Res.*, *103*(B11), 27,135–27,149.
Morgan, W. (1968), Rises, trenches, great faults, and crustal blocks, *J. Geophys. Res.*, *73*(6), 1959–1982.
Morgan, W. (1971), Convection plumes in the lower mantle, *Nature*, *230*, 42–43.
Müller, R., and W. Roest (1992), Fracture zones in the North Atlantic from combined Geosat and Seasat data, *J. Geophys. Res.*, *97*(B3), 3337–3350, doi:10.1029/91JB02605.
Naar, D., and R. Hey (1991), Tectonic evolution of the Easter microplate, *J. Geophys. Res.*, *96*(B5), 7961–7993, doi:10.1029/90JB02398.
Parson, L., et al. (1993), En echelon axial volcanic ridges at the Reykjanes Ridge: A life cycle of volcanism and tectonics, *Earth Planet. Sci. Lett.*, *117*(1–2), 73–87, doi:10.1016/0012-821X(93)90118-S.
Phipps Morgan, J., and D. Sandwell (1994), Systematics of ridge propagation south of 30°S, *Earth Planet. Sci. Lett.*, *121*(1–2), 245–258, doi:10.1016/0012-821X(94)90043-4.
Sæmundsson, K. (1979), Outline of the geology of Iceland, *Jokull*, *29*, 7–28.
Sandwell, D., E. Garcia, K. Soofi, P. Wessel, and W. Smith (2013), Towards 1 mGal Global Marine Gravity from CryoSat-2, Envisat, and Jason-1, *Leading Edge*, *32*(8), 892.
Schilling, J. (1973), Iceland mantle plume: Geochemical study of Reykjanes Ridge, *Nature*, *242*, 565–571, doi:10.1038/242565a0.
Schilling, J., P. Meyer, and R. Kingsley (1982), Evolution of the Iceland hotspot, *Nature*, *296*, 313–320, doi:10.1038/296313a0.
Searle, R., and A. Laughton (1981), Fine-scale sonar study of tectonics and volcanism on the Reykjanes Ridge, *Oceanol. Acta*, *4*, 5–13.
Searle, R., R. Rusby, J. Engeln, R. Hey, and J. Zukin (1989), Comprehensive sonar imaging of the Easter microplate, *Nature*, *341*, 701–705, doi:10.1038/341701a0.
Searle, R., J. Keeton, R. Owens, R. White, R. Mecklenburgh, B. Parsons, and S. Lee (1998), The Reykjanes Ridge: Structure and tectonics of a hot-spot-influenced, slow-spreading ridge, from multibeam bathymetry, gravity and magnetic investigations, *Earth Planet. Sci. Lett.*, *160*(3–4), 463–478, doi:10.1016/S0012-821X(98)00104-6.
Sempéré, J., P. Blondel, A. Briais, T. Fujiwara, L. Géli, N. Isezaki, J. Pariso, L. Parson, P. Patriat, and C. Rommevaux (1995), The Mid-Atlantic Ridge between 29°N and 31°30′N in the last 10 Ma, *Earth Planet. Sci. Lett.*, *130*(1), 45–55, doi:10.1016/0012-821X(94)00259-2.
Shih, J., and P. Molnar (1975), Analysis and implications of the sequence of ridge jumps that eliminated the Surveyor transform fault, *J. Geophys. Res.*, *80*(35), 4815–4822, doi:10.1029/JB080i035p04815.
Smallwood, J., and R. White (2002), Ridge-plume interaction in the North Atlantic and its influence on continental breakup and seafloor spreading, in *The North Atlantic Igneous Province: Stratigraphy, Tectonic, Volcanic and Magmatic Processes*, edited by D. W. Jolley and B. R. Bell, *Geol. Soc. London Spec. Publ.*, *197*, 15–37, doi:10.1144/GSL.SP.2002.197.01.02.
Sun, S., M. Tatsumoto, and J. Schilling (1975), Mantle plume mixing along the Reykjanes Ridge axis: Lead isotopic evidence, *Science*, *190*, 143–147, doi:10.1126/science.190.4210.143.
Talwani, M., C. Windisch, and M. Langseth (1971), Reykjanes Ridge crest: A detailed geophysical study, *J. Geophys. Res*, *76*(2), 473–517, doi:10.1029/JB076i002p00473.
Vogt, P. (1971), Asthenosphere motion recorded by the ocean floor south of Iceland, *Planet. Sci. Lett.*, *13*(1), 153–160, doi:10.1016/0012-821X(71)90118-X.
Vogt, P., and O. Avery (1974), Detailed magnetic surveys in the northeast Atlantic and Labrador Sea, *J. Geophys. Res.*, *79*(2), 363–389, doi:10.1029/JB079i002p00363.
Vogt, P., N. Cherkis, and G. Morgan (1983), Project investigator-I: Evolution of the Australia-Antarctic discordance deduced from a detailed aeromagnetic study, in *Antarctic Earth Science*, edited by R. Oliver, P. James, and J. Jago, pp. 608–613, Cambridge Univ. Press, Cambridge, U. K.
White, R. (1997), Rift–plume interaction in the North Atlantic, *Philos. Trans. R. Soc. A*, *355*(1723), 319–339, doi:10.1098/rsta.1997.0011.
White, R., J. Bown, and J. Smallwood (1995), The temperature of the Iceland plume and origin of outward-propagating V-shaped ridges, *J. Geol. Soc.*, *152*(6), 1039–1045, doi:10.1144/GSL.JGS.1995.152.01.26.
Wilson, D., and R. Hey (1995), History of rift propagation and magnetization intensity for the Cocos-Nazca spreading center, *J. Geophys. Res.*, *100*(B7), 10,041–10,056.
Wilson, D., R. Hey, and C. Nishimura (1984), Propagation as a mechanism of reorientation of the Juan de Fuca Ridge, *J. Geophys. Res.*, *89*(B11), 9215–9225, doi:10.1029/JB089iB11p09215.
Wilson, J. (1963), A possible origin of the Hawaiian Islands, *Can. J. Phys.*, *41*(6), 863–870, doi:10.1139/p63-094.

JOURNAL OF GEOPHYSICAL RESEARCH

Supporting Information for "A New Kinematic Model of the Mid-Atlantic Ridge between 55°55'N and The Bight Transform Fault for the Past 6 Ma"

Á. Benediktsdóttir,[1] R. Hey,[2] F. Martinez,[2] Á. Höskuldsson,[1]

Contents of this file

1. Tables S1 to S5

Additional Supporting Information (Files uploaded separately)

1. Captions for large Table S5.

Introduction

This supporting information provides tables with parameters used in the forward magnetic modeling.

---

[1]Nordic Volcanological Center, Institute of Earth Sciences, University of Iceland, Reykjavík, Iceland.

[2]Hawai'i Institute of Geophysics and Planetology, University of Hawai'i, Honolulu, Hawai'i, USA.

Table S1. Location of ridge axis for our profiles.

Profile Number	Longitude	Latitude
32	-34.266955	56.752351
47	-34.274762	56.718412
33	-34.281973	56.686869
46	-34.288414	56.655635
34	-34.296728	56.626300
35	-34.304285	56.563182
36	-34.321226	56.500802
37	-34.361021	56.438030
38	-34.357816	56.375419
39	-34.372813	56.313211
40	-34.391550	56.251123
41	-34.412566	56.189284
42	-34.441450	56.127667
43	-34.485123	56.066739
44	-34.512374	56.002435
45	-34.527851	55.941038

Table S2. Stage poles of rotation for Eu-Na (Eurasia fixed)[a]

	0-6.033 Ma	6.033-11.04Ma
Smallwood & White (2002)	0.2312°/Myr	0.2312°/Myr
Benediktsdóttir et. al. (2012)	0.2251°/Myr	0.2600°/Myr
This study	0.2243°/Myr	0.2579°/Myr

[a] The location of the pole for Smallwood & White (2002) (the closure pole for chron 8) and Benediktsdóttir et al. (2012) is 66.85°N, 135.46°E and the location of the pole for this study is 68.00°N,137.00°E (same as the chron 5A closure pole in Smallwood & White (2002)).

Table S3. Distance of anomalies from the ridge in kilometers.

Profile	3ro (6.033 Ma)			5n.2no (11.04 Ma)		
#	Na	Eu	Total	Na	Eu	Total
1	65±2	59±2	121±4	120±3	122±3	242±7
2	61±2	61±2	122±4	119±2	126±3	245± 5
3	64±2	60±3	124±5	121±2	121±2	242±4
4	61±2	61±2	122±4	-	-	-
5	-	-	-	-	-	-
6	-	-	-	-	-	-
7	66±2	55±3	121±5	-	-	-
8	67±3	56±2	123±5	-	-	-
9	66±2	58±2	124±4	123±2	119±2	242±4
10	66±2	57±3	123±5	125±2	123±2	245±4
11	-	-	-	-	-	-
12	-	-	-	123±2	119±2	242±4
13	66±2	59±2	125±4	124±2	120±2	244±4
14	-	-	-	-	-	-
15	74±2	51±2	125±4	-	-	-
16	-	-	-	-	-	-
17	65±2	59±2	124±4	-	-	-
18	-	-	-	-	-	-
19	-	-	-	-	-	-
20	-	-	-	-	-	-
21	63±2	64±2	127±4	-	-	-
22	-	-	-	-	-	-
23	67±2	56±2	123±4	-	-	-
2426	-	-	-	-	-	-
2527	62±3	60±3	122±6	-	-	-
28	-	-	-	-	-	-
29	-	-	-	-	-	-
30	-	-	-	118±2	126±2	244±4

Table S4. Full spreading rates (km/Myr) used in the forward magnetic modeling.

Profile	0-6.033 Ma	6.033-11.04 Ma
32	20.73	23.91
47	20.74	23.92
33	20.74	23.93
46	20.75	23.94
34	20.76	23.94
35	20.77	23.96
36	20.79	23.98
37	20.81	24.00
38	20.82	24.02
39	20.84	24.04
40	20.85	24.05
41	20.87	24.07
42	20.88	24.09
43	20.90	24.11
44	20.92	24.13
45	20.93	24.14

Table S5. Parameters used for the forward magnetic modeling. c, contamination coefficient. * identifies the jumps that are not well determined and lie within the shaded region of Figure 7. Jump # are as shown in Figure 7.

Paper II

Ambient noise tomography of Eyjafjallajökull volcano, Iceland

Ásdís Benediktsdóttir, Ólafur Gudmundsson, Bryndís Brandsdóttir, Ari Tryggvason
Journal of Volcanology and Geothermal Research, 2017., 347, p.250-263.

https://doi.org/10.1016/j.jvolgeores.2017.09.017

Journal of Volcanology and Geothermal Research 347 (2017) 250–263

Contents lists available at ScienceDirect

Journal of Volcanology and Geothermal Research

journal homepage: www.elsevier.com/locate/jvolgeores

Invited research article

Ambient noise tomography of Eyjafjallajökull volcano, Iceland

Ásdís Benediktsdóttir[a, b, *], Ólafur Gudmundsson[c, d], Bryndís Brandsdóttir[e], Ari Tryggvason[c]

[a] Nordic Volcanological Center, Institute of Earth Sciences, University of Iceland, Sturlugata 7, 101 Reykjavik, Iceland
[b] Department of Earth Sciences, University of Iceland, Sturlugata 7, 101 Reykjavik, Iceland
[c] Department of Earth Sciences, Uppsala University, Sweden
[d] School of Science and Engineering, Reykjavík University,Iceland
[e] Institute of Earth Sciences, Science Institute, University of Iceland,Iceland

ARTICLE INFO

Article history:
Received 20 January 2017
Received in revised form 30 July 2017
Accepted 19 September 2017
Available online 27 September 2017

Keywords:
Seismology
Eyjafjallajökull
Ambient seismic noise tomography
Surface waves

ABSTRACT

We present a shear-velocity model for the Eyjafjallajökull stratovolcano, based on ambient seismic noise tomography applied to seven months of data from six permanent stations and 10 temporary seismic stations, deployed during and after the 2010 volcanic unrest. Vertical components of noise were cross correlated resulting in 30 robust phase-velocity dispersion curves between 1.6 and 6.5 s in period, displaying a ±20% variation in phase velocity beneath the volcano. The uneven distribution of noise sources, evaluated using signal-to-noise ratios, was estimated to cause less than 2% error in most curves. Sensitivity kernels showed resolution down to 10 km and the lateral resolution of the resulting phase-velocity maps was about 5 km. The model reveals east-west oriented high-velocity anomalies due east and west of the caldera. Between these a zone of lower velocity is identified, coinciding with the location of earthquakes that occurred during the summit eruption in April 2010. A shallow, southwest elongated low-velocity anomaly is located 5 km southwest of the caldera. The limited depth resolution of the shear-velocity model precludes detection of melt within the volcano.

1. Introduction

The east-west oriented Eyjafjallajökull stratovolcano (Fig. 1) is located at the propagating tip of the SW-NE trending Eastern Volcanic Zone (EVZ) of Iceland. The EVZ is taking over the spreading between the North-American and Eurasian plates from the receding Western Volcanic Zone (WVZ), accommodating 40–100 % of the relative motion between the North America and Eurasia plates (LaFemina et al., 2005). Since 1991, Eyjafjallajökull has undergone four periods of unrest; 1–2) earthquakes and uplift in 1994 and 1999-2000, modeled as the effect of two horizontal sill intrusions (Dahm and Brandsdóttir, 1997; Sturkell et al., 2003; Pedersen and Sigmundsson, 2004; Pedersen and Sigmundsson, 2006; Hooper et al., 2009); 3) deep earthquakes at 20–25 km depth in 1996 (Hjaltadóttir et al., 2015); and 4) earthquakes and uplift in 2009–2010, preceding eruptions on the flank and summit of the volcano (Sigmundsson et al., 2010; Tarasewicz et al., 2011, 2012a, 2014). The recent unrest started with a few deep earthquakes in March/April 2009, followed by a swarm of 200 earthquakes in June–August 2009, and an increase in earthquake activity in January 2010 which culminated in a flank eruption at Fimmvörduháls on March 20th, 2010 (Hjaltadóttir et al., 2012). On April 14th, two days after the flank eruption ceased, a summit eruption began, accompanied by earthquake activity underneath the summit until the end of May 2010 (Sigmundsson et al., 2010; Tarasewicz et al., 2012a,b). Prior to 2010, Eyjafjallajökull had erupted three times during the past 1500 years; 1) a trachytic lava eruption with mafic and silicic tephra components in the 10th century, 2 km WNW from the caldera forming the NW trending 4.5 km long and 100 m wide Skerin ridge (Óskarsson, 2009); 2) a poorly described eruption in 1612 or 1613 (Jónsson, 1774; Larsen et al., 1999); and 3) a summit eruption in December 1821–January 1823, producing highly silicic magma (Larsen et al., 1999; Gudmundsson et al., 2010). For a comprehensive overview of the deformation and the seismicity of Eyjafjallajökull, see Hjaltadóttir et al. (2015) and for an overview of its tectonic setting and known eruptions, see Einarsson and Hjartardóttir (2015).

Several conceptual models have been proposed for Eyjafjallajökull volcano (Sigmundsson et al., 2010; Tarasewicz et al., 2014; Einarsson and Hjartardóttir, 2015). However, the internal structure of Eyjafjallajökull has thus far not been investigated with seismic tomography although various seismic studies have been carried out (Dahm and Brandsdóttir, 1997; Jónsdóttir et al., 2007; Tarasewicz et al., 2011, 2012a, 2014; Hjaltadóttir et al., 2015) and it has been investigated by electro-magnetic methods (Miensopust et al., 2014)

* Corresponding author.
E-mail address: asb1@hi.is (Á. Benediktsdóttir).

https://doi.org/10.1016/j.jvolgeores.2017.09.017
0377-0273/

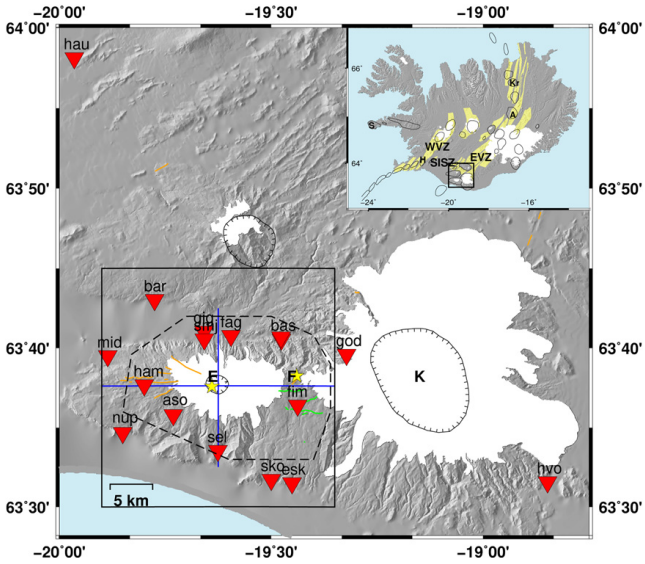

Fig. 1. Tectonic setting of Eyjafjallajökull. Seismic stations are inverted triangles, and solid and hatched lines are outlines of central volcanic systems and calderas, respectively. E = Eyjafjallajökull, F = Fimmvörduháls, K = Katla. Orange lines are eruptive fissures and green lines are faults (data compiled by Einarsson and Hjartardóttir, 2015, see references therein). The rectangular box shows the area of Figs. 6, 7 and 11 and the blue lines show the location of the cross sections in Fig. 12. In the small inlet; WVZ = Western Volcanic Zone, EVZ = Eastern Volcanic Zone, SISZ = South Iceland Seismic Zone, A = Askja, H = Hengill, Kr = Krafla, S = Snæfellsjöill.

revealing a low resistivity anomaly underneath Fimmvörduháls one year after the flank eruption, interpreted as the hot intrusive material of a flank intrusion. Until present, the internal material properties of Eyjafjallajökull have been approximated as a homogeneous and isotropic half-space (Sigmundsson et al., 2010; Albino and Sigmundsson, 2014; Hjaltadóttir et al., 2015) in all numerical deformation models.

Ambient noise tomography(ANT) has become a widely used method to image the subsurface of the Earth both globally (e.g. Nishida et al., 2009; Haned et al., 2016), regionally (Shapiro et al., 2005; Gudmundsson et al., 2007; Moschetti et al., 2007; Gao and Shen, 2015; Korostelev et al., 2015; Green et al., 2017), and on a smaller-scale, where localized low-velocity anomalies have been imaged (Brenguier et al., 2007; Stankiewicz et al., 2010; Jay et al., 2012; Matos et al., 2015; Spica et al., 2015; Tamura and Okada, 2016; Obermann et al., 2016). The method is used to infer the S-wave velocity structure in the subsurface by a traditional surface-wave inversion. The data, however, are not direct measurements of surface wave arrivals from earthquakes, instead they are derived from a few tens of days up to years of continuously recorded ambient noise on seismometers. By cross-correlating the ambient signal between two seismometers, waves travelling between the two are focused such that information about the material properties between the two stations is obtained (Campillo and Paul, 2003; Derode et al., 2003; Shapiro and Campillo, 2004; Wapenaar et al., 2010). The cross-correlated signal, here after referred to as a correlogram, is then processed as if it were a surface wave response recorded at one station with the source located at the other. The dispersive nature of the surface wave in between the two seismometers is examined by measuring a phase-velocity dispersion-curve (Boschi et al., 2012; Herrmann, 2013). Given enough station pairs (that is given a good path coverage) in the area, a phase-velocity map can be inverted for from the dispersion curves and given data in enough frequency-bands one can invert for depth variations in S-velocity in each node.

The ANT method complements the more traditional imaging techniques, which rely on recording waves from earthquakes or explosions. ANT does not depend on the in-homogeneous distribution of earthquakes and their irregular occurrence, and is not as expensive as active-source experiments. Located in the middle of the North-Atlantic ocean, in the pathway of low-pressure systems passing the ocean, generating strong microseismic noise, Iceland is an ideal place to apply ANT. We present the results of the first upper crustal tomographic study of Eyjafjallajökull.

2. Data acquisition and processing

This study is based on data from 16 seismic stations recording between March 6th and September 30th, 2010, ten temporary stations deployed by the Institute of Earth Sciences, University of Iceland and Uppsala University, and six permanent stations operated by the Icelandic Meteorological Office (IMO). Twelve stations were equipped with Lennartz 5 s seismometers, and four with broadband Guralp seismometers. The operational time of each station varied between tens of days to 7 months.

We partly followed the data processing procedure described in Bensen et al. (2007) and constructed correlograms between station pairs. Before daily cross-correlations were calculated, stations were prepared as follows; the data were demeaned, corrected for instrument response, filtered between 0.05 Hz and 4 Hz, decimated from 100 to 10 samples per second and one-bit normalized. We whitened

the data after the cross-correlations had been calculated, rather than before as described in Bensen et al. (2007). This was done in order to save computer time as whitening was only done to the final correlogram, rather then the entire time series. For each available station pair hour-long time segments of the vertical components were correlated and thus Rayleigh waves were captured. The hour-long correlograms were then stacked into day-long correlograms. The period range of interest lay between 1 and 7 s, corresponding to wavelengths between about 4 and 14 km, assuming a phase velocity of approximately 2 km/s. However, as stable measurements of phase velocity require an inter-station distance of at least one wavelength Luo et al. (2015), station pairs with distances smaller than 15 km were discarded. Later on we impose the one-wavelength criterion more precisely and systematically for each station as the phase velocity changes with period. The response of the Lennartz 5 s seismometers starts to fall off at 5 s. Nevertheless, data at longer periods are recorded; at 10 s the amplitude has dropped to 10% of the amplitude at 5 s.

The one-day correlations were stacked into monthly correlograms, with each one-day correlation weighted according to its signal-to-noise ratio (SNR). One-day correlations with unclear surface-wave arrivals, i.e. a SNR smaller than 6, were discarded. In order to enhance correlograms with a good SNR but to avoid the dominance of a few very high SNR correlograms, correlograms with SNR greater than 10 were given a weight equal to the square root of their SNR. Correlograms with SNR between 6 and 10 were weighted linearly from no weight at SNR of 6 to the square root of 10 at SNR of 10. This is an arbitrary weighting scheme arrived at through experimentation. Finally, the stacked correlograms were velocity filtered and whitened. Fig. 2 shows the correlograms as a function of inter-station distance.

The fundamental assumption in ANT is that the ambient noise wave-field is random and that sources generating the field are distributed homogeneously in the medium (Lobkis and Weaver, 2001; Weaver and Lobkis, 2004). Stehly et al. (2006) showed that this is not the case in reality, correlograms are most often asymmetrical. Sadeghisorkhani et al. (2016) showed that the azimuthal SNR distribution in ambient-noise correlograms captures broad features of the physical source distribution. Thus SNR can be used as a proxy for the source distribution strength. Our data exhibit an uneven azimuthal SNR distribution with the most intense ambient noise between 3 and 5 s. The highest SNR are measured on correlograms for station pairs with an east-west azimuth, on the side of the correlogram indicating noise coming from the west, whereas the lowest SNR are measured on correlogram for station pairs with a north-south azimuth, on the side of the correlogram indicating noise coming from the north

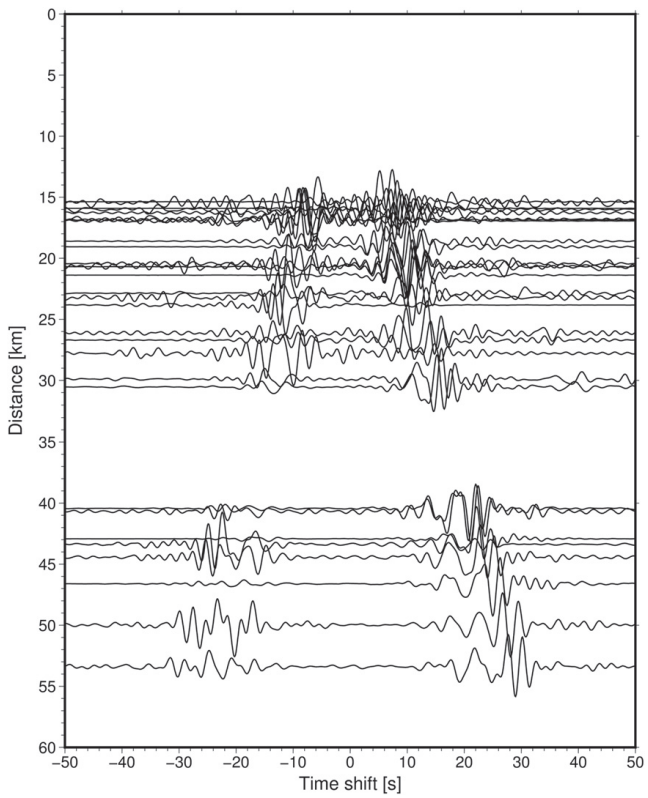

Fig. 2. Record sections showing the 30 correlograms we use to obtain the useable dispersion curves. Inter-station distance vs. time lag.

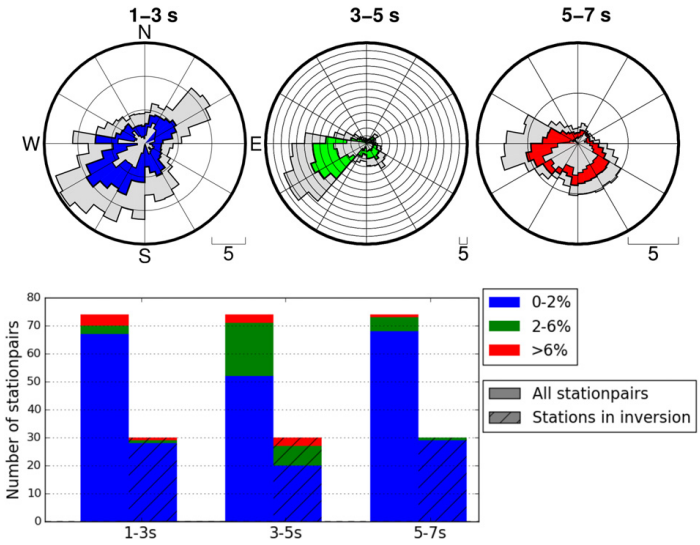

Fig. 3. Upper panel. Signal to noise ratio as a function of station to station azimuth. The sector diagrams show, with a median calculated over 30°, the directivity of the signal to noise ratio of the correlograms. All 74 correlograms from station pairs with more than 15 km inter-station distance were used for these calculations. Each correlogram gives two values with a 180° difference and most of the signal is coming from the south-west. Gray shades show the spread of the data. **Bottom panel**. The predicted velocity errors associated with the uneven source distribution as shown in the upper panel. The error estimate was done for each of the two azimuths for a given station pair and a weighted average, based on the SNR on each side, calculated. Blue, green and red represent stations with 0–2%, 2–6% and more than 6% velocity error estimate, respectively. Solid and hatched columns are the 74 station pairs with more than 15 km inter-station distance, and the 30 station pairs used in the inversion, respectively.

(upper panel of Fig. 3). This may be due to greater distance to the source of the noise, attenuation as the waves cross Iceland, or simply weaker generation of noise in the Denmark Strait than the broader Atlantic Ocean in other directions. Sadeghisorkhani et al. (2016) also estimated bias in phase velocity caused by an uneven source distribution, by comparing a correlogram predicted by a uniform power distribution with a correlogram from an uneven distribution (see also Sadeghisorkhani et al. (2017)). We use this method and weigh the two phase-velocity biases for each station pair in accordance with the power of the ambient signal from each direction. The estimated phase velocity differences lie between 0 and 2 % with a small proportion between 2 and 10 % (bottom panel of Fig. 3). Compared to the variation of the phase-velocity measurements discussed, in the next section, the uneven distribution of sources is a relatively small source of error for 1–3 s and 5–7 s periods, but a more substantial source of error for 3–5 s. Sadeghisorkhani et al. (2017) showed that when the inter station distance is small compared to a wavelength, as in this study, the amplitude of the phase-velocity bias due to an uneven source distribution scales with the period. However, the source distribution is simplest at the longest period, therefore, the bias is not largest there, but in the intermediate period range where the source distribution is more complex. If the source distribution were the same for all periods, the bias would increase with period.

Although eruption tremor has been shown to lie in a similar frequency range as the ambient noise used in ANT (Ballmer et al., 2013), this is not the case for Eyjafjallajökull as the tremor lies mainly in the range between 0.1 and 2 s with a peak at 1.4 s, while the ambient noise lies at longer periods, with a peak at 3 s. The spectral power associated with the unrest is, therefore, not a significant source of error in the ANT presented here.

The continuous recording time of seismic data used for ANT varies greatly between studies, ranging from a few tens of days (Shapiro et al., 2005; Ma et al., 2008; Masterlark et al., 2010) up to years (e.g. Brenguier et al. (2007), Lin et al. (2008), Nagaoka et al. (2012)) with an improving signal-to-noise ratio with longer recording time. We discarded station pairs with less than one month of data and compared one-month long correlograms from each station pair to get an estimate of the stability of the measurement. Later in the process, the comparison between monthly dispersion curves is used to estimate the uncertainty in the measurements.

2.1. Phase-velocity measurements

We constructed monthly phase-velocity dispersion curves for each station pair, for as many months as the stations were running simultaneously, by frequency-time analysis using the multiple filter-analysis in *Computer Programs in Seismology* (Herrmann, 1973, 2013). As the distribution of dispersion curves gives us an idea about the stability of the phase-velocity measurements of that particular station pair, the variability of monthly measurements (the standard deviation of the mean) was used as a measure of uncertainty of phase-velocity measurements.

Luo et al. (2015) showed that short paths down to one-wavelength in inter-station distances can be used in ANT studies. They found that time-domain cross-correlations, such as calculated here and used for this tomography, give the same results for short paths down to one-wavelength in inter-station distances as the spectral method of Ekström et al. (2009), which has been shown to give robust phase-velocity measurements for such short paths. Luo et al. (2015) did not include inter-station distances smaller than

one wavelength because of large uncertainties compared to longer paths and the number of such short paths that gave reliable measurements were to small for statistical comparison. We therefore used data with a wavelength smaller than the inter-station distance. Also we used data with an error estimate less than 5% of the phase velocity.

Out of 74 station pairs with inter-station distance larger than 15 km, 30 pairs yielded stable measurements, with an error-based-weighted average phase velocity of 2.1 to 2.8 km/s for periods between 2 and 7 s (Fig. 4). An example of a phase-velocity-dispersion curve and the monthly variability is shown for the Aso-Bas (NE azimuth) and Aso-Esk (WSW azimuth) station pairs in Fig. 4B and C, respectively. Generally, the monthly variability of phase velocity increases with increasing period, and therefore, there are fewer reliable data at the longer periods. The path coverage of the 30 station pairs that were used for the phase-velocity map inversions is densest on and around Eyjafjallajökull (Fig. 5). The variability of the stable dispersion curves about the average phase velocity dispersion curve is roughly ±20%, giving a rough estimate of the velocity variations in Eyjafjallajökull.

3. Inversion results

Two inversions are performed to obtain a three-dimensional shear-wave velocity model of Eyjafjallajökull. First, phase-velocities are inverted at each period for phase-velocity maps. Second, local dispersion curves are constructed at each node of the phase-velocity maps and inverted for local variations of shear velocity with depth. Interpolating between these, results in a three-dimensional model of shear velocity.

3.1. Phase-velocity maps

Phase-velocity maps were constructed for periods between 1.6 and 6.5 s using an iterative non-linear subspace inversion, where local linearity was assumed (Rawlinson and Sambridge, 2005). The choice of periods, for which phase-velocity maps were constructed, was based on the width of the Gaussian filter in the dispersion-measurement process. Each Gaussian filter was chosen such that it intersected the subsequent filter at the level corresponding to one standard deviation. Therefore, the individual measurements have limited overlap in period making them largely independent. Forward model calculations were based on a grid-based numerical Fast Marching Method (Rawlinson and Sambridge, 2005), where travel time of the advancing wave was computed at each grid point, using a finite-difference solution of the Eikonal-equation. It is important to note that the linearization was performed in terms of phase velocity, which controls the lateral refraction of surface waves (Woodhouse, 1974; Lay and Kanamori, 1985). Also, Sadeghisorkhani et al. (2016) showed that an uneven azimuthal distribution of noise causes larger bias for group velocities than for phase velocities.

The phase-velocity maps were calculated on a 2.5 × 2.5 km grid to be able to sample 5 km velocity anomalies without aliasing (Fig. 7). A unique damping factor was chosen for each period by constructing a trade-off curve from a wide range of damping factors. Initially, the inversion was run with a large damping factor (10,000) and a uniform starting model using the weighted, mean phase-velocity, weighted by the inverse error. In order to prevent different damping factors from leading to different minima in the linearized inversion, the resulting best-fit model, i.e. for the highest damping factor, was used as an initial model for the subsequent damping factor. We chose the damping factor where the trade-off curve flattened out after which the data misfit did not change much as damping was reduced (Table 1). A selection of a slightly

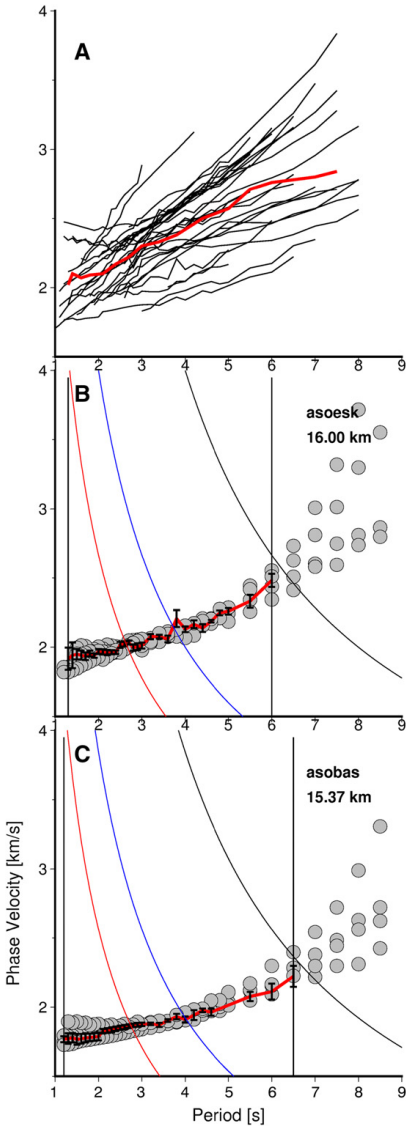

Fig. 4. Phase-velocity-dispersion curves used in the phase-velocity map inversion; phase velocity vs. period. **A**. 30 out of 74 available dispersion curves. Red line is the weighted average dispersion curve, which is also the starting model for the depth inversion. **B**. Phase-velocity-dispersion curve for the Aso-Bas station pair. Gray circles and red line are monthly measurements and their mean, respectively. The error bars of the mean dispersion curve are the standard deviation of the mean of the monthly measurements. Black, blue and red curved lines show the wavelength that corresponds to 1, 1/2 and 1/3 times the inter-station distance, respectively. The black vertical line indicates where we choose the cut-off periods, either where the wavelength is smaller than the inter-station distance (asobas) or where the ratio between the error estimate and the phase velocity is larger than 5% (asoesk). The inter-station distance is displayed in the upper right corner. **C**. Same as **B**. but for the Aso-Esk station pair.

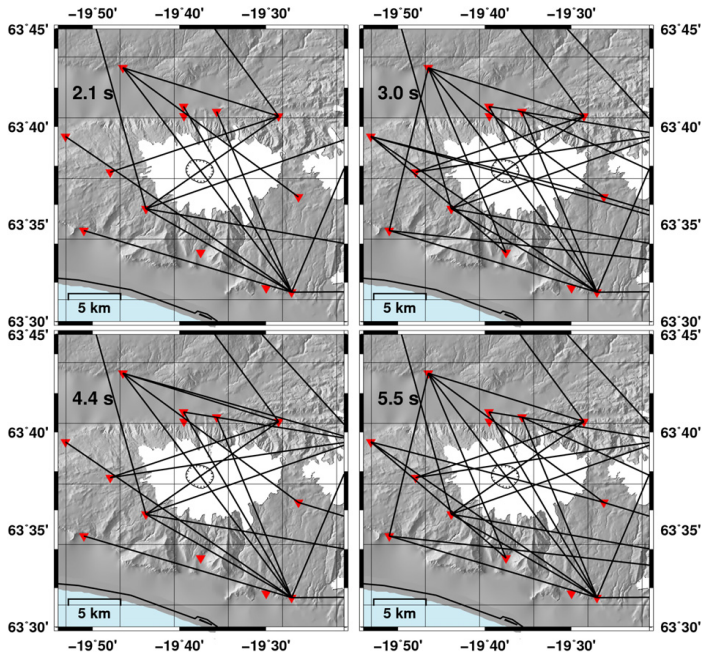

Fig. 5. Path coverage for 2.1 s, 3.0 s, 4.4 s and 5.0 s; after creating dispersion curves for all stations with inter-station distance larger than 15 km these are the station pairs that result in stable dispersion curves. Inverted red triangles are seismic stations.

higher or lower damping factor did not significantly alter the recovered structure in the phase-velocity maps. In general, denser path coverage lowers the damping factor and more detailed structure is recovered.

To estimate the lateral resolution of the phase-velocity maps two checkerboard resolution tests were performed. Both tests were calculated on a 2.5 × 2.5 km grid, but with different velocity-anomaly sizes, which had a maximum perturbation velocity of 0.3 km/s relative to the reference velocity (3.0 km/s) (Fig. 6). The parameterization and regularization of the checkerboard inversion were kept the same as in the data inversion.

Checkerboard anomalies of lateral dimension 7.5 km × 7.5 km were well recovered at all periods in the area of Eyjafjallajökull, including Fimmvörduháls, whereas the 5.0 km × 5.0 km checkerboard anomalies were best recovered where the path coverage was the densest. The path coverage varied with period, and therefore also

Table 1
Parameters used to estimate the goodness of fit for each period.

Period [s]	Mean velocity [km/s]	No. paths	Damping	Extrema	DOF	Q_0	Q	Q_N
1.6	2.07	15	125	9	6	2339	59	10
1.8	2.09	18	200	9	9	2341	46	5
2.1	2.10	20	150	13	7	2484	91	13
2.4	2.17	22	100	14	8	2560	122	15
2.7	2.22	28	200	13	15	2369	263	18
3.0	2.30	29	80	14	15	4423	284	19
3.4	2.33	28	200	15	13	3488	552	43
3.8	2.38	29	60	14	15	2421	687	46
4.4	2.50	28	60	11	17	5826	963	57
5.0	2.57	28	125	10	18	3360	1060	59
5.5	2.71	25	100	11	14	2223	864	62
6.0	2.76	20	80	11	9	1530	662	74
6.5	2.78	17	100	11	6	1959	606	101

DOF = degrees of freedom, Q = weighted least squares misfit, Q_0 = Q for the starting model (homogeneous velocity), Q_N = normalized Q with respect to degrees of freedom of the residual data.

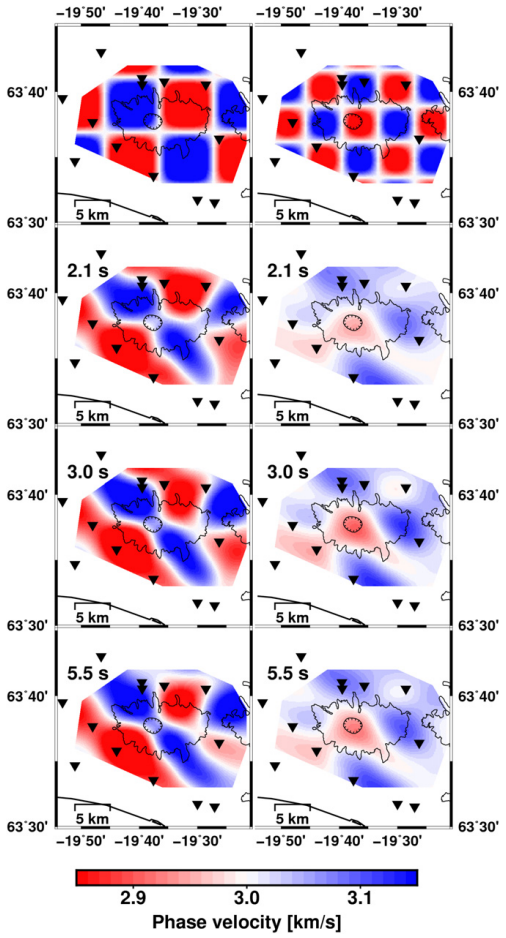

Fig. 6. Resolution tests. The input velocity anomaly cells are 7.5 × 7.5 and 5.0 × 5.0 km, for the top left and right panels, respectively, with a maximum perturbation velocity is 0.3 km/s at each cell. Panels below the checkerboard model show the recovered models for 2.1, 3.0 and 5.5 s. All models were calculated on a 2.5 × 2.5 km grid and the damping factor for each period was the same as in the actual phase-velocity-map inversion (Table 1). Inverted black triangles are seismic stations.

the spatial resolution. The greatest number of paths was for periods between 2.7 and 5.5 s (25–28 paths, Table 1).

These normalized weighted least-squares misfit and misfit normalized to the degrees of freedom in the model were calculated for each period. It is not trivial to estimate the number of degrees of freedom in the model since the inversion is non linear. Therefore, we counted the number of extrema (number of highs and lows) in each phase-velocity model and used that as a proxy. The degrees of freedom of the residual data are then the number of paths (N) minus the number of degrees of freedom in the model (d). These values are summarized in Table 1.

Although the variance reduction from a uniform velocity model (Q_0) to the final phase-velocity model (Q) was substantial for all periods, then Q_N was significantly bigger than unity, indicating that the estimated data uncertainty was under estimated. Our estimates of data uncertainty only took into account the month-by-month variation of phase velocity. This ignores other uncertainty factors, such as computational uncertainty of the forward solution, bias due to an uneven source distribution (as discussed above) and potential topography effects. Here, the surface-wave paths were assumed to be along a flat Earth, which was surely not the case. The path travelled by the surface waves depends on topography and the distances they travel are longer than that on a flat Earth. This leads to lower velocity estimates than if we assumed surface-wave paths along the topography. Köhler et al. (2012) explored the effects of topography on phase-velocity measurement in Norway and found a linear relationship between phase-velocity error and the local topographic gradient around the receiver. Furthermore, they showed that, globally, the maximum effect of topography on phase-velocity measurements was 0.7% for wavelengths between 7 and 20 km, an interval that contains most of the wavelengths used here. Note that these results were based on simulations using a homogeneous medium with a free surface with topography. This may not be a good approximation for the crust in Iceland, where the near-surface velocity gradient is very strong, affecting the dispersive nature of the surface waves. These results are, therefore, possibly not applicable to Iceland and may underestimate the velocity bias due to topography. We note, however, that the variation of our phase-velocity measurements is much larger than the size of their simulated effect and, therefore, conclude that topographic effects are likely to contribute significantly to our errors, but unlikely to affect our resulting structure significantly. We redefine the total uncertainty of our data to match the variance of the residual data for each period after inversion for phase-velocity maps in order to estimate the uncertainty of the inversion.

The uncertainty of the phase-velocity maps was estimated by repeatedly inverting synthetic data that simulate the error estimate of the data. The synthetic data were the path-averaged phase velocities predicted by the final model with random noise added, with a variance equal to the residual-data variance. This was repeated 80 times and the width of the distribution of all the different velocities obtained for each node was taken as an estimate of the uncertainty at that point. The variation of phase-velocity estimates resulting from those 80 realizations was used as an estimate of the error distribution. The distribution of uncertainties widens with increasing period (Fig. 8A), with the smallest standard deviation of 0.02 km/s at 1.6 s and the largest standard deviation of 0.08 km/s at 6.0 s.

The 4.4 s and 5.5 s phase-velocity maps (Fig. 7) show an east-west oriented high-velocity (>3.0 km/s) structure across Fimmvörduháls and a low-velocity zone (<2.0 km/s) under the Eyjafjallajökull caldera. These features are discussed in detail in Section 4.

3.2. Depth inversion

Local dispersion curves were constructed from the phase-velocity maps at each node on a 2.5 km × 2.5 km grid outlined in Fig. 1. The SURF96 program in *Computer Programs in Seismology* (Herrmann and Ammon, 2002) was used to invert the local dispersion curves for shear-wave velocity structure.

The starting model, for the depth inversion at each node, was generated by inverting the mean dispersion curve for the area (red line in Fig. 4). The initial model for the mean dispersion curve inversion consisted of eight layers with a constant V_s velocity equal to the mean regional Rayleigh wave velocity, obtained from the phase-velocity inversion. A constant V_p/V_s ratio of 1.77 (Jeddi et al., 2016) was used and a starting crustal density of 2520 kg/m^3, based on the

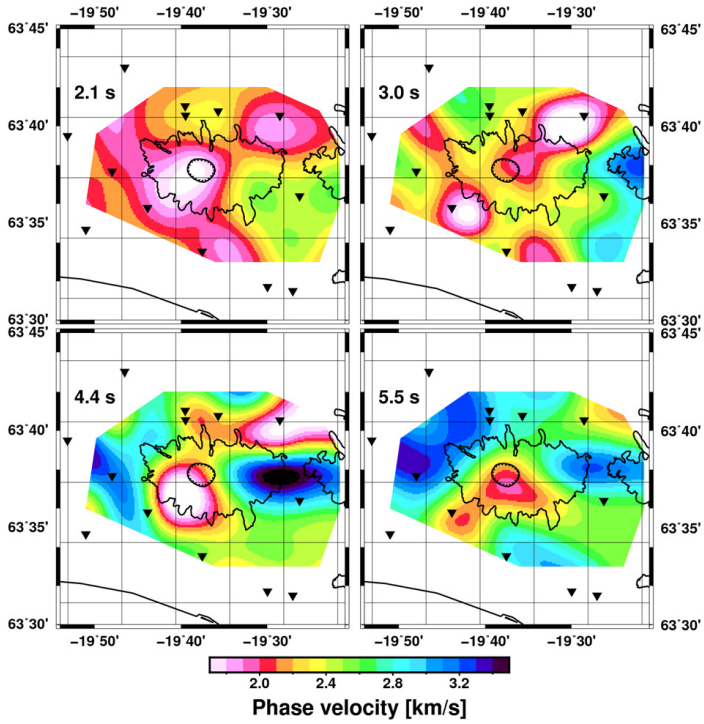

Fig. 7. Phase-velocity maps for 2.1 s, 3,0 s, 4,4 s and 5.0 s. Gridlines are 5 km apart. Inverted black triangles are seismic stations.

value for the Bouguer-correction density used by Kaban et al. (2002) for Icelandic crust.

Fig. 9 shows sensitivity kernels represented by phase-velocity derivatives, for each period. The majority of the periods are most sensitive to structure in the uppermost 6 km, but the longest periods are most sensitive to structure at 7 km depth. We limit the discussion of the depth inversion to the uppermost 10 km, based on the sensitivity kernels. By taking the difference between two sensitivity kernels, for subsequent periods, a maximum and a minimum is obtained at variable depths (middle panel in Fig. 9.). The distance between the two extrema is a simple proxy for the depth resolution at the average of their depths, and from this information we constructed a depth-resolution graph (bottom panel in Fig. 9).

The layer thickness was kept constant during the inversion with two one-kilometer thick top layers, two two-kilometer thick layers, two three-kilometer thick layers and two five-kilometer thick bottom layers. We experimented with the layer parameterization and found that this particular set of layers was well suitable to explain our measurements. A damping factor was chosen from a trade-off curve for each of the grid points and the spacial distribution of the damping factor values is shown in Fig. 8C. The damping factors ranged from 1 to 50 in the area of interest, with 10 cells out of 49 having a damping parameter greater than 8. The depth inversion was performed with 10 iterations and the mean shear-wave velocity structure for the area is shown in Fig. 10. Data points that lay farther than three times the uncertainty away the resulting model were removed, and the inversion was performed again, leaving out the outliers.

Fig. 8D shows a map of the misfit distribution after the depth inversion. The values mapped are the misfit between the predicted dispersion curves and the measured dispersion curves, normalized by both the uncertainty at each period and the number of data points. The largest misfit ranges between 0.1 and 2.0.

The same approach as for the phase-velocity maps was used to estimate the uncertainty of the final three-dimensional model. Synthetic data were generated, consisting of the local dispersion-curve estimate added to random noise with a standard deviation equal to the estimated uncertainty of the phase-velocity maps. These data were inverted and the process repeated 80 times. For each depth at each node, the distribution width of the resulting velocities was used as an estimate of uncertainty. Uncertainty estimates for all nodes, in the area of interest, were compiled into one distribution for each depth range (Fig. 8B). The standard deviation of the distributions increased from 0.06 km/s at 1.5 km depth to 0.10 km/s at 10.5 km.

Eyjafjallajökull rises 1666 meters above sea level and the slopes of the mountain are steep. In tomography, where the depth range is tens or hundreds of kilometers, the scale of the topography is such that a flat surface can be assumed. In this paper we present results down to a depth of 10 km and the elevation of Eyjafjallajökull is roughly 10% of that depth. A depth slice at a 1 km depth would be

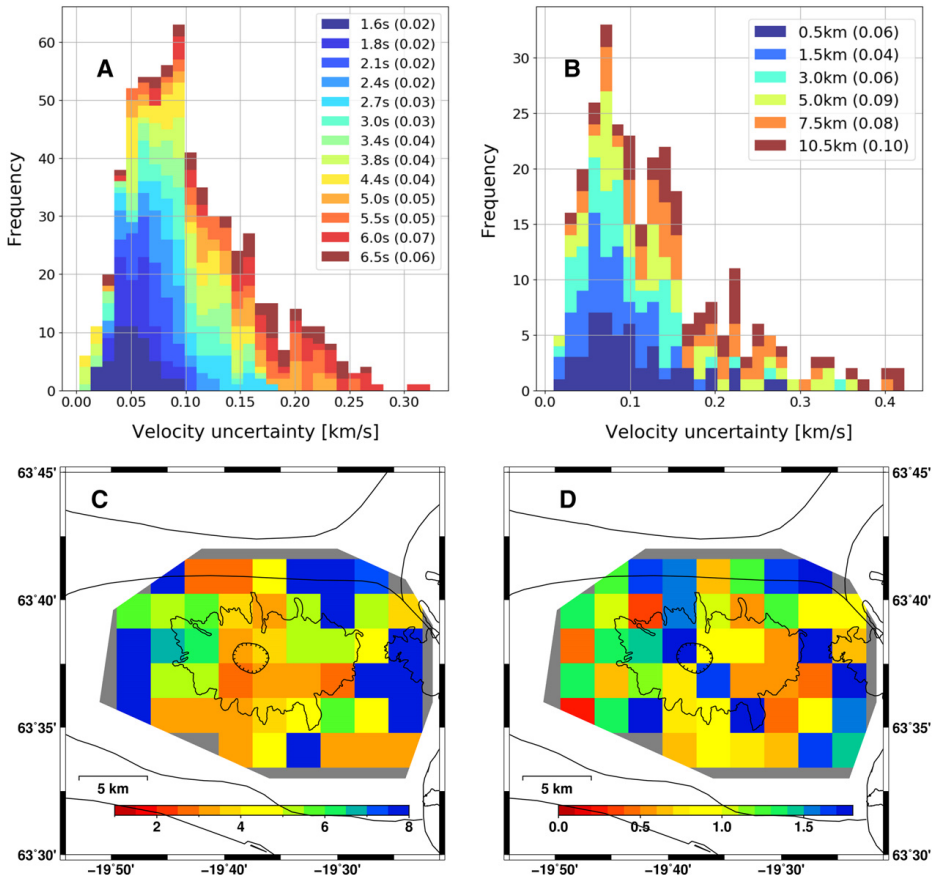

Fig. 8. Distribution of uncertainty for the phase-velocity maps (**A**) and the three dimensional model (**B**). The periods and depths are as labelled and numbers in parenthesis are the standard deviations ($1-\sigma$) of the uncertainty distribution in km/s. **C**. Map of the damping factor distribution used in the depth inversion. D. Map of the misfit distribution of the depth inversion.

below sea level at some points on the map, but above sea level at others. Therefore, by applying a first order correction by interpolating the local one-dimensional model at each location, and shifting it corresponding to the elevation at that point. The effect of this correction is most notable in the thinner upper most layers and becomes negligible where the layers are thicker than the elevation. Another effect is to make deeper structures shallower, and correspondingly changing the mean value of the depth slices. Depth slices and cross sections are shown in Figs. 11 and 12, respectively.

4. Discussion

The lateral parameter dimensions of the final shear-velocity model are 2.5 × 2.5 km for resolvability of features 5 km across. Based on the linear decrease in vertical resolvability with depth and the sensitivity kernels (Fig. 9), we limit our discussion to the top 10 km of the final model. The level of heterogeneity is ±30–35 % in the top 3 km and approximately ±15% below that depth. This is similar to the variation of measured phase velocities. It is also comparable to the level of heterogeneity modeled at neighbouring Katla volcano with similar resolution and using similar data (Jeddi per. comm., 2017). Our model is more heterogeneous than the model of Obermann et al. (2016) of Snæfellsjökull volcano in Western Iceland (±10%), but they applied linear inversion for group-velocity maps and may, therefore, underestimate the level of heterogeneity. Greenfield et al. (2016) and Schuler et al. (2015) found approximately ±15% variation in the S-wave velocity at 2 km depth under Askja volcano and Krafla volcano, north Iceland, respectively, using local-earthquake tomography, which is a little less heterogeneity than found in our model. Our model is considerably more heterogeneous than the model of Tryggvason et al. (2002) for Hengill volcano in southwest Iceland. These different levels of heterogeneity are affected by variable resolution limitations, but may reflect variations of the structure of volcanoes in different settings, with varying levels of activity and maturity.

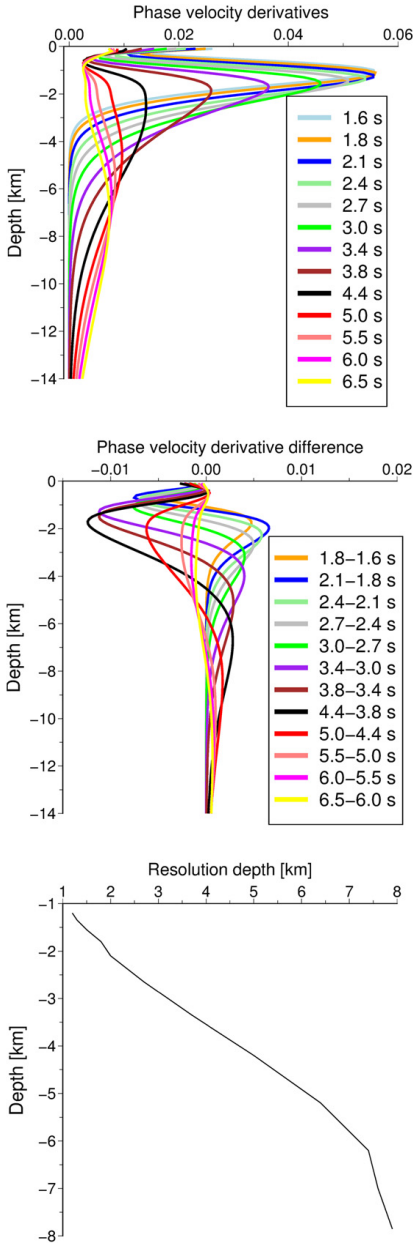

Fig. 9. Phase-velocity derivatives (top), the difference between two subsequent derivatives (middle), and a resolution-depth estimate (bottom).

Two east-west elongated high-velocity anomalies are prominent in our final model, due east and west of the caldera. The well resolved eastern high-velocity zone extends 8 km E-W, 2 km N-S and between 4 and 9 km in depth with a center at 6 km underneath Fimmvörduháls. The less resolved western high-velocity zone is roughly 6 km E-W and 2 km N-S, between 5 and 10 km depth (Figs. 7, 11 and 12). The high-velocity zones are divided above 5 km depth by a zone of lower shear velocities but joined at a depth of 7.5 km, forming a continuous high-velocity anomaly along the axis of the volcano. The high-velocity zone seems to diminish below 10 km depth, although, admittedly our resolution is severely reduced at that depth.

In a tomography study of Katla volcano, Jónsdóttir et al. (2007) reported a zone of higher-velocity underneath Fimmvörduháls, coinciding with the eastern high-velocity anomaly in this study. The amplitude of this high-velocity anomaly is comparable between the two studies.

The SW-NE oriented low-velocity anomaly (Fig. 7) located under the summit caldera at approximately 3 km depth has a center roughly 5 km southwest of the caldera. The obvious shift of the low-velocity anomaly, relative to the caldera, is not an artifact as the ray coverage is dense.

Pre-eruption events between 1991 and 2009 were confined to a vertical zone near the eastern caldera rim extending down to 24 km depth (Hjaltadóttir et al., 2015), i.e. within the zone of lower shear velocities (Fig. 12), discussed below. This summit seismicity was accompanied by isolated seismic swarms at shallower depths on the flanks of the volcano (Dahm and Brandsdóttir, 1997; Hjaltadóttir et al., 2015). The 2010 Fimmvörduháls flank eruption was also preceded by shallow flank seismicity illuminating several NE-SW striking subvertical dikes, emplaced at 2–6 km b.s.l. (Tarasewicz et al., 2012a), extending from the near summit zone of lower velocities to the E-NE, above the eastern high-velocity zone (black dots in Fig. 12).

The two seismically active periods prior to the 2010 flank eruption, 1994 and 1999 were modeled as sill intrusions at 5 km depth 4 km SE of the caldera and at a 6.3 km depth 4 km south of the caldera, respectively (Pedersen and Sigmundsson, 2004, 2006). These locations coincide with a location where the S-wave velocity is between 2.6 and 4 km/s in our model. The maximum opening of the sill was modeled as 1 m in the 1999 intrusion event. Sill of such thickness would crystallize in a relatively short time. The scale of these intrusions is below the resolution of our model. However, it is an indicator of the locations of such repeated intrusions and, therefore, the co-location with a zone of higher-velocities is logical (Fig. 11).

Detailed analyses of seismic activity propagating vertically through the entire crust during a ten-week period in 2010 coincides within the zone of lower velocity (blue and red circles in Fig. 12), attributed by Tarasewicz et al. (2012b) to a decompression wave propagating downward through the crust, indicating that this region may consist of more evolved material and possible higher temperatures.

Most of the lavas on Eyjafjallajökull studied by Jakobsson (1979) were reported to be of intermediate composition and the Skerin ridge eruption in 10th century was a trachytic fissure eruption (Óskarsson, 2009). Also, during the 2010 summit eruption, the output material was of basaltic, intermediate and silicic composition (Sigmarsson et al., 2011), with basaltic material coming from depth, injected into the silicic body, causing magma mixing. These data suggest that the composition of the material coming from the low-velocity zone is rather evolved.

Sigmarsson et al. (2011) constructed a time line of the 2010 unrest from geochemistry and concluded that a relatively primitive basalt ascended from a 16–18 km deep source (Keiding and Sigmarsson, 2012) (beyond the resolution of our model), which fractionally crystallized forming a more evolved basalt that accumulated below a partially molten residual silicic magma body beneath the summit of Eyjafjallajökull. The silicic body obstructed further ascent of the basaltic magma, forcing a fraction of the primitive basaltic magma to the surface and to the side, resulting in the flank eruption at Fimmvörduháls. Meanwhile, the silicic magma body was heated up

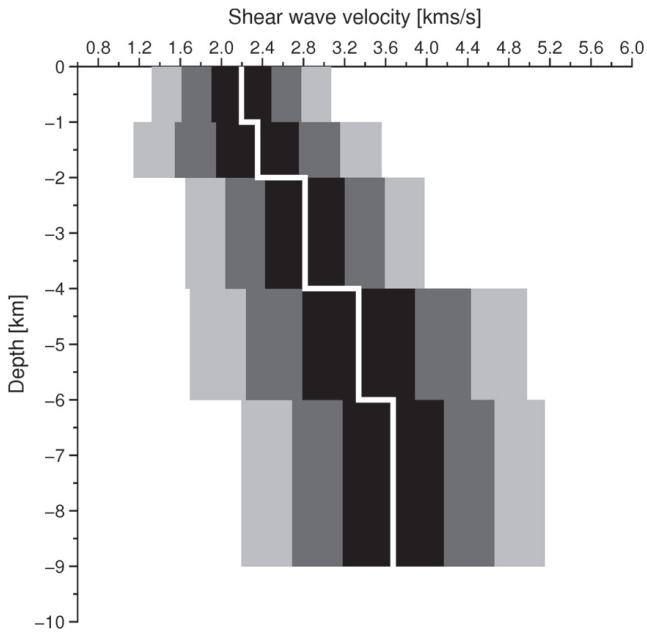

Fig. 10. Mean shear-wave velocity as a function of depth. The black, gray and light gray boxes represent one, two and three standard deviations, respectively.

by the non-erupted part of the basaltic intrusion, mobilized and eventually erupted through the summit as an injection of more basaltic material found its way to the silicic body. It is plausible that the low-velocity conduit represents the magma pathway to the surface. Interestingly, the earthquakes that occurred prior to the flank eruption (small black circles in Fig. 12) originate at the lower end of the low-velocity anomaly and then migrate toward the surface. If the partially molten silicic body which obstructed the ascending primitive basalt is located where these earthquakes start, then it is located at the bottom of the low-velocity anomaly.

A subsidence signal observed by InSAR data occurred after the onset of the top-crater eruption and modeled as a deflating sill at a 4.0–4.7 km depth underneath the summit of Eyjafjallajökull (Sigmundsson et al., 2010). The location of the deflating sill roughly coincides with the location of the low-velocity anomaly, suggesting a location of an emptying magma storage area.

Higher velocities have been observed beneath both extinct (Bjarnason et al., 1993; Darbyshire et al., 1998; Du and Foulger, 1999), and active (Gudmundsson et al., 1994; Brandsdóttir et al., 1997; Obermann et al., 2016; Jeddi et al., 2016) central volcanoes in Iceland as well as other volcanoes, e.g. Mt. Etna, Italy (Chiarabba et al., 2000; Aloisi et al., 2002) and Kilauea, Hawaii (Okubo et al., 1997). In the fore mentioned studies such high-velocity zones have been explained by the presence of cumulates and intrusive crystalline rocks.

Our data do not require a zone of molten material underneath the summit of Eyjafjallajökull. Undershooting experiments in Krafla and Katla volcanoes, Iceland, resulted in S-wave shadows, revealing a magma chamber at the top of a high-velocity anomaly (Brandsdóttir et al., 1997; Gudmundsson et al., 1994). The depth resolution of our shear velocity model inhibits us from stating anything about a magma chamber, but should there be one, it is most likely located within the low-velocity zone. As discussed above, the seismicity accompanying the 2010 outburst, was largely located within the low-velocity zone.

Two types of stress fields seem to dominate the region around Eyjafjallajökull. First, a local stress field with a maximum tensile stress direction pointing north which is evident from the east-west elongation of the high-velocity zones and surface structures on Eyjafjallajökull, which consist of east-west oriented hyaloclastic ridges and surface faults (Fig. 1) (Jóhannesson et al., 1990; Jónsson, 1998; Einarsson and Hjartardóttir, 2015). Einarsson and Hjartardóttir (2015) argue that the E-W orientation can be explained by the build up of the Eyjafjallajökull volcano on an old location of the insular shelf of Iceland; having more support to the north than the south. Second, a stress field caused by the large-scale tectonics in the area with a maximum tensile stress direction pointing NW-SE (Ziegler et al., 2016). The large-scale regional field gives rise to structures with a NE-SW orientation such as the Eastern Volcanic Zone (Einarsson, 2008). The NE-SW trend of the low-velocity zone and the NE-SW sub-vertical dikes emplaced prior to the 2010 flank eruption (Tarasewicz et al., 2012a) could be explained by these forces. However, these structures are on a small-scale and, therefore, other minor forces, such as radial stresses emanating from the caldera, should not be excluded.

5. Conclusions

We have resolved the uppermost crustal structure of the Eyjafjallajökull volcano using ambient noise tomography with a lateral resolution of about 5 km. Three prominent velocity anomalies are

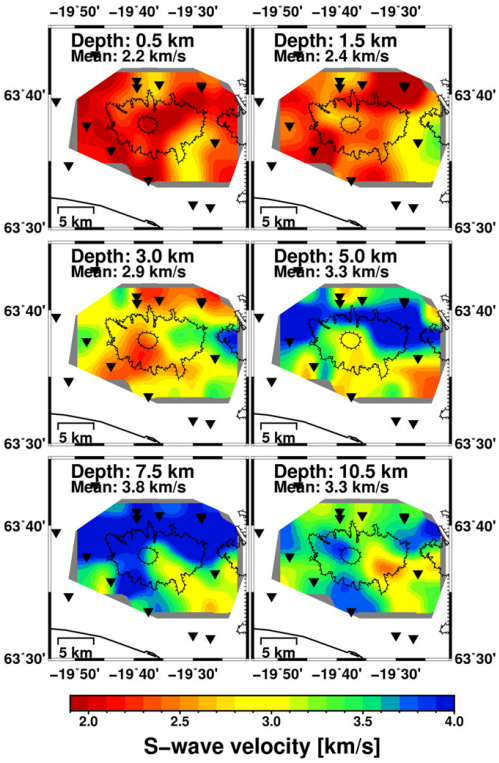

Fig. 11. Depth slices with a first order correction to topography. Mean velocities for each layer are indicated. Inverted black triangles are seismic stations.

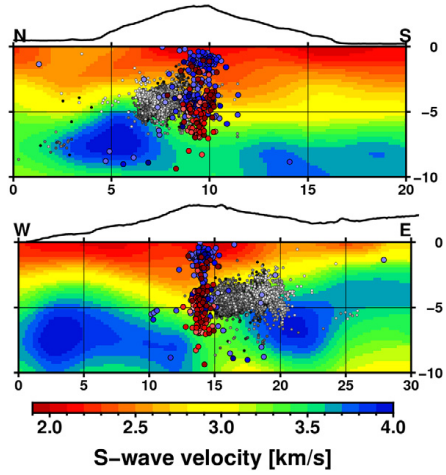

Fig. 12. Vertical S-wave velocity profiles for the first order topography corrected model. The location of the cross sections are shown as blue lines in Fig. 1. Upper and lower panels are N-S and East-West cross sections, respectively. The black lines show the topography. Gray, blue and red circles are earthquakes from March 5th–20th, April 13th–14th, and May 2010 respectively; all color codes progress from early (light) to late (dark), during the indicated time span of each dataset.

modeled within the uppermost 10 km; a low-velocity zone stretching southwest from underneath the caldera, and two east-west trending high-velocity zones (Fig. 12), interpreted as large intrusive bodies or magma cumulates. In between the high-velocity zones lies a narrow zone, of relatively low velocity, which coincides with the locations of earthquakes during the summit eruption in Eyjafjallaökull, possibly indicating the magma pathway from a deeper source. The east-west orientation of the high-velocity zones agree with other geological features in Eyjafjallajökull and we interpret this as further evidence for the N-S orientation of the local maximum tensile forces in the area.

Acknowledgments

This work was a part of the Volcano Anatomy project funded by the Icelandic Research Fund. We thank Martin Hensch, Sveinbjörn Steinthórsson, Thorsteinn Jónsson, Benedikt Ófeigsson, Björn Lund, and the helicopter crew of the Icelandic Coast Guard for help with deploying and maintaining seismometers around Eyjafjallajökull. We are indebted to the Icelandic Meteorological Office for providing data from their permanent network monitoring network and John Tarasewicz for providing us with earthquake locations. The data analysis was partly done with software made available by Robert Herrmann (Computer programs in Seismology) and Nick Rawlinson (Fast Marching inversion code). We thank Freysteinn Sigmundsson for his constructive reviews which greatly improved the manuscript. The majority of the figures was created using the Generic Mapping Tools (Wessel et al., 2013).

References

Albino, F., Sigmundsson, F., 2014. Stress transfer between magma bodies: influence of intrusions prior to 2010 eruptions at Eyjafjallajökull volcano, Iceland. J.Geophys. Res. 119, 2964–2975.

Aloisi, M., Cocina, O., Neri, G., Orecchio, B., Privitera, E., 2002. Seismic tomography of the crust underneath the Etna volcano, Sicily. Phys. Earth Planet. Int. 134, 139–155.

Ballmer, S., Wolfe, C., Okubo, P., Haney, M., Thurber, C., 2013. Ambient seismic noise interferometry in Hawai'i reveals long-range observability of volcanic tremor. Geophys. J. Int.ggt112.

Bensen, G., Ritzwoller, M., Barmin, M., Levshin, A., Lin, F., Moschetti, M., Shapiro, N., Yang, Y., 2007. Processing seismic ambient noise data to obtain reliable broad-band surface wave dispersion measurements. Geophys. J. Int. 169, 1239–1260.

Bjarnason, I., Menke, W., Flóvenz, Ó.G., Caress, D., 1993. Tomographic image of the mid-Atlantic plate boundary in southwestern Iceland. J. Geophys. Res. 98, 6607–6622.

Boschi, L., Weemstra, C., Verbeke, J., Ekström, G., Zunino, A., Giardini, D., 2012. On measuring surface wave phase velocity from station-station cross-correlation of ambient signal. Geophys. J. Int. 192, 346–358.

Brandsdóttir, B., Menke, W., Einarsson, P., White, R., Staples, R., 1997. Färoe-Iceland Ridge Experiment 2. Crustal structure of the Krafla central volcano. J. Geophys. Res. 102, 7867–7886.

Brenguier, F., Shapiro, N., Campillo, M., Nercessian, A., Ferrazzini, V., 2007. 3-D surface wave tomography of the Piton de la Fournaise volcano using seismic noise correlations. Geophys. Res. Lett. 34,

Campillo, M., Paul, A., 2003. Long-range correlations in the diffuse seismic coda. Science 299, 547–549.

Chiarabba, C., Amato, A., Boschi, E., Barberi, F., 2000. Recent seismicity and tomographic modeling of the Mount Etna plumbing system. J. Geophys. Res. 105, 10923–10938.

Dahm, T., Brandsdóttir, B., 1997. Moment tensors of microearthquakes from the Eyjafjallajökull volcano in South Iceland. Geophys. J. Int. 130, 183–192.

Darbyshire, F., Bjarnason, I., White, R., Flóvenz, Ó.G., 1998. Crustal structure above the Iceland mantle plume imaged by the ICEMELT refraction profile. Geophys. J. Int. 135, 1131–1149.

Derode, A., Larose, E., Tanter, M., De Rosny, J., Tourin, A., Campillo, M., Fink, M., 2003. Recovering the Green's function from field-field correlations in an open scattering medium. J. Acoust. Soc. Am. 113, 2973–2976.

Du, Z., Foulger, G., 1999. The crustal structure beneath the northwest fjords, Iceland, from receiver functions and surface waves. Geophys. J. Int. 139, 419–432.
Einarsson, P., 2008. Plate boundaries, rifts and transforms in Iceland. Jökull 58, 35–58.
Einarsson, P., Hjartardóttir, Á., 2015. Structure and tectonic position of the Eyjafjallajökull volcano, S. Iceland. Jökull 65,
Ekström, G., Abers, G.A., Webb, S.C., 2009. Determination of surface-wave phase velocities across USArray from noise and Aki's spectral formulation. Geophys. Res. Lett. 36,
Gao, H., Shen, Y., 2015. A preliminary full-wave ambient-noise tomography model spanning from the Juan de Fuca and Gorda spreading centers to the Cascadia volcanic arc. Seis. Res. Lett. 86, 1253–1260.
Green, R.G., Priestley, K.F., White, R.S., 2017. Ambient noise tomography reveals upper crustal structure of Icelandic rifts. Earth Planet. Sci. Lett. 466, 20–31.
Greenfield, T., White, R., Roecker, S., 2016. The magmatic plumbing system of the Askja central volcano, Iceland, as imaged by seismic tomography. J. Geophys. Res. 121, 7211–7229.
Gudmundsson, M., Pedersen, R., Vogfjörd, K., Thorbjarnardóttir, B., Jakobsdóttir, S., Roberts, M., 2010. Eruptions of Eyjafjallajökull volcano, Iceland. Eos, Transactions American Geophysical Union 91, 190–191.
Gudmundsson, O., Brandsdottir, B., Menke, W., Sigvaldason, G., 1994. The crustal magma chamber of the Katla volcano in south Iceland revealed by 2-D seismic undershooting. Geophys. J. Int. 119, 277–296.
Gudmundsson, Ó., Khan, A., Voss, P., 2007. Rayleigh-wave group-velocity of the Icelandic crust from correlation of ambient seismic noise. Geophys. Res. Lett. 34,
Haned, A., Stutzmann, E., Schimmel, M., Kiselev, S., Davaille, A., Yelles-Chaouche, A., 2016. Global tomography using seismic hum. Geophys. J. Int. 204, 1222–1236.
Herrmann, R., 1973. Some aspects of band-pass filtering of surface waves. Bull. Seis. Soc. Am. 63, 663–671.
Herrmann, R., 2013. Computer programs in seismology: an evolving tool for instruction and research. Seis. Res. Lett. 84, 1081–1088.
Herrmann, R., Ammon, C., 2002. Computer Programs in Seismology: Surface Waves, Receiver Functions and Crustal Structure. St. Louis University, St. Louis, MO.
Hjaltadóttir, S., Vogfjörd, K.S., Hreinsdóttir, S., Slunga, R., 2015. Reawakening of a volcano: activity beneath Eyjafjallajökull volcano from 1991 to 2009. J. Vol. Geoth. Res. 304, 194–205.
Hjaltadóttir, S., et al. 2012. 2010 pre-eruption phase. In: Thorkelsson, B. (Ed.), The 2010 Eyjafjallajökull Eruption, Iceland. A Report to the International Civil Aviation Organization (ICAO). Icelandic Meterological Office; Institute of Earth Sciences, University of Iceland; The National Commissioner of the Icelandi Police., pp. 54–65.
Hooper, A., Pedersen, R., Sigmundsson, F., 2009. Constraints on magma intrusion at Eyjafjallajökull and Katla volcanoes in Iceland, from time series SAR interferometry. In: Bean, C., Braiden, A., Lokmer, I., Martini, F., O'Brien, G. (Eds.), The VOLUME Project-Volcanoes: Understanding Subsurface Mass Movement. pp. 13–24.
Jakobsson, S., 1979. Petrology of recent basalts of the Eastern Volcanic Zone, Iceland. Acta. Nat. Islandica 1–103.
Jay, J.A., Pritchard, M., West, M., Christensen, D., Haney, M., Minaya, E., Sunagua, M., McNutt, S., Zabala, M., 2012. Shallow seismicity, triggered seismicity, and ambient noise tomography at the long-dormant Uturuncu Volcano, Bolivia. Bull. Vol. 74, 817–837.
Jeddi, Z., Tryggvason, A., Gudmundsson, O., 2016. The Katla Volcanic system imaged using local earthquakes recorded with a temporary seismic network. J. Geophys. Res. 102,
Jóhannesson, H., Jakobsson, S., Sæmundsson, K., 1990. Geological Map of Iceland, Sheet 6, South-Central Iceland. third, Institute of Natural History and Icelandic Geodetic Survey.
Jónsdóttir, K., Tryggvason, A., Roberts, R., Lund, B., Soosalu, H., Bödvarsson, R., 2007. Habits of a glacier-covered volcano: seismicity patterns and velocity structure of Katla volcano, Iceland. Ann. Glaciol. 45, 169–177.
Jónsson, B., 1774. Annalar Thess Froma og velvitra Sauluga Biørns Jonssonar a Skardsau Fordum Løgrettumanns i Hegranes-sýslu. Skardsárannáll., pp. 186.Available at: http://baekur.is/bok/000043701/Annalar_THess_froma_og.
Jónsson, J., 1998. Eyjafj "oll, drög a jardfrædi (Eyjafjöll,Geological overview, in Icelandic). Research Station Nedri Ás, Hveragerdi, Iceland.
Kaban, M.K., Flóvenz, Ó.G., Pálmason, G., 2002. Nature of the crust-mantle transition zone and the thermal state of the upper mantle beneath Iceland from gravity modelling. Geophys. J. Int. 149, 281–299.
Keiding, J., Sigmarsson, O., 2012. Geothermobarometry of the 2010 Eyjafjallajökull eruption: new constraints on Icelandic magma plumbing systems. J. Geophys. Res. 117,
Köhler, A., Weidle, C., Maupin, V., 2012. On the effect of topography on surface wave propagation in the ambient noise frequency range. J. Seis. 16, 221–231.
Korostelev, F., Weemstra, C., Leroy, S., Boschi, L., Keir, D., Ren, Y., Molinari, I., Ahmed, A., Stuart, G., Rolandone, F., et al. 2015. Magmatism on rift flanks: insights from ambient noise phase velocity in Afar region. Geophys. Res. Lett. 42, 2179–2188.
LaFemina, P., Dixon, T.H., Malservisi, R., Árnadóttir, T., Sturkell, E., Sigmundsson, F., Einarsson, P., 2005. Geodetic GPS measurements in south Iceland: strain accumulation and partitioning in a propagating ridge system. J. Geophys. Res. 110,
Larsen, G., Dugmore, A., Newton, A., 1999. Geochemistry of historical-age silicic tephras in Iceland. The Holocene 9, 463–471.
Lay, T., Kanamori, H., 1985. Geometric effects of global lateral heterogeneity on long-period surface wave propagation. J. Geophys. Res. 90, 605–621.
Lin, F., Moschetti, M., Ritzwoller, M., 2008. Surface wave tomography of the western United States from ambient seismic noise: Rayleigh and Love wave phase velocity maps. Geophys. J. Int. 173, 281–298.
Lobkis, O., Weaver, R., 2001. On the emergence of the Green's function in the correlations of a diffuse field. J. Acoust. Soc. Am. 110, 3011–3017.
Luo, Y., Yang, Y., Xu, Y., Xu, H., Zhao, K., Wang, K., 2015. On the limitations of interstation distances in ambient noise tomography. Geophys. J. Int. 201, 652–661.
Ma, S., Prieto, G., Beroza, G., 2008. Testing community velocity models for southern California using the ambient seismic field. Bull. Seismol. Soc. Am. 98, 2694–2714.
Masterlark, T., Haney, M., Dickinson, H., Fournier, T., Searcy, C., 2010. Rheologic and structural controls on the deformation of Okmok volcano, Alaska: FEMs, InSAR, and ambient noise tomography. J. Geophys. Res. 115,
Matos, C., Silveira, G., Matias, L., Caldeira, R., Ribeiro, M., Dias, N., Krüger, F., dos Santos, T., 2015. Upper crustal structure of Madeira Island revealed from ambient noise tomography. J. Vol. Geoth. Res. 298, 136–145.
Miensopust, M., Jones, A., Hersir, G., Vilhjálmsson, A., 2014. The Eyjafjallajökull volcanic system, Iceland: insights from electromagnetic measurements. Geophys. J. Int. 199, 1187–1204.
Moschetti, M., Ritzwoller, M., Shapiro, N., 2007. Surface wave tomography of the western United States from ambient seismic noise: Rayleigh wave group velocity maps. Geochem. Geophys. Geosys. 8,
Nagaoka, Y., Nishida, K., Aoki, Y., Takeo, M., Ohminato, T., 2012. Seismic imaging of magma chamber beneath an active volcano. Earth. Planet. Sci. Lett. 333, 1–8.
Nishida, K., Montagner, J.P., Kawakatsu, H., 2009. Global surface wave tomography using seismic hum. Science 326, 112–112.
Obermann, A., Lupi, M., Mordret, A., Jakobsdóttir, S., Miller, S., 2016. 3D-ambient noise Rayleigh wave tomography of Snæfellsjökull volcano, Iceland. J. Vol. Geoth. Res. 317, 42–52.
Okubo, P., Benz, H., Chouet, B., 1997. Imaging the crustal magma sources beneath Mauna Loa and Kilauea volcanoes, Hawaii. Geology 25, 867–870.
Óskarsson, B.V., 2009. The Skerin Ridge on Eyjafjallajökull, South Iceland: Morphology and Magma-Ice Interaction in an Ice-confined Silicic Fissure Eruption. Master's Thesis. Faculty of Earth Sciences, University of Iceland.Available at: http://hdl.handle.net/1946/4375.
Pedersen, R., Sigmundsson, F., 2004. InSAR based sill model links spatially offset areas of deformation and seismicity for the 1994 unrest episode at Eyjafjallajökull volcano, Iceland. Geophys. Res. Lett. 31,
Pedersen, R., Sigmundsson, F., 2006. Temporal development of the 1999 intrusive episode in the Eyjafjallajökull volcano, Iceland, derived from InSAR images. Bull. Volcanol. 68, 377–393.
Rawlinson, N., Sambridge, M., 2005. The fast marching method: an effective tool for tomographic imaging and tracking multiple phases in complex layered media. Explor. Geophys. 36, 341–350.
Sadeghisorkhani, H., Gudmundsson, O., Roberts, R., Tryggvason, A., 2016. Mapping the source distribution of microseisms using noise covariogram envelopes. Geophys. J. Int. 205, 1473–1491.
Sadeghisorkhani, H., Gudmundsson, Ó., Roberts, R., Tryggvason, A., 2017. Velocity-measurement bias of the ambient noise method due to source directivity: a case study for the Swedish National Seismic Network. Geophys. J. Int. 209, 1648–1659.
Schuler, J., Greenfield, T., White, R., Roecker, S., Brandsdóttir, B., Stock, J., Tarasewicz, J., Martens, H.R., Pugh, D., 2015. Seismic imaging of the shallow crust beneath the Krafla central volcano, NE Iceland. J. Geophys. Res. 120, 7156–7173.
Shapiro, N., Campillo, M., Stehly, L., Ritzwoller, M., 2005. High-resolution surface-wave tomography from ambient seismic noise. Science 307, 1615–1618.
Shapiro, N.M., Campillo, M., 2004. Emergence of broadband Rayleigh waves from correlations of the ambient seismic noise. Geophys. Res. Lett. 31,
Sigmarsson, O., Vlastelic, I., Andreasen, R., Bindeman, I., Devidal, J., Moune, S., Keiding, J., Larsen, G., Höskuldsson, A., Thordarson, T., 2011. Remobilization of silicic intrusion by mafic magmas during the 2010 Eyjafjallajökull eruption. Solid Earth 2, 271–281.
Sigmundsson, F., Hreinsdóttir, S., Hooper, A., Árnadóttir, T., Pedersen, R., Roberts, M., Óskarsson, N., Auriac, A., Decriem, J., Einarsson, P., et al. 2010. Intrusion triggering of the 2010 Eyjafjallajokull explosive eruption. Nature 468, 426–430.
Spica, Z., Legrand, D., Iglesias, A., Walter, T., Heimann, S., Dahm, T., Froger, J., Rémy, D., Bonvalot, S., West, M., et al. 2015. Hydrothermal and magmatic reservoirs at Lazufre volcanic area, revealed by a high-resolution seismic noise tomography. Earth Planet. Sci. Lett. 421, 27–38.
Stankiewicz, J., Ryberg, T., Haberland, C., Natawidjaja, D., et al. 2010. Lake Toba volcano magma chamber imaged by ambient seismic noise tomography. Geophys. Res. Lett. 37,
Stehly, L., Campillo, M., Shapiro, N., 2006. A study of the seismic noise from its long-range correlation properties. J. Geophys. Res. 111,
Sturkell, E., Sigmundsson, F., Einarsson, P., 2003. Recent unrest and magma movements at Eyjafjallajökull and Katla volcanoes, Iceland. J. Geophys. Res. 108,
Tamura, J., Okada, T., 2016. Ambient noise tomography in the Naruko/Onikobe volcanic area, NE Japan: implications for geofluids and seismic activity. Earth, Planets and Space 68, 1–11.
Tarasewicz, J., White, R., Brandsdóttir, B., Thorbjarnardóttir, B., 2011. Location accuracy of earthquake hypocentres beneath Eyjafjallajökull, Iceland, prior to the 2010 eruptions. Jökull 61, 33–50.
Tarasewicz, J., Brandsdóttir, B., White, R., Hensch, M., Thorbjarnardóttir, B., 2012a. Using microearthquakes to track repeated magma intrusions beneath the Eyjafjallajökull stratovolcano, Iceland. J. Geophys. Res. 117,
Tarasewicz, J., White, R., Brandsdóttir, B., Schoonman, C., 2014. Seismogenic magma intrusion before the 2010 eruption of Eyjafjallajökull volcano, Iceland. Geophys. J. Int. 198, 906–921.

Tarasewicz, J., White, R., Woods, A., Brandsdóttir, B., Gudmundsson, M., 2012b. Magma mobilization by downward-propagating decompression of the Eyjafjallajökull volcanic plumbing system. Geophys. Res. Lett. 39,

Tryggvason, A., Rögnvaldsson, S., Flóvenz, O., 2002. Three-dimensional imaging of the P-and S-wave velocity structure and earthquake locations beneath Southwest Iceland. Geophys. J. Int. 151, 848–866.

Wapenaar, K., Slob, E., Snieder, R., Curtis, A., 2010. Tutorial on seismic interferometry: part 2 — underlying theory and new advances. Geophysics 75, 75A211–75A227.

Weaver, R., Lobkis, O., 2004. Diffuse fields in open systems and the emergence of the Green's function. J. Acoust. Soc. Am. 116, 2731.

Wessel, P., Smith, W., Scharroo, R., Luis, J., Wobbe, F., 2013. Generic Mapping Tools: improved version released. EOS Trans. AGU 94, 409–410.

Woodhouse, J., 1974. Surface waves in a laterally varying layered structure. Geophys. J. Int. 37, 461–490.

Ziegler, M., Rajabi, M., Heidbach, O., Hersir, G., Ágústsson, K., Árnadóttir, S., Zang, A., 2016. The stress pattern of Iceland. Tectonophysics 674, 101–113.

Paper III

Volcanic tremor of the 2010 Eyjafjallajökull eruption

Ásdís Benediktsdóttir, Ólafur Gudumundsson, Ka Lok Li, Bryndís Brandsdóttir

Geophysical Journal International, in preparation, 2019

submitted to *Geophys. J. Int.*

Volcanic tremor of the 2010 Eyjafjallajökull eruption

Ásdís Benediktsdóttir[0,1⋆], Ólafur Gudmundsson[2], Ka Lok Li[2,3], Bryndís Brandsdóttir[0]

[0] *Nordic Volcanological Center, Institute of Earth Sciences, University of Iceland, Iceland*

[1] *Iceland Geosurvey, Iceland*

[2] *Department of Earth Sciences, Uppsala University, Sweden*

[3] *Geophysics Section, School of Cosmic Physics, Dublin Institute for Advanced Studies, Dublin, Ireland*

Received in the year of our lord MMXIX

SUMMARY

The 2010 summit eruption of Eyjafjallajökull, from April 14^{th} to May 22^{nd} 2010, had associated continuous volcanic tremor that varied considerably during the course of the eruption, following changes in eruptive style. The tremor had power at frequencies between 0.5 and 10 Hz, with increased tremor activity during an effusive-explosive phase, in comparison to purely explosive phases. The tremor was located using a method based on differential phase information extracted from inter-station correlograms. The location was found to be stable near the eruption vent, through time, for signals between 0.5 Hz and 2 Hz. Tremor bursts early in the eruption, related to flood-water measurements, are caused by processes at the eruption site. Analyses of power variations of the vertical component of the tremor with distance from the eruption site are consistent with tremor waveform content being dominated by surface waves in the 0.5-2 Hz frequency ranges. The tremor source was constrained to be shallow, less than about 1 km. The attenuation quality factor (Q) was found to be on the order of Q = 10-20 for paths in the area around Eyjafjallajökull and Q = 20-50 for paths outside the volcano. The pattern of radiated wave energy from the tremor source varied with time, defining ten different epochs during the eruption. Thus the tremor-source radiation did not remain isotropic, which

needs to be considered when locating tremor based on amplitude, i.e. azimuthally variable source radiation.

Key words: Volcanic tremor, Eyjafjallajökull, Iceland, Volcano seismology

1 INTRODUCTION

Understanding the mechanics and behavior of a volcano forms the basis for managing the risk associated with it. Although both geophysical and geochemical monitoring methods have advanced substantially in recent years, detailed understanding of magmatic signals emitted by active volcanoes, is still limited. Elevated levels of seismicity beneath volcanoes have long been interpreted as evidence of magma accumulation or migration. Accurate locations of seismic signals originating within an active volcano are important to track movements of magma at depth as well as the propagation of shallow magmatic dikes and sills (e.g. *Tarasewicz et al.*, 2012a; *Ágústsdóttir et al.*, 2016, and references therein). However, whilst seismicity is frequently a powerful indicator of eruption risk, earthquake patterns differ from one volcano to another.

An abrupt decrease of volcano-tectonic seismicity at the initiation of continuous volcanic tremor has been repeatedly observed at the beginning of volcanic eruptions in Iceland, e.g., Surtsey 1963, Heimaey 1973, Krafla during 1975-1984, Hekla 1970, 1980, 1991 and 2000, Bárdarbunga-Gjálp 1996, Grímsvötn 1998, 2004 and 2010 (*Sigtryggsson and Sigurdsson*, 1966; *Thorarinsson et al.*, 1973; *Einarsson et al.*, 1997; *Soosalu and Einarsson*, 2005; *Vogfjörd et al.*, 2005; *Pedersen et al.*, 2007; *Jakobsdóttir*, 2008; *Tarasewicz et al.*, 2012b; *Eibl et al.*, 2017; *Einarsson*, 2018). While earthquakes have been clearly related to both lateral and vertical dike propagation, the physical origin of volcanic tremor is not well understood.

Volcanic tremor is a signal recorded at seismic stations in the vicinity of volcanoes and hydrothermal areas. The characteristics of volcanic tremor vary, not only from one volcano to another, but also between eruptions of the same volcano (e.g. *Hofstetter and Malone*, 1986). For a comprehensive overview of volcanic tremor, see *Konstantinou and Schlindwein* (2003). Although

⋆ Email: ab@isor.is

the cause of volcanic tremor is not always the same, it is usually attributed to magma movement related to ongoing processes at a volcano at any given time. Therefore, analyses of tremor can give valuable insights into magma dynamics within a volcano.

Konstantinou and Schlindwein (2003) defined volcanic tremor as "a persistent seismic signal that is observed only near active volcanoes, lasting from several minutes to several days, preceding and/or accompanying most volcanic eruptions" (*Fehler*, 1983; *Julian*, 1994; *Ripepe*, 1996; *Métaxian et al.*, 1997). Volcanic tremor is usually attributed to fluid movement within the volcano. Such signals have been modeled as: fluid-filled tensile-cracks (*Aki et al.*, 1977), in which tremor is produced by an excess pressure in the magma that results in a jerky opening of the crack; as a nonlinear excitation by fluid flow (*Julian*, 1994); as an acoustic resonance of a fluid-filled volcanic pipe triggered by excess gas pressure (*Chouet*, 1985); and as a continuous bursting of small gas bubbles in the upper part of the magmatic column (*Ripepe*, 1996).

The character of tremor signals varies; it can be characterized by a fundamental frequency and its harmonics (e.g. Mt. Semeru, *Schlindwein et al.*, 1995), a monochromatic peak (e.g. Mt. Ruapehu *Hurst*, 1992), tremor bursts with quiescence in between (e.g. Mt. Miyakejima *Fujita*, 2008), continuous tremor with varying amplitude (e.g. Mt. Krafla *Brandsdóttir and Einarsson*, 1992) or by a series of long-period earthquakes that occur so densely in time that they merge into a continuous tremor signal (*Neuberg et al.*, 2000; *Baptie et al.*, 2002). These are only a few examples of how volcanic tremor has been classified.

Locating volcanic tremor is not possible using standard arrival time methods as it does usually not have a clear onset. There are a few exceptions (*Aki et al.*, 1977; *Fehler*, 1983). Also, the heterogeneity of volcanoes and potentially strong site effects (e.g. topography) add to the complexity of the location problem. Therefore, other techniques have been developed to locate the tremor sources. These include analysis of amplitude decay of the signal with distance from the source (e.g. *Gottschämmer and Surono*, 2000; *Battaglia and Aki*, 2003; *Di Grazia et al.*, 2006), where the source is assumed to radiate isotropically. If the source behaves as such, the method works well. However, this is not always the case, as in the 2010 Eyjafjallajökull summit eruption, reported in this paper.

Exploiting differential-phase information by waveform-semblance and beam-forming methods across a dense array of seismographs (e.g. *Furumoto et al.*, 1990, 1992; *Wassermann*, 1997; *Eibl et al.*, 2017) or by cross correlating adjacent recordings of tremor (*Gudmundsson and Brandsdóttir*, 2010; *Ballmer et al.*, 2013; *Droznin et al.*, 2015; *Li et al.*, 2017a,b; *Sgattoni et al.*, 2017) has proven to work well in several areas in order to locate tremor sources. In the former, the direction to the source and wave velocity or slowness are determined. In the latter, the time series from two seismographs in the vicinity of the tremor source(s) are cross-correlated to reveal the signal at the time delay that corresponds to the differential distance from the dominant source to the two receivers. If the tremor contains significant surface-wave energy and a suitable surface-wave speed is used, the correlograms can be back projected two dimensionally and stacked to reveal an image map of possible source locations (*Li et al.*, 2017b).

Here we analyse tremor associated with the 2010 Eyjafjallajökull summit eruption. First, tremor is located with a probabilistic inference method based on intra-station correlograms. Second, the power-spectral amplitude of the tremor is analysed to estimate wave attenuation, the geometrical spreading of the tremor waves and station corrections combining propagation and site effects. Spectral amplitudes relative to a fixed reference station vary with time indicating that the power-radiation pattern of the source varies with time.

2 EYJAFJALLAJÖKULL VOLCANO

Eyjafjallajökull is a 1651 metre high east-west oriented stratovolcano (Figure 1), partly covered by a glacier. It is located in southern Iceland, next to the subglacal Katla volcano. It extends 25 km in the east-west direction, 15 km in the north-south direction, and its southern cliffs lie only a few kilometers from Iceland's southern coastline. Its caldera is small, only 2.5 km wide, and ice filled.

In the past 30 years, four periods of unrest have taken place in Eyjafjallajökull. In 1994 and 1999-2000 earthquakes and uplift were recorded and modeled as two horizontal sill intrusions (*Dahm and Brandsdóttir*, 1997; *Sturkell et al.*, 2003; *Pedersen and Sigmundsson*, 2004, 2006; *Hooper et al.*, 2009) and in 1996 a deep earthquake swarm at 20-25 km depth was detected (*Hjaltadóttir et al.*, 2015). Two eruptions took place in 2010, first an effusive eruption at Fimmvörduháls

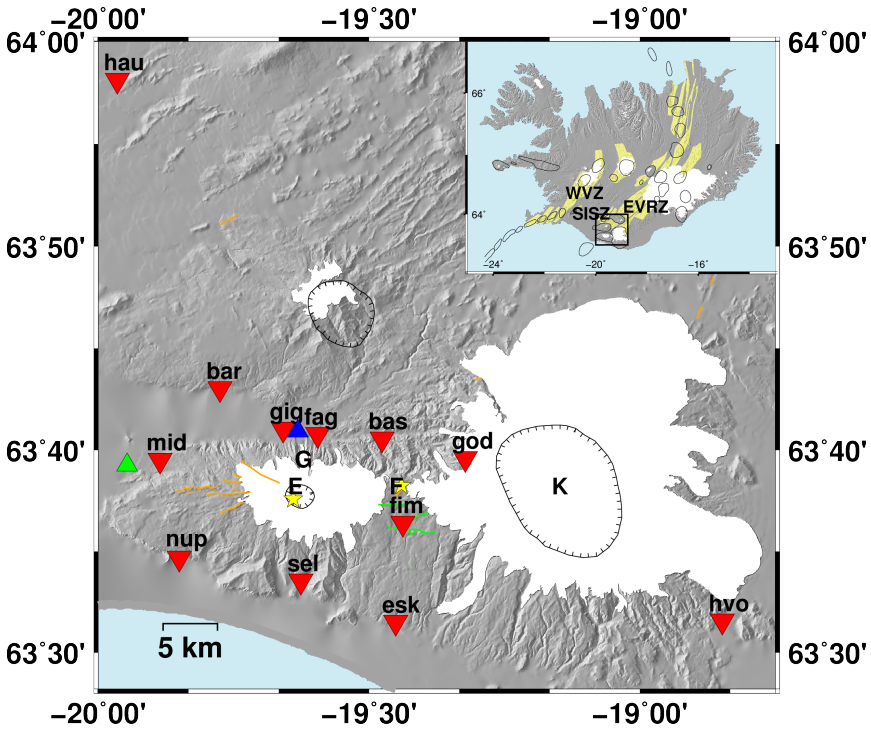

Figure 1. Observation sites and setting of Eyjafjallajökull. Red inverted triangles are seismic stations, green and blue triangles are the Markarfljót and Gígjökulsárlón flood gauges, respectively, and solid and hatched lines are outlines of central volcanic systems and calderas, respectively. E=Eyjafjallajökull, F=Fimmvörduháls, K=Katla, G=Gígjökull. Yellow stars indicate locations of the eruption sites of the flank eruption on Fimmvörduháls and the summit eruption of Eyjafjallajökull. Orange and green lines are eruptive fissures and faults, respectively (data compiled by *Einarsson and Hjartardóttir* (2015), see references therein).

on the eastern flank of the volcano (F in Figure 1), then a mostly explosive eruption in the summit caldera of Eyjafjallajökull (E in Figure 1). Prior to the two eruptions uplift and enhanced seismicity were recorded (*Sigmundsson et al.*, 2010; *Tarasewicz et al.*, 2011, 2012b, 2014).

Four known eruptions have occurred in Eyjafjallajökull during the past 1200 years, including the most recent in 2010. In the 10^{th} century a trachytic lava eruption with mafic and silicic tephra components formed the NW trending Skerin ridge (*Óskarsson*, 2009) about 2 km WNW from the caldera. A poorly described eruption took place in 1612 or 1613 (*Jónsson*, 1774; *Larsen et al.*,

1999). A summit eruption between December 1821 and January 1823 produced highly silicic magma (*Larsen et al.*, 1999; *Gudmundsson et al.*, 2010).

In 2010, Eyjafjallajökull erupted explosively (e.g. *Sigmundsson et al.*, 2010) causing a disruption of air traffic across the North-Atlantic ocean. This eruption was preceded by earthquake activity and an effusive flank eruption at Fimmvörduháls.

3 DATA

The data used in this study come from 12 seismographs (see Figure 1), six of which (*bas*, *esk*, *god*, *mid*, *hvo*, *hau*) are a part of the SIL network operated by the Icelandic Meteorological Office (IMO) and six (*bar*, *fag*, *fim*, *gig*, *sel*, *nup*) were temporarily deployed by the Institute of Earth Sciences, University of Iceland. The station locations are listed in Table 1 together with their distance and azimuth from the summit eruption site. All stations were equipped with Lennartz 5 s seismometers except for station god that had a broadband GURALP CMG-3ESPC seismometer. The SIL stations record continuous data, with some short gaps due to data transmission problems, to a central recording facility. The temporary stations were all deployed before the beginning of the eruption, except for station bar that was deployed on May 9^{th}. Short gaps occurred at most of the temporary stations due to power outages. The recording history of the stations is apparent in Figure 2 showing their Z-component spectrograms throughout the eruption period. All stations were operated at 100 samples per second with GPS timing. All records were calibrated in physical units ($\mu m/s$) and the response of the single broadband instrument replaced by that of a Lennartz 5 s sensor. Further processing steps were taken in some parts of the analyses and they are described where applicable in subsequent text. In the body of this paper we present results based on the vertical (Z) component recordings of 11 seismographs. We do not use station gig in other than the initial analyses as it was dismantled two days into the eruption. Results based on the horizontal components are presented in Appendices.

Table 1. Station locations, distances and azimuths relative to the summit eruption site at (-19.6365,63.629) (*Magnússon et al.*, 2012).

Station	Longitude	Latitude	Elevation [m]	Dist. from eruption site [km]	Azimuth from eruption site Degrees east of north
bas	63.67570	-19.47592	300	9.5	56
bar	63.71702	-19.77526	130	11.9	326
esk	63.52503	-19.45080	100	14.7	140
fag	63.67951	-19.59486	200	6.0	21
fim	63.60665	-19.43766	860	10.1	102
god	63.65976	-19.32236	1200	15.9	77
gig	63.68388	-19.65865	162	6.2	350
hau	63.52610	-18.84781	200	40.6	337
hvo	63.96851	-19.96471	100	41.1	106
mid	63.65833	-19.88573	130	12.7	286
nup	63.57787	-19.85037	30	12.0	243
sel	63.55901	-19.62575	70	7.8	175

4 THE EYJAFALLAJÖKULL TREMOR

Tremor began at the onset of the 2010 Eyjafjallajökull summit eruption, continued throughout its entire time span (April 14^{th} to May 22^{nd} 2010) and faded out towards its end. It was characterised by a broad frequency range up to 10 Hz at stations close to the source, but exceeding background noise up to 2-3 Hz at stations 40 kilometers away (Figure 2). Time invariant spectral peaks appear as horizontal bands in the spectrograms in Figure 2, sometimes extending throughout the eruption period, e.g. at station nup at about 0.8 Hz. Spectral peaks are less clear when the power of the eruption declines, and do not correlate in frequency for all stations. This may be due to resonances in the propagation process.

Gudmundsson et al. (2012) divided the eruption into four phases based on a combination of various data sets, including tephra fallout data, tephra dispersal outside Iceland, and plume height. The timing and description of each phase is shown in Table 2.

The temporal evolution of tremor amplitude spanning the four phases of the eruption is shown

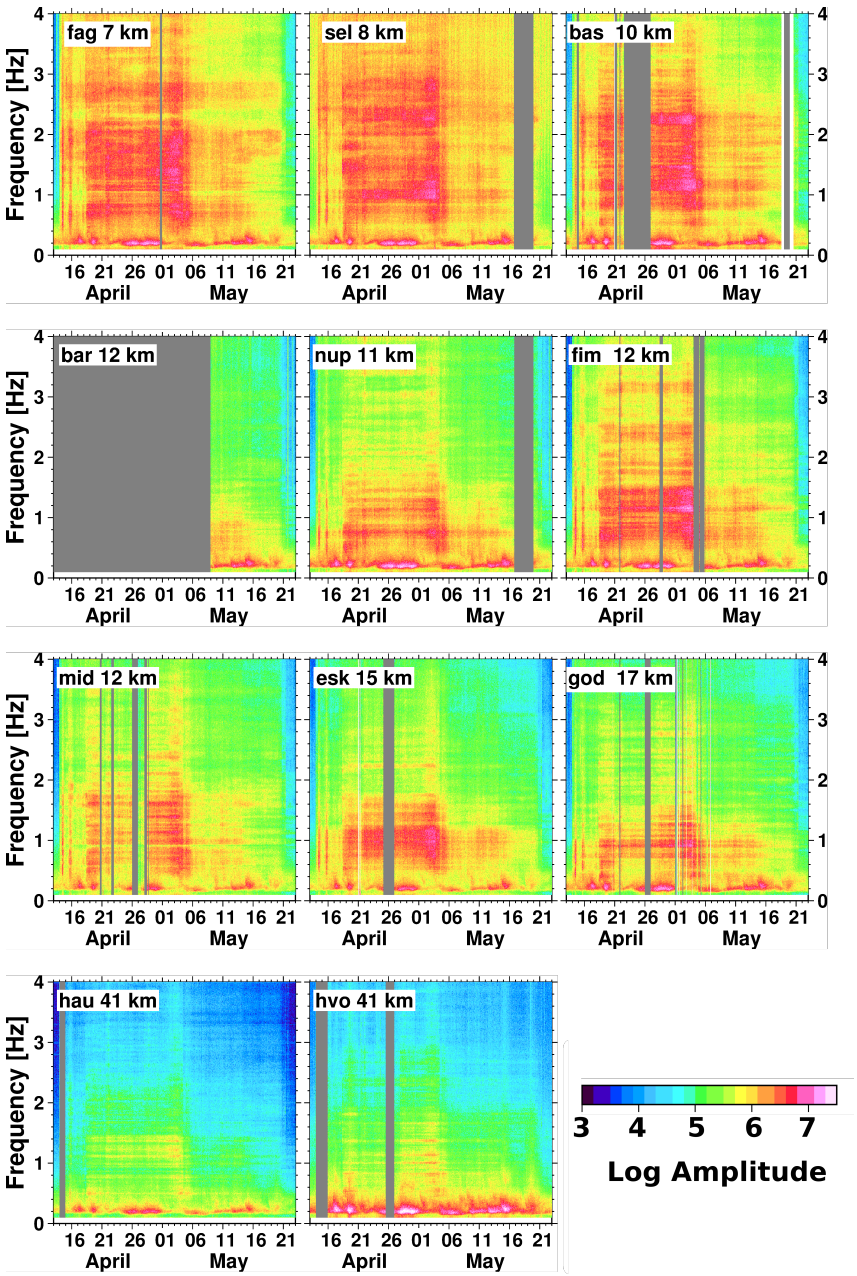

Figure 2. Z component spectrograms spanning the entire eruption period for all eleven stations used. The station name and distance from the eruption site is given in each frame

Table 2. Phases of the eruption as described by *Gudmundsson et al.* (2012)

Phase	Duration	Description
I	April 14-18	First explosive phase including several hours of jökullhlaups (meltwater floods) on April 14-15.
II	April 18-May 4	Effusive-explosive phase. Weak explosive activity and lava effusion as a 3 km long lava flow formed when magma flowed towards the north out of the caldera
III	May 5-17	Second explosive phasea. A new explosive phase with a change in melt composition.
IV	May 18-22	Final phase. The power from the eruption steadily decreased.

at four seismic stations (esk, fim, fag, nup) in Figure 3. Here the amplitude is the root-mean-square amplitude over one-hour time windows. The time evolution displays a distinct character within each phase of the eruption. During the first explosive phase (I) the tremor amplitude was highly variable. In particular two distinct and short-lived peaks are apparent in Figures 2 and 3 that occurred on April 14^{th} and late on April 15^{th} (see details in Figure 4).

During the 17-day long effusive-explosive phase II the amplitude of the tremor was high and relatively stable. The lava advanced slowly ($< 100m/day$) during April 18-26, thickening to 80-100 m under ice that was initially 150-200 m thick (*Oddsson et al.*, 2016). Subsequently, a more rapid advance (up to $500m/day$) formed a thinner (10-20 m) lava flow on the slopes outside the caldera where the ice was 60-100 m thick (*Oddsson et al.*, 2016). Interestingly, during the slow advance of the lava the tremor in the 0.5-1 Hz band decreased gradually, but during the faster advance of the lava, the tremor slowly increased again with time.

During the explosive phase III the tremor amplitude decayed steadily and during phase IV it dropped rapidly after an initial, short stable period.

The temporal evolution of the tremor during the first three days of the eruption is shown in Figure 4. The first signs of an imminent eruption was an intense microearthquake swarm at 22:30 on April 13^{th} (*Tarasewicz et al.*, 2012b; *Karlsdóttir et al.*, 2012) (1 in Figure 3), with earthquake locations clustered at 4-5 km depth within the caldera. Shortly after that, at 23:00, another microearthquake swarm started at about 1 km depth followed by elevated tremor levels (1a in Figure

4). As microearthquake activity ceased tremor levels became steady at approximately 1:10 on April 14^{th} (2 in Figure 4) and the eruption had started.

Magnússon et al. (2012) compiled the detailed course of events during the first few days of the eruption using SAR images, including observations of jökulhlaups (meltwater floods) associated with glacier melting. Four main tremor peaks are observed (A, B, C and D in Figure 4). These can also be seen in spectrograms (Figure 2) at the very beginning as two vertical bands. Discharge data (*Icelandic Meteoroglogical Office*, 2019a) from a gauge in Markarfljót (see location of the gauge in Figure 1) shows four main flood peaks (Figure 4). The first two flood peaks occurred on April 14^{th}, at about 11:20 and 19:10 for the first and second flood peaks, respectively. The third flow peak occurred at about 20:00 on April 15^{th} and the fourth one near midnight on April 16^{th}.

The time-lags between the tremor peaks and the flood peaks at Markarfljót were 2 hrs and 50 mins, 3 hrs and 30 mins, 3 hrs and 10 mins and 4 hrs for the four flood peaks, A, B, C and D. The onset of the third tremor peak was preceded by tremor pulses that grew in strength and culminated in tremor peak C.

According to *Magnússon et al.* (2012) the flood was observed to propagate from the lagoon in front of Gígjökull at 9:27 on April 14^{th}, which coincides with the onset of the first tremor peak (A) and matches a rapid increase of the water level at the gauge in front of Gígjökull (Figure 4 A). Therefore, the time lag between the onset of the tremor and the onset of the flow peaks at Markarfljót corresponds to the time it takes the jökullhaup to reach Markarfljót. However, the flood peaks observed at Markarfljót were not seen in the tremor data at nearby station mid. The discernible tremor peaks start at the same time at all stations. Therefore, recorded tremor must be dominated by processes near the common eruption source. Also, the tremor peaks vary in duration in a fashion that is not comparable to the flood peaks.

Figure 4C shows the tremor episode in tremor peak C. Periodic tremor peaks occur prior to the main burst, roughly every 12 minutes. Much of the energy is focused at 0.8 Hz, 1.4 Hz and 2.4 Hz, although it is distributed between 0.4 Hz and up to more than 10 Hz. The peaks start out with a small amplitude that increases until approximately 18:20 when a loud roar was heard (*Magnússon et al.*, 2012) and the floodwater most likely escaped and rushed down Gígjökull.

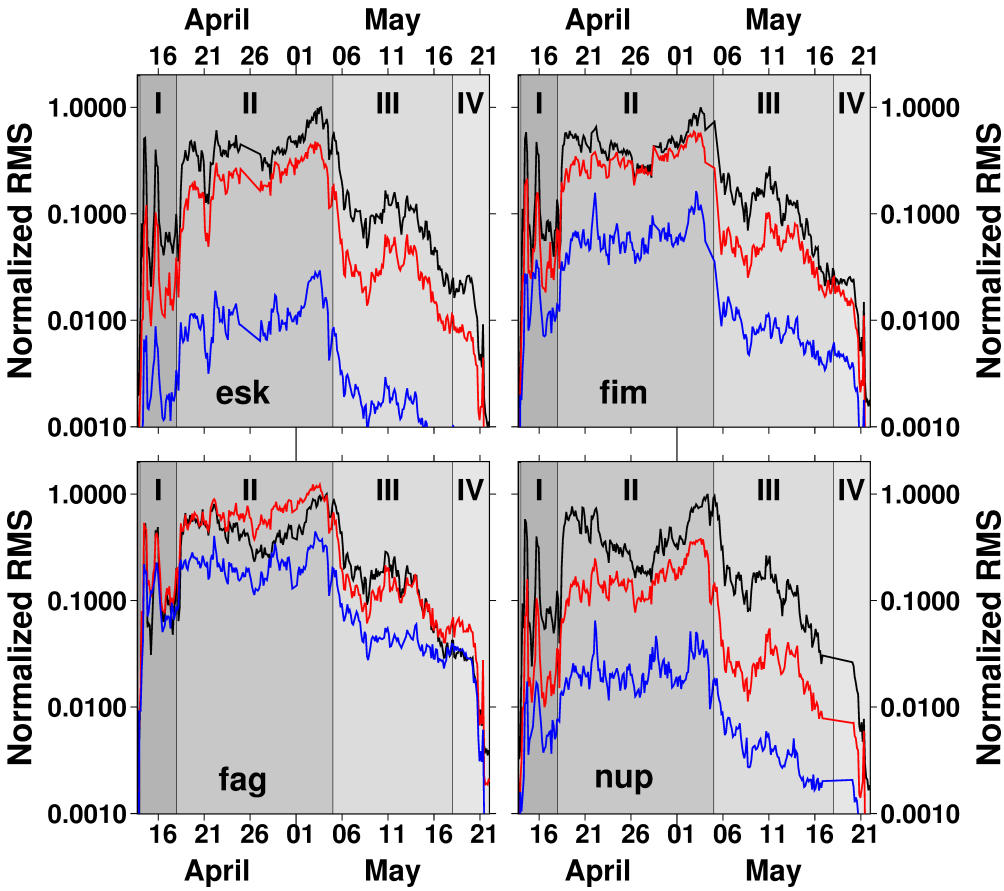

Figure 3. Semi-log plots of normalized one-hour-RMS amplitudes during the 2010 Eyjafjallajökull summit eruption for stations fag, nup, fim and esk for three different frequency ranges (0.5-1 Hz (black), 1-2 Hz (red) and 2-4 Hz (blue)), normalized by the maximumm amplitude of the 0.5-1 Hz frequency range. Four different phases, as defined by *Gudmundsson et al.* (2012), are indicated by gray shading (I - IV).

5 TREMOR LOCATION

5.1 Locating Tremor with probabilistic inference

Several methods, using differential-phase information and no clear onset as observed with earthquakes, have recently been presented in the literature to locate tremor-like signals. A number of

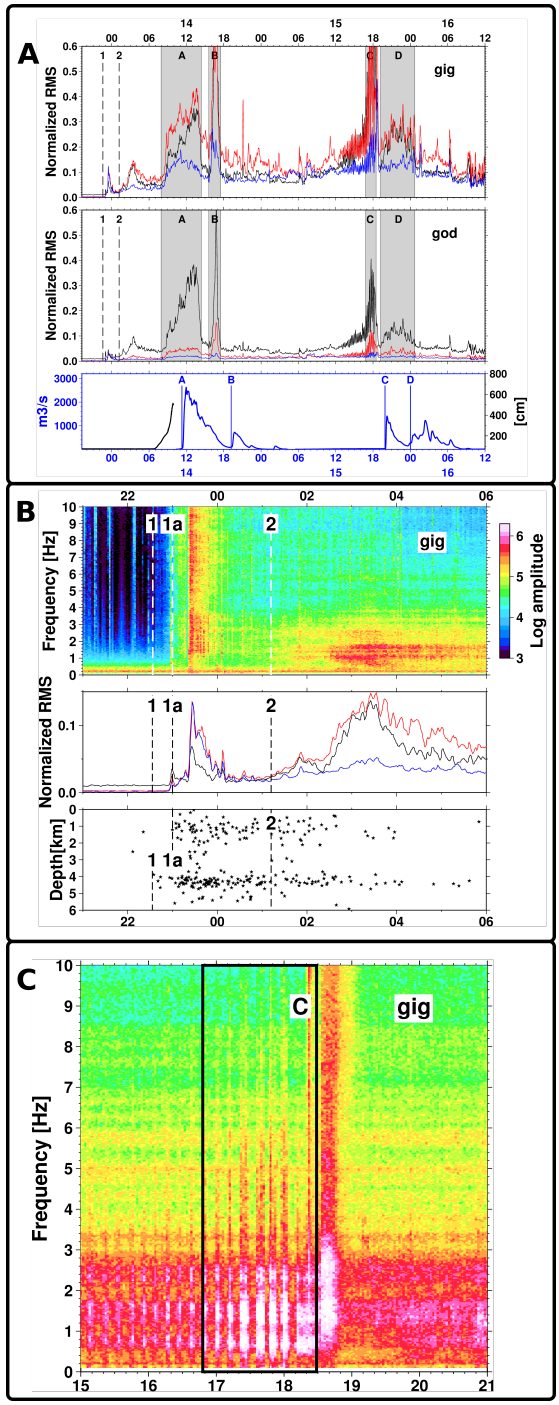

Figure 4. Caption next page.

Figure 4. (Previous page.) Course of events during the first 2 days of the eruption. **A** Root mean square amplitude over 2 minutes for stations gig (top) and god (middle) during the first 2.5 days of the eruption. Black, red and blue are the 0.5-1 Hz, 1-2 Hz and 2-4 Hz frequency bands, respectively, normalized by the maximum amplitude of the 0.5-1 Hz at station gig. Shaded areas indicate four tremor pulses observed, A-D. 1 and 2 refer to the onset of an microearthquake swarm and the onset of the eruption (*Karlsdóttir et al.* (2012)) when tremor levels increased considerably, respectively. The bottom panel shows flow data from a gauge in Markarfljót (*Icelandic Meteoroglogical Office*, 2019a) (blue) and water level at a gauge just north of Gígjökull (black) (*Icelandic Meteoroglogical Office*, 2019b), see gauge locations in Figure 1. Flow peaks A-D correlate with the corresponding tremor peaks. See text for detail. **B** Amplitude spectra on April 14^{th} for the first few hours of the eruption at station gig (top), normalized rms for station gig (colors and normalization as in **A**) (middle) and earthquakes in the caldera (from (*Tarasewicz et al.*, 2012b). 1 and 2 are as in **A** and 1a is when the earthquakes get shallower. **C** Spectrogram of station gig during tremor pulse C on April 15^{th} (black box). See text for details.

them are variations of the same theme that exploits the correlation of pairs of recordings of the tremor signal. This yields information about differential distance to the tremor source (*Haney*, 2010; *Gudmundsson and Brandsdóttir*, 2010; *Ballmer et al.*, 2013; *Droznin et al.*, 2015; *Sgattoni et al.*, 2017). A common feature of these methods is that some attribute of the correlograms (e.g. their envelope functions) is back projected in two-dimensions and stacked to construct an image of the source (distribution). *Li et al.* (2017a) introduced double correlation to suppress correlated noise in the correlograms and showed, by a synthetic study, that if the back projection is done with a suitable surface-wave velocity, it suffices that the tremor contain a significant amount of energy in surface waves, i.e., it need not be dominated by surface waves. This is because any potential body-wave component of the tremor signal will not be back projected coherently and therefore does not stack constructively. *Li et al.* (2017b) went further to introduce higher-order products of correlograms (than the second order of double correlation), thereby achieving further suppression of correlated noise in the correlograms. These methods can be regarded as imaging methods (imaging apparent back-projected energy emission) and do not provide any information about uncertainty.

Li et al. (2019) simulated the appearance of the correlograms of tremor at nearby Katla volcano. They found that they could simulate the tremor in terms of a primary source and multiple

scattered phases (with random orientation, random amplitude, random scattering width). The correlogram envelopes appear as a distributed signal with oscillatory decay away from a central maximal peak at the time shift of the primary source. The scattered content of the tremor constitutes noise in the correlograms from the perspective of locating the source(s). The oscillatory decay of the correlogram amplitudes, therefore, constitutes noise that is partially correlated from one correlogram to another. The higher-order correlations introduced by Li et al. (2017a, 2017b) help to suppress this noise. Correlograms of the Eyjafjallajökull tremor have similar characteristics to those of recorded tremor at nearby Katla.

Products of back-projected correlograms are reminiscent of computation of the joint probability of independent individual probabilities. In that context we would need to justify each back-projected correlogram attribute as representing a spatial probability density of the inferred source location due to data contributing to the correlogram in question, their uncertainties and the uncertainty of the back projection, i.e., as an inference likelihood function for the source location due to each correlogram. However, the likelihood should be high where the energy is great in the back-projected correlogram. Therefore, the likelihood should be a monotonic function of the back-projected energy, but we do not know that function. Li et al. (2019) apply Bayes' rule to define it.

They assume that the correlogram envelope, $f(t)$, consists of the sum of signal, $s(t)$, and noise, $n(t)$. They further assume that the noise process is continuous and characterized by a probability density, $p_n(n)$, and that the signal is described by two random processes, one describing its distribution, $p_s(s)$, the other binary process, S, describing its occurrence ($S = 1$ or $S = 0$), with a probability $P(S = 1) = 1 - P(S = 0)$. $S = 1$ when a signal is present and $S = 0$ when no signal is present. Then, according to Bayes rule:

$$p_{sf}(S = 1|f) \cdot p_f(f) = p_{fs}(f|S = 1) \cdot P(S = 1) \tag{1}$$

Here, the notation $|x$ is used to denote conditioned by x. $p_{sf}(S = 1|f)$ is the probability that a signal is present for any given value of f. This is what we want to describe.

Now, assume that $P(S = 1)$ is small and as we have no prior knowledge about when a signal might occur it is the same at all times, t. Then

$$p_{sf}(S=1|f) \propto \frac{p_{fs}(f|S=1)}{p_f(f)} \tag{2}$$

Since $P(S=1)$ is small, $p_f(f)$ is approximately equal to $p_n(n)$ and when a signal is present $f = s + n$. Therefore, at those points in time when $S = 1$:

$$p_f(f) \approx p_n(n) * p_s(s) \tag{3}$$

where $*$ stands for convolution. Therefore,

$$p_{sf}(S=1|f) \approx \frac{p_n(n) * p_s(s)}{p_n(n)} \tag{4}$$

If we know nothing about what values the signal may take, but assume that they are one sided (positive) it is natural to choose $p_s(s) = H(s)$, i.e., the Heavyside function. Then:

$$p_{sf}(S=1|f) \approx \frac{p_n(n) * H(s)}{p_n(n)} \tag{5}$$

Thus, we can transform the signal, $f(t)$, into a scaled probability density at any given point in time if we know $p_n(n)$. We can estimate $p_n(n)$ from a histogram of the values of the time series. We can then back project that probability density as a function of time shift into two-dimensional space to construct a spatial probability density or a likelihood function of space. This involves a heterogeneous mapping that is not unique. Each time delay maps to a hyperbolic curve in two-dimensional space and the density of that mapping varies along the hyperbola. In order to interpret the back-projected temporal probability density as a spatial probability density one must account for the heterogeneity of this mapping. Once done, we would have a description of the likelihood of location in space due to the correlation data uncertainty and its non-uniqueness. In addition, there will be an uncertainty associated with the back projection itself, i.e. the uncertainty of the relationship between time and space, i.e. velocity. This can be dealt with by defining a stochastic process that describes the uncertainty and variation of the velocity, computing the variation of predicted time for a given set of differential paths, and convolving the above estimate of likelihood with a distribution of width corresponding to that variation. This is the construct used by Li et al. (2019) to estimate source-location likelihood due to a single back-projected correlation. If the error processes in the correlograms are independent, then the combined likelihood based on all correlation data can be constructed by the product of all the individual likelihood functions.

However, this assumption is not as well-founed if parts of the correlation noise are correlated, e.g. due to common physical scatterers present for different paths in different correlograms. The peaks of that combined likelihood function would define where the source(s) is most likely to be located and, importantly, the widths of the peaks provide information about the location uncertainty. In that sense, the method presented by Li et al. (2019) can be regarded as an inference method.

There are several technical issues related to this approach. First, the probability density of noise in each correlogram needs to be evaluated. This is simply done by fitting a parameterised function to the histogram of values in each correlogram envelope. Second, the width of the smoothing function defined by the velocity variation and uncertainty used in the back projection needs to be defined. This can be done by defining velocity variation according to the results of local tomography. Details of these calculations are presented by Li et al. (2019).

Li et al. (2019) also performed synthetic tests of their uncertainty estimates for a study at nearby Katla volcano. They found that the width of the calculated joint likelihood function was in a good agreement with their reproducibility within the network at Katla, but underestimated the uncertainty outside the hull of the network. These results may depend on the path-coverage of the problem, velocity structure of the area, and nature of scattering, and are therefore only conclusive for the network around Katla volcano. However, the geology and velocity structure are similar to that at Eyjafjallajkll, so transferring their synthetic test results to the Eyjafjallajkull network is reasonable.

5.2 Application of the probabilistic inference method

The probabilistic tremor-location method of Li et al. (2019) is based on inter-station correlograms. Before calculating cross correlations the mean of each seismogram is removed and the data are low-pass filtered at 4 Hz and then decimated from 100 to 10 samples per second. Data were corrected for instrument response and a 1-bit, time-domain normalization was applied. Seismograms were then correlated. The frequency content of the tremor signal overlaps with the secondary microseisms that peak at roughly 0.2 Hz (Figure 2). The lower limit of the lowest frequency band to be analysed was chosen at 0.5 Hz in order to avoid overlap with the microseisms. The correlograms

were filtered in three frequency bands; 0.5-1 Hz, 1-2 Hz and 2-4 Hz. Examples of the temporal evolution of the envelopes of daily correlograms are shown in Figure 5 for two station pairs. The character is different for the three frequency bands shown, with the signal becoming more complex as frequency increases. The signal is very stable for the 0.5-1 Hz band (Figure 5A,B) during the course of the eruption. This is also the case for the 1-2 Hz band (Figure 5C) for the majority of the station-pairs, although a few pairs exhibit a little more complexity (e.g, mid-fag, Figure 5D) where a shift to larger negative differential time is suggested at the very end of the eruption. In the 2-4 Hz band, the signal spans a broader range of time shifts, which we attribute to enhanced scattering with increased frequency. Again, the correlograms for station pair mid-fag suggest a shift to larger negative time shifts at the end of the eruption. It is in this highest frequency range that the temporal changes in the signal correlate best with the eruption history as defined by *Gudmundsson et al.* (2012) (Figure 5E,F).

The stations used for locating the tremor were the ones closest to the eruption site (bas, esk, fag, fim, god, nup, mid, sel) as the signal in the cross correlations for pairs including stations farther away ($> 40\ km$) was weaker and less distinct. A homogeneous velocity distribution was used for the back projection. We apply Li et al.'s (2019) method to correlogram envelopes and back project in two dimensions. Therefore, the appropriate choice of velocity is group velocity of a surface wave. We used group velocities of $v = 1.4\ km/s$, $1.3\ km/s$ and $1.2\ km/s$ for the 0.5-1 Hz, 1-2 Hz and 2-4 Hz frequency bands, respectively. These velocities are smooth extrapolations of the phase-velocity measurements reported by *Benediktsdóttir et al.* (2017) from Eyjafjallajökull and *Jeddi et al.* (2017) from nearby Katla and their group-velocity measurements (not reported). These choices of velocity also focus the location-likelihood functions optimally for the respective frequency bands. Varying the velocity by $0.1km/s$ changed the outcome less than by a few hundred meters for the two lower frequency bands, but affected the 2-4 Hz frequency band more

In order to simulate the effects of a two-dimensional velocity structure we generated random velocity fields with a correlation length of 5 km and 15% root-mean-square velocity variation to predict travel-time variations. This is in accordance with the velocity models derived for Eyjafjallajökull and Katla by *Benediktsdóttir et al.* (2017) and *Jeddi et al.* (2016), respectively. This

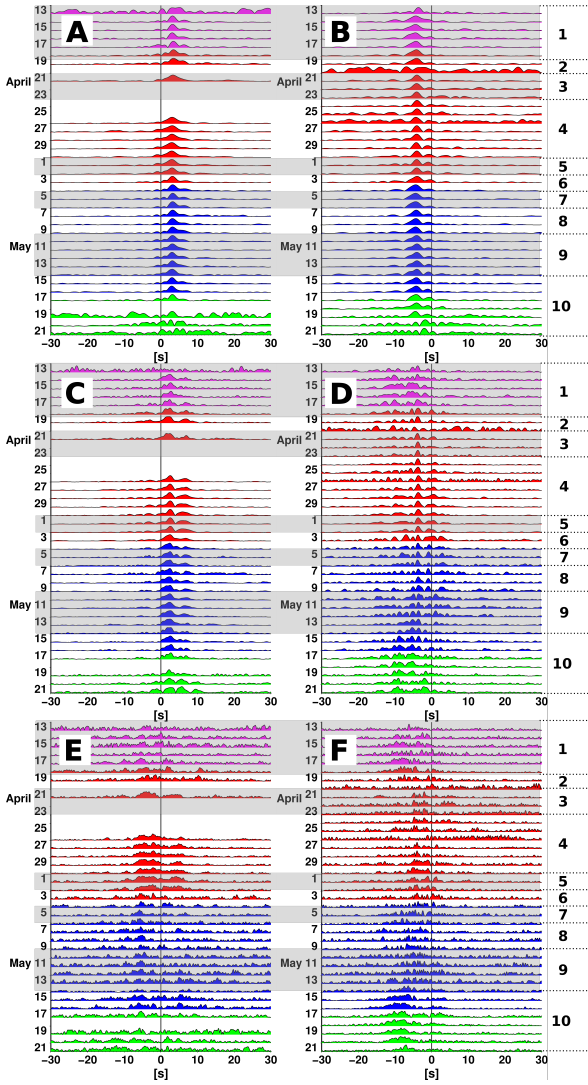

Figure 5. Correlograms for two station pairs during the course of the eruption. Station pair bas-esk and frequency intervals 0.5-1 Hz, 1-2 Hz and 2-4 Hz in **A**,**C**,**E**, respectively and station pair mid-fag and frequency intervals 0.5-1 Hz, 1-2 Hz and 2-4 Hz in **B**,**D**,**F**, respectively. Colouring of the correlograms represent the phases of the eruption as defined by *Gudmundsson et al.* (2012); phases I, II, II and IV are purple, red, blue and green, respectively. Ten time intervals defined in section 5 based on power ratios at the different stations are gray shaded and indexed on the right hand side (see also Table 3).

Table 3. Epochs of the Eyjafjallajökull eruption as defined by the power-ratios analyses.

Epoch #	**Duration**
1	April $14^{th} - 18^{th}$
2	April $18^{th} - 20^{st}$
3	April $20^{st} - 23^{th}$
4	April $23^{th} - 29^{th}$
5	April 29^{th}–May 2^{nd}
6	May $2^{rd} - 4^{th}$
7	May $4^{th} - 6^{th}$
8	May $6^{th} - 9^{th}$
9	May $9^{th} - 14^{th}$
10	May $14^{th} - 21^{st}$

may underestimate the strength of heterogeneity and overestimate the scale length of the structure. However, it is not obvious that this will underestimate the effect on travel time as its variation is in proportion to the product of scale length and heterogeneity strength in the ray-theoretical limit (*Chernov and Silverman*, 1960; *Gudmundsson et al.*, 1990). The estimated travel-time variance was then used to construct a Gaussian filter that was convolved with the back-projected likelihood of each correlogram.

To estimate the noise distribution necessary to translate attribute signal to likelihood (see Equation 5) we constructed a histogram of the attribute signal values and fitted that with a two-parameter function of the form:

$$p_n(n) = \frac{(n/a)}{1 + (n/a)^k} \tag{6}$$

The parameter a defines the width of the distribution and the parameter k defines the rate of decay in its tail. This form was selected as it was found to fit the empirical data well (given only two parameters) and the parameters were determined by least-squares fitting of the distribution for each correlogram envelope.

5.3 Tremor location: results

We experimented with locating the tremor with single-day correlograms at the high-resolution end to correlograms for the whole duration of the eruption at the other extreme. Figures 6A-C show the tremor-location likelihood using stacked cross correlations over the whole duration of the eruption. Differences between the location predicted by daily cross correlations and eruption-long correlations are shown in Figures 6D-F with time colour coded. The location of the tremor, as predicted by daily cross correlations, varies by less than 1 km in the 0.5-1 Hz frequency range, less than 2 km in the 1-2 Hz frequency range, but by as much as 3-4 km in the 2-4 Hz frequency range. The inferred location is the same in the two lower frequency ranges and very close to the eruption site, while the average location in the highest frequency range is 2 km to the NNE from the main eruption site and outside the caldera.

The width of the likelihood peak is about 0.5 km in the lowest frequency range and 0.7 km in the intermediate range. At the highest frequencies the width approaches 1 km and significant secondary peaks begin to appear. The inferred locations can not be clearly distinguished from the eruption site. The scatter diagrams in Figures 6D-F suggest that the uncertainty of daily locations is less than 1 km at 0.5-1 Hz, but larger than 1 km at 1-2 Hz. Notice how stable the correlograms are in Figure 5, also suggesting a stability of the tremor location.

The scatter of the daily locations is comparable to the width of the location-likelihood peak in the lowest-frequency range. One clear outlier is present at the end of the eruption in the 0.5-1 Hz frequency range. This relates to the falling levels of power in the tremor at the end of the eruption. In the intermediate-frequency range the scatter is considerably bigger. Some of the outliers of the distribution occur near the beginning of the eruption (red dots), but most of them towards the end (dark blue dots). Many of the daily locations between epochs 3 and 8 lie within 1 km of the average location, which is comparable to the width of the location-likelihood peak of the eruption-long location estimate. There is a suggestion that the location drifts towards the SW at the very end of the eruption in tune with the evolution of some of the correlograms shown in Figure 5.

The daily-location scatter is higher yet in the highest-frequency range. The most likely location in this case is about 2 km NNE of the locations in the lower frequency bands. Most of the daily

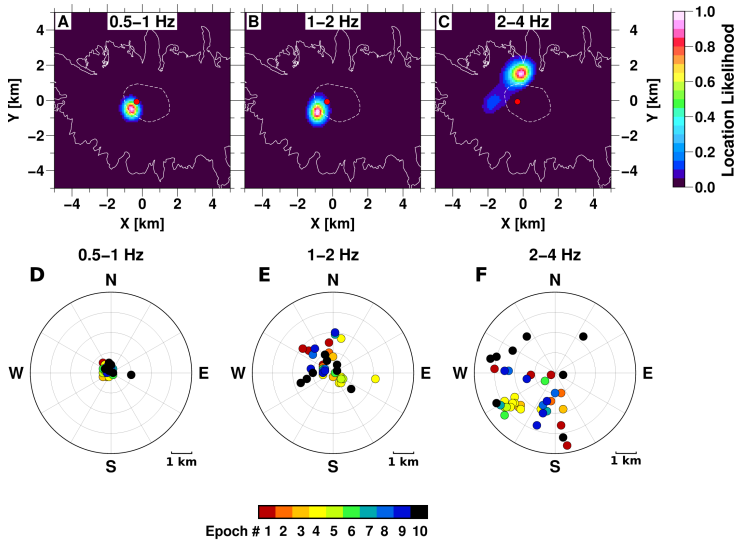

Figure 6. Location likelihood and its stability. **A**, **B**, **C** show the location likelihood of the tremor source for eruption-long correlograms filtered between 0.5-1 Hz, 1-2 Hz and 2-4 Hz, respectively. White and dashed lines depict the outline and caldera of Eyjafjallajökull, respectively. The red circle shows the eruption site (*Gudmundsson et al.*, 2012). The colour palette on the right defines the location likelihood and. **D-F** show the location of daily peak likelihood for the three frequency intervals, relative to the long-term average location. Red colours denote days near the beginning of the eruption, blue colours denote days at its end according to a subdivision of the eruption history into 10 epoch defined in section 5. Circular grid lines define 1 kilometer distance increments.

locations fall between W and S of the most likely location. The most likely location over the whole eruption is not a linear combination of the daily locations, which can explain the uneven distribution of the daily locations around the likelihood peak in Figure 5C. The scatter to the south and west suggests locations closer to the most likely locations in the two lower frequency bands. One cluster of locations spanning epochs 3 to 7 is found about 2-3 km SW of the average location. This corresponds to the secondary peak in the likelihood in Figure 5C. Daily locations for epoch 10 behave differently, which can be attributed to declining power in the eruption. We cannot discuss the uncertainties of these locations with confidence. It is likely that a scaling of a

factor of two is conservative for these frequencies due to a more vigorous scattering process at the higher frequencies.

We have applied Li et al.'s (2019) method to surface waves in two dimensions. Consequently, we cannot say much about depth. With better station density, good enough travel-time information, and sufficient body-wave content in the tremor the method could potentially be applied to body waves in three dimensions. This might provide useful constraints on the depth of the source of the tremor. We were not able to do that with the data here. We can, however, say something about the depth based on the excitation efficiency of surface waves. At 1 Hz and with a phase velocity of approximately 1.5 km/s (somewhat higher than the group velocity) the wavelength will be 1.5 km. Eigenfunctions of fundamental-mode surface waves with that wavelength have energy concentrated in the top 0.5-1 km. Thus, if these surface waves are fundamental mode, they are most effectively excited quite near the surface, i.e. approximately within top kilometer. Note, that if the source is at depth in a layered structure, that would cause a common phase shift to the surface waves at two stations, which would cancel in the correlation.

In conclusion, we argue, based on the stability of correlograms between 0.5 and 2 Hz over time, and the narrowness and stability of the location likelihood over time that the tremor source at these frequencies is very localized and stable in location over the entire 5-6 weeks of the eruption. The map location of the source cannot be distinguished from the eruption site (Figure 6A). The source of the surface waves in the tremor most likely lies within the top kilometer of the volcano.

6 ANALYSES OF POWER VARIATIONS

The stability of the source location allows for a simplification in the analysis of the amplitude or power behaviour with distance.

The decay of the amplitude of a wave with distance, r, can be described as

$$A = A_0 g(r) s(r) \tag{7}$$

where A_0 represents the source strength, $g(r)$ is a geometrical spreading function, and $s(r)$

describes attenuation (e.g. *Battaglia and Aki*, 2003; *Battaglia et al.*, 2005). For a homogeneous medium (velocity), the effect of geometrical spreading is given by

$$g(r) = r^{-a} \tag{8}$$

where the exponent is a=1 for body waves and a=0.5 for surface waves. The uniform attenuation factor is given by

$$s(r) = exp(\frac{-\pi f r}{Qv}) \tag{9}$$

where Q is an attenuation quality factor, v is the velocity of the wave, r is distance from the source, and f is frequency.

When velocity and attenuation are not uniform the factors $g(r)$ and $s(r)$ become path or station dependent. For the i-th station we write

$$g_i = \gamma_i {r_i}^{-a} \tag{10}$$

introducing a station amplitude correction γ_i. The attenuation term becomes

$$s_i = exp(-\pi f \int_{path_i} \frac{dr}{Qv}) = exp(-\pi f q_i) \tag{11}$$

where

$$q_i = \int_{path_i} \frac{dr}{Qv} \tag{12}$$

This simple formulation has been commonly used in analyses of tremor amplitude (e.g *Battaglia and Aki*, 2003; *Battaglia et al.*, 2005).

In the presence of noise, $n(t)$, the amplitude recorded at the i-th station can then be described with

$$A_i(t) = h_i A_0(t) + n_i(t) \tag{13}$$

where $h_i = g_i s_i$ describes a decay factor incorporating both geometrical spreading and attenuation along the path from the tremor source to the i-th station. This factor depends on the properties of the path between the receiver and the source. If the source is stationary, then the path between the receiver and the source remains unchanged with time and this station dependent amplitude coefficient also remains unchanged.

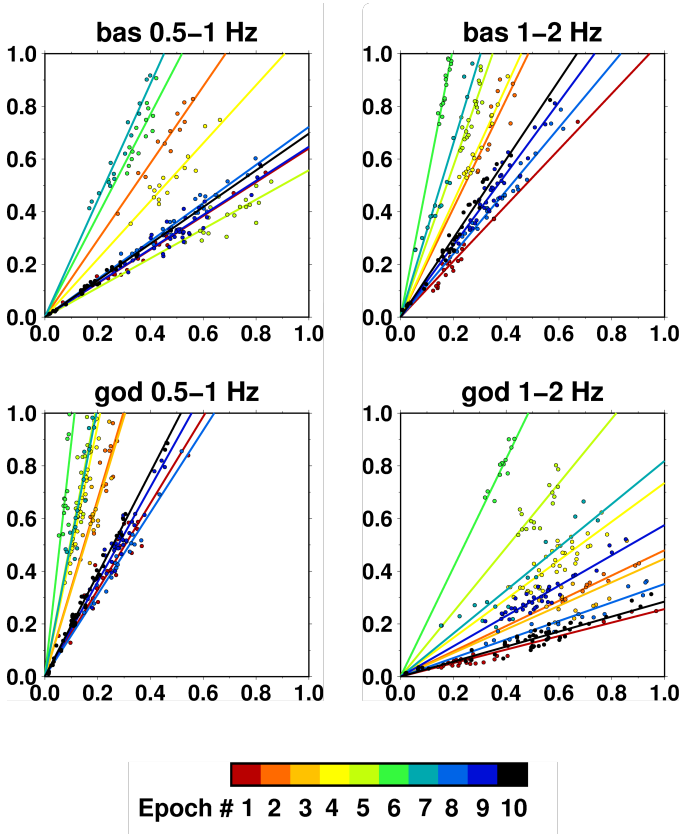

Figure 7. Power of stations bas and god vs. the power of station fag during the entire eruption of Eyjafjallajökull, filtered in two frequency bands. Colour code is by epochs of the eruption as defined in this study (see Table 3). Each point on the plot is the mean power calculated over three hours.

In Section 5.1 we showed that the map location of the tremor source was stationary during the entire duration of the eruption for frequency intervals 0.5-1 Hz and 1-2 Hz. If the noise source is also stationary in time and if the tremor source and the noise source are independent with zero mean, then

$$p_i(t) = {h_i}^2 p_0(t) + m_i(t) \tag{14}$$

where p_i, p_0 and m_i are the power of the time series recorded at station i, the tremor source,

and the background noise at station *i*, respectively. The same formulation is used for a reference station, $i = r$,

$$p_r(t) = {h_r}^2 p_0(t) + m_r(t) \tag{15}$$

Combining the two power equations we get

$$p_i(t) = \frac{{h_i}^2}{{h_r}^2} p_r(t) + m_i(t) - \frac{h_i^2}{h_r^2} m_r(t) \tag{16}$$

Thus, if the noise process is stationary in time, and we plot the power at the i-th station against the reference station, we should get a straight line with slope

$$\alpha_i = \frac{{h_i}^2}{{h_r}^2} \tag{17}$$

and intercept

$$\beta_i = m_i - \frac{h_i^2}{h_r^2} m_r \tag{18}$$

With the above description the slope of this line will be unchanged with time if the source location is stationary and the velocity and attenuation in the medium do not change significantly. We have plotted the power-spectral density for each station versus that of a reference station within the two frequency ranges that resulted in a stable location using the probabilistic inference method. We have chosen to use station fag for reference because it is that station which lies closest to the source and has the least disrupted recording throughout the eruption. Examples of results are presented in Figure 7 and a full range of similar figures for all components are in Appendix A1.

Before calculating the power-spectral density we clipped earthquakes that exceed the continuous tremor in amplitude by calculating the standard deviation of the time series over hour-long windows and setting values larger than 2 standard deviation to that value. This was then iterated several times. The power-spectral density was then calculated within three hour windows throughout the eruption period. Figure 7 shows the power-spectral density at station god versus that at station fag in the two lower frequency ranges. Station god is far from station fag and relatively far away from the eruption site. It also shows the power-spectral density at station bas versus that of station fag. Station bas is close to station fag, but slightly further away from the eruption site. The temporal variation of the ratio between the stations' power clearly arranges itself into time

periods when the slope is relatively stable, while it changes significantly from one period to the next. This leads us to define 10 epochs (Table 3) spanning the eruption during each of which the power ratio is apparently constant, and measure the slopes in each case by linear regression. Each measurement of slope is associated with an uncertainty estimate based on the scatter around the best line in each case. If the uncertainty of the slope exceeded 30% of its value, that measurement was not considered. Also, 10 or more points were required to define a line.

The slopes become progressively smaller with increasing frequency at station god which is a clear attenuation effect. The slopes are high (> 1) for station god despite the fact that it is about twice as far away from the eruption site than station fag suggesting significant site amplification at station god. The same does not hold for station bas as the difference in distance is small and the differential attenuation between stations bas and fag is in fact negative as will become apparent later.

From these observations we can extract information about the attenuation quality factor. We also must introduce some aspect of the source that varies with time to produce varying slopes. We will come back to this point later where we propose that the power-radiation pattern of the source may have changed with time.

6.1 Estimates of attenuation

Concentrating on the attenuation effect, we can write the amplitude factor at the i-th station as

$$h_i = g_i exp(-\pi f q_i) \tag{19}$$

Plugging this into Equation 16 for the slopes in Figure 7 and taking the logarithm we get

$$ln(\alpha_i) = 2(ln(h_i) - ln(h_r)) = 2(ln(g_i) - ln(g_r)) + 2\pi f(q_r - q_i) \tag{20}$$

Calculating the difference between the natural logarithm of measured slopes at different frequencies during the same epoch at the same station we get

$$ln(\alpha_i(f_1)) - ln(\alpha_i(f_2)) = 2\pi(f_1 - f_2)(q_r - q_i) \tag{21}$$

This assumes that a, γ_i and Q are not frequency dependent. We can now estimate the difference $q_r - q_i$, i.e a measure of differential attenuation between two paths. We use only the two lowest

frequency ranges to do this as we are not confident that the source location is stationary in time for the third and highest frequency range. We simply take the mean frequency of each frequency range as our measure of frequency. For each station we have many such measurements at different epochs. Their average (weighted) is our measure of differential attenuation and their scatter defines their uncertainty. The results are shown in Figure 8 as a function of the distance to the eruption site of the i-th station in each case. The stations define two groups. The stations close to the eruption site, i.e. those stations that are located around the periphery of Eyjafjallajökull (red), fall close to a line, while the distal stations hvo and hau (black) fall off the line. This suggests that this measure of attenuation is a linear function of horizontal distance from the eruption site within the volcano, i.e. that the attenuation quality factor, Q, is more or less constant. Assuming this, the slope of the line in Figure 8 is a measure of Q inside the volcano and its intercept is a measure of the attenuation along the path to station fag. The regression parameters are shown in Table 4). Assuming a uniform phase velocity of $v = 1.5\ km/s$ we find a quality factor of $Q = 16 \pm 8$ for the volcanic region and from the intercept we get $Q_{fag} = 12 \pm 9$. Using this value for Q_{fag} we can calculate a path averaged Q for the distal stations to be $Q_{hau} = 39 \pm 15$ and $Q_{hvo} = 48 \pm 22$. Individual Q values were evaluated using the same calculation and the results are shown in Table 5. Q values for paths within the volcano are relatively low (high attenuation) but reasonable, nevertheless, in comparison with estimates in a similar frequency range at other volcanoes (e.g., *Kumagai et al.* (2018); *Del Pezzo et al.* (2006); *Gudmundsson et al.* (2004) and references therein). These Q values are also similar to those estimated by *Gudmundsson and Brandsdóttir* (2010) at Hengill volcano in SW Iceland and those proposed by *Jeddi et al.* (2016, 2017) in order to reconcile unrealistic Vp/Vs values inferred by comparing Vp from body waves to Vs from lower-frequency surface waves around nearby Katla volcano.

We note that the lowest point in Figure 8 (second from the left) represents station bas. The differential attenuation is negative despite the fact that station bas is further away from the eruption site than station fag. This was evident from the slope analyses (Figure 7) where the slope of the power ratios for station bas increased with increasing frequency, opposite to the character of other stations (Figure A1). We conclude that the attenuation along the path from the source to station

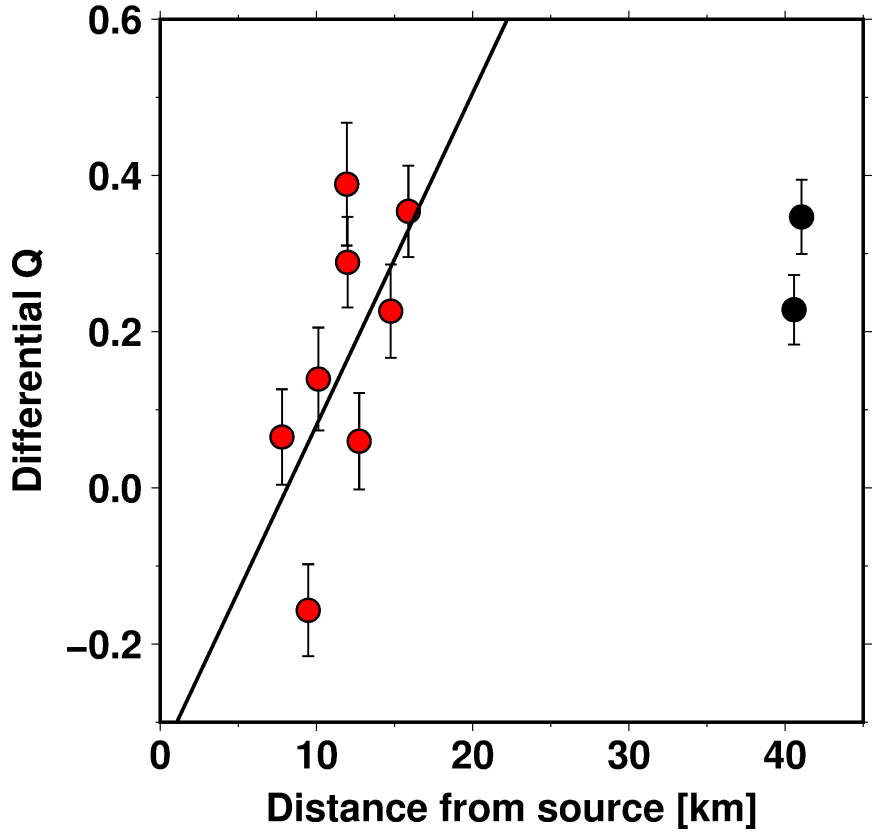

Figure 8. Differential quality factors as a function of distance from the eruption site. Data for all stations (red circles) except hau and hvo (black circles) lie on a line with a slope 0.042 and intercept with the y-axis at -0.33. Numerical values for the differential attenuation parameters ($q_r - q_i$) and inferred path-averaged attenuation parameters (Q) to individual stations are listed in Table 5.

bas has low attenuation and when Q_{bas} is calculated directly from the Q value for fag (from the intercept) the result is $Q = 34 \pm 47$, which is substantially, but not significantly higher than the average, $Q = 16 \pm 8$, for paths within the volcano.

Note that we used horizontal distance in Figure 8 to reduce the estimated attenuation measures, q_i, to a constant Q for Eyjafjallajökull volcano. This assumes surface waves in the tremor. The behaviour with horizontal distance in Figure 8 would not be expected for body waves from a source at depth. In that case the path length through the shallowest parts of the volcano would be

shortest at the distal stations. Therefore, assuming that attenuation is concentrated near the surface (*Kumagai et al.*, 2018), that would require the quality factor to decrease away from the edifice of the volcano, i.e. the attenuation would need to be weaker around the erupting central part of the volcano than out on its flanks. Thus, this behaviour of differential attenuation argues for the tremor being dominated by surface-wave energy at the analysed frequencies.

The same analysis was carried out for the horizontal components and differential Q versus distance from the eruption site can be seen in Figures A4 and A5 in the appendix.

6.2 Estimates of geometrical spreading factors

We can now use the estimates of attenuation to account for some of our data. What remains are measures of geometrical spreading factors, a and γ_i.

$$\lambda_i = ln(\alpha_i) - 2\pi f(\hat{q}_r - \hat{q}_i) = 2(ln(g_i) - ln(g_r)) = 2(ln(\gamma_i) - ln(\gamma_r) - a(ln(r_i) - ln(r_r)) \quad (22)$$

We have multiple redundant data to estimate these. However, the equations are not all independent. Obviously, the geometrical spreading exponent, a, cannot be determined with independent station corrections. A common strategy is to use regional events (*Battaglia and Aki*, 2003) to estimate the station corrections, γ_i. This is not obviously appropriate. First of all, these station-amplitude corrections must be seen to include both focusing or defocusing effects along each path and site amplification. Therefore, the geometry of the calibrating wave must be the same as that of the tremor waves. Second, the radiation pattern of the event must be similar to that of the tremor. Third, the correction must of course be evaluated at the same frequency as the tremor. Calibration with a single phase from a regional event will include effects of energy transfer (in time) in the seismogram by scattering which may differ from the power-spectral density of the tremor. We looked for regional events in the vicinity of the eruption site with sufficiently high signal-to-noise ratio in the frequency range of the analysed tremor and found none. We are, therefore, left with no means of estimating geometrical spreading parameters other than from our tremor-power observations. We do this by applying Occam's razor. We estimate the geometrical spreading exponent, a, so as to minimize the quadratic size of the station correction terms, $ln(\gamma_i)$. This yields the simplest possible parameter model in just that sense. To do this, we set up a quadratic regression for the

Table 4. Regression parameters for attenuation

	Z	T	R
slope	0.043 ± 0.022	0.078 ± 0.014	0.067 ± 0.012
intercept	-0.34 ± 0.26	-0.79 ± 0.17	-0.60 ± 0.15
Q from slope	16 ± 8	9 ± 2	10 ± 2

station corrections using the linear expression in Equation 22 in terms of reduced (by attenuation) logarithmic station corrections, λ_i, fixing a. Then, we estimated a so that the quadratic sum of the correction terms was minimized. This is a straight forward least-squares problem. We have ten stations, i.e. 10 unknown differential station corrections, $ln(\gamma_i) - ln(\gamma_r)$. We have 160 reduced measures of logarithmic slopes, λ_i, i.e. a highly redundant problem. We add one constraint, namely that the logarithmic station corrections are evenly distributed around zero (i.e. the station corrections themselves are evenly distributed around unity according to logarithmic distance). We find $a = 0.53 \pm 0.05$ using a jack-knife approach to estimate the uncertainty. This value is very close to the theoretical value for surface waves emanating from a point source. Thus, the power-spectral decay with distance suggests that the tremor at the analyzed frequencies consists mostly of surface waves. Therefore, we simply fix $a = 0.5$ and compute the station corrections accordingly. The results are shown in Figure 9 and Table 6 in terms of their azimuthal and distance variation.

Most of the relative station corrections lie in the range 0.7-2. They do not exhibit any simple azimuthal pattern. Neither is there a systematic behaviour with distance. Station god sticks out with its high value (5.3). It is at 1200 m above sea level in the highland region called Godaland. The site is close to the edge of the highland facing Eyjafjallajökull rising some 1000 m above its surroundings and with a very rugged outline eroded by small outlet glaciers from Mýrdalsjökull that cover Katla volcano to the east. It is conceivable that this rather extreme topography cause significant site amplification for waves from the west.

6.3 Residual analyses

Having estimated a and the γ_i we can reduce our measured slopes or power ratios. According to our above description of amplitude and power the residuals should be

Table 5. Attenuation parameters evaluated for each station-source path

Station	$q_r - q_i$			**Q**		
	Z	T	R	Z	T	R
bas	-0.16 ± 0.06	-0.23 ± 0.16	-0.10 ± 0.11	34 ± 47	11 ± 5	13 ± 5
bar	0.39 ± 0.08	0.24 ± 0.21	0.13 ± 0.16	11 ± 4	8 ± 2	10 ± 3
esk	0.23 ± 0.06	0.32 ± 0.13	0.35 ± 0.10	17 ± 8	9 ± 2	10 ± 2
fag	-	-	-	12 ± 9	5 ± 1	6 ± 2
fim	0.14 ± 0.07	0.08 ± 0.15	0.16 ± 0.10	14 ± 8	8 ± 2	9 ± 2
god	0.35 ± 0.06	0.42 ± 0.14	0.45 ± 0.10	15 ± 6	9 ± 2	10 ± 2
hau	0.23 ± 0.04	-0.09 ± 0.21	0.08 ± 0.09	39 ± 15	22 ± 3	24 ± 4
hvo	0.35 ± 0.05	0.46 ± 0.10	0.51 ± 0.07	48 ± 22	39 ± 15	40 ± 10
mid	0.06 ± 0.06	0.22 ± 0.15	0.29 ± 0.11	21 ± 14	9 ± 2	10 ± 2
nup	0.29 ± 0.06	0.23 ± 0.14	0.34 ± 0.12	13 ± 5	8 ± 2	8 ± 2
sel	0.07 ± 0.06	-0.18 ± 0.14	-0.08 ± 0.09	13 ± 8	9 ± 3	10 ± 3

Table 6. Station correction parameters evaluated for each station-source path

Station	$\ln(\gamma_i/\gamma_r)$			γ_i		
	Z	T	R	Z	T	R
bas	-0.31 ± 0.24	-0.30 ± 0.69	0.17 ± 0.42	0.48 ± 0.12	0.62 ± 0.43	0.72 ± 0.30
bar	1.00 ± 0.32	0.17 ± 0.79	0.06 ± 0.50	1.78 ± 0.56	0.99 ± 0.78	0.65 ± 0.32
esk	0.80 ± 0.25	0.59 ± 0.52	0.78 ± 0.44	1.46 ± 0.37	1.50 ± 0.78	1.33 ± 0.53
fag	-	-	-	0.65 ± 0.50	0.83 ± 1.59	0.61 ± 0.74
fim	0.54 ± 0.28	0.00 ± 0.61	0.42 ± 0.36	1.13 ± 0.32	0.83 ± 0.51	0.93 ± 0.34
god	1.68 ± 0.25	1.59 ± 0.58	1.90 ± 0.38	3.53 ± 0.88	4.08 ± 2.36	4.09 ± 1.5
hau	-0.54 ± 0.18	-1.55 ± 0.74	-0.92 ± 0.32	0.38 ± 0.07	0.18 ± 0.13	0.24 ± 0.08
hvo	0.48 ± 0.19	1.28 ± 0.37	1.32 ± 0.27	1.06 ± 0.20	2.99 ± 1.10	2.29 ± 0.62
mid	0.03 ± 0.23	0.45 ± 0.58	0.68 ± 0.37	0.68 ± 0.16	1.30 ± 0.76	1.21 ± 0.45
nup	0.72 ± 0.21	0.39 ± 0.52	0.97 ± 0.42	1.35 ± 0.18	1.23 ± 0.64	1.61 ± 0.68
sel	0.20 ± 0.25	-0.59 ± 0.53	0.03 ± 0.34	0.80 ± 0.20	0.46 ± 0.24	0.63 ± 0.21

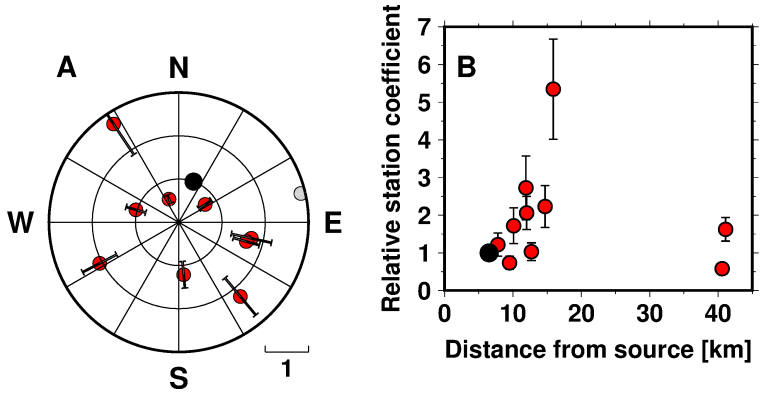

Figure 9. Estimates of relative station coefficients for each station (γ_i/γ_r) in a rose diagram (**A**) and as a function of distance away from eruption site (**B**). Black point represents the reference station *fag*. The gray point for station god plots off scale in **A**. Numerical values of the lograrithm of the relative station correction parameters and the inferred station correction parameters themselves are displayed in Table 6.

$$d\lambda_i = \lambda_i - 2(ln(\hat{\gamma}_i) - ln(\hat{\gamma}_r) + 2\hat{a}(ln(r_i) - ln(r_r)) = 0 \tag{23}$$

i.e. trivial. But, the quadratic norm of these residuals normalized by the remaining number of freedom was on the order of $6 >> 1$. This model of attenuation and spreading does not account for the observed variability and is, therefore, missing something. The residuals still contain information about the variable power ratios with time, a temporal variation that has not been accounted for. We argue that it can be accounted for by adding a temporal variation to power radiation. This can be done by adding a temporal term in the description of the source term in Equation 13.

$$A_i(t) = h_i A_0(t) B(\phi, t) + n_i(t) \tag{24}$$

where ϕ stands for azimuth from the source and the added term,$B(\phi, t)$, represents relative amplitude-radiation variations with azimuth, ϕ, and time. B does not vary within each epoch. We can therefore absorb the temporal variation of B in its epoch index, k, i.e., $B_i^k = B(\phi_i, t_k)$. The logarithm of measured power-spectral ratios would then be described as

$$ln\left(\alpha_i^k\right) = 2ln\left(\frac{\gamma_i}{\gamma_r}\right) - 2aln\left(\frac{r_i}{r_r}\right) - 2\pi f\left(q_i - q_r\right) + 2ln\left(\frac{B_i^k}{B_r^k}\right) \tag{25}$$

and the residuals after correction for attenuation and geometrical spreading become

$$d\lambda_i = \lambda_i - 2(ln(\hat{\gamma}_i) - ln(\hat{\gamma}_r) + 2\hat{a}(ln(r_i) - ln(r_r))) = ln\left(\frac{C_i^k}{C_r^k}\right) \quad (26)$$

where $C_i^k = \left(B_i^k\right)^2$, i.e., the relative power radiation. We now have a relation to estimate the variable relative power-radiation pattern at each station for each epoch. In Equation 26, we have assumed that the power-radiation patterns do not depend on frequency. But, we need not do that as we can group our residual measurements within each frequency range. This, however, involves no redundancy. Such estimated relative power-radiation patterns, C_i^k/C_r^k, are shown in the left and middle columns of Figure 10 for the 0.5-1 Hz and 1-2 Hz frequency ranges, respectively. The right column of Figure 10 shows the weighted average of the other two with weight inversely proportional to the error estimate in each case. The reference station, *fag*, is shown as a black circle, located 55° east of north. Relative power-radiation patterns for the horizontal components are shown in Figures A8 and A9.

It is important to note that the definition of the ten different epochs was exclusively based on the tremor data, i.e., independent of any other data. Figure 5 shows how the ten epochs, defined here, and the four intervals of *Gudmundsson et al.* (2012) compare.

The resulting power-radiation patterns relative to station *fag* (Figure 10) generally show a marginally significant difference between the two analyzed frequency bands (with several exceptions, e.g. station hau in epoch 2 and station hvo in epoch 6). In some cases, the estimated patterns differ significantly from one epoch to another, e.g., epochs 7 and 8, but in others the epochs are almost the same, e.g. epochs 8, 9 and 10. Some apparent inconsistencies are present and station hvo sticks out in that regard. Stations hvo and fim are at very similar easterly azimuth and are not always comparable.

Epochs 1,8,9 and 10 exhibit a nearly isotropic power-radiation pattern. These epochs are synchronous to phases I, III and IV, where the tremor had lower amplitudes and the activity was primarily explosive. It is mainly within phase II (epochs 2-7) that there is variation in the power-radiation pattern. Some of the epochs are poorly defined, because of lack of data (e.g. epoch 3) while others show a wide scatter of points with large error bars (e.g. epochs 2 and 6).

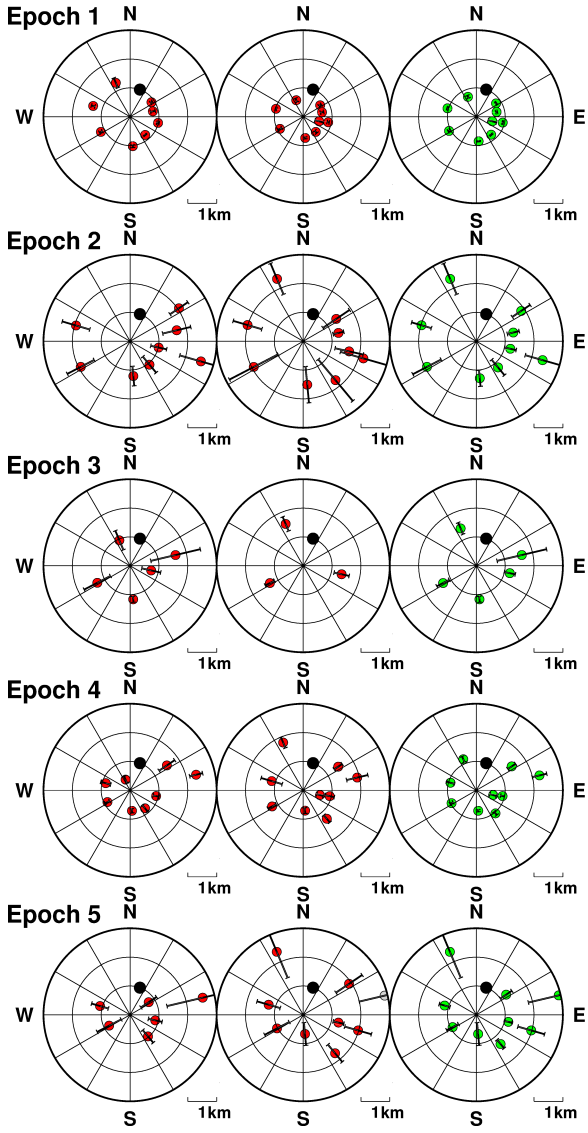

Figure 10. Estimates of the power-radiation pattern relative to station *fag* for 0.5-1 Hz (left), 1-2 Hz (middle), and a weighted mean of the two frequency intervals (right). Where only one measurement was available for one frequency interval, that value was taken as the weighted mean. The error bars are the estimated errors of power-spectral ratios (slope). *fag* is plotted as a larger black circle without an error bar.

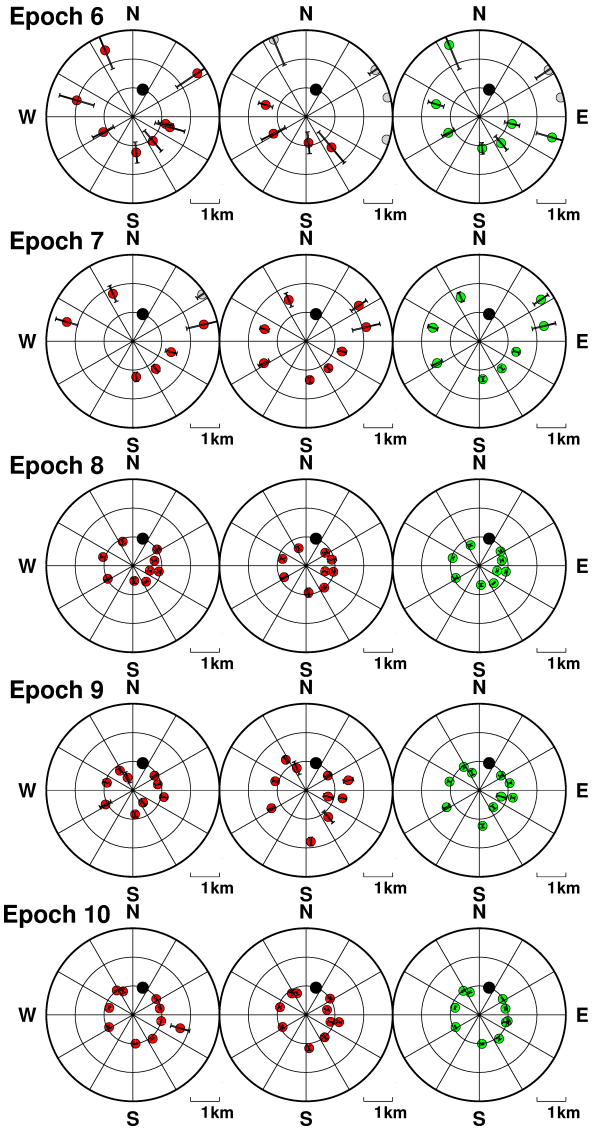

Figure 10. continued.

6.3.1 Addendum

In the appendix, we present results of parameter estimation based on the horizontal components of data. We note that the time behaviour of power is similar on all components on all stations.

The power ratio between the horizontal components and the vertical component is consistently on the order of 1 (varies in general between 0.3 and 1.7). In the linear regression for power-spectral ratios the slope is the datum we seek, but the intercept is an indicator of power in the noise process in each case. We find that the intercepts range from equal to higher by up to a factor of 10 on the horizontal components than on the vertical. This indicates that the noise on the horizontal components is often higher than that on the vertical. We rotated the horizontal components into the radial and transverse for each path. From the horizontal components (R and T) we estimate parameters that are quite similar to those determined from the vertical component (Z).

The path-averaged attenuation coefficients are estimated to be $Q = 10 \pm 2$ and 9 ± 2 for the volcanic region and $Q_{fag} = 6 \pm 2$ and 5 ± 1 from the R and T components, respectively, as opposed to $Q = 16 \pm 8$ and $Q_{fag} = 12 \pm 9$ from the Z component. For the distal stations, hau and hvo, we estimate a path averaged Q to be $Q_{hau} = 24 \pm 4$ and 22 ± 3 and $Q_{hvo} = 40 \pm 10$ and 39 ± 15, for the R and T components, respectively. The Q estimates from the horizontal components are comparable, but somewhat lower than the estimates based on the Z-component. This may indicate that the attenuation of Love waves is greater than for Rayleigh waves. Figures A5 and A4 show the differential quality factor for the R and T components as a function of horizontal distance from the eruption site. Numerical values for the differential attenuation parameters ($q_i - q_r$) and the attenuation parameters (Q) are displayed in Table 5.

Estimates of station corrections are also similar based on the horizontal components as those based on the vertical component.

The two stations that stick out are station god and hvo with a high relative station correction ($\approx 3 - 4$). The estimated relative radiation patterns are also similar (Figures A8 and A9). We refer the reader to Figures A6 and A7 and Table 6 for numerical values of the station correction parameters for the horizontal components.

7 DISCUSSION

We have measured the time-space variation of tremor associated with the 2010 Eyjafjallajökull summit eruption based on differential-phase information. In the following, we discuss the spatial and amplitude variation of this tremor.

The beginning of the 2010 Eyjafjallajökull is similar to the prelude to eruption at other volcanoes in Iceland, i.e. Krafla (*Brandsdóttir and Einarsson*, 1992), Grímsvötn (*Vogfjörd et al.*, 2005) and Bárdarbunga (*Einarsson and Brandsdóttir*, 1984). An intense and short microearthquake precursory volcano-tectonic swarm (*Tarasewicz et al.*, 2012b) is accompanied by increased tremor levels at a wide range of frequencies that precedes steady eruption tremor at lower frequencies (0.5-10 Hz).

The tremor was strictly associated with the eruption itself; it began when the eruption started and faded out in the eruptions waning stages. Tremor was continuous in time with varying amplitude, distributed in frequency between about 0.5 Hz and 5 Hz or 10 Hz. This description is similar to other volcanoes, e.g., tremor associated with the unrest at Katla volcano in 2011 (*Sgattoni et al.*, 2017), tremor during the Grímsvötn eruption in 2004 (*Vogfjörd et al.*, 2005) and tremor observed during the Krafla Fires (*Brandsdóttir and Einarsson*, 1992). Levels of tremor were lower in amplitude and concentrated at lower frequencies during the explosive phases I and III, compared to the effusive-explosive phase II. A similar behavior, a shift of the main tremor to lower frequencies during the explosive phase, has been observed at Mt. Etna in Italy (*Cannata et al.*, 2008). Also, *Thompson et al.* (2002) found a that the tremor shifted to lower frequencies during the explosive phase of the 1999 Shishaldin eruption, Alaska.

Features of the temporal variation of the tremor amplitude during the summit eruption correlate with the four main phases (see Figure 2) of the eruption as defined by (*Gudmundsson et al.*, 2012). During the initial explosive phase (I) tremor intensity varied and included strong tremor bursts that can be associated with subsequent flooding in the lowlands north and west of the volcano (see Figures 3 and 4). It is probable that this phase of the eruption, and the tremor associated with it, was dominated by explosive activity due to the interaction between magma and melt water from the overlying glacier. During the following mixed effusive-explosive phase (II), a 3 km long

lava flow within the caldera drained through its northern rim and explosive activity was relatively weak (*Gudmundsson et al.*, 2012). However, the tremor intensity increased and it was redistributed towards higher frequencies. This negative correlation between eruptive plume height and tremor intensity can also be found in the variation within this phase of the eruption (compare Figure 3 to Figure 2a of *Gudmundsson et al.* (2012). A second explosive phase (III) started on May 5^{th} with ash changing to a slightly more evolved and possibly more volatile-rich (trachytic) composition (*Sigmarsson et al.*, 2011). While eruption intensity and plume height increased during this phase, tremor intensity declined slowly but steadily. The negative correlation between plume height and tremor intensity during phases II and III suggests that effusion generates tremor more efficiently than explosive activity near the surface. *Hibert et al.* (2015) found a linear relationship between effusion rate and volcanic tremor during several summit eruptions at Piton del la Fournaise. They found no such correlation with infrasound records. During the final phase (IV), both eruption and tremor intensity dropped rapidly.

The location likelihood of the tremor using the probabilistic inference method of Li et al. (2019) resulted in a very stable location in the 0.5-1 Hz frequency band, a somewhat less stable location in the 1-2 Hz frequency band, and an unstable location in the 2-4 frequency band. The steady reduction of location stability with increasing frequency may be explained by increasing vigour of the scattering suffered by propagating waves from the tremor source with frequency. The low-frequency tremor (0.5-2 Hz) emanated from a single dominant source, which cannot be distinguished from the main eruption site throughout the course of the eruption. The daily scatter of this location reflects the uncertainty of the location and is less than a kilometer in the lowest frequency range. With a daily resolution, any events with a shorter duration than that cannot be resolved. We do not exclude the presence of other sources for the higher frequencies. In fact, the average tremor location in the frequency range between 2 and 4 Hz is substantially displaced from that of the lower frequencies and lies close to the northern caldera rim where floodwater and lava drained down the Gígjökull glacial stream (see Figure 6). It is therefore tempting to associate the higher frequencies in the tremor with either flooding or the lava flow. However, due to a high level of scatter in the daily high-frequency locations it is questionable if this displacement of the source

is significant, the flooding only occurred in the early stages of the eruption and the effusive activity is concentrated in phase II of the eruption that spans less than half of the eruption's duration.

We have located the tremor bursts in the early stages of the eruption with a time resolution of one hour (in the 0.5-2 Hz frequency range). The locations are similar to the average tremor-source location (see Figure 6), although they are naturally less precisely and stably estimated due to lesser redundancy in data over a shorter time period. Although these bursts (see Figure 4) are clearly associated with jökulhlaups (*Magnússon et al.*, 2012), this suggests that they have little to do with the floodwater, but rather that the floods are a consequence of increased ice melting due to enhanced eruptive activity. Some of the floodwater may have accumulated before flooding. Perhaps the presence of accumulated water caused enhanced interaction with magma during these relatively short tremor bursts.

We have analyzed the amplitude behavior of the recorded tremor with distance and time, by measuring power ratios between each of the recordings and the recording at a reference station. This allows us to separate variation in the tremor from variation in local noise by assuming independence of the tremor and noise signals. This is important as some of the temporarily deployed seismographs were installed in very noisy conditions (in particular station sel that had a constant noise at 5 Hz). We find that the power ratios vary significantly (by up to a factor of 7) between the 10 epochs spanning the eruption period (Table 3), while remaining relatively constant within each epoch (see Figure 7, A1, A2 and A3).

Since the tremor-source location at frequencies between 0.5 and 2 Hz is found to be stable with time based on independent data (i.e. phase and not amplitude or power data) we conclude that the observed variation in the power ratios must be due to either changes in the physical properties of the rocks, that waves in the tremor pass through, or changes in the nature of the source. The former must be considered unlikely. It is difficult to envisage changes in relative power by a factor of 7 over time due to path averaged changes of attenuation or spreading of waves from a single, stable source. Therefore, we conclude that some aspect of the tremor-source radiation has changed with time. This could reflect changes in the horizontal radiation pattern of the source, or changes in the depth of the source and in the wave content of the tremor. Since we find that the tremor consists

mostly of surface waves at the analyzed frequencies we conclude that the observed variation with time of power ratios at all stations is most likely due to changes in the radiation of the source.

Analyses of tremor amplitude often assume isotropic radiation. The argument can be that the diffusive nature of the scattering process will mix any directivity of the source (*Morioka et al.*, 2017). This appears not to be the case at Eyjafjallajökull and points out the need to consider potential variation of the power radiation when locating tremor based on amplitude.

We have estimated a stable epicentre of the tremor source in two independent frequency ranges, 0.5-1 Hz and 1-2 Hz and also obtained redundant estimates of logarithmic amplitude decay of the tremor in the same frequency ranges within 10 different epochs of the eruption. Using these data we can estimate the path averaged differential attenuation between the reference station and each of the other seismic stations from which we have observations of tremor power. This, in turn, allows us to estimate path averaged attenuation coefficients for each station. Estimates of path averaged attenuation coefficients range from $Q \approx 10 - 20$ for some of the shorter paths to $Q \approx 20 - 50$ for the distal paths based on the vertical component of motion and somewhat lower based on the horizontal components. These are indications of strong attenuation, but within the range of $Q = 10 - 100$ found in volcanic regions (see e.g. *Kumagai et al.*, 2018; *Del Pezzo et al.*, 2006; *Gudmundsson et al.*, 2004). The lower estimates based on horizontal components of motion may indicate that both Rayleigh and Love waves are present in the tremor, scattered so that they are mixed between the horizontal components, and that the quality factor, Q, is lower for Love waves than Rayleigh waves.

We have also estimated the rate of decay of the tremor with distance due to geometrical spreading. We have simply allowed for a decay described by a power law, but also allowed for frequency-independent station corrections. This parameterization is similar to that commonly used in analysis of tremor amplitudes (e.g. *Battaglia and Aki*, 2003; *Battaglia et al.*, 2005), but the analysis is admittedly simplistic. These station corrections should not be seen as corrections for effects of structure beneath each station, but rather as a correction for the entire path between source and station. They can contain frequency-dependent effects of multipathing and scattering, focusing and defocusing along each path, as well as frequency dependent site amplification. Note that, having

estimated differential attenuation, we can correct for it, and thus have many redundant measurements of the decay rate of relative power with distance and relative station corrections for each of ten epochs for which we have data at each of the stations. We have not been able to calibrate the station corrections with independent data as we have not found earthquakes located in the tremor-source region with a useful signal-to-noise ratio in the frequency range of the tremor. We find, upon application of Occams razor, i.e., by seeking the power-law exponent that yields the smallest possible variation of station corrections, a power-law exponent of $a \approx 0.5$ (see equation 8). This is consistent with tremor primarily propagating as surface waves. The station corrections for the vertical component are plotted against azimuth and distance in Figure 9 (for the horizontal components see Figures A6 and A7). No systematic behavior is apparent with azimuth. Their behavior with distance suggests a steady increase with increasing distance for those of the stations that are near Eyjafjallajökull volcano, but not for the distal stations which might indicate a change of the wave content in the tremor with distance. However, that would require an effective decay rate slower than that of surface waves so that the near stations have been overcompensated by the surface-wave decay requiring recompensation in the station corrections. Such distance behavior is neither found in body waves nor near-field displacement terms.

We find that differential attenuation increases approximately linearly with horizontal distance from the tremor source for those of the stations that are in the near vicinity of Eyjafjallajökull volcano. This holds for analyses of all three components of the tremor records (see Figures 8, A4 and A5). That is consistent with tremor primarily composed of surface waves. If the tremor consisted primarily of body waves, then the depth variation of attenuation would control this behavior with distance. A concentration of attenuation near the surface, which is likely (*Kumagai et al.*, 2018), would in that case lead to a reduced rate of increase of differential attenuation with distance, ultimately a weakening, simply because the incidence angles of the body waves near the surface decrease with distance. Therefore, this corroborates that the 2010 Eyjafjallajökull tremor consists mostly of surface waves.

Surface waves around 1 Hz at Eyjafjallajökull have phase velocity around 1.5 km/s and a wavelength of about 1.5 kilometers based on extrapolation of the results of *Benediktsdóttir et al.*

(2017). The eigenfunctions of fundamental-mode surface waves with that wavelength have energy concentrated in the top 0.5-1 km of the crust. Thus, if the surface waves are fundamental mode, they are most effectively excited quite near the surface, i.e. approximately in the top kilometer or less. If they consisted of higher modes, the group velocity would be expected to be higher than that which best concentrates the likelihood of epicentral locations (1.3 km/s). Therefore, we estimate that the source lies in the top 1 km of the crust.

We find that the power in the tremor was generally stronger on the vertical component than the horizontals, although the power on the three components is sometimes comparable. This is consistent with tremor containing both Rayleigh and Love waves (the definition of both becomes unclear in a scattering medium). If the tremor consisted of body waves this would imply significant P-wave content. Instantaneous particle motion is not diagnostic of this in a strongly scattering medium at high frequency. For example, *Neuberg et al.* (1994) demonstrated failure of the particle motion of P waves at Stromboli volcano to point to the source at frequencies higher than about 0.5 Hz and very short distance (1500 m). Neither is time-averaged particle motion diagnostic, since the same interference pattern of scattered surface waves is present at all times if the source remains stationary and the medium does not change with time.

With the tremor dominated by surface waves, we cannot determine the depth of its source (other than to constrain it through the depth distribution of their eigenfunctions). If the tremor did contain a significant component of body waves, then the depth of that component could possibly be determined based on the amplitude distribution with distance by matching that with the distance behavior predicted by a one-dimensional velocity model. Similarly, the depth could be estimated using the differential-time information contained in correlograms by back projecting them, or their rendition as a probability density, in 3D using a travel-time table based on the same one-dimensional model. In general, this would require more data and it does require substantial knowledge about the average velocity model. Ideally, the velocity model should be three dimensional. Using differential-phase information in this way becomes ambiguous in that it becomes difficult to distinguish a correlation peak of a minor component of the wave field and a secondary scattered arrival if the scattering process is not perfectly diffuse (uniform, dense and isotropic).

Estimating depth from amplitudes or power has many degrees of freedom (velocity model) and typically involves relatively few data. It also becomes ambiguous in that the tremor may contain both P and S waves and the effects of a scattering process on polarity remains unclear. We have not attempted this with the Eyjafjallajökull data.

If the source were non-isotropic in the same fashion during the entire time-span of the eruption, then that variation would be accounted for in the station correction parameter. The estimated power-radiation pattern is therefore a measure of the deviation of a mean power-radiation pattern, relative to station *fag*. Therefore, it is not possible to link the pattern in Figure 10 to an absolute power-radiation pattern.

Phase I and epoch 1 cover the same time span. Phase II spans epochs 2-6, phase III spans epochs 7-9 and a part of 10 and phase IV spans rest of epoch 10. The relative power-radiation pattern is approximately circular, i.e. isotropic, in epochs 1,8,9 and 10. These epochs cover phases where the activity was explosive (I and III) and when the activity was waning (IV). During phase II, the activity was effusive with low-discharge and the relative power-radiation pattern was highly variable.

8 CONCLUSIONS

We have described, analysed the amplitude of, and located the tremor associated with the 2010 Eyjafjallajökull summit eruption based on differential-phase information. The main conclusions are:

(i) The character of eruptive tremor during the 2010 Eyjafjallajökull eruption resembled that during many other eruptions in Icelandic volcanoes. It was continuous in time with varying amplitude and distributed in frequency between about 0.5 and 5 or 10 Hz.

(ii) The negative correlation between plume height and tremor intensity during phases II and III suggests that effusion generates tremor more efficiently than explosive activity at the surface.

(iii) The low-frequency tremor (0.5-2 Hz) emanated from a single dominant source epicentre, which cannot be distinguished from the main eruption site throughout the course of the eruption.

(iv) Tremor bursts during the first days of the eruption that can clearly be associated with

jökulhlaups do not distinguish themselves from the epicentral location of the tremor as a whole and the tremor bursts, therefore, have little to do with the floodwater itself. Instead, the floods appear to be a consequence of increased ice melting due to enhanced eruptive activity, i.e., enhanced tremor.

(v) Observed variation with time of power ratios at all stations is most likely due to changes in the radiation of the source.

(vi) The path averaged attenuation quality factor is $Q \approx 10-20$ for some of the nearby stations and $Q \approx 20-50$ for the distal stations based on the vertical component. It is somewhat lower for the horizontal components indicating that the tremor consists of a mix of Love and Rayleigh waves and that the quality factor is lower for Love than Rayleigh waves.

(vii) The 2010 Eyjafjallajökull tremor consists mostly of surface waves.

(viii) The source lies in the top kilometer of the crust.

ACKNOWLEDGMENTS

This work was a part of the Volcano Anatomy project funded by the Icelandic Research Fund. We thank Martin Hensch, Sveinbjörn Steinthórsson, Thorsteinn Jónsson, Benedikt Ófeigsson, and the helicopter crew of the Icelandic Coast Guard for help with deploying and maintaining seismometers around Eyjafjallajökull. We are indebted to the Icelandic Meteorological Office for providing data from their permanent network monitoring network. The majority of the figures was created using the Generic Mapping Tools (*Wessel et al.*, 2013).

REFERENCES

Ágústsdóttir, T., J. Woods, T. Greenfield, R. Green, R. White, T. Winder, B. Brandsdóttir, S. Steinthórsson, and H. Soosalu (2016), Strike-slip faulting during the 2014 Bárdarbunga-Holuhraun dike intrusion, central Iceland, *Geophys. Res. Lett.*, *43*(4), 1495–1503.

Aki, K., M. Fehler, and S. Das (1977), Source mechanism of volcanic tremor: fluid-driven crack models and their application to the 1963 Kilauea eruption, *J. Volcanol. Geotherm. Res.*, *2*(3), 259–287.

Ballmer, S., C. Wolfe, P. Okubo, M. Haney, and C. Thurber (2013), Ambient seismic noise interferometry in Hawai'i reveals long-range observability of volcanic tremor, *Geophys. J. Int.*, p. ggt112.

Baptie, B., R. Luckett, and J. Neuberg (2002), Observations of low-frequency earthquakes and volcanic tremor at Soufrière Hills Volcano, Montserrat, *Geological Society, London, Memoirs*, *21*(1), 611–620.

Battaglia, J., and K. Aki (2003), Location of seismic events and eruptive fissures on the piton de la fournaise volcano using seismic amplitudes, *J. Geophys. Res.*, *108*(B8).

Battaglia, J., K. Aki, and V. Ferrazzini (2005), Location of tremor sources and estimation of lava output using tremor source amplitude on the piton de la fournaise volcano: 1. location of tremor sources, *J. Volcanol. Geotherm. Res.*, *147*(3-4), 268–290.

Benediktsdóttir, Á., O. Gudmundsson, B. Brandsdóttir, and A. Tryggvason (2017), Ambient noise tomography of Eyjafjallajökull volcano, Iceland, *J. Volcanol. Geotherm. Res.*, *347*, 250–263.

Brandsdóttir, B., and P. Einarsson (1992), Volcanic tremor and low-frequency earthquakes in Iceland, in *Volcanic seismology*, pp. 212–222, Springer.

Cannata, A., A. Catania, S. Alparone, and S. Gresta (2008), Volcanic tremor at Mt. Etna: Inferences on magma dynamics during effusive and explosive activity, *J. Volcanol. Geotherm.Res.*, *178*(1), 19–31.

Chernov, L., and R. Silverman (1960), *Wave propagation in a random medium*, McGraw-Hill, New York.

Chouet, B. (1985), Excitation of a buried magmatic pipe: a seismic source model for volcanic tremor, *J. Geophys. Res.*, *90*(B2), 1881–1893.

Dahm, T., and B. Brandsdóttir (1997), Moment tensors of microearthquakes from the Eyjafjallajökull volcano in South Iceland, *Geophys. J. Int.*, *130*(1), 183–192.

Del Pezzo, E., F. Bianco, and L. Zaccarelli (2006), Separation of Qi and Qs from passive data at Mt. Vesuvius: A reappraisal of the seismic attenuation estimates, *Phys. Earth Planet Int.*, *159*(3-4), 202–212.

Di Grazia, G., S. Falsaperla, and H. Langer (2006), Volcanic tremor location during the 2004 mount etna lava effusion, *Geophys. Res. Lett.*, *33*(4).

Droznin, D., N. Shapiro, S. Y. Droznina, S. Senyukov, V. Chebrov, and E. Gordeev (2015), Detecting and locating volcanic tremors on the Klyuchevskoy group of volcanoes (Kamchatka) based on correlations of continuous seismic records, *Geophys. J. Int.*, *203*(2), 1001–1010.

Eibl, E. P., C. Bean, I. Jónsdóttir, Á. Höskuldsson, T. Thordarson, D. Coppola, T. Witt, and T. Walter (2017), Multiple coincident eruptive seismic tremor sources during the 2014–2015 eruption at Holuhraun, Iceland, *J. Geophys. Res.*, *122*(4), 2972–2987.

Einarsson, P. (2018), Short-term seismic precursors to Icelandic eruptions 1973-2014., *Front. Earth Sci.*, *6*, 45.

Einarsson, P., and B. Brandsdóttir (1984), Seismic activity preceding and during the 1983 volcanic eruption in Grímsvötn, Iceland, *Jökull*, *34*, 13–23.

Einarsson, P., and Á. Hjartardóttir (2015), Structure and tectonic position of the Eyjafjallajökull volcano, S. Iceland, *Jökull*, *65*.

Einarsson, P., B. Brandsdóttir, M. Gudmundsson, H. Björnsson, K. Grínvold, and F. Sigmundsson (1997), Center of the Iceland hotspot experiences volcanic unrest, *Eos*, *78*(35), 369–375.

Fehler, M. (1983), Observations of volcanic tremor at mount st. helens volcano, *J. Geophys. Res.*, *88*(B4), 3476–3484.

Fujita, E. (2008), Banded tremor at Miyakejima volcano, Japan: Implication for two-phase flow instability, *J. Geophys. Res.*, *113*(B4).

Furumoto, M., T. Kunitomo, H. Inoue, I. Yamada, K. Yamaoka, A. Ikami, and Y. Fukao (1990), Twin sources of high-frequency volcanic tremor of Izu-Oshima Volcano, Japan, *Geophys. Res. Lett.*, *17*(1), 25–27.

Furumoto, M., T. Kunitomo, H. Inoue, and K. Yamaoka (1992), Seismic image of the volcanic tremor source at Izu-Oshima volcano, Japan, in *Volcanic Seismology,IAVCEI Proc. Volcanol. 3*, edited by P. Gasparini, R. Scarpa, and K. Aki, pp. 201–211, Springer.

Gottschämmer, E., and I. Surono (2000), Locating tremor and shock sources recorded at bromo volcano, *J. Volcanol. Geotherm. Res.*, *101*(1), 199–209.

Gudmundsson, M., R. Pedersen, K. Vogfjörd, B. Thorbjarnardóttir, S. Jakobsdóttir, and M. Roberts (2010), Eruptions of Eyjafjallajökull Volcano, Iceland, *Eos, Transactions American Geophysical Union*, *91*(21), 190–191.

Gudmundsson, M., T. Thordarson, Á. Höskuldsson, G. Larsen, H. Björnsson, F. Prata, B. Oddsson, E. Magnússon, T. Högnadóttir, G. Petersen, et al. (2012), Ash generation and distribution from the april-may 2010 eruption of eyjafjallajökull, iceland, *Scientific reports*, *2*, 572.

Gudmundsson, Ó., and B. Brandsdóttir (2010), Geothermal noise at Ölkelduháls, SW Iceland, *Jökull*, *60*, 89–102.

Gudmundsson, Ó., J. Davies, and R. Clayton (1990), Stochastic analysis of global traveltime data: mantle heterogeneity and random errors in the ISC data, *Geophys. J. Int.*, *102*(1), 25–43.

Gudmundsson, Ó., D. Finlayson, I. Itikarai, Y. Nishimura, and W. Johnson (2004), Seismic attenuation at Rabaul volcano, Papua new Guinea, *J. Volcanol. Geotherm. Res*, *130*(1-2), 77–92.

Haney, M. (2010), Location and mechanism of very long period tremor during the 2008 eruption of Okmok Volcano from interstation arrival times, *J. Geophys. Res.*, *115*(B10).

Hibert, C., A. Mangeney, M. Polacci, A. Di Muro, S. Vergniolle, V. Ferrazzini, A. Peltier, B. Taisne, M. Burton, T. Dewez, et al. (2015), Toward continuous quantification of lava extrusion rate: Results from the multidisciplinary analysis of the 2 January 2010 eruption of Piton de la Fournaise volcano, La Réunion, *J. Geophys. Res.*, *120*(5), 3026–3047.

Hjaltadóttir, S., K. S. Vogfjörd, S. Hreinsdóttir, and R. Slunga (2015), Reawakening of a volcano: Activity beneath Eyjafjallajökull volcano from 1991 to 2009, *J. Vol. Geoth. Res.*, *304*, 194–205.

Hofstetter, A., and S. Malone (1986), Observations of volcanic tremor at Mount St. Helens in April and

May 1980, *Bull. Seismol. Soc. Am.*, *76*(4), 923–938.

Hooper, A., R. Pedersen, and F. Sigmundsson (2009), Constraints on magma intrusion at Eyjafjallajökull and Katla volcanoes in Iceland, from time series SAR interferometry, in *The VOLUME Project–Volcanoes: Understanding Subsurface Mass Movement.*, edited by C. Bean, A. Braiden, I. Lokmer, F. Martini, and G. O'Brien, pp. 13–24.

Hurst, A. (1992), Stochastic simulation of volcanic tremor from Ruapehu, *J. Volcanol. Geotherm. Res.*, *51*(3), 185–198.

Icelandic Meteoroglogical Office (2019a), Database of the Icelandic Meteoroglogical Office, afgreidsla nr. 2019-02-11/01.

Icelandic Meteoroglogical Office (2019b), Database of the Icelandic Meteoroglogical Office, afgreidsla nr. 2019-03-01/01.

Jakobsdóttir, S. (2008), Seismicity in Iceland: 1994–2007, *Jökull*, *58*, 75–100.

Jeddi, Z., A. Tryggvason, and Ó. Gudmundsson (2016), The Katla volcanic system imaged using local earthquakes recorded with a temporary seismic network, *J. Geophys. Res.*, *121*(10), 7230–7251.

Jeddi, Z., Ó. Gudmundsson, and A. Tryggvason (2017), Ambient-noise tomography of Katla volcano, south Iceland, *J. Volcanol. Geotherm. Res.*, *347*, 264–277.

Jónsson, B. (1774), *Annalar Thess Froma og velvitra Sauluga Biørns Jonssonar a Skardsau Fordum Løgrettumanns i Hegranes-sýslu*, 186 pp., Skardsárannáll, available at: http://baekur.is/bok/000043701/Annalar_THess_froma_og.

Julian, B. R. (1994), Volcanic tremor: nonlinear excitation by fluid flow, *J. Geophys. Res.*, *99*(B6), 11,859–11,877.

Karlsdóttir, S., Á. Gylfason, Á. Höskuldsson, B. Brandsdóttir, E. Ilyinskaya, M. Gudmundsson, and T. Högnadóttir (2012), in *The 2010 Eyjafjallajökull eruption, Iceland, IMO, IES and NCIP-DCPEM Rport to ICAO 2012*, edited by B. Thorkelsson, p. 209.

Konstantinou, K. I., and V. Schlindwein (2003), Nature, wavefield properties and source mechanism of volcanic tremor: a review, *J. Volcanol. Geotherm. Res.*, *119*(1), 161–187.

Kumagai, H., J. Londoño, Y. Maeda, C. López Velez, and R. Lacson Jr (2018), Envelope widths of volcano-seismic events and seismic scattering characteristics beneath volcanoes, *J. Geophys. Res.*, *123*(11), 9764–9777.

Larsen, G., A. Dugmore, and A. Newton (1999), Geochemistry of historical-age silicic tephras in Iceland, *The Holocene*, *9*(4), 463–471.

Li, K., G. Sgattoni, H. Sadeghisorkhani, R. Roberts, and O. Gudmundsson (2017a), A double-correlation tremor-location method, *Geophys. J. Int.*, *208*(2), 1231–1236.

Li, K. L., H. Sadeghisorkhani, G. Sgattoni, O. Gudmundsson, and R. Roberts (2017b), Locating tremor using stacked products of correlations, *Geophys. Res. Lett.*, *44*(7), 3156–3164.

Magnússon, E., M. Gudmundsson, M. Roberts, G. Sigurdsson, F. Höskuldsson, and B. Oddsson (2012), Ice-volcano interactions during the 2010 Eyjafjallajökull eruption, as revealed by airborne imaging radar, *J. Geophys. Res.*, *117*(B7).

Métaxian, J., P. Lesage, and J. Dorel (1997), Permanent tremor of masaya volcano, nicaragua: Wave field analysis and source location, *J. Geophys. Res.*, *102*(B10), 22,529–22,545.

Morioka, H., H. Kumagai, and T. Maeda (2017), Theoretical basis of the amplitude source location method for volcano-seismic signals, *J. Geophys. Res.*, *122*(8), 6538–6551.

Neuberg, J., R. Luckett, M. Ripepe, and T. Braun (1994), Highlights from a seismic broadband array on Stromboli volcano, *Geophys. Res. Lett.*, *21*(9), 749–752.

Neuberg, J., R. Luckett, B. Baptie, and K. Olsen (2000), Models of tremor and low-frequency earthquake swarms on Montserrat, *J. Vol. Geotherm. Res.*, *101*(1-2), 83–104.

Oddsson, B., M. Gudmundsson, B. Edwards, T. Thordarson, E. Magnússon, and G. Sigurdsson (2016), Subglacial lava propagation, ice melting and heat transfer during emplacement of an intermediate lava flow in the 2010 Eyjafjallajökull eruption, *Bull. Volcanol.*, *78*(7), 48.

Óskarsson, B. V. (2009), *The Skerin ridge on Eyjafjallajökull, south Iceland: Morphology and magma-ice interaction in an ice-confined silicic fissure eruption. Master's thesis.*, Faculty of Earth Sciences, University of Iceland, available at: http://hdl.handle.net/1946/4375.

Pedersen, R., and F. Sigmundsson (2004), InSAR based sill model links spatially offset areas of deformation and seismicity for the 1994 unrest episode at Eyjafjallajökull volcano, Iceland, *Geophys. Res. Lett.*, *31*(14).

Pedersen, R., and F. Sigmundsson (2006), Temporal development of the 1999 intrusive episode in the Eyjafjallajökull volcano, Iceland, derived from InSAR images, *Bull. Volcanol.*, *68*(4), 377–393.

Pedersen, R., F. Sigmundsson, and P. Einarsson (2007), Controlling factors on earthquake swarms associated with magmatic intrusions; Constraints from Iceland, *J. Vol. Geotherm. Res.*, *162*(1-2), 73–80.

Ripepe, M. (1996), Evidence for gas influence on volcanic seismic signals recorded at Stromboli, *J. Volcanol. Geotherm. Res.*, *70*(3), 221–233.

Schlindwein, V., J. Wassermann, and F. Scherbaum (1995), Spectral analysis of harmonic tremor signals at Mt. Semeru volcano, Indonesia, *Geophys. Res. Lett.*, *22*(13), 1685–1688.

Sgattoni, G., Ó. Gudmundsson, P. Einarsson, F. Lucchi, K. Li, H. Sadeghisorkhani, R. Roberts, and A. Tryggvason (2017), The 2011 unrest at katla volcano: Characterization and interpretation of the tremor sources, *J. Volcanol. Geotherm. Res.*, *338*, 63–78.

Sigmarsson, O., I. Vlastelic, R. Andreasen, I. Bindeman, J. Devidal, S. Moune, J. Keiding, G. Larsen, A. Höskuldsson, and T. Thordarson (2011), Remobilization of silicic intrusion by mafic magmas during the 2010 Eyjafjallajökull eruption, *Solid Earth*, *2*(2), 271–281.

Sigmundsson, F., S. Hreinsdóttir, A. Hooper, T. Árnadóttir, R. Pedersen, M. Roberts, N. Óskarsson, A. Au-

riac, J. Decriem, P. Einarsson, et al. (2010), Intrusion triggering of the 2010 Eyjafjallajokull explosive eruption, *Nature*, *468*(7322), 426–430.

Sigtryggsson, H., and E. Sigurdsson (1966), Earth Tremors from the Surtsey Eruption 1963–1965, *Surtsey Research Progress Report*, *2*, 131–138.

Soosalu, H., and B. Einarsson, P.and Thorbjarnardóttir (2005), Seismic activity related to the 2000 eruption of the Hekla volcano, Iceland, *Bull. Volc.*, *68*(1), 21–36.

Sturkell, E., F. Sigmundsson, and P. Einarsson (2003), Recent unrest and magma movements at Eyjafjallajökull and Katla volcanoes, Iceland, *J. Geophys. Res.*, *108*(B8).

Tarasewicz, J., R. White, B. Brandsdóttir, and B. Thorbjarnardóttir (2011), Location accuracy of earthquake hypocentres beneath Eyjafjallajökull, Iceland, prior to the 2010 eruptions, *Jökull*, *61*, 33–50.

Tarasewicz, J., R. White, A. Woods, B. Brandsdóttir, and M. Gudmundsson (2012a), Magma mobilization by downward-propagating decompression of the Eyjafjallajökull volcanic plumbing system, *Geophys. Res. Lett.*, *39*(19).

Tarasewicz, J., B. Brandsdóttir, R. White, M. Hensch, and B. Thorbjarnardóttir (2012b), Using microearthquakes to track repeated magma intrusions beneath the Eyjafjallajökull stratovolcano, Iceland, *J. Geophys. Res.*, *117*(B9).

Tarasewicz, J., R. White, B. Brandsdóttir, and C. Schoonman (2014), Seismogenic magma intrusion before the 2010 eruption of Eyjafjallajökull volcano, Iceland, *Geophys. J. Int.*, *198*(2), 906–921.

Thompson, G., S. R. McNutt, and G. Tytgat (2002), Three distinct regimes of volcanic tremor associated with the eruption of Shishaldin Volcano, Alaska 1999, *Bulletin of Volcanology*, *64*(8), 535–547.

Thorarinsson, S., S. Steinthórsson, T. Einarsson, H. Kristmannsdottir, and N. Oskarsson (1973), The eruption on Heimaey, Iceland, *Nature*, *241*(5389), 372.

Vogfjörd, K., S. Jakobsdóttir, G. Gudmundsson, M. Roberts, K. Ágústsson, T. Arason, H. Geirsson, S. Karlsdóttir, S. Hjaltadóttir, U. Ólafsdóttir, et al. (2005), Forecasting and monitoring a subglacial eruption in Iceland, *Eos, Transactions American Geophysical Union*, *86*(26), 245–248.

Wassermann, J. (1997), Locating the sources of volcanic explosions and volcanic tremor at Stromboli volcano (Italy) using beam-forming on diffraction hyperboloids, *Phys. Earth Planet. Inter.*, *104*(1-3), 271–281.

Wessel, P., W. Smith, R. Scharroo, J. Luis, and F. Wobbe (2013), Generic Mapping Tools: Improved version released, *EOS Trans. AGU*, *94*, 409–410.

APPENDIX A: ADDITIONAL FIGURES

A1 Slope analyses for all stations

Figures A1, A2 and A3 show power-spectral density for each station versus that of the reference station fag.

We estimated the geometrical spreading factor as described in the paper and found $a = 0.55 \pm 0.10$ and $a = 0.36 \pm 0.13$ for the radial and transverse components, respectively.

A2 Estimation of quality factor and station correction parameters

Figures A4 and A5 show differential Q as a function of horizontal distance to source for the transverse and radial components, respectively. Figures A6 and A7 show the station correction parameters for the transverse and radial components, respectively. Parameters shown here and derived quality factors (Q) and station corrections (γ) can be seen in Tables 4, 5 and 6.

A3 Relative power-radiation pattern for horizontal components

Figures A8 and A9 show the relative power-radiation pattern for the transverse and radial components, respectively. The pattern is a measure of the deviation from a mean power-radiation pattern, relative to station *fag*.

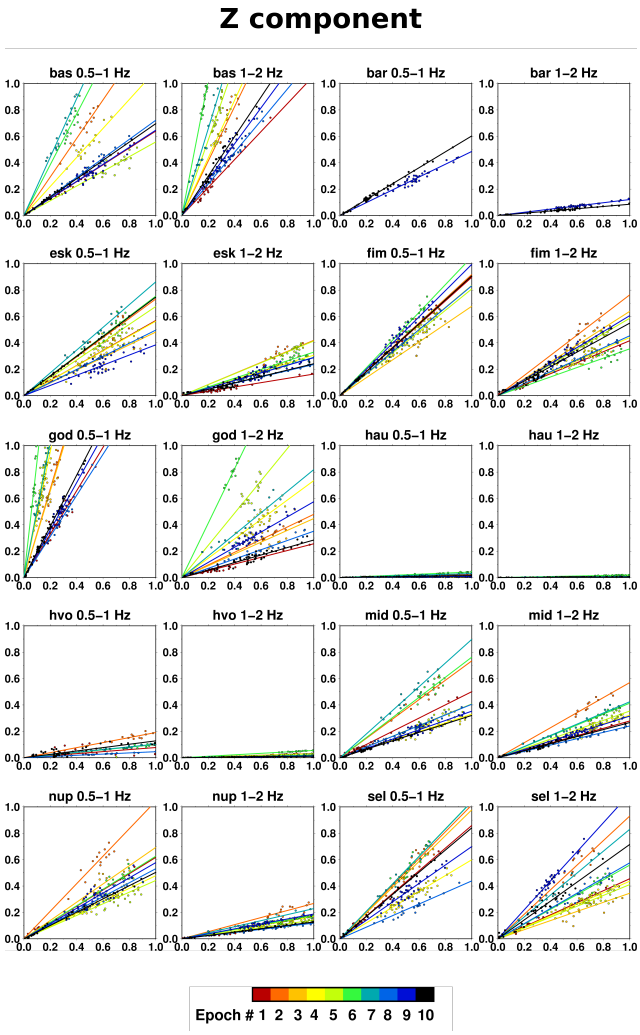

Figure A1. Power of the vertical component for all stations vs. the power of station fag during the entire eruption of Eyjafjallajökull, filtered in two frequency bands. Colour code is by epochs of the eruption as defined in this study (see Table 3). Each point on the plot is the mean power calculated over three hours.

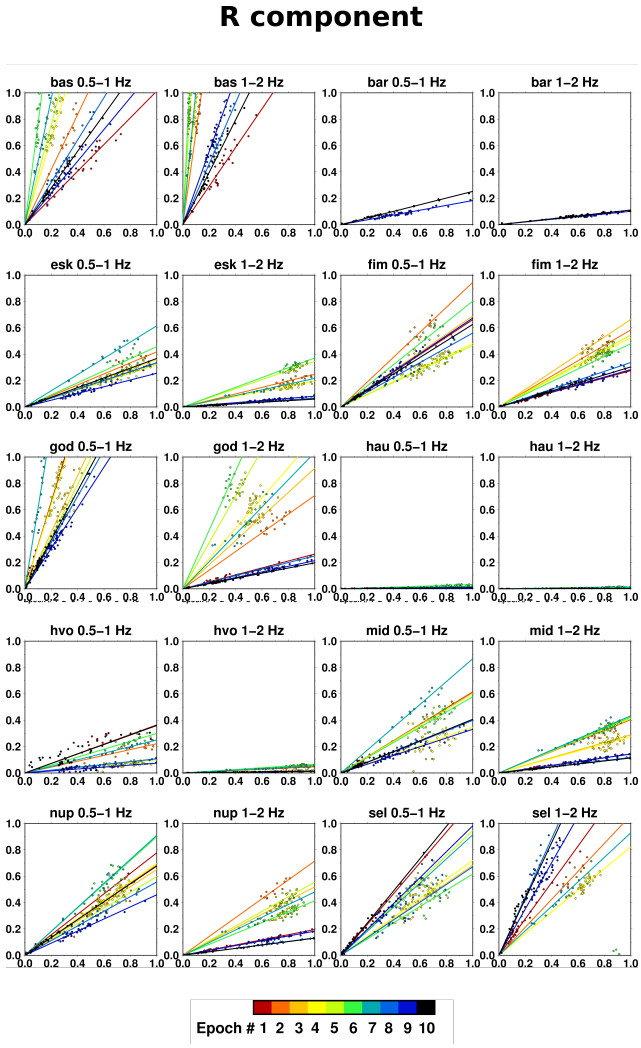

Figure A2. Power of the radial component for all stations vs. the power of station fag during the entire eruption of Eyjafjallajökull, filtered in two frequency bands. Colour code is by epochs of the eruption as defined in this study (see Table 3). Each point on the plot is the mean power calculated over three hours.

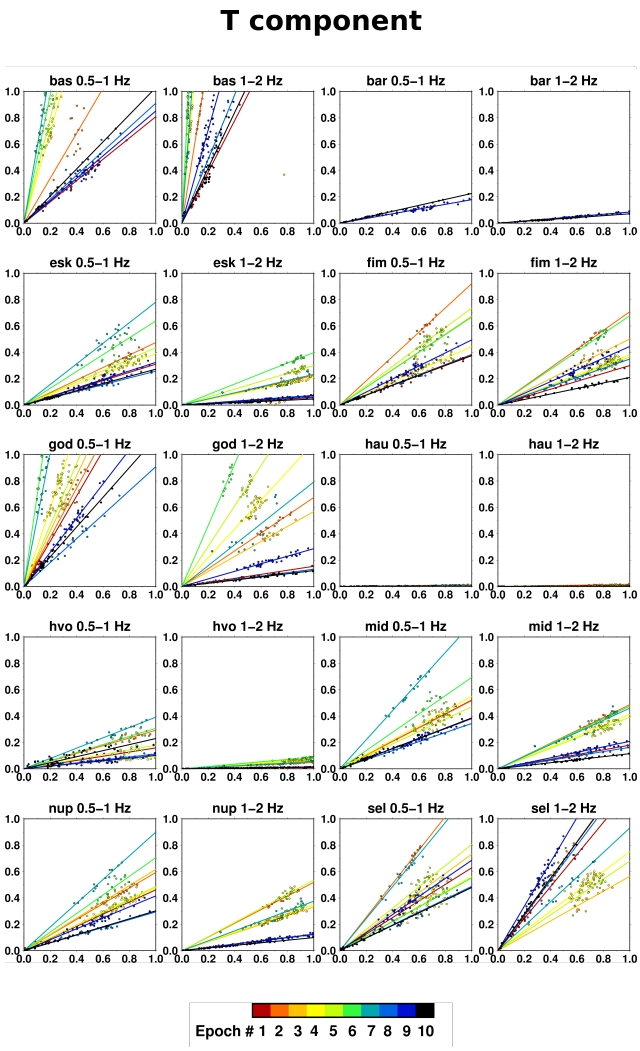

Figure A3. Power of the transverse component for all stations vs. the power of station fag during the entire eruption of Eyjafjallajökull, filtered in two frequency bands. Colour code is by epochs of the eruption as defined in this study (see Table 3). Each point on the plot is the mean power calculated over three hours.

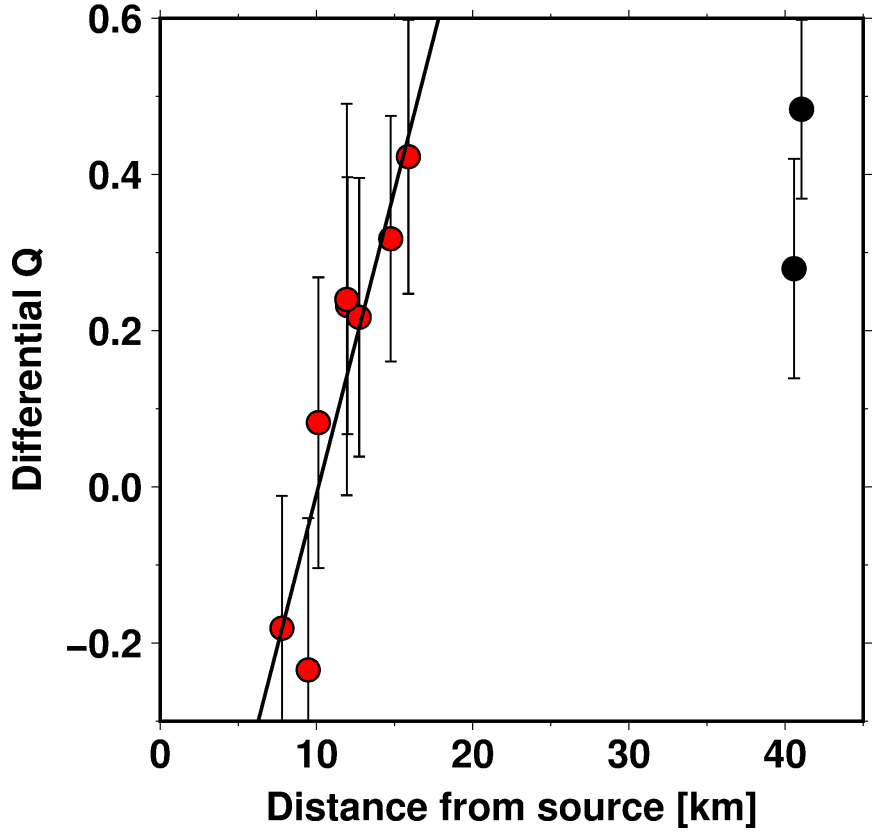

Figure A4. Differential quality factors as a function of distance from the source (horizontal) for the transverse component. Data for all stations (red circles) except hau and hvo (black circles) lie approximately on a straight line.

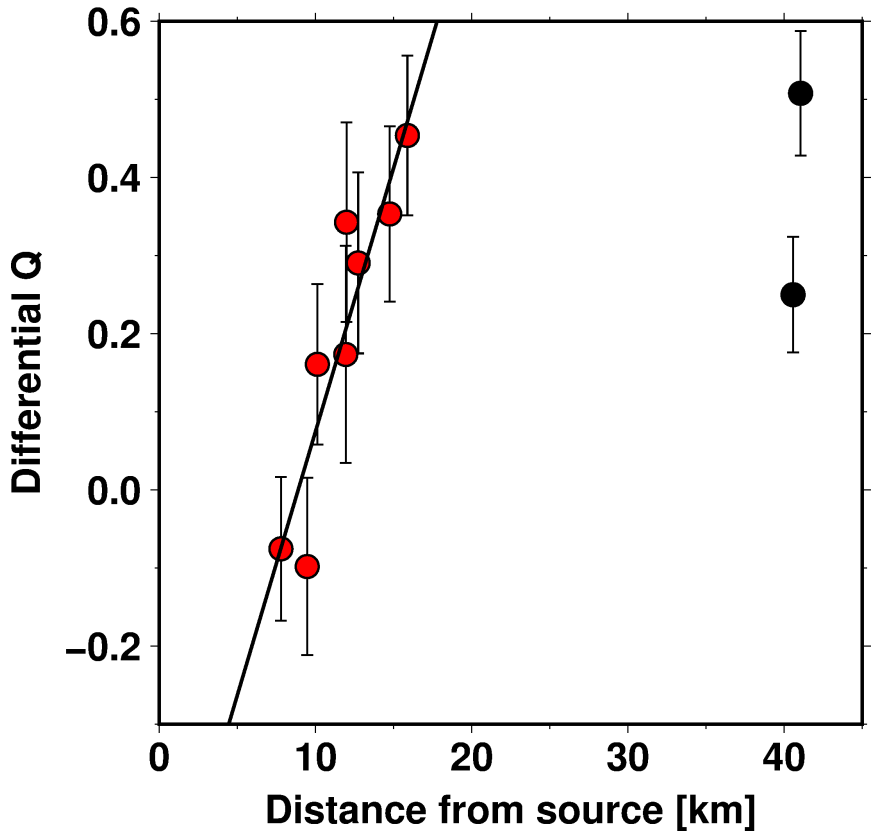

Figure A5. Differential quality factors as a function of distance from the source (horizontal) for the radial component. Data for all stations (red circles) except hau and hvo (black circles) lie approximately on a straight line.

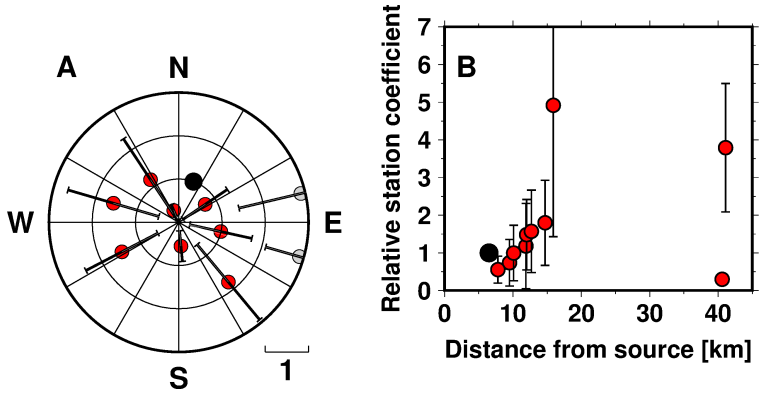

Figure A6. Transverse component. Estimates of relative station coefficients for each station (γ_i/γ_r) in a rose diagram (**A**) and as a function of distance away from eruption source (**B**). Black point represents the reference station *fag*. The gray point for station god plots off scale in **A**.

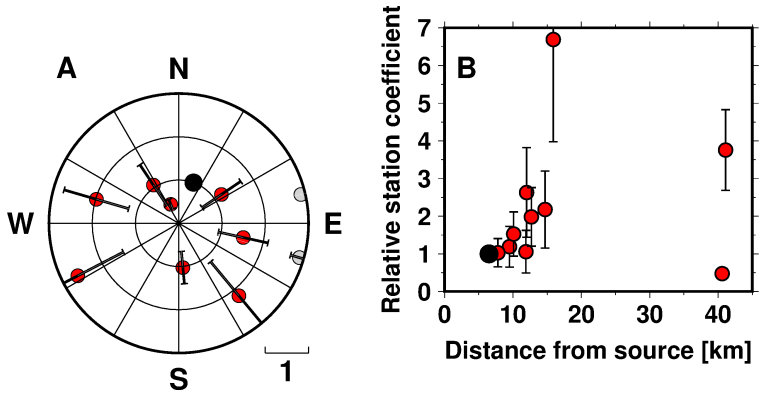

Figure A7. Radial component. Estimates of relative station coefficients for each station (γ_i/γ_r) in a rose diagram (**A**) and as a function of distance away from eruption source (**B**). Black point represents the reference station *fag*. The gray point for station god plots off scale in **A**.

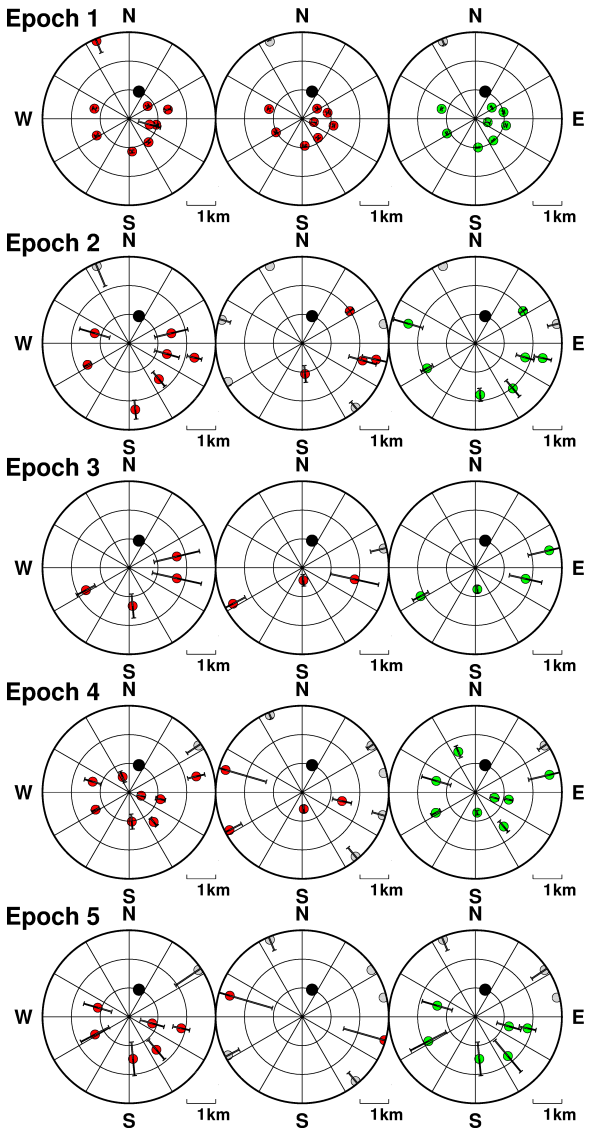

Figure A8. Transverse component. Estimates of the power-radiation pattern relative to station *fag* for 0.5-1 Hz (left), 1-2 Hz (middle), and a weighted mean of the two frequency intervals (right). Where only one measurement was available for one frequency interval, that value was taken as the weighted mean. The error bars are the estimated errors of power-spectral ratios (slope). *fag* is plotted as a larger black circle without an error bar.

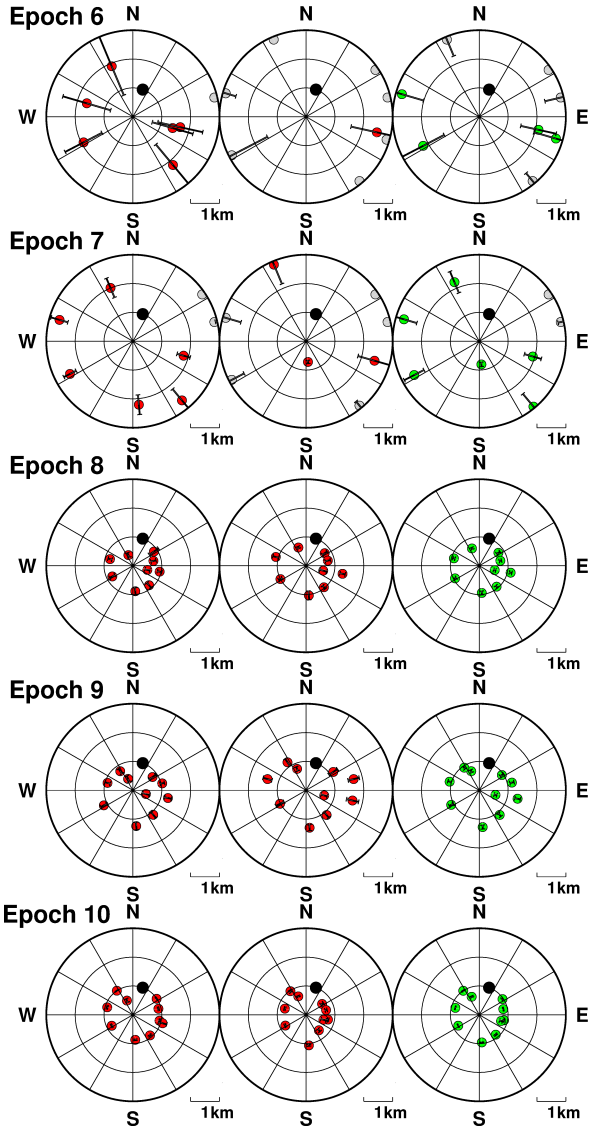

Figure A8. continued.

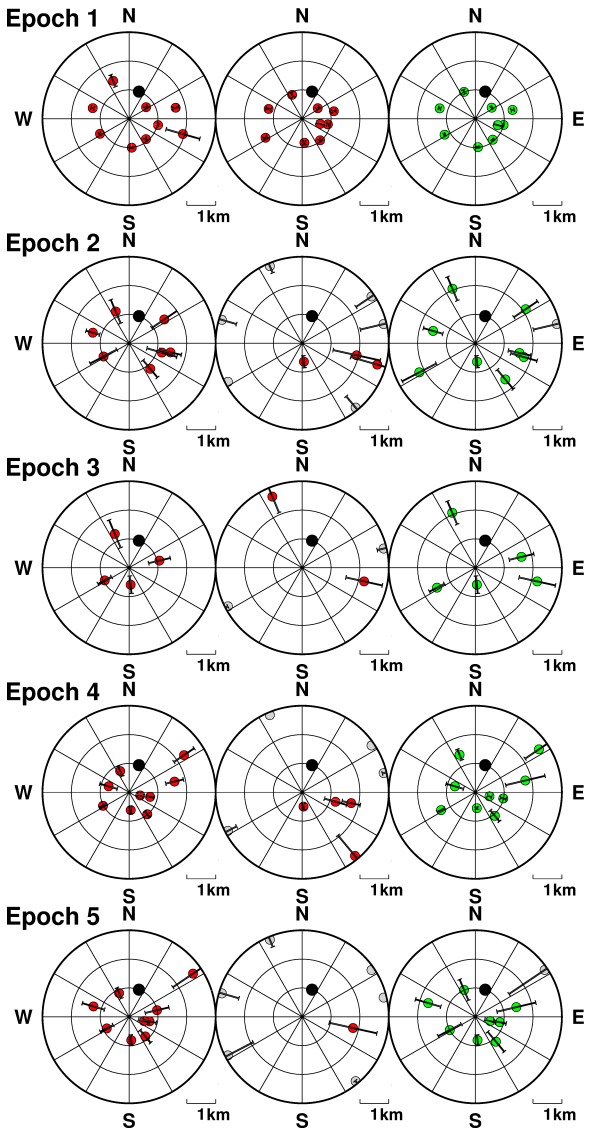

Figure A9. Radial component. Estimates of the power-radiation pattern relative to station *fag* for 0.5-1 Hz (left), 1-2 Hz (middle), and a weighted mean of the two frequency intervals (right). Where only one measurement was available for one frequency interval, that value was taken as the weighted mean. The error bars are the estimated errors of power-spectral ratios (slope). *fag* is plotted as a larger black circle without an error bar.

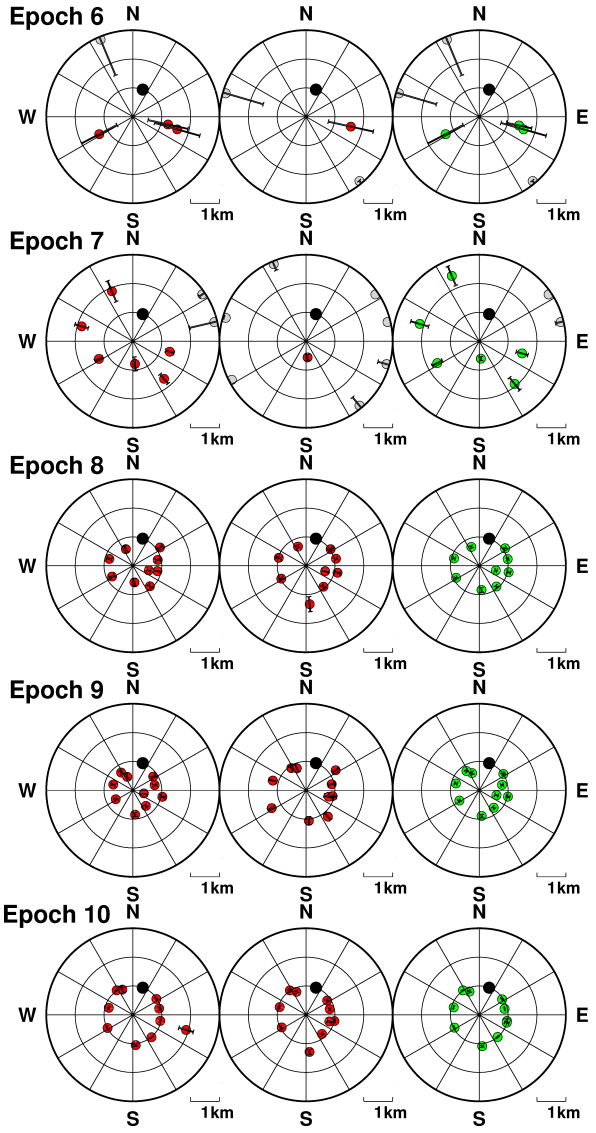

Figure A9. continued.